

THE DEVELOPMENT OF ZEOLITE PARTICLES FOR POSITRON IMAGING  
APPLICATIONS

by

DANIEL SCOTT PARSONS

A thesis submitted to the University of Birmingham for the degree of DOCTOR  
OF PHILOSOPHY

School of Chemistry  
College of Engineering and Physical Sciences  
University of Birmingham

January 2020

UNIVERSITY OF  
BIRMINGHAM

**University of Birmingham Research Archive**

**e-theses repository**

This unpublished thesis/dissertation is copyright of the author and/or third parties. The intellectual property rights of the author or third parties in respect of this work are as defined by The Copyright Designs and Patents Act 1988 or as modified by any successor legislation.

Any use made of information contained in this thesis/dissertation must be in accordance with that legislation and must be properly acknowledged. Further distribution or reproduction in any format is prohibited without the permission of the copyright holder.

## Abstract

The development of particles with diameters between 5 – 50  $\mu\text{m}$  are of interest for application as tracers in the positron imaging technique, positron emission particle tracking (PEPT).

Building on previous studies, the influence of ethanol and the intrapore cation content on the size and morphology of mordenite microparticles has been investigated. A method for producing monodisperse microspheres of the zeolite, gmelinite, has also been developed. Moreover, previously reported crystal growth conditions have been tailored to produce zeolite A and X crystals in the desired size range.

As fluorine-18 is a widely employed  $\beta^+$ -emitting isotope, reactivity between aqueous fluoride and zeolite Y, with different intrapore cations, has been studied. Fluorine environments in the zeolites, and the likely mechanism for the reaction, have been determined by MAS NMR spectroscopy. The essential role of Brønsted acids in mediating the reaction, and the promoting effect of divalent metal cations, have also been established.

Finally, the influence of applicable post-synthetic treatments (*viz.* divalent metal ion exchange, dealumination and iron(III) surface sorption) on fluoride uptake by large crystals, or particles, of mordenite, gmelinite and zeolites A and X has been investigated. Ultimately, the most suitable post-synthetic treatment for enhancing fluoride loadings on large particles of each zeolite has been determined.

## Acknowledgements

I would like to express my appreciation to the following people for their direct or indirect contributions to this work.

Firstly, I would like to thank my supervisors, Dr Joe Hriljac and Dr Andy Ingram, without whom this work would not have been possible. I would like to express gratitude for their invaluable mentorship, continued support and the many opportunities that I have been afforded throughout this project.

I would like to thank Dr David Apperley at the Durham Solid-state NMR service for recording the solid-state NMR spectra and for his invaluable expertise that shaped the NMR experiments. Many of the other analyses presented in this work would not have been possible without training by, and assistance from, the staff who maintain, or have maintained, the instruments used, so I would like to thank Mr Paul Stanley (SEM), Dr Jackie Deans (XRF & PXRD), Dr Louise Male (PXRD) and Mr Chris Stark (ICP-OES).

I would also like to acknowledge the many colleagues who strive to make the “fifth floor” a relaxed and friendly environment to work in. In particular, I would like to thank Ryan George and Dan Smith for the many laughs and good times over the past few years, whether in the lab, the pub or on our various other excursions.

Finally, I would like to thank those in my personal life for their continued and unwavering support in everything I do. Special thanks to my parents, my brother Ryan, my girlfriend Chloe, and my friends.

## Contents

CHAPTER 1: INTRODUCTION .....	1
1.1 Positron Emission Particle Tracking (PEPT) .....	1
1.1.1 Positron Emission Particle Tracking: The Fundamentals .....	1
1.1.2 PEPT: Visualising Chemical Engineering Processes .....	4
1.1.3 Conclusions .....	7
1.2 Speciation of Radionuclides: $^{18}\text{F}$ and $^{68}\text{Ga}$ .....	7
1.3 Zeolites .....	9
1.3.1 Introduction .....	9
1.3.2 Zeolite A (LTA) .....	10
1.3.3 Faujasite (FAU) .....	11
1.3.4 Mordenite (MOR) .....	13
1.3.5 Gmelinite (GME) .....	14
1.3.6 Chabazite (CHA) .....	15
1.3.7 Zeolite P (GIS) .....	16
CHAPTER 2: EXPERIMENTAL .....	18
2.1 Experimental Techniques .....	18
2.1.1 Hydrothermal Synthesis of Zeolites .....	18
2.1.2 Aqueous Ion Exchange .....	18
2.1.3 Adsorption .....	19
2.2 Characterisation .....	23
2.2.1 Powder X-ray Diffraction (PXRD) .....	23
2.2.1.1 Fundamental Crystallography .....	23
2.2.1.2 Powder X-ray Diffraction .....	24
2.2.2 X-ray Fluorescence (XRF) Spectrometry .....	27
2.2.3 Scanning Electron Microscopy .....	29
2.2.4 Nuclear Magnetic Resonance (NMR) Spectroscopy .....	30
2.2.4.1 Fundamental Concepts .....	30
2.2.4.2 The NMR Experiment .....	31
2.2.4.3 Magic-Angle Spinning (MAS) NMR Spectroscopy .....	32
2.2.4.4 Cross-Polarisation MAS NMR Spectroscopy .....	32
2.2.4.5 $^{29}\text{Si}$ MAS NMR Spectroscopy of Zeolites .....	33
2.2.5 Fluoride Ion-Selective Electrodes .....	34
2.2.6 Inductively Coupled Plasma Optical Emission Spectrometry (ICP-OES).....	35
CHAPTER 3: INVESTIGATIONS INTO MORDENITE MICROPARTICLES .....	37
3.1 Introduction .....	37
3.2 Experimental .....	39
3.2.1 Mordenite Synthesis: TEOS System .....	39

3.2.2 Mordenite Synthesis: Colloidal Silica System .....	40
3.2.3 Calcined Mordenite .....	40
3.2.4 Gallium Adsorption Experiments .....	40
3.2.5 Powder X-ray Diffraction (PXRD) .....	41
3.2.6 X-ray Fluorescence Spectrometry (XRF) .....	41
3.2.7 Scanning Electron Microscopy (SEM) .....	42
3.3 Results and Discussion .....	42
3.3.1 TEOS System: Effect of Varying the Gel Si/Al Ratio .....	42
3.3.2 TEOS System: Absence of TEA <sup>+</sup> .....	46
3.3.3 Colloidal Silica System .....	47
3.3.4 Colloidal Silica System: The Influence of Ethanol .....	50
3.3.5 TEOS System: The Influence of Ethanol .....	52
3.3.6 Sieving Efficacy .....	55
3.3.7 Gallium Uptake .....	57
3.4 Conclusions .....	60
CHAPTER 4: GROWING LARGE ZEOLITE CRYSTALS AND PARTICLES .....	62
4.1 Introduction .....	62
4.2 Experimental .....	63
4.2.1 Large Zeolite A and X Crystal Growths .....	63
4.2.2 Zeolite Y Crystal Growths .....	63
4.2.3 The Synthesis of GME Microspheres .....	64
4.2.4 Powder X-ray Diffraction (PXRD) .....	65
4.2.5 Scanning Electron Microscopy (SEM) .....	65
4.2.6 Sieving .....	65
4.3 Results and Discussion .....	66
4.3.1 Large Zeolite A Crystals .....	66
4.3.2 Large Zeolite X Crystals .....	69
4.3.3 Large Zeolite Y Crystals and the Associated Gel System .....	72
4.3.4 The Synthesis of Gmelinite Microspheres .....	77
4.3.5 Gmelinite Microspheres: The Role of Aging .....	81
4.4 Conclusions .....	86
CHAPTER 5: THE INFLUENCE OF INTRAPORE CATION ON FLUORIDE UPTAKE BY ZEOLITE Y .....	87
5.1 Introduction .....	87
5.2 Experimental .....	90
5.2.1 NH <sub>4</sub> -Y, Na-Y and H-Y .....	90
5.2.2 Synthesis of Dealuminated NH <sub>4</sub> -Y .....	90
5.2.3 Preparation of M <sub>x</sub> (NH <sub>4</sub> ) <sub>1-2x</sub> -Y and M <sub>x</sub> Na <sub>1-2x</sub> -Y by Ion Exchange .....	91
5.2.4 Batch Fluoride Adsorption Measurements .....	91
5.2.5 Batch Fluoride Adsorption Measurements for ICP-OES .....	92

5.2.6 Preparation of Acidic Fluoride Solutions .....	93
5.2.7 Powder X-ray Diffraction (PXRD) .....	93
5.2.8 X-ray Fluorescence Spectrometry (XRF) .....	94
5.2.9 Scanning Electron Microscopy (SEM) .....	94
5.2.10 Magic-Angle Spinning Nuclear Magnetic Resonance Spectroscopy .....	94
5.2.11 Inductively Coupled Plasma Optical Emission Spectroscopy (ICP-OES).....	95
5.2.12 Adsorption Isotherms .....	96
5.3 Results Part 1: Fluoride Uptake in H-Y, NH <sub>4</sub> -Y and Na-Y .....	97
5.3.1 Zeolite Characterisation .....	97
5.3.2 Fluoride Loadings .....	101
5.3.3 The Role of Protons .....	102
5.3.4 H-Y and NH <sub>4</sub> -Y: Adsorption Isotherms .....	106
5.3.5 <sup>19</sup> F MAS NMR spectroscopy .....	111
5.3.6 Fluorination Mechanism .....	115
5.3.7 Na-Y in 1:1 NaF:HNO <sub>3</sub> Solutions: Adsorption Isotherms .....	119
5.3.8 Conclusions .....	122
5.4 Results Part 2: Fluoride Uptake in M <sub>x</sub> (NH <sub>4</sub> ) <sub>1-2x</sub> -Y and M <sub>x</sub> Na <sub>1-2x</sub> -Y .....	123
5.4.1 Introduction .....	123
5.4.2 Characterisation .....	123
5.4.3 M <sub>x</sub> (NH <sub>4</sub> ) <sub>1-2x</sub> -Y: Fluoride Loadings .....	127
5.4.4 M <sub>x</sub> (NH <sub>4</sub> ) <sub>1-2x</sub> -Y: Adsorption Isotherms .....	130
5.4.5 M <sub>x</sub> (NH <sub>4</sub> ) <sub>1-2x</sub> -Y: <sup>19</sup> F MAS NMR spectroscopy .....	137
5.4.6 M <sub>x</sub> Na <sub>1-2x</sub> -Y: Fluoride Loadings .....	149
5.4.7 Conclusions .....	150
5.5 Results Part 3: Fluoride Uptake in Dealuminated NH <sub>4</sub> -Y .....	152
5.5.1 Introduction .....	152
5.5.2 Characterisation .....	153
5.5.3 Fluoride Loadings and Adsorption Isotherms .....	154
5.5.4 <sup>19</sup> F MAS NMR Spectroscopy .....	157
5.5.5 Conclusions .....	159
5.6 Overall Conclusions .....	159
CHAPTER 6: ENHANCING FLUORIDE UPTAKE IN LARGE ZEOLITE PARTICLES THROUGH POST-SYNTHETIC MODIFICATIONS .....	161
6.1 Introduction .....	161
6.2 Experimental .....	162
6.2.1 Zeolite Syntheses .....	162
6.2.1.1 Large Zeolite A Crystals .....	163
6.2.1.2 Large Zeolite X Crystals .....	163
6.2.1.3 GME Microspheres .....	163

6.2.1.4 Mordenite Microparticles .....	164
6.2.2 Fluoride Adsorption Measurements .....	165
6.2.3 Post-Synthetic Modifications .....	166
6.2.3.1 Ion Exchange .....	166
6.2.3.2 Iron(III) Modification .....	167
6.2.3.3 EDTA Treatments .....	167
6.2.3.4 Attempts to Dealuminate Mordenite .....	168
6.2.4 Instruments .....	168
6.2.4.1 Powder X-ray Diffraction (PXRD) .....	168
6.2.4.2 X-ray Fluorescence Spectrometry (XRF) .....	169
6.2.4.3 Scanning Electron Microscopy (SEM) .....	169
6.2.5 Adsorption Isotherms .....	170
6.3 Results and Discussion .....	170
6.3.1 Gmelinite Microspheres .....	170
6.3.1.1 Fluoride Uptake by Na-GME Microspheres .....	170
6.3.1.2 Dealumination .....	170
6.3.1.3 Iron(III) Modification .....	172
6.3.1.4 Divalent Metal Ion Exchange .....	174
6.3.1.5 Adsorption Isotherms .....	177
6.3.1.6 Conclusions .....	182
6.3.2 Mordenite .....	183
6.3.2.1 Fluoride Uptake by Mordenite and Iron(III) Modification .....	183
6.3.2.2 Proton Ion Exchange and Iron(III) Modification .....	187
6.3.2.3 Divalent Metal Ion Exchange .....	189
6.3.2.4 Conclusions .....	191
6.3.3 Large Crystals of Zeolites A and X .....	192
6.3.3.1 Iron(III) Treatments .....	192
6.3.3.2 EDTA Treatments .....	197
6.3.3.3 Divalent Metal Ion Exchange .....	202
6.3.3.4 Conclusions .....	211
6.4 Overall conclusions .....	212
CHAPTER 7: MOVING FORWARD, THE FUTURE OF PEPT TRACERS .....	214
CHAPTER 8: APPENDICES .....	216
Appendix 1: Supplementary Isotherms .....	216
Appendix 2: Supplementary NMR spectra .....	224
Appendix 3: Scaled-up Zeolite Syntheses Characterisation Data .....	227
Appendix 4: Products of Zeolites A and X Treated with 0.25 M Copper(II) Nitrate .....	230
Appendix 5: X-ray Fluorescence Data .....	231
REFERENCES .....	234

## List of Figures

<u>Figure 1.1.</u> (A) A 6-membered ring with Si or Al atoms and O atoms. (B) The same 6-membered ring as depicted in representations of zeolite framework structures. ....	10
<u>Figure 1.2.</u> (A) The structure of zeolite A as viewed along [100] with the unit cell shown as a dashed blue line. (B) A sodalite cage and (C) a double-4-ring. ....	11
<u>Figure 1.3.</u> (A) The faujasite framework as viewed along [110], (B) a double-6-ring (D6R) and (C) a projection of part of a faujasite unit cell viewed along [111], depicting the supercage. ....	12
<u>Figure 1.4.</u> The mordenite framework as viewed down [001]. ....	13
<u>Figure 1.5.</u> (A) The gmelinite framework viewed along [001], (B) a gmelinite cage and (C) a projection of gmelinite along [100], demonstrating the ABAB stacking sequence. ....	15
<u>Figure 1.6.</u> (A) The chabazite framework as viewed along [111] with the unit cell shown as a dashed blue line and (B) a chabazite cage. ....	16
<u>Figure 1.7.</u> (A) A projection of the zeolite P framework as viewed down [100]. (B) A gismondine cage and (C) a double crankshaft chain. ....	17
<u>Figure 2.1.</u> A schematic of the Bragg diffraction of X-rays. ....	25
<u>Figure 3.1.</u> Scanning electron micrographs of mordenite produced from gels with Si/Al ratios: (A) 7.7, (B) 8.3, (C) 8.9 and (D) 9.5. ....	43
<u>Figure 3.2.</u> PXRD patterns for mordenite produced from gels with Si/Al = 7.7, 8.3, 8.9 and 9.5, along with a stick plot of a reference mordenite PDF pattern. ....	45
<u>Figure 3.3.</u> Scanning electron micrograph of mordenite produced from a gel Si/Al = 7.7 and containing no TEA <sup>+</sup> cations. ....	46
<u>Figure 3.4.</u> PXRD pattern of the product from a gel with Si/Al = 7.7 and containing no TEA <sup>+</sup> . ....	47
<u>Figure 3.5.</u> Scanning electron micrographs for products of gels with Si/Al = 7.5 (A), 8.8 (B) and 10.0 (C), with colloidal silica as the silicon source. ....	48
<u>Figure 3.6.</u> PXRD patterns for products of gels with colloidal silica as the silicon source. ....	49
<u>Figure 3.7.</u> PXRD patterns for mordenite produced from the colloidal silica system with different ethanol contents, as labelled. ....	51
<u>Figure 3.8.</u> Scanning electron micrographs for mordenite produced from the colloidal silica system with (A) 0 ml, (B) 5 ml, (C) 10 ml and (D) 15 ml of ethanol added to the gel. ....	52
<u>Figure 3.9.</u> PXRD patterns of mordenite produced in the TEOS system with added ethanol. ....	53
<u>Figure 3.10.</u> Scanning electron micrographs of mordenite produced from gels with Si/Al = 7.7 from the TEOS system with (A) 0 ml, (B) 1 ml and (C) 2 ml of ethanol added ....	54

<u>Figure 3.11.</u> A scanning electron micrograph depicting (A) pre-sieved uncalcined mordenite (Si/Al = 7.8(2)) and (B) the calcined sample sieved between 25 and 50 $\mu\text{m}$ . .....	55
<u>Figure 3.12.</u> Particle size distributions for unsieved mordenite and the 25 < x < 50 $\mu\text{m}$ fraction. ....	56
<u>Figure 3.13.</u> PXRD patterns of mordenite and mordenite following gallium loading. ....	58
<u>Figure 4.1.</u> PXRD patterns of zeolite A crystals grown for 14, 21 and 28 days. ....	67
<u>Figure 4.2.</u> Scanning electron micrographs for zeolite A grown for (A) 14, (B) 21 and (C) 28 days. ....	68
<u>Figure 4.3.</u> Scanning electron micrograph of the > 25 $\mu\text{m}$ fraction of zeolite A grown for 28 days. ....	68
<u>Figure 4.4.</u> PXRD patterns for zeolite X grown for 14, 21 and 28 days. ....	70
<u>Figure 4.5.</u> Scanning electron micrographs for zeolite X grown for (A) 14, (B) 21 and (C) 28 days. ....	70
<u>Figure 4.6.</u> Scanning electron micrographs depicting the range of morphologies present in zeolite X samples grown for 28 days. ....	71
<u>Figure 4.7.</u> A scanning electron micrograph of the > 25 $\mu\text{m}$ fraction of zeolite X. ....	72
<u>Figure 4.8.</u> Scanning electron micrographs of A1, A2, A3, B1, B2 and B3, as labelled. ....	73
<u>Figure 4.9.</u> PXRD pattern of A1 and reference patterns for Na-Y, Na-CHA and Na-P. ....	74
<u>Figure 4.10.</u> PXRD patterns of A2 and A3, and reference patterns of Na-P, Na-CHA and Na-Y. ....	75
<u>Figure 4.11.</u> PXRD patterns for B1, B2 and B3, and reference patterns of Na-Y, Na-GME, Na-P and ECR 26. ....	76
<u>Figure 4.12.</u> PXRD patterns of GME produced by heating for 14 and 21 days, and reference patterns of ECR-26 and Na-CHA. ....	78
<u>Figure 4.13.</u> PXRD pattern of GME (21 days) and reference patterns of Na-GME, Na-CHA and ECR-26. ....	79
<u>Figure 4.14.</u> Scanning electron micrographs of GME synthesised following heating for (A) 14 and (B) 21 days. ....	80
<u>Figure 4.15.</u> Particle size distribution of diameters of GME microspheres heated for 14 days and 21 days. ....	81
<u>Figure 4.16.</u> PXRD patterns of unaged gels heated for 3, 5, 7, 14 and 21 days, and reference patterns of CHA and ECR-26. ....	82
<u>Figure 4.17.</u> Scanning electron micrographs of products of unaged gels heated for (A) 3, (B) 5, (C) 7, (D) 14 and (E) 21 days. ....	83

<u>Figure 4.18.</u> Particle size distributions for microspheres produced from unaged gels heated for 14 and 21 days. ....	85
<u>Figure 5.1.</u> PXRD patterns of Na-Y, NH <sub>4</sub> -Y and H-Y, compared with a reference Na-Y pattern.....	98
<u>Figure 5.2.</u> <sup>29</sup> Si MAS NMR spectrum of H-Y. ....	99
<u>Figure 5.3.</u> Scanning electron micrographs of (A) NH <sub>4</sub> -Y, (B) Na-Y and (C) H-Y. ....	100
<u>Figure 5.4.</u> A plot of equilibrium fluoride loading (mg F <sup>-</sup> g <sup>-1</sup> ), by zeolites H-Y, NH <sub>4</sub> -Y and Na-Y, at different temperatures as a function of initial fluoride concentration (ppm F <sup>-</sup> ). ....	102
<u>Figure 5.5.</u> A plot of equilibrium ion loading (mol g <sup>-1</sup> ), Na <sup>+</sup> or F <sup>-</sup> , by each zeolite at 25°C as a function of initial fluoride concentration (ppm F <sup>-</sup> ). ....	104
<u>Figure 5.6.</u> A plot of fluoride loading as a function of initial solution pH for zeolites H-Y, NH <sub>4</sub> -Y and Na-Y from 60 ppm F <sup>-</sup> solutions at 25°C. ....	105
<u>Figure 5.7.</u> A plot of equilibrium fluoride loadings attained by Na-Y from 1:1 NaF:HNO <sub>3</sub> solutions as a function of initial fluoride concentration. ....	106
<u>Figure 5.8.</u> Langmuir plots for H-Y and NH <sub>4</sub> -Y at 25 and 40°C. ....	107
<u>Figure 5.9.</u> Temkin plots for H-Y and NH <sub>4</sub> -Y at 25 and 40°C. ....	108
<u>Figure 5.10.</u> Freundlich plots for H-Y and NH <sub>4</sub> -Y at 25 and 40°C. ....	108
<u>Figure 5.11.</u> Plot of adsorption data fitted to the linear Dubinin-Radushkevitch equation for H-Y and NH <sub>4</sub> -Y. ....	110
<u>Figure 5.12.</u> <sup>19</sup> F MAS NMR spectrum for H-Y(F). ....	112
<u>Figure 5.13.</u> <sup>19</sup> F MAS NMR spectrum for NH <sub>4</sub> -Y(F). ....	113
<u>Figure 5.14.</u> Proposed mechanisms for the fluorination of zeolite frameworks. ....	116
<u>Figure 5.15.</u> Normalised <sup>29</sup> Si{ <sup>1</sup> H} CP MAS NMR spectra for NH <sub>4</sub> -Y and NH <sub>4</sub> -Y(F). ....	118
<u>Figure 5.16.</u> Temkin plot for Na-Y in 1:1 NaF:HNO <sub>3</sub> . ....	119
<u>Figure 5.17.</u> Freundlich plot for Na-Y in 1:1 NaF:HNO <sub>3</sub> . ....	120
<u>Figure 5.18.</u> Dubinin-Radushkevitch plot for Na-Y in 1:1 NaF:HNO <sub>3</sub> . ....	120
<u>Figure 5.19.</u> PXRD patterns of M <sub>x</sub> (NH <sub>4</sub> ) <sub>1-2x</sub> -Y species. ....	125
<u>Figure 5.20.</u> PXRD patterns for M <sub>x</sub> Na <sub>1-2x</sub> -Y species. ....	126
<u>Figure 5.21.</u> Equilibrium fluoride loadings achieved for M <sub>x</sub> (NH <sub>4</sub> ) <sub>1-2x</sub> -Y species at 25°C, where M = Mg <sup>2+</sup> , Ca <sup>2+</sup> or Sr <sup>2+</sup> , as a function of initial fluoride concentration. ....	128
<u>Figure 5.22.</u> Equilibrium fluoride loadings achieved for M <sub>x</sub> (NH <sub>4</sub> ) <sub>1-2x</sub> -Y species at 25°C, where M = Cu <sup>2+</sup> or Ba <sup>2+</sup> , as a function of initial fluoride concentration. ....	129

<u>Figure 5.23.</u> Equilibrium fluoride loadings achieved for $M_x(NH_4)_{1-2x}Y$ species at 40°C, where $M = Mg^{2+}, Ca^{2+}$ or $Sr^{2+}$ , as a function of initial fluoride concentration. ....	129
<u>Figure 5.24.</u> Equilibrium fluoride loadings achieved for $M_x(NH_4)_{1-2x}Y$ species at 40°C, where $M = Cu^{2+}$ or $Ba^{2+}$ , as a function of initial fluoride concentration. ....	130
<u>Figure 5.25.</u> Freundlich plots for $Mg_{0.15}(NH_4)_{0.70}Y$ and $Ca_{0.17}(NH_4)_{0.66}Y$ at 25°C and 40°C. ....	131
<u>Figure 5.26.</u> Freundlich plots for $Sr_{0.14}(NH_4)_{0.72}Y$ at 25°C and 40°C. ....	132
<u>Figure 5.27.</u> Freundlich plots for $Ba_{0.21}(NH_4)_{0.58}Y$ at 25°C and 40°C. ....	132
<u>Figure 5.28.</u> Freundlich plots for $Cu_{0.24}(NH_4)_{0.52}Y$ at 25°C and 40°C. ....	133
<u>Figure 5.29.</u> Dubinin-Radushkevitch plots for $Mg_{0.15}(NH_4)_{0.70}Y$ and $Ca_{0.17}(NH_4)_{0.66}Y$ at 25°C and 40°C. ....	135
<u>Figure 5.30.</u> Dubinin-Radushkevitch plots for $Sr_{0.14}(NH_4)_{0.72}Y$ at 25°C and 40°C. ....	135
<u>Figure 5.31.</u> Dubinin-Radushkevitch plots for $Ba_{0.21}(NH_4)_{0.58}Y$ at 25°C and 40°C. ....	136
<u>Figure 5.32.</u> Dubinin-Radushkevitch plots for $Cu_{0.24}(NH_4)_{0.52}Y$ at 25°C and 40°C. ....	136
<u>Figure 5.33.</u> $^{19}F$ MAS NMR spectrum of fluorinated $Mg_{0.15}(NH_4)_{0.70}Y$ . ....	138
<u>Figure 5.34.</u> $^{19}F$ MAS NMR spectrum of fluorinated $Ca_{0.17}(NH_4)_{0.66}Y$ . ....	139
<u>Figure 5.35.</u> $^{19}F$ MAS NMR spectrum of fluorinated $Sr_{0.14}(NH_4)_{0.72}Y$ . ....	139
<u>Figure 5.36.</u> $^{19}F$ MAS NMR spectrum of fluorinated $Ba_{0.21}(NH_4)_{0.58}Y$ . ....	140
<u>Figure 5.37.</u> $^{19}F$ MAS NMR spectrum of fluorinated $Cu_{0.24}(NH_4)_{0.52}Y$ . ....	140
<u>Figure 5.38.</u> $^{29}Si$ MAS NMR spectrum of fluorinated $Sr_{0.14}(NH_4)_{0.72}Y$ . ....	142
<u>Figure 5.39.</u> $^{29}Si$ MAS NMR spectrum of fluorinated $Cu_{0.24}(NH_4)_{0.52}Y$ . ....	143
<u>Figure 5.40.</u> PXRD patterns for $Mg_{0.15}(NH_4)_{0.70}Y$ , $Ca_{0.17}(NH_4)_{0.66}Y(F)$ and $Sr_{0.14}(NH_4)_{0.72}Y$ , along with reference patterns for Na-Y, $MgF_2$ , $CaF_2$ and $SrF_2$ . ....	147
<u>Figure 5.41.</u> Schematic representation of dealumination of $NH_4Y$ and the formation of silanol nests. ....	152
<u>Figure 5.42.</u> PXRD pattern for (D)- $NH_4Y$ and a reference pattern for Na-Y.....	153
<u>Figure 5.43.</u> Scanning electron micrograph of (D)- $NH_4Y$ . ....	154
<u>Figure 5.44.</u> Equilibrium fluoride loadings attained for (D)- $NH_4Y$ and $NH_4Y$ at 25°C as a function of initial fluoride concentration. ....	155
<u>Figure 5.45.</u> Equilibrium fluoride loadings attained for (D)- $NH_4Y$ and $NH_4Y$ at 40°C as a function of initial fluoride concentration. ....	155
<u>Figure 5.46.</u> Freundlich plots for (D)- $NH_4Y$ at 25 and 40°C. ....	156

<u>Figure 5.47.</u> DR plots for (D)-NH <sub>4</sub> -Y at 25 and 40°C. ....	157
<u>Figure 5.48.</u> <sup>19</sup> F MAS NMR spectrum of fluorinated (D)-NH <sub>4</sub> -Y. ....	158
<u>Figure 6.1.</u> PXRD patterns of Na-GME and (D)-Na-GME, dealuminated Na-GME. ....	171
<u>Figure 6.2.</u> A scanning electron micrograph of dealuminated Na-GME. ....	171
<u>Figure 6.3.</u> Scanning electron micrographs of GME microspheres treated with (A) 0.01 M and (B) 0.025 M Fe(NO <sub>3</sub> ) <sub>3</sub> solutions. ....	173
<u>Figure 6.4.</u> PXRD patterns recorded on GME microspheres treated with 0.01 M and 0.025 M Fe(NO <sub>3</sub> ) <sub>3</sub> solutions, as well as the parent material. ....	174
<u>Figure 6.5.</u> PXRD patterns recorded on Na-GME and divalent metal ion-exchanged products. ..	176
<u>Figure 6.6.</u> Equilibrium fluoride loadings plotted as a function of initial fluoride concentration for Na-GME, Ca-GME, Fe <sup>III</sup> -loaded Na-GME and (D)-Na-GME. ....	178
<u>Figure 6.7.</u> Dubinin-Radushkevitch plots for Na-GME, Ca-GME, Fe <sup>III</sup> -loaded Na-GME and (D)-Na-GME. ....	179
<u>Figure 6.8.</u> Freundlich plots for Na-GME, Ca-GME, Fe <sup>III</sup> -loaded Na-GME and (D)-Na-GME. ....	179
<u>Figure 6.9.</u> Temkin plots for Na-GME, Ca-GME, Fe <sup>III</sup> -loaded Na-GME and (D)-Na-GME. ....	180
<u>Figure 6.10.</u> Langmuir plot for (D)-Na-GME. ....	180
<u>Figure 6.11.</u> PXRD patterns recorded for Na <sub>0.54</sub> H <sub>0.46</sub> -MOR and Fe <sup>3+</sup> -loaded Na <sub>0.54</sub> H <sub>0.46</sub> -MOR. ....	184
<u>Figure 6.12.</u> Freundlich plot for Fe <sup>3+</sup> -loaded Na <sub>0.54</sub> H <sub>0.46</sub> -MOR. ....	185
<u>Figure 6.13.</u> Dubinin-Radushkevitch plot for Fe <sup>3+</sup> -loaded Na <sub>0.54</sub> H <sub>0.46</sub> -MOR. ....	186
<u>Figure 6.14.</u> PXRD patterns for Na <sub>0.54</sub> H <sub>0.46</sub> -MOR, Na <sub>0.39</sub> H <sub>0.61</sub> -MOR and Fe <sup>3+</sup> -loaded Na <sub>0.39</sub> H <sub>0.61</sub> -MOR. ....	188
<u>Figure 6.15.</u> PXRD patterns recorded on Na <sub>0.54</sub> H <sub>0.46</sub> -MOR and ion-exchanged products. ....	189
<u>Figure 6.16.</u> Scanning electron micrographs of products of treatments with (A) 0.01 M, (B) 0.025 M and (C) 0.25 M Fe(NO <sub>3</sub> ) <sub>3</sub> on zeolite A crystals. ....	193
<u>Figure 6.17.</u> PXRD patterns of products of zeolite A crystals following treatment with 0.01 M and 0.025 M Fe(NO <sub>3</sub> ) <sub>3</sub> solutions, recorded on a Bruker D2 diffractometer with a Co K <sub>α</sub> X-ray source (λ = 1.7902 Å). ....	193
<u>Figure 6.18.</u> Scanning electron micrographs of products of treatments with (A) 0.01 M, (B) 0.025 M and (C) 0.25 M Fe(NO <sub>3</sub> ) <sub>3</sub> on zeolite X crystals. ....	195
<u>Figure 6.19.</u> PXRD patterns of products following treatment of zeolite X crystals with 0.01 M and 0.025 M Fe(NO <sub>3</sub> ) <sub>3</sub> solutions, recorded on a Bruker D2 diffractometer with a Co K <sub>α</sub> X-ray source (λ = 1.7902 Å). ....	196

<u>Figure 6.20.</u> Scanning electron micrographs of zeolite A crystals treated with EDTA: (A) (E1)-Na-A, (B) (E2)-Na-A, (C) (E3)-Na-A and (D) (E4)-Na-A. ....	198
<u>Figure 6.21.</u> PXRD patterns for zeolite Na-A and (E1)-Na-A. ....	198
<u>Figure 6.22.</u> PXRD patterns for (E2)-Na-A, (E3)-Na-A and (E4)-Na-A. ....	199
<u>Figure 6.23.</u> Scanning electron micrographs on zeolite A crystals treated with EDTA: (A) (E1)-Na-X, (B) (E2)-Na-X, (C) (E3)-Na-X and (D) (E4)-Na-X. ....	200
<u>Figure 6.24.</u> PXRD patterns of Na-X and (E1)-Na-X. ....	201
<u>Figure 6.25.</u> PXRD patterns recorded for (E2)-Na-X, (E3)-Na-X and (E4)-Na-X. ....	202
<u>Figure 6.26.</u> PXRD patterns recorded on Na-A and ion-exchanged products. ....	205
<u>Figure 6.27.</u> PXRD patterns recorded on Na-X and ion-exchanged products. ....	207
<u>Figure 6.28.</u> Equilibrium F <sup>-</sup> loadings as a function of initial F <sup>-</sup> concentration for Ca-A and Ca-X. ....	209
<u>Figure 6.29.</u> Temkin plots for Ca-A and Ca-X. ....	210
<u>Figure 6.30.</u> Freundlich plots for Ca-A and Ca-X. ....	210
<u>Figure 6.31.</u> Dubinin-Radushkevitch plots for Ca-A and Ca-X. ....	211
<u>Figure 8.1.</u> Langmuir plot for F <sup>-</sup> uptake by Na-Y in 1:1 NaF:HNO <sub>3</sub> solutions at 25°C. ....	216
<u>Figure 8.2.</u> Langmuir plot for F <sup>-</sup> uptake by M <sub>x</sub> (NH <sub>4</sub> ) <sub>1-2x</sub> -Y species at 25°C, where M = Mg, Ca and Cu. ....	217
<u>Figure 8.3.</u> Langmuir plot for F <sup>-</sup> uptake by M <sub>x</sub> (NH <sub>4</sub> ) <sub>1-2x</sub> -Y species at 25°C, where M = Sr and Ba. ....	217
<u>Figure 8.4.</u> Langmuir plot for F <sup>-</sup> uptake by M <sub>x</sub> (NH <sub>4</sub> ) <sub>1-2x</sub> -Y species at 40°C, where M = Ca and Cu. ....	218
<u>Figure 8.5.</u> Langmuir plot for F <sup>-</sup> uptake by Mg <sub>0.15</sub> (NH <sub>4</sub> ) <sub>0.70</sub> -Y species at 40°C. ....	218
<u>Figure 8.6.</u> Langmuir plot for F <sup>-</sup> uptake by M <sub>x</sub> (NH <sub>4</sub> ) <sub>1-2x</sub> -Y species at 40°C, where M = Sr and Ba. ....	219
<u>Figure 8.7.</u> Temkin plot for F <sup>-</sup> uptake by M <sub>x</sub> (NH <sub>4</sub> ) <sub>1-2x</sub> -Y species at 25°C, where M = Ca, Cu and Ba. ....	219
<u>Figure 8.8.</u> Temkin plot for F <sup>-</sup> uptake by M <sub>x</sub> (NH <sub>4</sub> ) <sub>1-2x</sub> -Y species at 40°C, where M = Ca, Cu and Ba. ....	220
<u>Figure 8.9.</u> Temkin plot for F <sup>-</sup> uptake by M <sub>x</sub> (NH <sub>4</sub> ) <sub>1-2x</sub> -Y species at 25°C, where M = Mg and Sr. ...	220
<u>Figure 8.10.</u> Temkin plot for F <sup>-</sup> uptake by M <sub>x</sub> (NH <sub>4</sub> ) <sub>1-2x</sub> -Y species at 40°C, where M = Mg and Sr. ....	221
<u>Figure 8.11.</u> Langmuir plot for F <sup>-</sup> uptake by (D)-NH <sub>4</sub> -Y at both 25°C and 40°C. ....	221
<u>Figure 8.12.</u> Temkin plot for F <sup>-</sup> uptake by (D)-NH <sub>4</sub> -Y at both 25°C and 40°C. ....	222
<u>Figure 8.13.</u> Langmuir plot for F <sup>-</sup> uptake by Fe <sup>3+</sup> -loaded MOR at 25°C. ....	222

<u>Figure 8.14.</u> Temkin plot for F <sup>-</sup> uptake by Fe <sup>3+</sup> -loaded MOR at 25°C. ....	223
<u>Figure 8.15.</u> Langmuir plot for F <sup>-</sup> uptake by Na-GME, Ca-GME and Fe <sup>III</sup> -loaded Na-GME at 25°C. ....	223
<u>Figure 8.16.</u> Langmuir plot for F <sup>-</sup> uptake by Ca-A and Ca-X at 25°C. ....	224
<u>Figure 8.17.</u> <sup>29</sup> Si{ <sup>1</sup> H} CP MAS NMR spectra recorded on H-Y and fluorinated H-Y, H-Y(F). ....	224
<u>Figure 8.18.</u> <sup>19</sup> F MAS NMR spectra recorded on H-Y at a spin rates of 18 kHz and 20 kHz. ....	225
<u>Figure 8.19.</u> Peak fit of the <sup>19</sup> F MAS NMR spectrum of H-Y(F).....	225
<u>Figure 8.20.</u> Peak fit of the <sup>19</sup> F MAS NMR spectrum of NH <sub>4</sub> -Y(F).....	226
<u>Figure 8.21.</u> Peak fit of the <sup>19</sup> F MAS NMR spectrum of fluorinated Ca <sub>0.17</sub> (NH <sub>4</sub> ) <sub>0.66</sub> -Y.....	226
<u>Figure 8.22.</u> PXRD pattern recorded on Na-X grown for 28 days in a scaled-up synthesis. ....	227
<u>Figure 8.23.</u> PXRD pattern recorded on Na-A grown for 28 days in a scaled-up synthesis. ....	227
<u>Figure 8.24.</u> PXRD pattern recorded on MOR grown produced by a scaled-up synthesis. ....	228
<u>Figure 8.25.</u> PXRD pattern recorded on Na-GME grown for 28 days in a scaled-up synthesis. ...	228
<u>Figure 8.26.</u> Scanning electron micrographs of (A) zeolite A, (B) zeolite X, (C) GME and (D) MOR produced from scaled up syntheses. ....	229
<u>Figure 8.27.</u> PXRD pattern recorded on the product of zeolite A treated with 0.25 M Cu(NO <sub>3</sub> ) <sub>2</sub> .	230
<u>Figure 8.28.</u> PXRD pattern recorded on the product of zeolite X treated with 0.25 M Cu(NO <sub>3</sub> ) <sub>2</sub> .	230

## List of Tables

<u>Table 1.1.</u> Materials used as radiotracers in PEPT studies on fluidisation. ....	6
<u>Table 2.1.</u> Langmuir, Freundlich, Temkin and DR adsorption isotherms, and their linear forms, as applied to adsorption at the solid-liquid interface. ....	21
<u>Table 2.2.</u> The unit cell shapes for different crystal systems. ....	23
<u>Table 3.1.</u> Amount of TEOS added, gel Si/Al ratio and the measured Si/Al and Na/Al ratios. ....	43
<u>Table 3.2.</u> Measured Si/Al ratio and lattice constants for mordenite samples. ....	46
<u>Table 3.3.</u> The amount of ethanol added, gel Si/Al ratios and product Si/Al and Na/Al ratios measured by XRF spectrometry.....	50
<u>Table 3.4.</u> Gel Si/Al, measured Si/Al and Na/Al ratios, as well as ethanol added and expected ethanol content for products of the TEOS system. ....	53
<u>Table 4.1.</u> Statistical analysis of diameters for GME microspheres. ....	80
<u>Table 4.2.</u> Statistical analysis of microspheres in products of unaged gels. ....	84
<u>Table 5.1.</u> Metal salts, suppliers and masses used to make 0.25 M solutions. ....	91
<u>Table 5.2.</u> Unit cell parameters, volumes and bulk Si/Al ratios for H-Y, NH <sub>4</sub> -Y and Na-Y. ....	97
<u>Table 5.3.</u> Chemical shifts, relative peak areas and assignments for peaks in the <sup>29</sup> Si MAS NMR spectrum of H-Y. ....	98
<u>Table 5.4.</u> Isotherm parameters and <i>R</i> <sup>2</sup> for fits of equilibrium fluoride uptake data for H-Y and NH <sub>4</sub> -Y to the Freundlich, Temkin and Langmuir isotherms. ....	109
<u>Table 5.5.</u> <i>R</i> <sup>2</sup> , isotherm parameters and <i>E</i> <sub>c</sub> for fits to the linear Dubinin-Radushkevitch equation. ....	110
<u>Table 5.6.</u> Chemical shifts for peaks in the <sup>29</sup> Si{ <sup>1</sup> H} CP MAS NMR spectra for NH <sub>4</sub> -Y and NH <sub>4</sub> -Y(F). ....	118
<u>Table 5.7.</u> Unit cell parameters, volumes and compositional ratios for M <sub>x</sub> Na <sub>1-2x</sub> -Y and M <sub>x</sub> (NH <sub>4</sub> ) <sub>1-2x</sub> -Y. ....	124
<u>Table 5.8.</u> <i>R</i> <sup>2</sup> for fits to the Freundlich, Temkin and Langmuir isotherms, and Freundlich isotherm parameters, for M <sub>x</sub> (NH <sub>4</sub> ) <sub>1-2x</sub> -Y and NH <sub>4</sub> -Y. ....	133
<u>Table 5.9.</u> <i>R</i> <sup>2</sup> , isotherm parameters and <i>E</i> <sub>c</sub> for fits to the linear Dubinin-Radushkevitch equation for M <sub>x</sub> (NH <sub>4</sub> ) <sub>1-2x</sub> -Y. ....	134
<u>Table 5.10.</u> Approximate chemical shifts for resonances <b>1 - 4</b> in <sup>19</sup> F MAS NMR spectra recorded on fluorinated M <sub>x</sub> (NH <sub>4</sub> ) <sub>1-2x</sub> -Y. ....	138
<u>Table 5.11.</u> Compositional data for M <sub>x</sub> (NH <sub>4</sub> ) <sub>1-2x</sub> -Y fluorinated at 25°C with 60 ppm F <sup>-</sup> . ....	148
<u>Table 5.12.</u> Equilibrium fluoride loadings achieved by M <sub>x</sub> Na <sub>1-2x</sub> -Y and M <sub>x</sub> (NH <sub>4</sub> ) <sub>1-2x</sub> -Y from 20 ppm F <sup>-</sup> NaF solutions at 25°C. ....	150
<u>Table 5.13.</u> <i>R</i> <sup>2</sup> for fits to the Temkin, Langmuir and Freundlich isotherms, and Freundlich isotherm parameters, for (D)-NH <sub>4</sub> -Y and NH <sub>4</sub> -Y at 25 and 40°C. ....	156

<u>Table 5.14.</u> $R^2$ , isotherm parameters and $E_c$ for fits to the DR isotherm for (D)-NH <sub>4</sub> -Y and NH <sub>4</sub> -Y at 25 and 40°C. ....	157
<u>Table 6.1.</u> Metal salts, suppliers and masses to make 0.25 M solutions. ....	166
<u>Table 6.2.</u> Si/Al, Na/Al and M/Al ratios measured for ion-exchanged GME microspheres. ....	175
<u>Table 6.3.</u> Fluoride loadings attained following an hour and at equilibrium for Na-GME and divalent ion-exchanged derivatives. ....	176
<u>Table 6.4.</u> $R^2$ , isotherm parameters and derived terms for fits to the listed isotherms for Na-GME, Ca-GME, Fe <sup>III</sup> -loaded Na-GME and (D)-Na-GME. ....	181
<u>Table 6.5.</u> Lattice constants for Na <sub>0.54</sub> H <sub>0.46</sub> -MOR and Fe <sup>3+</sup> -loaded Na <sub>0.54</sub> H <sub>0.46</sub> -MOR. ....	184
<u>Table 6.6.</u> $R^2$ and isotherm parameters for fits to the listed isotherms for Fe <sup>3+</sup> -loaded Na <sub>0.54</sub> H <sub>0.46</sub> -MOR. ....	186
<u>Table 6.7.</u> Lattice constants for Na <sub>0.54</sub> H <sub>0.46</sub> -MOR, Na <sub>0.39</sub> H <sub>0.61</sub> -MOR and Fe <sup>3+</sup> -loaded Na <sub>0.39</sub> H <sub>0.61</sub> -MOR. ....	187
<u>Table 6.8.</u> Unit cell parameters and volumes for ion-exchanged mordenites, as well as Na/Al and M/Al ratios measured by XRF spectrometry. ....	190
<u>Table 6.9.</u> Fluoride loadings attained following an hour of contact and at equilibrium for Na <sub>0.54</sub> H <sub>0.46</sub> -MOR (Na/H-MOR) and ion-exchanged products. ....	191
<u>Table 6.10.</u> Unit cell parameters and volumes, along with Na/Al, M/Al and Si/Al measured for both Na-A and Na-X and their ion-exchanged products. ....	204
<u>Table 6.11.</u> Fluoride loadings attained following an hour of contact and at equilibrium for both zeolites Na-A and Na-X and their ion-exchanged products. ....	208
<u>Table 6.12.</u> $R^2$ and isotherm parameters for fits to the listed isotherms for zeolites Ca-A and Ca-X. ....	209
<u>Table 8.1.</u> Elemental weight fractions (wt%) of mordenite samples discussed in sections 3.3.1 – 3.3.5. ....	231
<u>Table 8.2.</u> Elemental weight fractions (wt%) of mordenite samples discussed in sections 3.3.7. ....	231
<u>Table 8.3.</u> Elemental weight fractions (wt%) of zeolite Y samples employed in Chapter 5 ....	232
<u>Table 8.4.</u> Elemental weight fractions (wt%) of zeolite Y samples treated with 60 ppm F <sup>-</sup> NaF solutions at the specified temperature. ....	232
<u>Table 8.5.</u> Elemental weight fractions (wt%) for scaled-up zeolites employed in Chapter 6. ....	232
<u>Table 8.6.</u> Elemental weight fractions (wt%) for products of dealumination treatments. ....	233
<u>Table 8.7.</u> Elemental weight fractions (wt%) for Fe <sup>3+</sup> -treated zeolite samples. ....	233
<u>Table 8.8.</u> Elemental weight fractions (wt%) for zeolites A, X, GME and MOR samples following ion-exchange. ....	233

## List of Abbreviations

CHA	Chabazite
CP	Cross Polarisation
DR	Dubinin-Radushkevitch
ED	Energy Dispersive
FAU	Faujasite
GIS	Gismondine
GME	Gmelinite
HDPE	High Density Polyethylene
ICDD	International Centre for Diffraction Data
ICP	Inductively Coupled Plasma
ISE	Ion-Selective Electrode
LTA	Linde Type A/Zeolite A
MAS	Magic-Angle Spinning
MCC	Microcrystalline Cellulose
MOR	Mordenite
NMR	Nuclear Magnetic Resonance
OES	Optical Emission Spectroscopy
OSDA	Organic Structure Directing Agent
PDF	Powder Diffraction File
PEPT	Positron Emission Particle Tracking
PET	Positron Emission Tomography
PTFE	Polytetrafluoroethylene
PXRD	Powder X-ray Diffraction
SEM	Scanning Electron Microscopy
TEA	Tetraethylammonium
TEOA	Triethanolamine
TEOS	Tetraethyl orthosilicate
TISAB	Total Ionic Strength Adjustment Buffer
XRF	X-ray Fluorescence
WD	Wavelength Dispersive

## CHAPTER 1: INTRODUCTION

### 1.1 Positron Emission Particle Tracking (PEPT)

#### 1.1.1 Positron Emission Particle Tracking: The Fundamentals

In  $\beta^+$ -emission, a proton within the nucleus of an unstable isotope decays to a neutron by emission of a positron and an electron neutrino, hence lowering the atomic number by 1, transmuting the element.<sup>1</sup> After reaching thermal equilibrium, the ephemeral positron rapidly undergoes particle-antiparticle annihilation with a proximal electron, via a metastable positronium intermediate, to produce two collinear  $\gamma$ -rays. As the  $\gamma$ -rays have trajectories  $180 (\pm 0.5)^\circ$  apart, the origin of the  $\gamma$ -rays may be traced following detection by position-sensitive scintillation detectors. The ability to trace the origin of labelled molecules via  $\gamma$ -emission, resulting from positron annihilation, is the foundation of positron emission tomography (PET), a medical technique which utilises radiotracers that emit  $\beta^+$ -radiation to probe various aspects of physiology.<sup>2,3</sup> By extension of the working principles of PET, over time the change in the Cartesian co-ordinates of a single particle labelled with a  $\beta^+$ -emitting isotope may be determined; this application is termed positron emission particle tracking (PEPT).<sup>3</sup>

PEPT has wide-ranging applications in the non-invasive observation of particle distribution within engineering processes. As it is based on  $\gamma$ -ray detection, it provides imaging of tracer distributions, with high sensitivity, within “real plant” processes that would otherwise be opaque to lower energy electromagnetic radiation, such as visible light or radio waves. The  $\gamma$ -rays initially have an energy of 511 keV, but attenuation and Compton scattering may occur between production and detection, due to atomic absorption and interactions with electrons. An algorithm is employed to ensure scattered photons are discounted from the detected results and that only photons which may be traced to their true origin contribute to the experimental result. The algorithm works by first calculating the centroid of all detected photons, then omitting those which are furthest from the centroid. Successive

iterations continue until a set-fraction of the detected photons remain. The optimal set-fraction depends on factors such as the detector geometry and the scattering factor of the ambient media.<sup>3</sup>

The most common isotope used in PET, and PEPT, is fluorine-18 ( $t_{1/2} = 110$  minutes) which decays via  $\beta^+$ -emission to oxygen-18, a stable isotope. In PEPT, the popularity of  $^{18}\text{F}$  is principally due to its short half-life and relative ease of production. The radionuclide may be produced at a cyclotron by irradiation of  $^{16}\text{O}$  atoms, within a solid material or in water molecules, by a  $^3\text{He}$  beam. The  $^3\text{He}$  nuclei collide with the  $^{16}\text{O}$  nuclei in a nuclear “knock-out” reaction producing fluorine-18 and a proton. Alternatively, the collision may lead to the production of  $^{18}\text{Ne}$  and the emission of a neutron. Neon-18 ( $t_{1/2} = 1.67$  seconds) decays via electron capture to fluorine-18.<sup>2</sup> Convention is to denote these reactions as  $^{16}\text{O}(^3\text{He},p)^{18}\text{F}$  and  $^{16}\text{O}(^3\text{He},n)^{18}\text{Ne}$ , respectively. Labelling a particle directly with a  $^3\text{He}$  beam is termed direct activation.<sup>4</sup>

In principle, any  $\beta^+$ -emitting isotope of a chemically suitable element, with a sufficiently long half-life to be used in an experiment, may be used in PEPT, provided the half-life is not so long that equipment is contaminated for impractical lengths of time. Gallium-68 is a  $\beta^+$ -emitting isotope ( $t_{1/2} = 68$  minutes) often applied in PET imaging studies. At cyclotrons, gallium-68 can be produced by the  $^{68}\text{Zn}(p,n)^{68}\text{Ga}$  nuclear reaction. Alternatively, gallium-68 may be eluted from  $^{68}\text{Ge}/^{68}\text{Ga}$  generators using concentrated hydrochloric acid (0.05 – 1 M) without the need for a proximal cyclotron, as  $^{68}\text{Ge}$  ( $t_{1/2} = 271$  days) decays to  $^{68}\text{Ga}$  via electron capture.<sup>5,6</sup> The relative ease of production, coupled with a half-life that is neither too long nor too short, makes  $^{68}\text{Ga}$  an attractive alternative to  $^{18}\text{F}$ . PET imaging of biological systems with the radioisotope  $^{68}\text{Ga}$  requires a bifunctional chelator, typically macrocycles that chelate  $\text{Ga}^{3+}$  and that are functionalised with moieties that interact with the biomolecule of interest, usually a protein.<sup>7</sup>

In a typical PEPT experiment, a single particle, with an elemental composition including oxygen, undergoes direct activation, whereby the particle is irradiated by a  $^3\text{He}$  beam converting some  $^{16}\text{O}$  atoms in the particle into  $^{18}\text{F}$ , by the  $^{16}\text{O}(^3\text{He},p)^{18}\text{F}$  reaction. There are inherent requirements for direct

activation to be viable, including the particle must contain oxygen and must also be resistant to the heat produced upon irradiation. Moreover, direct activation is only possible for particles above 1 mm in diameter as the radioactivity of the particle achieved following irradiation is dependent upon the cross-sectional area of the particle. Sufficient radioactivity to allow accurate tracking cannot be imparted by direct activation on particles below 1 mm in diameter. In experiments involving smaller particles ( $d < 1$  mm), alternative methods must be used to introduce  $^{18}\text{F}$  into, or onto, the particle. The two principal alternative methods are ion-exchange or surface modification, depending on the material of interest.<sup>4</sup>

Ion exchange as a method for labelling a tracer particle is typically extended only to strong base anion exchange resins, which are polymers comprising quaternary ammonium derivatives with chloride counter-anions. As the resin has a higher affinity for chloride than fluoride, the chloride counter ion is first exchanged with fluoride by elution of 1 M KF through a column packed with the resin. Facile exchange may then ensue between the fluoride counter-ions in the resin and  $^{18}\text{F}^-$  ions in solution. Although labelling of strong base anion exchange resins has been routinely employed in PEPT experiments, the low density and perfectly spherical morphology of resin particles render them a poor representation of granular material in many model systems.<sup>4</sup> Ion exchange experiments have also been trialled for hydroxyapatite, microcrystalline cellulose (MCC), polyethylene, quartz and calcite, all of which comprised particles within the size range: 212 – 250  $\mu\text{m}$ , with undisclosed, or unknown, particle morphologies. A radioisotope calibrator was used to quantify uptake from nanomolar solutions of  $^{18}\text{F}^-$ . Hydroxyapatite demonstrated appreciable uptake from solution; however, the uptake was insufficient to allow accurate tracking of the labelled tracer particles. The fluoride uptakes observed for quartz, calcite, polyethylene and MCC were, unsurprisingly, minimal. The uptakes measured for all other materials were an order of 10 lower in magnitude than hydroxyapatite, owing to their chemical nature.<sup>8</sup>

As particles of ion-exchange resins poorly simulate granular material in systems of interest, an alternate method is required for labelling particles too small to be labelled by direct activation but that also have an insufficient ion exchange capacity with aqueous fluoride. Surface modification of materials has proven effective in manipulating the labelling capacity of particles not suitable for ion exchange or direct activation. Surface modification has been achieved by adding a source of iron(III) ions to the  $^{18}\text{F}^-$  solution during labelling. Iron(III) ions are believed to adsorb to “active sites” on the surface of the particles of the various materials studied, fluoride ions then adhere in the double layer of the particle by Coulombic attraction to the iron(III) ion. An increase in zeta potential has been empirically observed for quartz particles upon addition of iron(III) ions, which has been attributed to the increase in fluoride and hydroxide ions in the double layer, due to adsorbed iron(III). Surface modification has been applied to MCC, polyethylene, quartz, calcite and hydroxyapatite. Following immersion of particles in a nanomolar solution of  $^{18}\text{F}^-$  and an unknown amount of iron(III), the particles of all mentioned materials displayed sufficient radioactivity to be traced accurately. In the most dramatic increase, the radioactivity of MCC increased by a factor of 200 compared with the absence of iron(III) ions.<sup>8</sup>

#### 1.1.2 PEPT: Visualising chemical engineering processes

In a system containing a single radioactive source, PEPT enables the location of the source to be determined rapidly and may then be repeated at regular intervals. In closed systems containing granular material that recirculates, a labelled particle within a system containing like-particles may be tracked enabling the production of time-averaged density and velocity maps, providing information on the dynamics of the system.<sup>3</sup> While the applications of PEPT are wide ranging, two processes where PEPT has routinely been applied efficaciously to study particle dynamics are studies on fluidisation and mixing phenomena.

The transformation of static solid particles into a fluid-like state by suspension in a liquid or gas is a phenomenon termed fluidisation. If a fluid, liquid or gas, is passed up through a bed of fine particles, beyond a critical flow rate the particles will become fluidised, and thus the solid will exhibit behaviour typically attributed to fluids. Fluidisation is exploited in numerous chemical engineering processes owing to the intrinsic better contact time between solid and fluid offered in fluidised beds, as well as the ability to transport and maintain heat with uniform temperature. Fluidised beds have wide industrial applications in processes such as drying solids, coating particles and controlling particle size during crystallisation. Fluidised beds are also used extensively in the chemical industry as reactors. In the petrochemical industry, fluidised beds are employed as vessels for many solid-catalysed gaseous reactions such as the Fischer-Tropsch process for producing hydrocarbons from syngas ( $H_2$  and  $CO$ ) over an iron catalyst.<sup>9</sup> Modelling the behaviour of fluidised beds is often difficult due to many competing phenomena, including heat and mass transfer, particle-particle and particle-wall collisions.<sup>10,11</sup> As a result, empirical validation of models and investigation of dynamics within fluidised systems is warranted. PEPT is uniquely placed among techniques to accurately and non-invasively determine the time-averaged particle distribution of a single labelled particle within a fluidised bed of like-particles.

Fluidised beds visualised by PEPT have utilised tracers of various materials. At the date of this report, all literature was surveyed that applied PEPT to studies on fluidisation phenomena; Table 1.1 lists the materials used as radiotracers in these studies, in addition to the particle size ranges and how radioactivity was imparted on the particle. In all cases, the particle was labelled with the radionuclide  $^{18}F$ . Two unique “materials” have been omitted from Table 1.1, a poppy seed and a radish seed, both of which had a diameter of *ca.* 500  $\mu m$ . The latter was labelled by surface modification, whereas the former was labelled simply by immersion in a nanomolar solution of fluoride.<sup>12,13</sup> The materials listed in Table 1.1 are representative of the typical materials, size ranges and methods of labelling used in many studies utilising PEPT.

In a recent review on experimental methods to study the effectiveness of fluidisation processes, PEPT was widely extolled. The only reasonable disadvantages outlined in the study were the complexity of experimental set-up, limited size of the inspection zone and the comparatively large tracer sizes used.<sup>14</sup> All disadvantages, but the latter, are innate to the technique; however, the limitation of tracer size is not inherent and the development of smaller tracers for application in PEPT is clearly in demand. The smallest radiotracer used to date is not included in Table 1.1, as it was not employed in a study on fluidisation. In a rudimentary study, it was determined that a resin bead with a diameter of 50  $\mu\text{m}$  may be viable as a PEPT tracer. The resin, a styrene divinylbenzene co-polymer with iminodiacetate moieties, differs from many resins applied to PEPT studies as it binds  $^{68}\text{Ga}^{3+}$ , rather than  $^{18}\text{F}^-$ , by chelation from the carboxyl components of iminodiacetate functional groups.<sup>15</sup>

Table 1.1. Materials used as radiotracers in PEPT studies on fluidisation.

Material	Size Range	Method of Activation
Anion-exchange resin beads	100 $\mu\text{m}$ – 4 mm	> 1 mm diameter: direct activation <sup>16</sup> < 1 mm diameter: ion-exchange <sup>17</sup>
$\gamma\text{-Al}_2\text{O}_3$	300 $\mu\text{m}$ – 3 mm	3 mm diameter: direct activation <sup>18</sup> 300 $\mu\text{m}$ diameter: not reported <sup>19</sup>
Glass	108 $\mu\text{m}$ – 4 mm	> 1 mm diameter: direct activation <sup>20</sup> < 1 mm diameter: surface modification <sup>17</sup>
Sand	120 $\mu\text{m}$	surface modification <sup>12</sup>

Processes involving solid-solid and solid-liquid mixing are used extensively in the chemical industry, including in the production of fine chemicals, pharmaceuticals and polymers. Mixing phenomena, however, are complex and still not well understood. In 1990, a contemporary estimate for the monetary loss resulting from poorly understood dynamics within stirred vessels was placed at \$10 billion per annum, in the US alone.<sup>21</sup> A comparable estimate was also made in 2004.<sup>22</sup> Evidently, there are inherent economic advantages to better understanding the dynamics of mixing processes. PEPT has been used to visualise flow within systems that utilise both solid-solid and solid-liquid mixing.

PEPT has been used to visualise solid-solid mixing in varied examples of mixing apparatus including high shear mixers,<sup>23</sup> rotating drums<sup>24</sup> and ploughshare mixers.<sup>25</sup> Moreover, solid-liquid mixing has been evaluated in apparatus including twin screw granulators,<sup>26</sup> pitched blade turbines<sup>27</sup> and planetary mixers.<sup>28</sup>

### 1.1.3 Conclusions

The use of smaller tracers in PEPT imaging is of significant interest as it may develop a better understanding of the dynamics in systems employed widely in the chemical industry, in turn a better understanding may enable more efficient designs with inherent economic advantages. The smallest tracer used to date is a resin bead with a reported diameter of 50  $\mu\text{m}$ ; however, resin tracers are often poor representations of the actual granular material in systems of interest, particularly if the material is crystalline. Resins often have much lower densities than crystalline materials which may in turn influence other properties pertinent to the movement of a particle within a system of interest, such as deformation of the particle following a collision and restitution (the relative loss of kinetic energy following a collision).<sup>29</sup> Ultimately, mechanically robust particles with diameters in the range 5 – 50  $\mu\text{m}$ , and ideally with controlled particle morphologies, synthesised from crystalline materials are in demand for application as PEPT tracers. Naturally, the crystalline material must also have an affinity for one of the routinely employed  $\beta^+$ -emitting radionuclides,  $^{18}\text{F}$  or  $^{68}\text{Ga}$ .

### 1.2 Speciation of Radionuclides: $^{18}\text{F}$ and $^{68}\text{Ga}$

Understanding the speciation of as-produced  $\beta^+$ -emitting radionuclides of interest,  $^{18}\text{F}$  or  $^{68}\text{Ga}$ , in aqueous solutions is crucial in determining how adsorption of the radionuclide onto a tracer particle occurs. Fluorine-18 produced by the  $^{16}\text{O}(^3\text{He},\text{p}^+)^{18}\text{F}$  nuclear reaction is obtained as fluoride anions with

an aqueous proton, from the dissociation of the water molecule, as a counter-cation so is produced as a very dilute solution of hydrofluoric acid.<sup>30</sup>

Aqueous gallium-68 is typically eluted from generators with the aid of concentrated hydrochloric acid.<sup>5</sup> The speciation of gallium in aqueous solutions is governed by pH; at low pH ( $\leq 3$ ), the predominant form of gallium is the hexaaquagallium(III) ion,  $[\text{Ga}(\text{H}_2\text{O})_6]^{3+}$ . As the pH increases, hydrolysis of the complex ensues, progressively generating hydroxide ions in the inner co-ordination sphere, represented by the general formula  $[\text{Ga}(\text{H}_2\text{O})_{6-x}(\text{OH})_x]^{(3-x)+}$  (for  $x = 1 - 3$ ). Eventually, in the pH range 4 – 5, precipitation of  $\alpha$ -GaOOH occurs.<sup>31</sup> The precipitate dissolves in basic media (pH  $\geq 8$ ) forming gallate ions,  $[\text{Ga}(\text{OH})_4]^-$ , as evidenced by Raman and  $^{71}\text{Ga}$  NMR spectroscopy. In contrast to the acidic system, gallate ions are the exclusive form of aqueous gallium in basic media.<sup>32</sup> The form of gallium that exists in acidic solutions is also dependent upon the counter-anion. Studies by Raman spectroscopy have shown both nitrate and sulfate ions can bind to gallium in the inner sphere of the complex, although at room temperature the ions tend to occur in the outer sphere with only a minor amount directly co-ordinated to the gallium ion.<sup>33</sup> By contrast, the interaction between gallium and the halides, chloride and bromide, is much stronger. In acidic solutions containing chloride, appreciable amounts of both  $[\text{Ga}(\text{H}_2\text{O})_6]^{3+}$  and  $[\text{GaCl}_4]^-$  have been detected by Raman spectroscopy, in addition to intermediate complexes of the general form  $[\text{GaCl}_n(\text{H}_2\text{O})_m]^{(3-n)+}$ . Accordingly, in  $^{68}\text{Ga}$  solutions eluted from  $^{68}\text{Ge}/^{68}\text{Ga}$  generators with concentrated hydrochloric acid, the predominant forms of gallium in solution would be expected to be hexaaquagallium(III) ions,  $[\text{Ga}(\text{H}_2\text{O})_6]^{3+}$ , and tetrachlorogallium(III) ions,  $[\text{GaCl}_4]^-$ , along with a range of intermediate species with either tetrahedral or octahedral co-ordination.<sup>34</sup>

## 1.3 Zeolites

### 1.3.1 Introduction

Zeolites are a class of microporous solids, that may be natural or synthetic, constituting crystalline aluminosilicates with 3-dimensional open frameworks comprising corner-shared  $[\text{SiO}_4]$  and  $[\text{AlO}_4]$  tetrahedra.<sup>35,36</sup> As the framework is rendered anionic by the presence of aluminium(III), charge compensation is fulfilled by exchangeable cations held electrostatically within the cages or pores of the material. The remaining pore volume is occupied by sorbed water.<sup>36</sup> Zeolites containing only one form of intrapore cation may be described by the general formula:  $(\text{M}^{n+})_{x/n}\text{Al}_x\text{Si}_{1-x}\text{O}_2 \cdot z\text{H}_2\text{O}$ , where  $n$  is the charge on the cation,  $x$  is the proportion of tetrahedral sites occupied by aluminium and  $z$  is the amount of sorbed water per formula unit. The exchangeable nature of non-framework cations allows tuning of zeolite properties by ion-exchange, enabling regulation of both molecular sieving behaviour and the selectivity of zeolite sorbents. Ion exchange is also exploited in the preparation of zeolite-based catalysts,<sup>37</sup> but ion-exchange itself is a valuable property utilised in a variety of applications including water softening and nuclear waste remediation.<sup>38,39</sup>

Zeolite frameworks may adopt a wide array of topologies, each with different connectivity between the corner shared tetrahedra in the structure. The description of framework structures is simplified by the identification of repeating structural motifs, termed secondary or composite building units. The simplest composite building units are rings, but rings may also join to form more complex units such as cages and chains. The size of a ring is conventionally described by the number of tetrahedral atoms (T atoms) in the ring, i.e. silicon or aluminium, rather than the total number of atoms. In the depiction of zeolite frameworks, straight lines join the silicon and aluminium atoms in neighbouring tetrahedra, rather than depicting chemical bonds.<sup>37</sup> In Figure 1.1, a single 6-membered ring (S6R) is shown in a conventional chemical representation with bonding between silicon or aluminium and oxygen atoms, as well as the simplified depiction of this ring conventionally used in illustrating zeolite frameworks. Figures 1.1 – 1.7 were made using Vesta 3 software.<sup>40</sup>

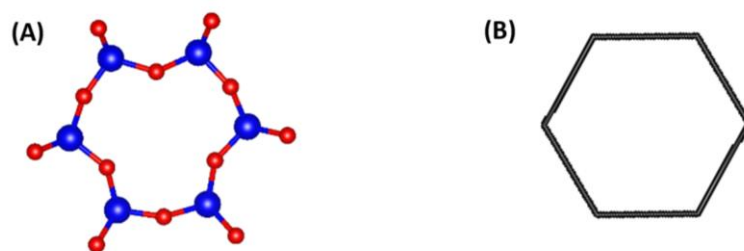


Figure 1.1. (A) A 6-membered ring with Si or Al atoms (blue) and O atoms (red). (B) The same 6-membered ring (S6R) as depicted in representations of zeolite framework structures.

Zeolites boast a rich and varied chemistry; cations may be ion-exchanged into the zeolite and neutral guest species may also migrate into the pores and cages, provided there is both a sufficient thermodynamic driving force for the process and that the guest species are appropriately sized.<sup>37</sup> Moreover, the large surface area of the zeolite can facilitate adsorption of varied cationic species for which appreciable ion-exchange does not occur.<sup>41</sup> The capability to introduce varied guest species, coupled with the ability to grow large crystals,<sup>42</sup> and synthesise large particles,<sup>43</sup> in the size range of interest (5 – 50  $\mu\text{m}$ ) render zeolites an attractive candidate for new PEPT tracers. A brief introduction to the nature, and structures, of the zeolites relevant to this work follows.

### 1.3.2 Zeolite A (LTA)

Zeolite A, also termed Linde Type A, is a synthetic zeolite which adopts the cubic space group  $Fm-3c$ , with  $a \approx 24.6 \text{ \AA}$  and the idealised formula:  $\text{Na}_{12}\text{Al}_{12}\text{Si}_{12}\text{O}_{48} \cdot 27\text{H}_2\text{O}$ .<sup>44</sup> The structure of zeolite A comprises a face-centred cubic array of sodalite cages (Figure 1.2A), a secondary building unit with 24 T atoms tracing a truncated octahedron, joined by double-4-rings.<sup>36,45</sup> A sodalite cage and a double-4-ring (D4R) are depicted in Figures 1.2B and 1.2C, respectively. Zeolite A may alternately be described as a primitive cubic array of sodalite cages in the lower symmetry  $Pm-3m$  cubic space group with  $a \approx 12.3 \text{ \AA}$ . Although the  $Fm-3c$  cell is a more accurate representation than the  $Pm-3m$  pseudo-cell, the  $Pm-3m$

space group is also widely used to describe the zeolite A crystal structure.<sup>44-46</sup> The ideal composition of the zeolite has a framework Si/Al ratio of 1, the maximum permitted aluminium content of a zeolite as Al-O-Al linkages are considered unfavourable, a principle termed Loewenstein's rule.<sup>37</sup> The high ion-exchange capacity engendered by the aluminium content, and a preference for divalent metal cations, has led to the application of zeolite A as a commercial detergent builder, softening water by selectively exchanging intrapore sodium for aqueous calcium.<sup>38</sup>

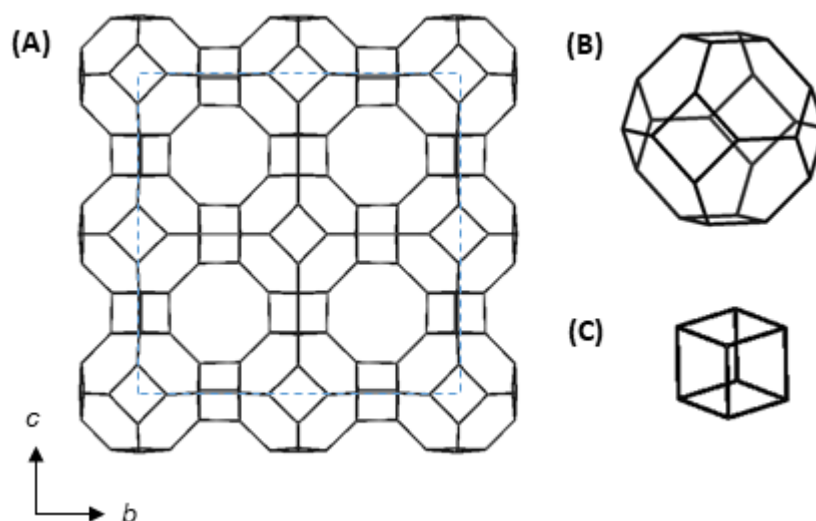


Figure 1.2. (A) The structure of zeolite A as viewed along [100] with the unit cell shown as a dashed blue line. (B) A sodalite cage and (C) a double-4-ring.

### 1.3.3 Faujasite (FAU)

Faujasite is a naturally occurring zeolite that can also be synthesised hydrothermally. Synthetic faujasite analogues are more commonly known as zeolites X and Y according to the framework Si/Al ratio; zeolite X is more aluminous ( $1 < \text{Si/Al} < 1.5$ ), whereas zeolite Y is more siliceous ( $1.5 < \text{Si/Al} < 3$ ).<sup>36</sup> Both zeolites X and Y adopt the cubic space group  $Fd-3m$ , with the idealised unit cell parameters:  $a = 25.0 \text{ \AA}$ , for zeolite X, and  $a = 24.6 \text{ \AA}$ , for zeolite Y.<sup>44</sup> The faujasite topology contains sodalite cages joined by double-6-rings, with each sodalite cage connected to another four in a tetrahedral

orientation about the central sodalite cage. The structure is, therefore, analogous to diamond.<sup>46</sup> The arrangement of sodalite cages gives rise to large cavities termed supercages, as depicted in Figure 1.3C. Each supercage has 4 tetrahedrally orientated 12-membered ring openings permitting porosity in the  $[110]$  direction, as shown in Figure 1.3A, as well as between adjacent supercages. Both zeolites X and Y are applied in their  $H^+$ -exchanged forms as catalysts in the petrochemical industry, catalysing fluid catalytic cracking, a process whereby large chain hydrocarbons are reduced to shorter chain hydrocarbons, desirable due to the improved octane rating of the latter.<sup>37</sup>

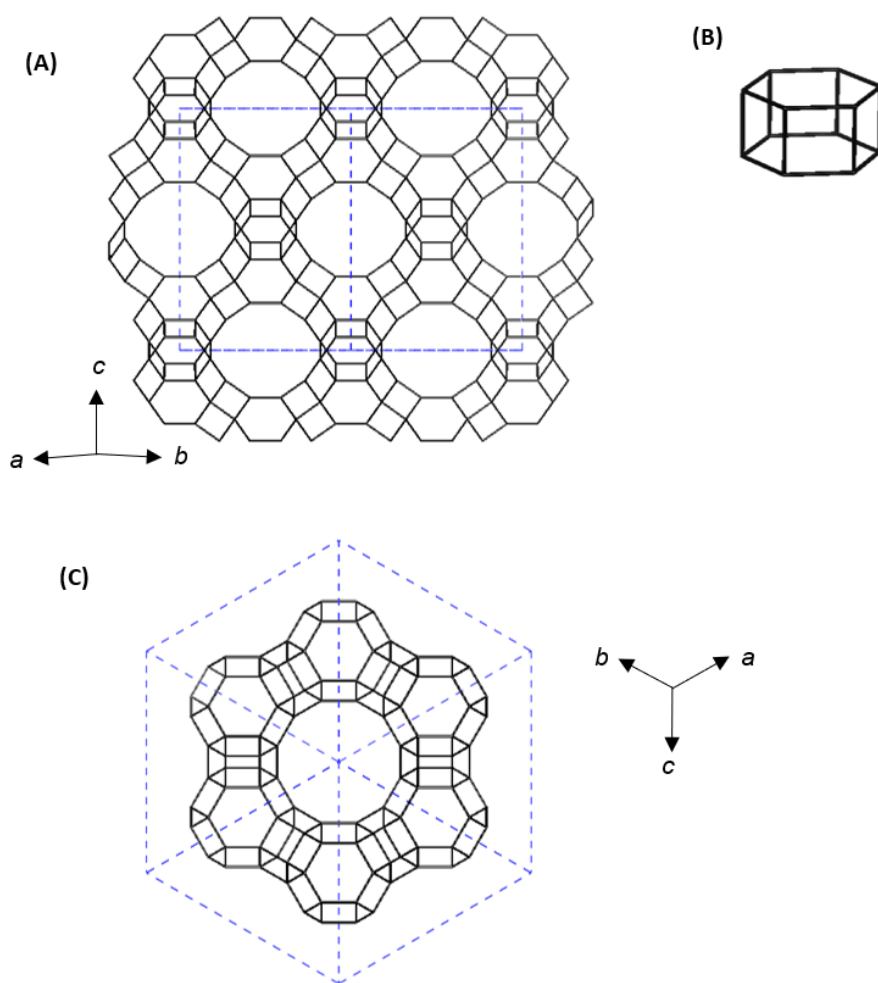


Figure 1.3. (A) The faujasite framework as viewed along  $[110]$ , (B) a double-6-ring (D6R) and (C) a projection of part of a faujasite unit cell as viewed along  $[111]$ , depicting the supercage. In (A) and (C), the blue dashed line corresponds to the unit cell.

### 1.3.4 Mordenite (MOR)

Mordenite is a more siliceous zeolite with idealised formula,  $\text{Na}_8\text{Al}_8\text{Si}_{40}\text{O}_{96} \cdot 24\text{H}_2\text{O}$ . The zeolite adopts the orthorhombic space group  $Cmcm$  with idealised unit cell parameters:  $a = 18.3 \text{ \AA}$ ,  $b = 20.5 \text{ \AA}$  and  $c = 7.8 \text{ \AA}$ .<sup>44</sup> The structure comprises 4 and 5-membered rings which share common edges forming chains. Mirror images of these chains are connected via oxygen bridges forming corrugated sheets. Adjacent sheets are displaced by half a translation about the c-axis and are connected to one another forming oval-shaped 12-membered ring channels, as shown in Figure 1.4. The channels are lined with 8-membered apertures; however, adjacent 8-membered rings are displaced such that transport between adjoining 12-membered ring channels is inhibited, rendering porosity in the framework essentially one-dimensional.<sup>46</sup> Proton-exchanged mordenite is a versatile, industrially important catalyst utilised to catalyse alkylation, reforming and hydroisomerisation reactions, all of which are critical reactions in improving the octane rating of hydrocarbon fuels in the petrochemical industry.<sup>37</sup>

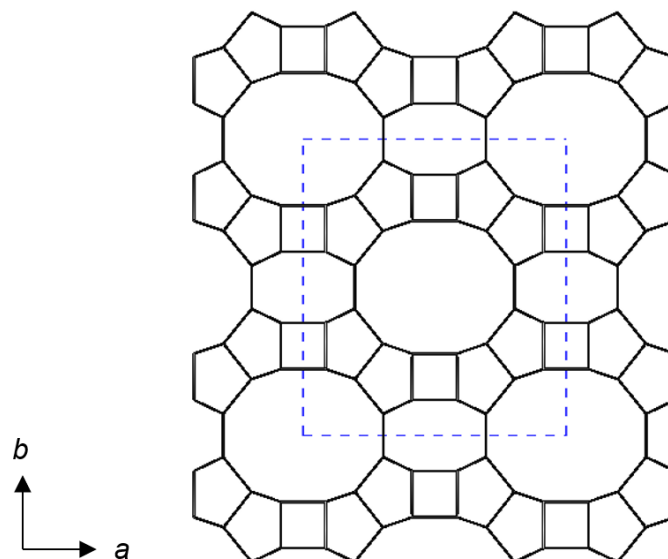


Figure 1.4. The mordenite framework as viewed down [001]; the unit cell is shown as a dashed blue line.

### 1.3.5 Gmelinite (GME)

Gmelinite is a natural zeolite which adopts the hexagonal space group  $P6_3/mmc$  with idealised unit cell parameters:  $a = 13.7 \text{ \AA}$  and  $c = 9.9 \text{ \AA}$ .<sup>44</sup> The structure comprises parallel stacks of double-6-rings (D6R) in an ABAB sequence along the  $c$  axis, as depicted in Figure 1.5C. The stacking of double-6-rings in this fashion gives rise to gmelinite cages (Figure 1.5B), bounded by 2 D6R in the same B layer and one D6R each from the A layer above and below.<sup>46</sup> Twelve-membered ring channels run along  $[001]$ , as shown in Figure 1.5A, but stacking faults and intergrowth of chabazite, a zeolite with a related structure, often compromise the porosity exhibited by the zeolite despite the relatively large pores. Fault free gmelinite has been reportedly synthesised by using a polymeric structure directing agent.<sup>47</sup> Gmelinite accommodates both monovalent and divalent intrapore cations with 2 available cations sites, one within the gmelinite cages (M1) and one in the large channel near the single-8-membered ring aperture (M2). In Na-GME and K-GME, full occupancy is observed at cation site M1 with the remaining cations occupying site M2. In contrast, the calcium ions in Ca-GME occupy both M1 and M2 sites with the occupancy at each reduced by approximately half compared with those in Na-GME and K-GME.<sup>48</sup>

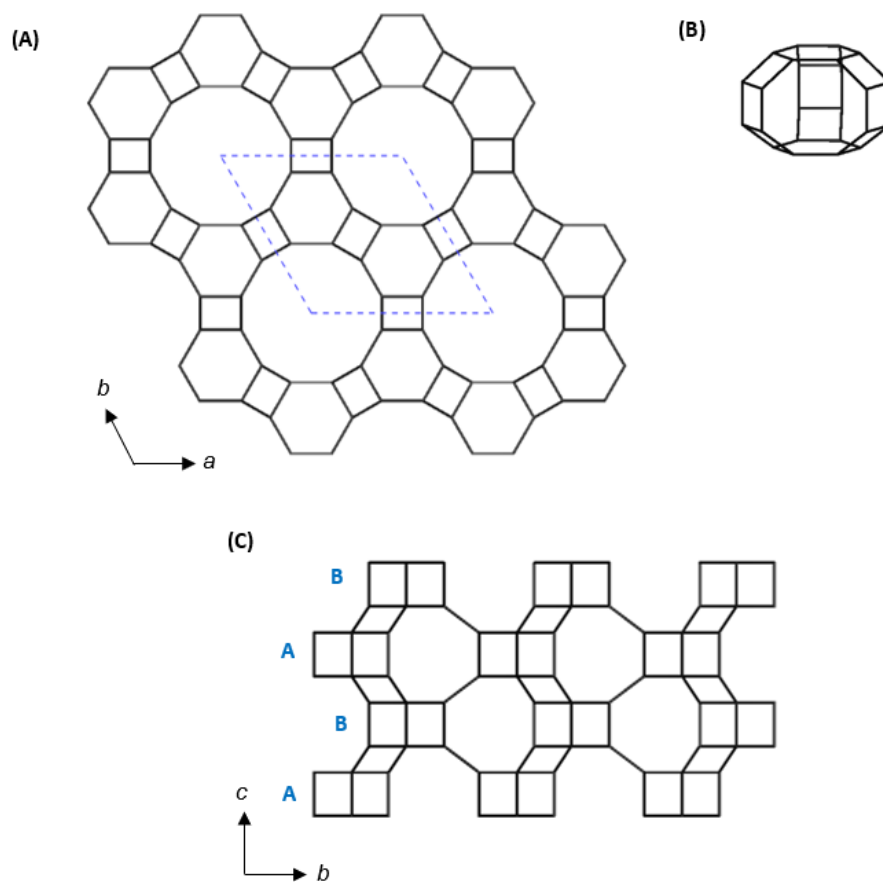


Figure 1.5. (A) The gmelinite framework viewed along [001], (B) a gmelinite cage and (C) a projection of gmelinite along [100], demonstrating the ABAB stacking sequence, as labelled.

### 1.3.6 Chabazite (CHA)

Chabazite is another natural zeolite which adopts the trigonal space group  $R\bar{3}m$  with idealised unit cell parameters:  $a = 13.7 \text{ \AA}$  and  $c = 14.8 \text{ \AA}$ .<sup>44</sup> The chabazite structure (Figure 1.6A), like gmelinite, also comprises double-6-rings but stacked in an ABCABC sequence.<sup>46</sup> In the chabazite unit cell, the double-6-ring sets are rotated  $60^\circ$  relative to those in gmelinite. The additional layer in the repeating structure gives rise to a larger cavity than is observed in gmelinite, the chabazite cage (Figure 1.6B).<sup>44</sup>

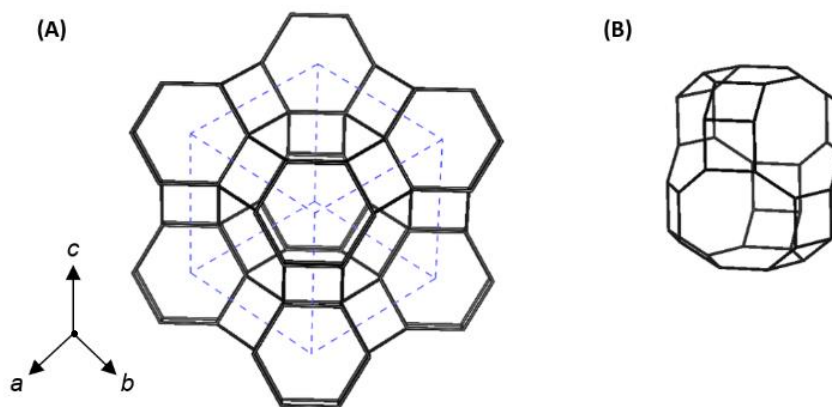


Figure 1.6. (A) The chabazite framework as viewed along [111] with the unit cell shown as a dashed blue line and (B) a chabazite cage.

### 1.3.7 Zeolite P (GIS)

Zeolite P is a synthetic zeolite with a framework topology analogous to the monoclinic mineral gismondine, thus the framework is denoted GIS.<sup>44</sup> Although it shares the same framework topology as gismondine, the zeolite P structure displays higher symmetry adopting the tetragonal space group  $I4_1/amd$  with idealised unit cell parameters:  $a = 9.8 \text{ \AA}$  and  $c = 10.2 \text{ \AA}$ .<sup>44,49</sup> The GIS framework (Figure 1.7A) contains a composite building unit termed a double crankshaft chain, a repeating motif of 9 contiguous single-4-rings, depicted in Figure 1.7C. The GIS framework comprises two sets of double crankshaft chains, one parallel to [100] and the other parallel to [010], giving rise to 8-membered ring channels running in the [100] direction.<sup>44,49</sup> Zeolite P may be synthesised over a broad range of Si/Al ratios, from relatively high Si/Al ratios,  $\text{Si/Al} \approx 3.5$ ,<sup>50</sup> to maximum aluminium zeolite P (MAP) with  $\text{Si/Al} = 1$ .<sup>49</sup> Favourable ion-exchange with divalent cations, including  $\text{Ca}^{2+}$ , has led to use of MAP as a commercial detergent builder, rivalling zeolite A.<sup>38</sup>

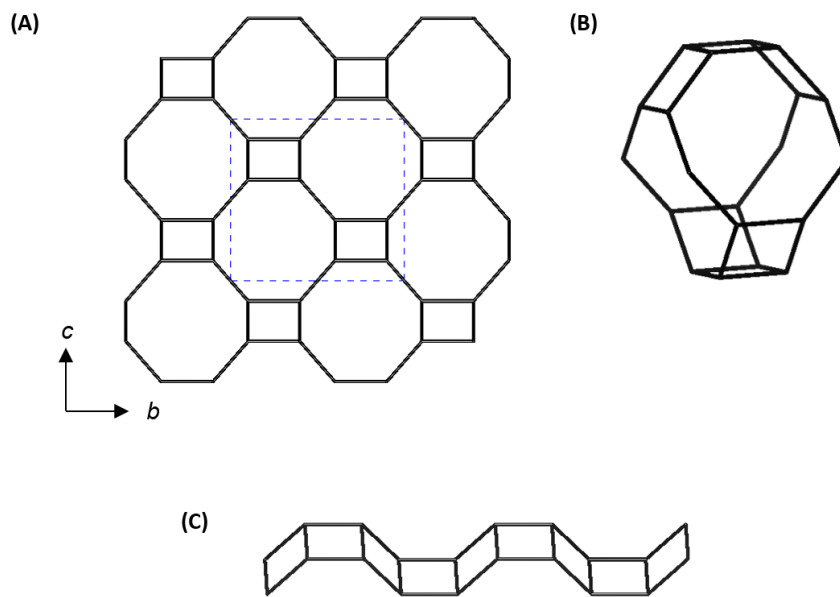


Figure 1.7. (A) A projection of the zeolite P framework as viewed down [100], with the unit cell shown as a dashed blue line. (B) A gismondine cage and (C) a double crankshaft chain.

## CHAPTER 2: EXPERIMENTAL

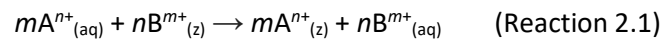
### 2.1 Experimental Techniques

#### 2.1.1 Hydrothermal Synthesis of Zeolites

Zeolites are most commonly synthesised hydrothermally by heating solutions under autogenous pressure. The solutions comprise silicon and aluminium-containing precursors, a mineraliser, a source of intrapore cations and a solvent, usually water.<sup>51,52</sup> The role of the mineraliser, typically hydroxide ions, includes solubilising the silicon or aluminium-containing precursor, participating in the condensation reactions between silicon and aluminium-containing species leading to the formation of a gel, and enhancing transport of reactive species from solution to growing crystallites.<sup>51</sup> The zeolite gel is heated to allow crystallisation to occur, at temperatures typically between 80 – 200°C, for periods of hours to days, depending on the optimum conditions for the crystallisation of the desired zeolite phase. In zeolite syntheses, gels are usually heated under autogenous pressure, typically using autoclaves as reaction vessels.<sup>52</sup>

#### 2.1.2 Aqueous Ion Exchange

The intrapore cations within zeolites may be exchanged with aqueous cations, provided the process is both kinetically and energetically favourable under the given conditions. The simplest example of zeolite ion exchange may be described by the equilibrium reaction below (Reaction 2.1), in which the cation  $A^{n+}$  in solution replaces cation  $B^{m+}$  in the zeolite, releasing cation  $B^{m+}$  into the solution. In the reaction, the subscript state symbol “z” denotes an intrapore cation in the zeolite. The viability of ion exchange, and the extent to which it occurs, is governed by several kinetic and thermodynamic factors, including the ability of the incoming ion to diffuse to an appropriate site within the zeolite, as well as the free energy of the aqueous ion compared with the ion in an intrapore environment.<sup>53,54</sup>



For ion exchange to occur, the zeolite must be contacted with a solution containing the ion of interest. Immersion of the zeolite in solution may occur in a simple vessel, such as a plastic bottle, or may be performed by eluting the solution through a column packed with the zeolite. The former method is often referred to as a “batch ion exchange” experiment, owing to the closed nature of the system, a “batch reactor”, with no flow of reactants in or products out of the system, unlike in columnar vessels. In batch ion-exchange experiments, agitation is often provided to the solution by stirring or shaking, and heat may also be provided to drive the ion-exchange reaction.<sup>54</sup> In batch ion exchange experiments performed in subsequent chapters, both agitation and heat are provided to the vessel by immersion in a water bath equipped with a shaking attachment.

### 2.1.3 Adsorption

Adsorption refers to phenomena in which an adsorbate (gas, liquid or solute) adheres to the surface of an adsorbent (liquid or solid). Adsorption refers to several different attractive interactions that may occur between an adsorbate and an adsorbent, ranging in strength from relatively weak physical adsorption, such as van der Waal’s interactions or ion-dipole interactions, to the stronger chemical adsorption, in which a chemical bond is formed between the adsorbate and the adsorbent surface.<sup>55</sup>

Adsorption phenomena in a system that has reached equilibrium under isothermal conditions is commonly modelled by adsorption isotherms, which were first developed to describe the adsorption of gas molecules onto solid adsorbents.<sup>55,56</sup> Many of these models may be translated to studying adsorption phenomena in other systems, including adsorption of a solute onto a solid adsorbent,<sup>56</sup> which is of interest in subsequent chapters for studying the interaction between aqueous fluoride and solid zeolite particles. In the case of adsorption from solutions, adsorption isotherms relate the equilibrium concentration of the solute ( $c_e$ ) to the equilibrium loading of the solute on the

adsorbent ( $q_e$ ). The simplest isotherm is Henry's law, Equation 2.1, where the equilibrium concentration is related to the equilibrium loading by a single constant, Henry's constant ( $K_H$ ). In many cases, adsorption is better modelled by more complex isotherms which contain two parameters. Isotherm parameters may be calculated by measuring  $q_e$  and  $c_e$  under isothermal conditions with different starting concentrations, then applying regression analysis to the adsorption isotherm to determine the parameters.<sup>56</sup> In the subsequent chapters, four models are considered in their forms most commonly applied to adsorption at the solid-liquid interface: the Langmuir, Freundlich, Temkin and Dubinin-Radushkevitch isotherms. An introduction to these models and, where appropriate, the significance of their isotherm parameters follows.

$$q_e = K_H \cdot c_e \quad (\text{Eq. 2.1})$$

The Langmuir model of adsorption (Equations 2.2 and 2.3 in Table 2.1) is based on three assumptions: adsorption is restricted to monolayer coverage; the surface is uniform with all sites being energetically equivalent and the ability to adsorb at a given site is independent of occupation at neighbouring sites. In reality, these three criteria are often not met due to surface inhomogeneity, adsorbate-adsorbate interactions and multi-layer adsorption, rendering the Langmuir model a poor representation of adsorptive processes, in particular for those occurring at the solid-liquid interface.<sup>55</sup> The Freundlich (Equations 2.4 and 2.5 in Table 2.1) and Temkin (Equations 2.6 and 2.7 in Table 2.1) models are more complex and compensate for surface inhomogeneity and adsorbate-adsorbate interactions, respectively. As loading increases, the enthalpy of adsorption decreases due to occupation at less energetically favourable sites, as well as repulsion between adsorbates at neighbouring sites.<sup>56,57</sup> The Temkin isotherm assumes a linear decrease in adsorption enthalpy with increasing loading, whereas the decrease is assumed to be logarithmic in the Freundlich model.<sup>56,57</sup>

Table 2.1. Langmuir, Freundlich, Temkin and DR adsorption isotherms, and their linear forms, as applied to adsorption at the solid-liquid interface.

	Adsorption isotherm	Linear form
Langmuir	$q_e = \frac{q_m b c_e}{1 + b c_e}$ (Eq. 2.2)	$\frac{c_e}{q_e} = \frac{1}{q_m b} + \frac{1}{q_m} c_e$ (Eq. 2.3)
Freundlich	$q_e = K_F c_e^n$ (Eq. 2.4)	$\ln q_e = \ln K_F + n \ln c_e$ (Eq. 2.5)
Temkin	$q_e = \frac{RT}{b_T} \ln A_T c_e$ (Eq. 2.6)	$q_e = \frac{RT}{b_T} \ln A_T + \frac{RT}{b_T} \ln c_e$ (Eq. 2.7)
Dubinin-Radushkevitch (DR)	$q_e = \frac{V_0}{V_m} \exp(-K \varepsilon^2)$ (Eq. 2.8)	$\ln q_e = \ln \left( \frac{V_0}{V_m} \right) - K \varepsilon^2$ (Eq. 2.9)
Definitions: $c_e$ , equilibrium concentration ( $\text{mg L}^{-1}$ ); $q_e$ , equilibrium uptake ( $\text{mg g}^{-1}$ ); $b$ , Langmuir constant ( $\text{L g}^{-1}$ ); $q_m$ , maximum monolayer coverage ( $\text{mg g}^{-1}$ ); $n$ , exponent (dimensionless); $K_F$ , adsorption co-efficient ( $(\text{mg g}^{-1})/(\text{mg L}^{-1})^n$ ); $b_T$ , Temkin constant ( $\text{kJ mol}^{-1}$ ); $A_T$ , Temkin isotherm constant ( $\text{L g}^{-1}$ ); $R$ , universal gas constant ( $\text{kJ K}^{-1} \text{mol}^{-1}$ ); $T$ , absolute temperature (K); $V_0$ , specific micropore volume ( $\text{cm}^3 \text{g}^{-1}$ ); $V_m$ , adsorbate volume ( $\text{cm}^3 \text{mg}^{-1}$ ); $K$ , Dubinin-Radushkevitch constant ( $\text{mol}^2 \text{kJ}^{-2}$ ); $\varepsilon$ , adsorption potential ( $\text{kJ mol}^{-1}$ ).		

Modelling adsorption data using the Freundlich isotherm enables the determination of the adsorption co-efficient,  $K_F$ , and exponent,  $n$ .  $K_F$  is a relative measure of the characteristic strength of the adsorptive process;  $K_F$  is also found to increase with increasing loading achievable for the adsorbate. The exponent,  $n$ , provides a measure of the favourability of adsorption. The exponent adopts values lower than 1 when adsorption is favourable and values greater than 1 when the process is unfavourable.<sup>56</sup> The discussion of favourability, with respect to adsorption, is akin to the concept of spontaneity in the thermodynamic description of chemical process; unfavourable adsorptive processes may occur but require work to be done in order to take place.<sup>55</sup>

The Dubinin-Radushkevitch (DR) isotherm (Equations 2.8 and 2.9 in Table 2.1) was initially developed for vapour deposition on microporous solids. Although the DR equation was devised to model adsorption at the solid-gas interface, it is also routinely applied in the study of adsorption at the solid-liquid interface.<sup>56</sup> The adsorption potential,  $\varepsilon$ , in the DR isotherm may be calculated from either Equation 2.10 or 2.11. In Equation 2.11,  $c_s$  is the solubility of the adsorbate.<sup>56-58</sup> The use of Equation 2.10 to calculate the adsorption potential is widespread; however, compelling arguments by Hu and Wang<sup>58</sup> are put forward for the preferential use of Equation 2.11 for enhanced accuracy. Fitting to the DR isotherm enables the determination of the characteristic adsorption energy ( $E_c$ ) by Equation 2.12, providing a quantitative measure of the favourability of adsorption.<sup>57</sup> Moreover, the magnitude of  $E_c$  is indicative of the nature of adsorption: values below  $8 \text{ kJ mol}^{-1}$  are associated with physical adsorption processes, whereas values greater than  $8 \text{ kJ mol}^{-1}$  indicate chemisorption is occurring.<sup>60</sup>

$$\varepsilon = RT \ln\left(1 + \frac{1}{c_e}\right) \quad (\text{Eq. 2.10})$$

$$\varepsilon = RT \ln\left(\frac{c_s}{c_e}\right) \quad (\text{Eq. 2.11})$$

$$E_c = 2K^{-0.5} \quad (\text{Eq. 2.12})$$

## 2.2 Characterisation

### 2.2.1 Powder X-ray Diffraction (PXRD)

#### 2.2.1.1 Fundamental Crystallography

A crystalline solid is a material with long range order in the form of a repeating arrangement of atoms or molecules. The structures of crystalline solids are most conveniently described by the unit cell, a repeating motif defined as the smallest parallel-sided three-dimensional volume element which contains all the necessary symmetry to produce the entire lattice by replication. A unit cell is described by the lattice constants: three sides,  $a$ ,  $b$  and  $c$ , and three angles,  $\alpha$ ,  $\beta$  and  $\gamma$ ; where  $\alpha$  is the angle between sides  $b$  and  $c$ ,  $\beta$  between  $a$  and  $c$ , and  $\gamma$  between  $a$  and  $b$ . There are 7 possible crystal systems, each with a different unit cell shape, presented in Table 2.2 along with the relationship between the lattice constants for each crystal system.<sup>60</sup>

Table 2.2. The unit cell shapes for different crystal systems.

Crystal system	Unit cell shape
Cubic	$a = b = c, \alpha = \beta = \gamma = 90^\circ$
Tetragonal	$a = b \neq c, \alpha = \beta = \gamma = 90^\circ$
Orthorhombic	$a \neq b \neq c, \alpha = \beta = \gamma = 90^\circ$
Hexagonal	$a = b \neq c, \alpha = \beta = 90^\circ, \gamma = 120^\circ$
Trigonal	$a = b \neq c, \alpha = \beta = 90^\circ, \gamma = 120^\circ$ or $a = b = c, \alpha = \beta = \gamma \neq 90^\circ$
Monoclinic	$a \neq b \neq c, \alpha = \gamma = 90^\circ, \beta \neq 90^\circ$
Triclinic	$a \neq b \neq c, \alpha \neq \beta \neq \gamma \neq 90^\circ$

Two essential concepts in the description of crystalline solids are Bravais lattices, infinite arrays of discrete points generated by a set of discrete translation operations, and crystallographic point groups, sets of symmetry operations in 3-dimensions that permit the construction of an infinite lattice from a unit cell by action of symmetry operations on the atoms.<sup>60,61</sup> There are 14 possible Bravais lattices, produced from the 7 crystal systems along with the permitted centring of the unit cell for

each crystal system, and 32 possible crystallographic point groups. Combining the two concepts, the Bravais lattices and the crystallographic point groups, gives rise to the space group, describing both the symmetry of the unit cell (Bravais lattice) and symmetry operations necessary to produce an infinite array of atoms from the unit cell (crystallographic point group).<sup>61,62</sup>

#### 2.2.1.2 Powder X-ray Diffraction

Powder X-ray diffraction is a versatile and important technique in the structural analysis of crystalline solids. In the discussion of the underlying principles of PXRD, it is useful to consider crystalline solids as comprising parallel planes of atoms separated by a constant distance, the interplanar spacing,  $d_{hkl}$ . Planes of atoms are described by Miller indices in the format  $(hkl)$ , where  $h$  is the reciprocal of the fractional co-ordinate at which the plane intercepts the  $a$  axis of the unit cell,  $k$  is related to  $b$  in an analogous manner, as is  $l$  to  $c$ . If a plane is parallel to an axis of the unit cell, rather than intercepting it, zero is given for the appropriate Miller index.<sup>60</sup>

PXRD relies on measuring the Bragg diffraction of X-rays from a polycrystalline sample. In the Bragg model, incident X-rays may either be reflected from a plane of atoms,  $(hkl)$ , at an angle equal to the incident angle ( $\theta$ ) or may be transmitted through the plane to be diffracted by a subsequent plane. Constructive interference of the reflected X-rays occurs only when the interplanar spacing ( $d_{hkl}$ ) is related to the incident angle ( $\theta$ ) such that Bragg's law is satisfied (Equation 2.13). In Bragg's law,  $\lambda$  corresponds to the wavelength of the incident X-rays and  $n$  is an integer. A visual representation of Bragg diffraction adapted from *Basic Solid State Chemistry*<sup>60</sup> is presented in Figure 2.1. Naturally, constructive interference from sets of a given  $(hkl)$  plane will only occur at the angle that satisfies Bragg's law, thus a diffracted beam is only observed for the given plane at a specific incident angle.<sup>60</sup>

$$2d_{hkl} \sin \theta = n\lambda \quad (\text{Eq. 2.13})$$

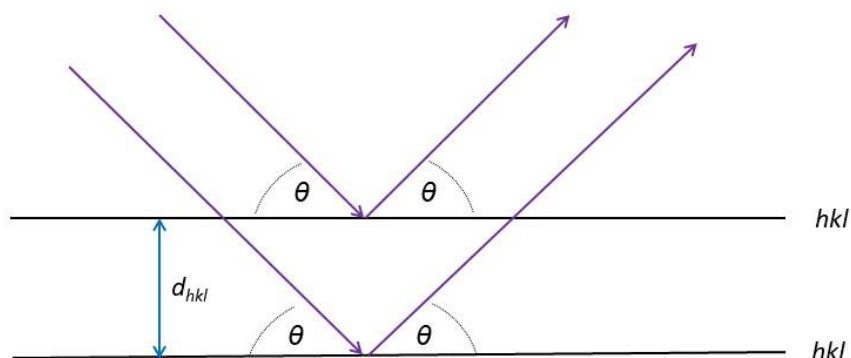


Figure 2.1. A schematic of the Bragg diffraction of X-rays (purple). Black lines represent planes of atoms ( $hkl$ ),  $\theta$  is the incident angle and  $d_{hkl}$  is the interplanar spacing.

In PXRD, a sample is irradiated with a parallel monochromatic beam of X-rays over a range of successive incident angles, separated by a defined step-size. The diffracted X-rays are then measured as a function of the incident angle. In a PXRD pattern, the intensity of diffracted X-rays is plotted as a function of  $2\theta$ , where each peak in the pattern corresponds to planes with a given ( $hkl$ ) value. The peak may be described as a Bragg reflection, denoted:  $hkl$ . The intensity of a Bragg reflection is proportional to the square of the structure factor,  $F_{hkl}$ , which in turn is proportional to the scattering power of the atoms present in the sample,  $f_{hkl}$ . As X-rays are scattered by electrons, the scattering power of an element increases with increasing atomic number.<sup>60</sup>

Powder diffractometers require both an X-ray source and a detector to measure diffracted X-rays. In diffractometers in reflection geometry, an X-ray beam strikes a powdered polycrystalline sample at a given incident angle,  $\theta$ , and the X-ray beam diffracted at angle  $\theta$  is measured by a detector. A range of desired incident angles is scanned by the co-operative motion of the X-ray source and detector about the sample. The most common detectors in laboratory diffractometers, including those used in PXRD analysis in subsequent chapters, are scintillation detectors. In scintillation detectors, X-rays collide with a scintillator material, such as thallium-doped sodium iodide, which subsequently emits lower energy photons, corresponding to the visible spectrum. A photomultiplier then converts the visible photons to a voltage pulse with an intensity proportional to the number of photons.<sup>63</sup>

In laboratory diffractometers, the X-ray source, also termed an “X-ray tube”, comprises a tungsten filament acting as a cathode to which an electrical current is applied, heating the filament. Electrons emitted from the surface of the filament by thermionic emission are accelerated through a potential towards a metal target, the anode. Ionisation of the metal target upon bombardment with electrons gives rise to the emission of X-rays, as a core shell electron is ejected and the remaining “vacancy” is filled by a second electron from a higher energy orbital, giving rise to the emission of characteristic X-rays as the second electron is stabilised, with the energy of the X-ray corresponding to the difference in energy between the orbitals.<sup>60</sup>

Several characteristic X-rays may be emitted from the metal target in an X-ray tube, with the most intense typically being the  $K_{\alpha}$  and  $K_{\beta}$  lines, corresponding to the 2p to 1s transition and 3p to 1s transition, respectively. Naturally, a monochromatic beam of X-rays is necessary for powder diffraction; accordingly, the  $K_{\alpha}$  radiation is separated from others by passing the beam through a thin foil of an element with an appropriate absorption edge, such that all radiation apart from the  $K_{\alpha}$  X-rays is absorbed by the element. In the case of copper X-ray sources, nickel foil is used to remove the  $K_{\beta}$  radiation, whereas iron foil is used to remove  $K_{\beta}$  radiation produced by cobalt X-ray sources.  $K_{\alpha}$  radiation is composite of two similar but distinct wavelengths,  $K_{\alpha 1}$  and  $K_{\alpha 2}$ , owing to the 2 possible spin states of the 2p electron involved in the transition. The wavelength of copper  $K_{\alpha}$  radiation is 1.5418 Å, from the weighted average of the  $K_{\alpha 1}$  ( $\lambda = 1.5406$  Å) and  $K_{\alpha 2}$  ( $\lambda = 1.5443$  Å) wavelengths.  $K_{\alpha 2}$  radiation may be removed by a monochromator; however, the PXRD patterns presented in the subsequent chapters were recorded on diffractometers without a monochromator, therefore the incident X-rays were both  $K_{\alpha 1}$  and  $K_{\alpha 2}$ .<sup>63</sup>

### 2.2.2 X-ray Fluorescence (XRF) Spectrometry

X-ray fluorescence (XRF) spectrometry is a non-destructive technique for elemental analysis, in which the energy of characteristic X-rays emitted from a sample, bombarded with an X-ray beam, are measured to determine the elements present and their concentrations in the sample. An incident X-ray may ionise a given atom, provided the energy of the X-ray exceeds the ionisation energy. Upon bombarding a sample with high energy X-rays, electrons are ejected from core orbitals within the atoms in the sample; in order to stabilise the resulting unstable electron configuration, an electron from a higher energy orbital must move into the partially vacant core orbital. One of two processes may result from the stabilisation, either an X-ray is emitted from the atom with a wavelength characteristic of the energy between the higher energy orbital and core orbital, or alternatively, the characteristic X-ray may instead be transferred to another electron in the atom, and the resulting photoelectron is then emitted from the atom, a phenomenon termed the Auger effect. The probability of X-ray emission resulting from ionisation of the atom, rather than the Auger effect occurring, is termed the fluorescence yield, which increases with increasing atomic number. Sodium is the lightest element for which routine analysis by XRF spectrometry may be performed on account of the very low fluorescence yields of lighter elements. In Siegbahn notation, commonly used to describe the X-rays emitted from electron transitions,  $K_{\alpha}$  corresponds to the 2p to 1s transition,  $K_{\beta}$  to the 3p to 1s and  $L_{\alpha}$  to the 3d to 2p.<sup>64</sup>

XRF spectrometers comprise an excitation source, a sample presentation system, a detection system and a data processing system. The most commonly employed excitation sources are X-ray tubes, analogous in operation to those used in powder X-ray diffractometers (Section 2.2.1.2). In the Bruker S8 Tiger spectrometer used in XRF analysis in later chapters, the anode target is rhodium. XRF spectrometers are termed wavelength dispersive XRF (WD-XRF) or energy dispersive XRF (ED-XRF) spectrometers, according to the detection system.<sup>64</sup> In wavelength-dispersive systems, X-rays emitted from the sample are separated by wavelength prior to detection, exploiting Bragg's law by using

diffraction on the faces of dispersing crystals within the instrument. In contrast, energy-dispersive systems directly detect the emitted X-rays with a semiconducting detector, typically Si(Li), which converts the X-ray into an electrical pulse, with the height of the pulse being proportional to the energy of the X-ray. The Bruker S8 Tiger is a wavelength-dispersive XRF (WD-XRF) spectrometer containing multiple dispersing crystals, permitting sequential measurement of wavelengths by changing the geometry of the scintillation detector and the dispersing crystal, according to the optimal crystal for a given wavelength.<sup>64,65</sup>

XRF spectrometry permits both qualitative and quantitative analysis of sample composition. In qualitative analysis, elements may be identified by the presence of characteristic emission lines in the resulting XRF spectrum. In quantitative analysis, the weight fraction of an element ( $C$ ) is related to the relative integrated peak intensity ( $I_R$ ) by two factors: the matrix factor ( $M$ ) and instrument factor ( $K$ ), as shown in Equation 2.14. The matrix and instrument factors are complicated mathematical formulae which consider the influence of either known or estimated parameters on the relationship between the peak integral and the weight fraction.<sup>65</sup>

$$C = M \times K \times I_R \quad (\text{Eq. 2.14})$$

The matrix factor in the calculation of weight fractions from peak integrals takes into consideration sample dependent phenomena such as primary absorption, secondary absorption and secondary fluorescence. Primary absorption refers to absorption of radiation from the X-ray source, secondary absorption to fluorescent radiation from the sample that is absorbed, and secondary fluorescence refers to excitation by fluorescent radiation from other elements within the sample. Both secondary absorption and fluorescence are particularly prevalent in samples containing elements over a wide range of atomic numbers. While the matrix factor attempts to model the influence of these phenomena, precise matrix factors are only possible when elements with reasonably close atomic numbers are present. Naturally, any inaccuracy in the matrix factor carries through to inaccuracy in the calculated weight fraction.<sup>65</sup>

### 2.2.3 Scanning Electron Microscopy

Multiple interactions occur when a focused beam of high energy electrons is incident upon a solid sample, including elastic scattering of the incident electrons (backscattered electrons), the emission of secondary electrons from the sample surface and the emission of characteristic X-rays. Scanning electron microscopy exploits these interactions, among others, to provide information on the topography, composition and distribution of elements within a solid sample. Ionisation of core shell electrons and the consequent filling of core shell vacancies from a higher energy orbital gives rise to the emission of characteristic X-rays. The detection of these X-rays permits determination of the sample composition, by energy dispersive X-ray fluorescence spectrometry (ED-XRF), as described in Section 2.2.3. The proportion of elastically scattered electrons may be correlated with the atomic number of the elements present in the sample, as larger atoms will give rise to more elastic collisions. In greyscale images produced by detecting backscattered electrons, brighter areas correspond to those with greater atomic number and darker areas with those with lower atomic number.<sup>64</sup>

The key interaction that permits topographical imaging in SEM is secondary electron emission from the sample surface, resulting from sample ionisation by the incident beam. All scanning electron micrographs presented in the subsequent chapters were obtained by secondary electron imaging. To improve the images obtained by secondary electron imaging, samples are often sputter coated with a thin film (thickness  $\approx 20$  nm) of a precious metal, such as gold or platinum. The conductive metal prevents the accumulation of static electric fields in the sample, which would compromise image quality, as well as enhancing the secondary electron signal, in turn improving image quality.<sup>65</sup>

In the operation of a scanning electron microscope, electrons are produced by an electron gun then focused by a series of lenses before being beamed on to the sample surface. As the narrow-focused electron beam is scanned over the sample, emitted secondary electrons are detected then amplified, allowing an image to be reconstructed that reveals the sample topography. Electron guns may produce electrons by either thermionic or field emission. Thermionic emission is analogous to electron

production in X-ray tubes (as described in Section 2.2.1.2), where a cathode within a filament is heated by an electrical current to temperatures sufficiently high that ionisation of the cathode occurs, leading to electron ejection from the surface. By contrast in field emission guns, a high electric field is applied to a metal, giving rise to tunnelling effects that remove electrons from the conduction band. Once electrons are produced, they are then accelerated by a voltage which produces the high energy beam; the voltage determines the electron energy, which in turn influences the resolution of the image. Critically, field emission guns provide much higher intensity beams than those obtained by thermionic emission.<sup>65</sup> In micrographs recorded in subsequent chapters, the JEOL 6060 microscope is equipped with a thermionic emission electron gun with a tungsten filament, whereas the Phillips XL30 ESEM FEG microscope is fitted with a field emission gun.

## 2.2.4 Nuclear Magnetic Resonance (NMR) Spectroscopy

### 2.2.4.1 Fundamental Concepts

In NMR spectroscopy, the response of a sample to radiofrequency radiation within a strong magnetic field is measured, revealing information about the electronic environments surrounding the probed nuclei.<sup>66</sup> Any atomic nucleus with a non-integer spin exhibits angular momentum ( $P$ ), and in turn a magnetic moment ( $\mu$ ), with both terms related by a constant of proportionality, the magnetogyric ratio,  $\gamma$ , (Equation 2.15). Nuclei with a spin quantum number ( $I$ ) of  $\frac{1}{2}$ , including  $^1\text{H}$ ,  $^{19}\text{F}$  and  $^{29}\text{Si}$ , exist in two possible degenerate spin states described by the magnetic quantum numbers,  $m_I = +\frac{1}{2}$  and  $-\frac{1}{2}$ , alternatively described as  $\alpha$  and  $\beta$ . In a static magnetic field ( $B_0$ ), the Zeeman effect is observed where the  $\alpha$  and  $\beta$  states are no longer degenerate, but rather exist as a higher ( $\beta$ ) and lower ( $\alpha$ ) energy state, separated in energy by the Zeeman splitting energy ( $\Delta E$ ), proportional to the strength of the magnetic field ( $B_0$ ) and the magnetogyric ratio ( $\gamma$ ) (Equation 2.16, where  $h$  = Planck's constant).<sup>67</sup>

$$\mu = \gamma P \quad (\text{Eq. 2.15})$$

$$\Delta E = \gamma h B_0 \quad (\text{Eq. 2.16})$$

#### 2.2.4.2 The NMR Experiment

In a direct excitation Fourier transform-NMR experiment (FT-NMR), the sample is placed in a strong magnetic field, thus the nuclear spin may adopt one of the two non-degenerate spin states,  $\alpha$  and  $\beta$ . In the static magnetic field ( $B_0$ ), directed along the z-axis, nuclear spins align with the field in the z-direction; this is the lower energy spin state ( $\alpha$ ). Applying a radiofrequency (RF) pulse at the Larmor frequency ( $\nu_0 = \gamma B_0$ ) excites some nuclear spins to the higher energy spin state ( $\beta$ ), where the spins align with the y-direction, orthogonal to the applied magnetic field. Following the RF pulse, nuclei in the excited  $\beta$  state relax to the  $\alpha$  state by emission of a radio wave, termed free induction decay, which induces a time signal in the receiver coil of the spectrometer. Fourier transformation of the time signal yields the frequency signal observed in an NMR spectrum. The energy of the radio wave emitted upon relaxation reflects the local magnetic field experienced by the nucleus, and thus the chemical environment. Signals, termed peaks or resonances, are presented in NMR spectra according to the chemical shift ( $\delta$ ), the extent to which the frequency of the free induction decay differs from the nuclei in a given standard material.<sup>67</sup> A peak that appears at a more negative chemical shift relative to another peak is described as *upfield* and reflects greater shielding of the nuclei in that environment. Conversely, peaks appearing at a more positive chemical shift relative to another peak are described as *downfield*, reflecting deshielding of the nuclei.

In the NMR experiment, the duration of the RF pulse is termed the *contact time*, and the duration for which the signal is detected is the *acquisition time*. The signal to noise received in the NMR experiment is inherently low, as a result the experiment must be repeated many times to improve the signal to noise ratio, enhancing the magnitude of the NMR signal. The time between successive repetitions of the NMR experiment (i.e. the pulse and acquire sequence) is termed the *recycle delay*; an appropriate recycle delay is selected depending on the relaxation time of the nuclei under study.<sup>67</sup>

#### 2.2.4.3 Magic-Angle Spinning (MAS) NMR Spectroscopy

The two main factors that influence the Zeeman splitting energy of a given nuclear environment are shielding, the electron density surrounding the nuclei of interest, and spin coupling, arising from interactions between proximal nuclei. The extent of both shielding and spin coupling is dependent on the orientation of the relevant moiety in the magnetic field. In solution NMR, the rapid tumbling of molecules leads to averaged isotropic interactions in the magnetic field, but as solids have no motional disorder and are comparatively static, the extent of shielding and spin coupling will depend on the orientation of the moiety in the magnetic field, giving rise to anisotropic interactions and leading to many signals for the same chemical environment. Moreover, in a polycrystalline sample the orientation of different crystallites in the applied field will also lead to nuclei in identical chemical environments appearing at different chemical shifts. In order to record lucid and informative NMR spectra on solids, rapid sample spinning at  $54.74^\circ$  relative to the applied field is required to average orientational effects, a technique termed magic-angle spinning (MAS) NMR spectroscopy.<sup>67</sup>

#### 2.2.4.4 Cross-Polarisation MAS NMR Spectroscopy

Cross-Polarisation (CP) is an alternative method to the direct excitation experiment (Section 2.2.4.2), used to enhance the signal of a given dilute nuclei ( $I = \frac{1}{2}$ ), by the transfer of magnetisation from an abundant nucleus in the sample, most often  $^1\text{H}$ , to the more dilute nucleus under study. CP is often used to increase the signal to noise in shorter experiments as the recycle delay depends on the relaxation of the  $^1\text{H}$  nuclei rather than the nuclei under study.<sup>67</sup> In subsequent chapters, most MAS NMR spectra were performed by direct excitation; however, some  $^{29}\text{Si}\{^1\text{H}\}$  CP MAS NMR spectra have also been recorded, involving the transfer of magnetisation from  $^1\text{H}$  to  $^{29}\text{Si}$ .

In a  $^{29}\text{Si}\{^1\text{H}\}$  CP MAS NMR experiment, an initial  $90^\circ$  pulse directed along the x-axis rotates magnetisation for some  $^1\text{H}$  nuclei onto the y-axis. A second  $90^\circ$  pulse “spin-locks” the magnetisation

in place, as the relaxation time is greatly increased in a RF magnetic field. While the second 90° pulse is applied, a simultaneous pulse is applied to  $^{29}\text{Si}$ , and during this period  $^{29}\text{Si}$  magnetisation builds up by the transfer of magnetisation from  $^1\text{H}$ , provided the conditions are conducive. The free induction decay of  $^{29}\text{Si}$  is then measured as described in Section 2.2.4.2.<sup>67</sup>

#### 2.2.4.5 $^{29}\text{Si}$ MAS NMR Spectroscopy of Zeolites

In seminal work by Lippmaa *et al.*,<sup>68</sup> it was discovered that the chemical shift of silicon in tetrahedral  $[\text{SiO}_4]$  units in silicates depends upon the amount of surrounding corner-shared  $[\text{SiO}_4]$  tetrahedra. The possible silicon environments are termed  $\text{Q}^n$ , where  $n$  corresponds to the number of corner-shared  $[\text{SiO}_4]$  tetrahedra. A  $\text{Q}^0$  silicon environment describes a discrete  $[\text{SiO}_4]$  unit with no corner sharing to other  $[\text{SiO}_4]$  tetrahedra, whereas a  $\text{Q}^4$  silicon environment describes a  $[\text{SiO}_4]$  unit where all four corners of the tetrahedron are shared with another  $[\text{SiO}_4]$  unit. As  $n$  increases, the associated chemical shift becomes more negative reflecting increased shielding at the silicon centre.<sup>68</sup>

In a perfect zeolite crystal, all silicon environments would be  $\text{Q}^4$  in the respect that they are corner shared with another four tetrahedral units. In  $^{29}\text{Si}$  MAS NMR spectra recorded on zeolites, there are 5 possible  $\text{Q}^4$  signals, differentiated from each other by the number of aluminium atoms in the second co-ordination sphere of the silicon atom. Each of the possible signals is labelled:  $\text{Si}(n\text{Al})$ , where  $n$  corresponds to the number of aluminium atoms in the second co-ordination sphere, and therefore may adopt a number between, and including, zero and four. The  $\text{Si}(0\text{Al})$  peaks, corresponding to silicon in  $[\text{SiO}_4]$  units which share corners with a further four  $[\text{SiO}_4]$  units, appear at the most negative chemical shift ( $\delta_{\text{Si}} \approx -110$  ppm). Each successive  $\text{Si}(n\text{Al})$  peak appears at a chemical shift a few ppm downfield of the previous peak, i.e. the  $\text{Si}(1\text{Al})$  peak would be expected at  $\delta_{\text{Si}} \approx -105$  ppm, a few ppm downfield of the  $\text{Si}(0\text{Al})$  peak. If present, the  $\text{Si}(4\text{Al})$  peak appears at the most positive chemical shift ( $\delta_{\text{Si}} \approx -85$  ppm).<sup>69</sup>

A common defect in zeolites, apparent particularly at the surface, are hydroxyl groups such as silanol (Si-OH) and aluminol (Al-OH) moieties, produced by incomplete condensation about the tetrahedral centre during synthesis. A silicon atom bonded to one hydroxyl group and through oxygen atoms to a further three tetrahedral centres is Q<sup>3</sup> rather than Q<sup>4</sup>; accordingly, the chemical shift at which a Q<sup>3</sup> Si(*n*Al) peak (*n* = 0 – 3) appears is a few ppm downfield of the corresponding Q<sup>4</sup> Si(*n*Al) peak.<sup>70</sup>

### 2.2.5 Fluoride Ion-Selective Electrodes

The quantitative determination of fluorine in solids by conventional analytical techniques presents challenges, owing to the chemical nature of fluorine. Fluorine cannot be routinely quantified in solids by X-ray fluorescence spectrometry, due to an insufficient fluorescence yield. Calibrated X-ray photoelectron spectroscopy has been used in some studies to measure the fluorine content of solids;<sup>71</sup> however, reports are limited. The direct determination of fluorine in solution by inductively coupled plasma mass spectrometry (ICP-MS) is not possible as the ionisation energy of fluorine is higher than the argon in the plasma. Furthermore, the production of volatile hydrofluoric acid in the acidification of analyte solutions for delivery to ICP systems introduces a further source of error.<sup>72</sup>

The most routine and convenient determination of fluoride concentrations in solution are performed by fluoride ion-selective electrodes (ISE). Fluoride ion-selective electrodes are tipped with a lanthanum(III) fluoride crystal, with lanthanum(III) partially doped with europium(II), i.e. La<sub>1-x</sub>Eu<sub>x</sub>F<sub>3-x</sub>. The presence of europium(II) creates vacancies on the anion site in the crystal, enabling conduction of the analyte, fluoride, when the crystal is immersed in a solution containing the analyte, thus generating a potential. The potential generated is modelled by the Nernst equation, and therefore can be related by a linear calibration curve to potentials produced by known standards enabling the determination of the fluoride concentration in the analyte solution.<sup>72,73</sup>

In analysis by fluoride ion-selective electrodes, there are numerous potential sources of error arising from the matrix. Hydroxide ions are the only appreciable interferent in measurements made by fluoride ion-selective electrodes, with a selectivity co-efficient of 0.1, meaning 10% of the hydroxide present in solution will contribute to the fluoride signal. Moreover, at low pH hydrofluoric acid is formed which the electrode does not detect. Further error may also be introduced by ion-pair formation between fluoride and charge dense cations in the matrix. Total ionic strength adjustment buffer, TISAB, is added to solutions prior to measurement in order to eliminate errors caused by the matrix. TISAB has the optimal pH for accurate fluoride ion measurement (pH = 5.5), sufficiently high that minimal hydrofluoric acid is formed, and also eliminating interference from hydroxide ions. Numerous formulations of TISAB are available; TISAB-II, used throughout fluoride concentration measurements in later chapters, is made from sodium chloride, sodium hydroxide and glacial acetic acid, as well as a complexing agent, 1,2-cyclohexylenedinitrilotetracetic acid, which chelates cations with high charge density that would otherwise form ion-pairs with fluoride in solution.<sup>72</sup>

#### 2.2.6 Inductively Coupled Plasma Optical Emission Spectrometry (ICP-OES)

In optical emission spectrometry (OES), also termed atomic emission spectrometry (AES), chemical analysis is performed on solutions by measuring the intensity of photons emitted from atoms in excited electronic states. As emission intensity is proportional to the concentration, the solution concentration of an element may be determined from a calibration of solutions with known concentrations of the element of interest. In the operation of an optical emission spectrometer, the emitted photons are passed through a wavelength isolation device, after which the isolated photons are converted into a signal by a transducer.<sup>74</sup>

The most widely employed method for producing atoms in excited states is the use of inductively coupled plasma (ICP). The plasma, a gas comprising ions and free electrons, is produced by applying radiofrequency to a gas, in most cases argon. The analyte solution is introduced to the plasma by a

nebuliser; the high temperature of the plasma leads to the excitation of electrons within atoms which upon relaxation emit photons of a characteristic wavelength. In the case of sodium, analysed by ICP-OES in Chapter 5, the characteristic wavelength of light emitted, and quantified in OES, is 589.6 nm.<sup>74</sup>

## CHAPTER 3: INVESTIGATIONS INTO MORDENITE MICROPARTICLES

### 3.1 Introduction

Natural mordenite samples typically comprise fibrous needle-like crystals, whereas synthetic mordenite may be made over a range of particle sizes, from 100 nm - 1 mm in diameter, with different particle morphologies.<sup>75-77</sup> The International Zeolite Association (IZA) verified synthesis of mordenite (MOR) produces particles with a platy morphology in thin discs, with diameters between 5 – 8  $\mu\text{m}$ , without the addition of an organic structure-directing agent (OSDA) or other additive to the gel.<sup>52,78</sup> It is unclear if seeding was employed in the synthesis of these particles. The authors noted that aging the gel at ambient temperature prior to heating led to larger particle sizes, albeit with reduced crystallinity; however, sizes and micrographs for these aged samples are not reported.<sup>78</sup>

Owing to the catalytic applications of mordenite and the easier application of large crystals, or particles, in vessels such as columns and fluidised beds, synthetic methods have been developed that produce large particles of mordenite. In addition to aging zeolite gels prior to heating, larger particle sizes have been achieved by the addition of either aliphatic alcohols<sup>79</sup> or tetraethylammonium ( $\text{TEA}^+$ ) cations<sup>43,80</sup> to synthesis gels. The presence of aliphatic alcohols, most notably butan-1-ol, led to the synthesis of large prismatic crystals with diameters between 20 – 40  $\mu\text{m}$ , which were compared to discs of *ca.* 1  $\mu\text{m}$  in diameter from a commercially available mordenite. It was proposed that “chelation” of the aqueous silicon or aluminium source reduces the available concentration in the gel, leading to the synthesis of larger crystals from more dilute solutions. It was not possible to compare directly the influence of the alcohol against the absence of it, as the absence of alcohol in the gels led to amorphous products.<sup>79</sup>

Tetraethylammonium ( $\text{TEA}^+$ ) cations are a commonly employed OSDA in the synthesis of zeolites with relatively high Si/Al ratios, such as mordenite, zeolite beta and ZSM-5.<sup>52,81</sup> While  $\text{TEA}^+$  cations are not essential to mordenite formation,  $\text{TEA}^+$  has been utilised in many varied syntheses of mordenite, not

all of which produce large particles. TEA<sup>+</sup> was used as a structure directing agent in the microwave synthesis of mordenite, which possessed particle diameters *ca.* 1  $\mu\text{m}$ ,<sup>82</sup> as well as in the synthesis of nanoparticulate mordenite using the mineral magadiite as the silicon source.<sup>76</sup>

Spherical particles of mordenite ( $d \approx 10 - 20 \mu\text{m}$ ) constituting aggregates of nanocrystals have been prepared from gels containing TEA<sup>+</sup> and a surfactant, using colloidal silica as the silicon source. In the same study, particles synthesised in the absence of both TEA<sup>+</sup> and a surfactant possessed similar sizes but with platy morphologies.<sup>80</sup> Spherical particles have also been produced from gels containing TEA<sup>+</sup>, without a surfactant and using tetraethyl orthosilicate (TEOS) as the silicon source, as reported by Mao *et al.*<sup>43</sup> Morphological control by changing the gel composition was reported, with spherical particles synthesised at lower Si/Al ratios (Si/Al = 7.0), whereas upon increasing the gel Si/Al ratio, “circular pie” (Si/Al = 8.0) and “flat prism” (Si/Al = 9.5) particle shapes were observed. It was noted that the presence of TEA<sup>+</sup> is critical to synthesising spherical particles, and in its absence large particles with other morphologies are instead observed.<sup>43</sup>

In this study, the gel system reported by Mao *et al.*<sup>43</sup> has been further examined. The extent of TEA<sup>+</sup> incorporation in products with different morphologies has been studied, by measuring Na/Al ratios in the zeolites using XRF spectrometry, to determine how this governs the observed morphologies. The effect of replacing TEOS with colloidal silica on particle size and morphology has also been studied, as well as the influence of gel ethanol content in both the TEOS and colloidal silica gel systems. Practical considerations in the application of mordenite radiotracers have also been evaluated, such as the ability to control particle dispersity using sieving, as well as the affinity of mordenite for aqueous gallium(III) ions, and the influence of pH on gallium loading.

## 3.2 Experimental

### 3.2.1 Mordenite Synthesis: TEOS System

Mordenite was synthesised according to a modification of the preparation reported by Mao *et al.*,<sup>43</sup> in which tetraethyl orthosilicate, TEOS, (7.4 ml) was added to deionised water (10 ml) with stirring; the pH of the solution was then adjusted to 1.0 by the addition of 2 M hydrochloric acid. The pH was monitored with a HI1131 pH electrode connected to a pH 211 microprocessor pH meter (Hanna Instruments). The resulting solution was stirred at ambient temperature for 24 hours. A second solution was made by dissolving sodium hydroxide (1.00 g) and aluminium sulfate hexadecahydrate (1.35 g) in deionised water (10 ml), followed by adding 35 wt% aqueous tetraethylammonium hydroxide, TEAOH, solution by micropipette (2.16 ml). The hydrolysed TEOS was then added to the second solution with vigorous stirring and homogenised for a further 30 minutes. The resulting gel was aged for 24 hours, following which the residual ethanol from the hydrolysis, expelled from the gel by syneresis, was decanted. The gel was then placed in a Parr® Teflon™-lined stainless-steel autoclave with a 45 ml capacity and heated at 170°C for 96 hours. The product was recovered by vacuum filtration, washed with deionised water and dried overnight at 60°C. In evaluating the influence of different gel Si/Al ratios on the product, only the concentration of TEOS was adjusted with all other components maintained equivalent. The amount of TEOS added to achieve particular gel Si/Al ratios may be found in the discussion where appropriate. In syntheses where ethanol was added to the gel, ethanol was added to the aluminate solution following the addition of TEAOH but prior to the addition of the hydrolysed TEOS solution. Tetraethyl orthosilicate (> 98%) and sodium hydroxide (> 97%) were obtained from Sigma-Aldrich, technical grade aluminium sulfate hexadecahydrate was obtained from Fisher Chemical and the 35 wt% tetraethylammonium hydroxide aqueous solution was obtained from Alfa Aesar. The 2 M HCl solution was made by dilution of analytical re-agent grade 37 wt% hydrochloric acid obtained from Fisher Chemical.

### 3.2.2 Mordenite Synthesis: Colloidal Silica System

In syntheses where the silicon source was colloidal silica rather than TEOS, Ludox™ HS-40 colloidal silica, 40 wt% silica solution, (4.57 g) was added to deionised water (7.26 ml) for gels with Si/Al = 7.5. In gels with Si/Al = 8.8 and Si/Al = 10.0, 5.34 g and 6.12 g of Ludox™ HS-40 colloidal silica was added to 6.80 ml and 6.33 ml of deionised water, respectively. The pH of the silica solutions was then adjusted to 1.0 by addition of 2 M hydrochloric acid. The synthesis then proceeded as described for the TEOS system (Section 3.2.1). In syntheses where ethanol was also added to the gel, the ethanol was added to the aluminate solution following the addition of TEAOH but prior to the addition of the silica solution. Ludox™ HS-40 colloidal silica and ethanol (> 99%) were obtained from Sigma-Aldrich and Fisher Chemical, respectively.

### 3.2.3 Calcined Mordenite

Calcined mordenite samples were obtained by heating the mordenite sample (as synthesised in Section 3.2.1) in porcelain crucibles in air at 550°C in a muffle furnace for 12 hours.

### 3.2.4 Gallium Adsorption Experiments

Gallium(III) sulfate solutions (2000 ppm Ga) were produced by dissolving gallium(III) sulfate (0.25 g) in deionised water (250 ml). Mordenite (0.30 g) was added to a portion of the gallium(III) sulfate solution (30 ml), then agitated on a mechanical shaker at ambient temperature for 1 hour, following which the product was recovered by centrifuge, washed with deionised water and dried overnight at 60°C. Gallium(III) sulfate (> 99%) was obtained from Sigma-Aldrich.

The pH adjustment of 30 ml portions of gallium(III) sulfate solutions (2000 ppm Ga) was performed by dropwise addition of either hydrochloric or sulfuric acid, in an appropriate concentration for the desired pH, such that changes to the overall volume of the solution were minimised. 4 M HCl and

H<sub>2</sub>SO<sub>4</sub> solutions were used to adjust the pH to 1.0, whereas 0.25 M HCl and H<sub>2</sub>SO<sub>4</sub> were used to adjust the pH of solutions to either 2.0 or 2.5. The solution pH was monitored with a HI1131 pH electrode (Hanna Instruments) connected to a pH 211 microprocessor pH meter (Hanna Instruments). The HCl and H<sub>2</sub>SO<sub>4</sub> solutions were made by dilution of analytical re-agent grade 37 wt% hydrochloric acid and 95 wt% sulfuric acid, respectively, obtained from Fisher Chemical.

### 3.2.5 Powder X-ray Diffraction (PXRD)

PXRD was performed on a Bruker D8 Advance diffractometer, in reflection geometry, equipped with a Ni-filtered Cu K<sub>α</sub> X-ray source ( $\lambda = 1.5418 \text{ \AA}$ ) and fitted with a solid-state LynxEye position sensitive detector. PXRD patterns were recorded on finely ground samples mounted on silicon low background holders that were first covered in a thin layer of Vaseline. Scans were measured over the  $2\theta$  range 5 - 60° at a scan rate of 0.04° s<sup>-1</sup> with a 0.02° step-size, except for scans measured on Ga-loaded MOR and the parent material (Section 3.3.7), which were recorded at a scan rate of 0.006° s<sup>-1</sup>. All reference pattern stick plots are derived from the appropriate Powder Diffraction File (PDF) in the International Centre for Diffraction Data (ICDD) PDF 4+ database.<sup>83</sup> Lattice constants have been derived by unit cell refinements using Chekcell software,<sup>84</sup> based on peak positions identified in Bruker EVA software and assuming the *Cmcm* space group. All PXRD patterns were plotted in SigmaPlot.<sup>85</sup>

### 3.2.6 X-ray Fluorescence Spectrometry (XRF)

XRF spectrometry was performed on a Bruker S8 Tiger WD-XRF spectrometer. All mordenite samples were measured as pressed pellets ( $d = 13 \text{ mm}$ ), obtained by intimately grinding *ca.* 0.400 g of the mordenite sample with *ca.* 0.200 g of wax binder (SpectroBlend™ Blending, Grinding and Briquetting Additive), then pressing at approximately 3 tons. Gallium loaded samples were instead analysed as loose powders mounted on Mylar™ thin film. All samples were measured for the maximum 18 minute data collection time; quantitative results were obtained from Bruker SPECTRA<sup>plus</sup> software with the K<sub>α</sub>

emission lines used to quantify all elements. Elemental weight fractions for all samples measured by XRF spectrometry may be found in Appendix 5.

### 3.2.7 Scanning Electron Microscopy (SEM)

Scanning electron micrographs were obtained on a JEOL 6060 microscope at an accelerating voltage of 20 keV and a working distance of *ca.* 13 mm. The imaged samples were mounted on graphite tape then sputter coated with a gold thin film, with an approximate thickness of 20 nm, prior to imaging. All particle measurements were performed using ImageJ software.<sup>86</sup>

## 3.3 Results and Discussion

### 3.3.1 TEOS System: Effect of Varying the Gel Si/Al Ratio

In an initial study on the gel system reported by Mao *et al.*,<sup>43</sup> the Si/Al ratio of the gel was adjusted by increasing the amount of tetraethyl orthosilicate (TEOS) added, while maintaining all other components equivalent. The volume of TEOS added, calculated Si/Al ratio of the gel and both the product Si/Al and Na/Al ratios determined by XRF spectrometry, along with associated error in the final value in parentheses, are presented in Table 3.1. In all instances, the product Si/Al ratio agrees within error with the Si/Al ratio of the antecedent gel. While the errors in Si/Al ratios may appear high, all relative errors in the measured Si/Al ratios fall between 2.4 – 3.5%. Similarly, relative errors between 3.3 – 4.5% are calculated for all Na/Al ratios.

In Figure 3.1, scanning electron micrographs depict the particles produced from varying the gel Si/Al ratio. In line with previous observations on the gel system,<sup>43</sup> at lower Si/Al ratios (Si/Al = 7.8(2) and 8.2(2)) spherical particles are produced with *ca.* 40  $\mu\text{m}$  diameters, whereas at the highest Si/Al ratio (Si/Al = 9.5(3)) prismatic morphology is observed. The product with an intermediate Si/Al ratio (Si/Al = 8.6(3)) displays particle morphologies intermediate to the spherical and prismatic particles

observed at lower and higher Si/Al content, respectively. The “intermediate” morphology, as it will be described in this discussion, comprises particles with similar diameters to the microspheres but that are more disc-shaped than spherical, and show a greater propensity towards forming aggregates. In many cases, the edges of the discs are rough and uneven like the prismatic particles produced from more siliceous gels.

Table 3.1. Amount of TEOS added, gel Si/Al ratio and the measured Si/Al and Na/Al ratios in the product.

TEOS added (ml)	Gel Si/Al	Measured Si/Al	Measured Na/Al
7.40	7.7	7.8(2)	0.45(2)
7.90	8.3	8.2(2)	0.46(2)
8.50	8.9	8.6(3)	0.54(2)
9.10	9.5	9.5(3)	0.92(3)

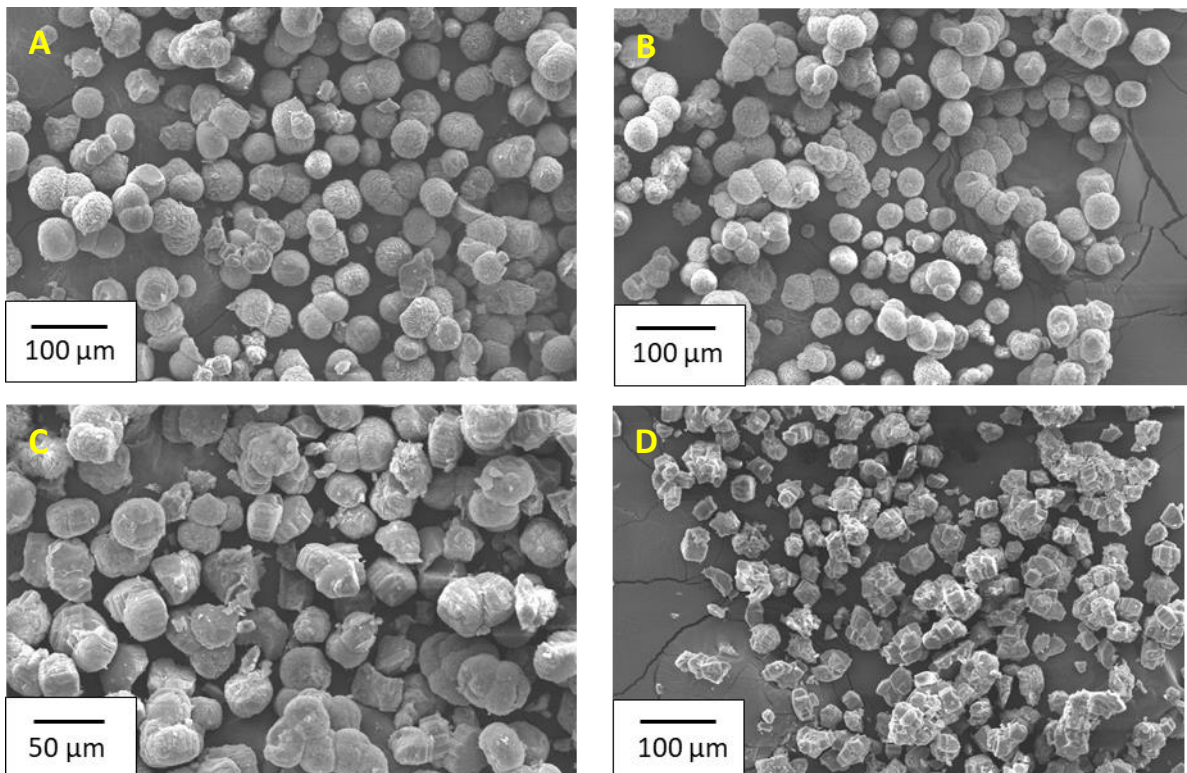


Figure 3.1. Scanning electron micrographs of mordenite produced from gels with Si/Al ratios: (A) 7.7, (B) 8.3, (C) 8.9 and (D) 9.5.

The Na/Al ratios for the spherical products are equivalent within error, Na/Al = 0.45(3) and 0.46(2), for products with Si/Al = 7.8(2) and 8.2(2), respectively. In addition to Na<sup>+</sup>, the only other possible intrapore cation is TEA<sup>+</sup>, therefore equivalent TEA<sup>+</sup> contents would be anticipated in both spherical products. The Na/Al ratio increases to 0.54(2) for the product with intermediate morphology, intimating that less TEA<sup>+</sup> is incorporated compared with the microspheres. In the prismatic sample, a much higher Na/Al ratio is observed (0.92(3)), intimating much less TEA<sup>+</sup> is incorporated in the product compared with the other samples. While the critical role of TEA<sup>+</sup> in producing microspheres was established previously,<sup>43</sup> the extent of TEA<sup>+</sup> incorporation in the zeolite was not previously examined. It would appear the particle morphologies observed may be correlated with the extent of TEA<sup>+</sup> intrapore cation incorporation in the zeolite product, as inferred from the measured Na/Al ratios.

PXRD patterns recorded on the products are presented in Figure 3.2, in addition to a stick plot of observed reflections for a reference mordenite sample (Si/Al = 9.8) containing both intrapore NH<sub>4</sub><sup>+</sup> and Na<sup>+</sup> cations (ICDD PDF 00-043-0171). Pure mordenite is synthesised across the range of gel Si/Al ratios, as all the reflections present in the PXRD patterns correspond to those expected for mordenite. Differences in the relative intensity of reflections between the observed PXRD patterns and the reference pattern may arise from differences in Si/Al ratio, as this influences intrapore cation concentration. The presence of intrapore TEA<sup>+</sup> rather than NH<sub>4</sub><sup>+</sup> may lead to further differences in relative intensity, however, there is no PXRD pattern in the ICDD PDF-4+ database for mordenite containing both intrapore Na<sup>+</sup> and TEA<sup>+</sup> cations.<sup>83</sup> Additional instrumental and sample dependent factors may give rise to differences in relative intensities such as the extents of axial divergence at low angle, preferred orientation and Scherrer broadening.<sup>63</sup>

Lattice constants for the mordenite products derived from unit cell refinements are presented in Table 3.2. All lattice constants and unit cell volumes are equivalent across the Si/Al range within an appropriate confidence interval: the standard error of the lattice constant multiplied by 3. In subsequent discussion, only variation in lattice constants beyond this confidence interval will be

considered significant. The lack of variation in unit cell parameters with changing composition could be attributed to multiple factors. Critically, as the mordenite samples possess relatively high Si/Al ratios, there are few intrapore cations within each unit cell, therefore the impact of changing the intrapore cation concentration and composition on the size of the unit cell is minimised.

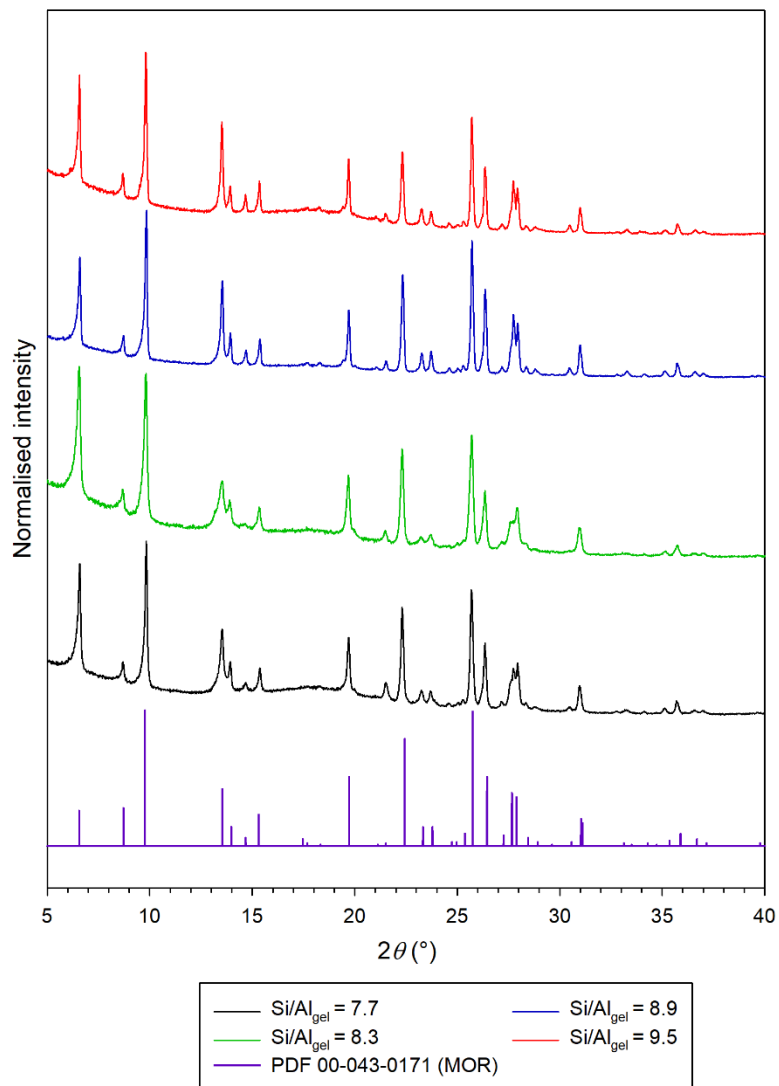


Figure 3.2. PXRD patterns for mordenite produced from gels with Si/Al = 7.7, 8.3, 8.9 and 9.5, along with a stick plot of a reference mordenite pattern (PDF 00-043-0171).

Table 3.2. Measured Si/Al ratio and lattice constants for mordenite samples.

Measured Si/Al	$a$ (Å)	$b$ (Å)	$c$ (Å)	$V$ (Å <sup>3</sup> )
7.8(2)	18.04(1)	20.42(1)	7.50(1)	2763(7)
8.2(2)	18.09(1)	20.38(1)	7.49(1)	2761(7)
8.6(3)	18.07(1)	20.42(1)	7.49(1)	2764(7)
9.5(3)	18.09(2)	20.42(1)	7.49(1)	2767(9)

### 3.3.2 TEOS System: Absence of TEA<sup>+</sup>

To further probe the influence of TEA<sup>+</sup> on particle morphology, a gel with Si/Al = 7.7 was made without TEAOH but with an increased amount of sodium hydroxide added such that the overall hydroxide concentration, and therefore pH, of the gel was equivalent to those containing TEAOH. A scanning electron micrograph in Figure 3.3 reveals the particle sizes and morphology in the product differ from those where the gel contains TEA<sup>+</sup>; irregular particles are produced with diameters between 5 – 15 μm, rather than the larger microspheres produced from gels containing TEA<sup>+</sup>. Interestingly, the particles are similar in appearance to those observed by Sano *et al.*<sup>79</sup> for mordenite samples synthesised in the presence of butan-1-ol. Naturally, ethanol produced by the hydrolysis of TEOS is present in the gel during aging and may exert a similar influence in governing the particle growth in systems where TEA<sup>+</sup> is not present.

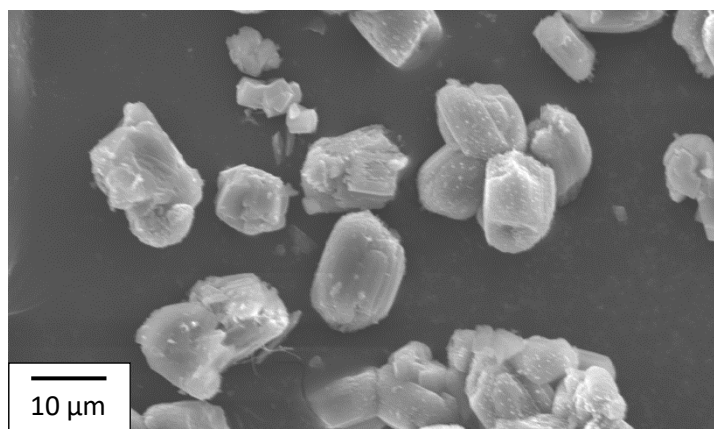


Figure 3.3. Scanning electron micrograph of mordenite produced from a gel with Si/Al = 7.7 and containing no TEA<sup>+</sup> cations.

Most reflections in the PXRD pattern correspond to mordenite (Figure 3.4), however, some additional reflections are also present. Low intensity reflections are observed at the lower angle side of some mordenite reflections, including the 110, 020 and 111 reflections at  $2\theta \approx 6.0^\circ$ ,  $8.2^\circ$  and  $13.1^\circ$ , respectively. The low intensity unindexed reflections may be produced by mordenite crystallites within the sample with a larger unit cell, indicating some inhomogeneity in the composition. A further reflection is present at  $2\theta \approx 11.0^\circ$ , but the phase responsible for this reflection is unknown.

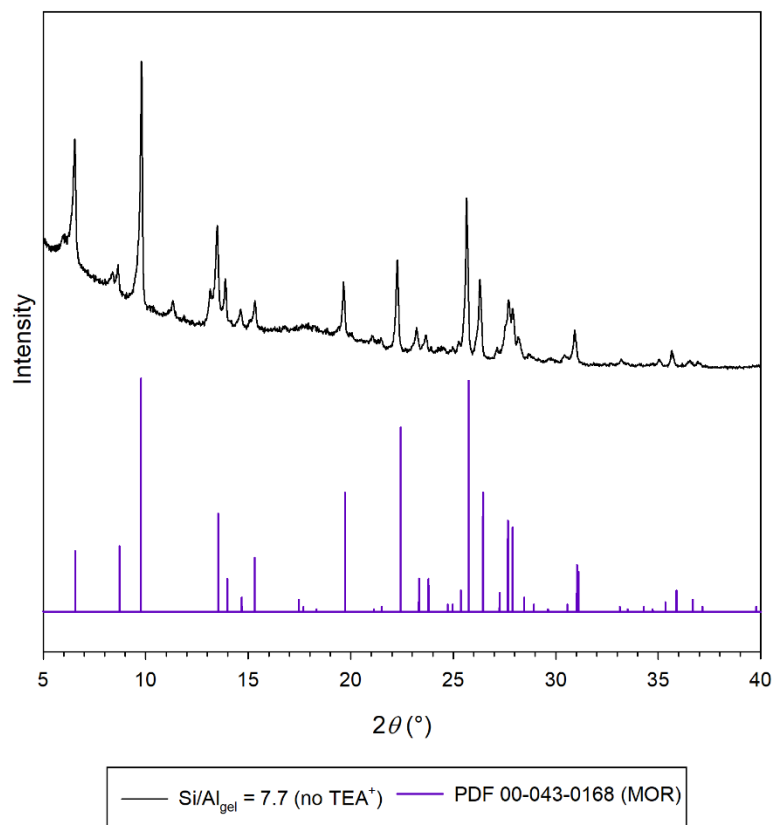


Figure 3.4. PXRD pattern of the product from a gel with Si/Al = 7.7 and containing no TEA<sup>+</sup>.

### 3.3.3 Colloidal Silica System

The influence of replacing TEOS with colloidal silica as the silicon source, where the overall water content in the gel has been maintained, on the product morphology and composition has been tested for gels with Si/Al = 7.5. SEM reveals the particles produced chiefly adopt spherical morphologies (Figure 3.5); however, the diameters are mostly in the range 17 – 20  $\mu\text{m}$ , approximately half the

diameters observed when TEOS is the silicon source. Interestingly, the microsphere diameters agree well with those reported by Yuan *et al.*<sup>80</sup> ( $d \approx 10 - 20 \mu\text{m}$ ) from another gel system containing  $\text{TEA}^+$  with colloidal silica as the silicon source. The micrographs also reveal the presence of some fibrous material in the product, rendering the particles produced by this preparation unsuitable for application as radiotracers, owing to the associated health risks of fibrous siliceous material. The PXRD pattern contains only reflections attributable to mordenite (Figure 3.6), however, the peaks are broader than those observed in products of the TEOS system. The product Si/Al ratio (7.7(2)) agrees within error of the Si/Al ratio of the gel, and the Na/Al ratio (0.44(3)) is comparable to those observed for spherical particles in the TEOS system indicating  $\text{TEA}^+$  is incorporated to a similar extent.

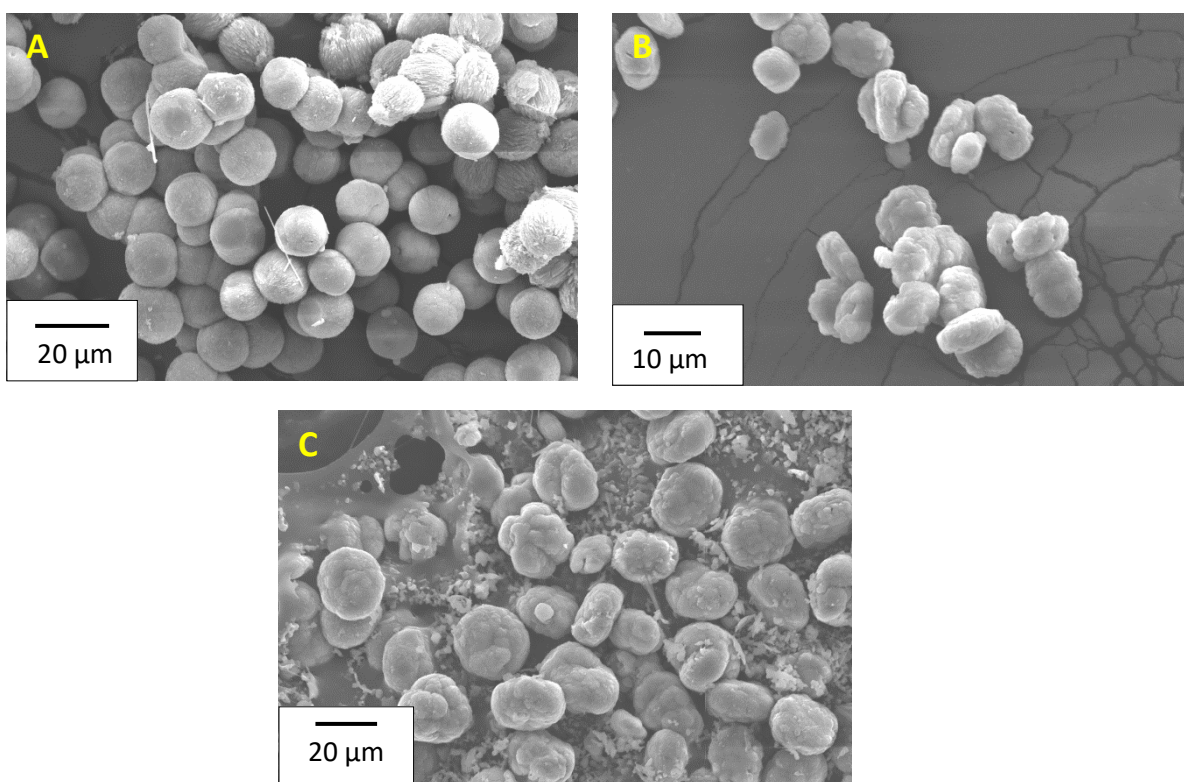


Figure 3.5. Scanning electron micrographs for products of gels with Si/Al = 7.5 (A), 8.8 (B) and 10.0 (C), with colloidal silica as the silicon source.

Increasing the gel Si/Al ratio to 8.8 and 10.0 in the colloidal silica system also produces pure mordenite with similarly broad peaks to those observed for Si/Al = 7.5 (PXRD pattern in Figure 3.6). Si/Al ratios

of 9.1(3) and 9.6(3) have been measured for products of gels with Si/Al contents of 8.8 and 10.0, respectively. A moderate increase in product Na/Al ratio is observed upon increasing the gel Si/Al ratio to 10.0, however, the increase is less pronounced than that observed upon increasing the gel Si/Al in the TEOS system: Na/Al = 0.44(2) and 0.63(3) were measured for the products of gels with Si/Al = 8.8 and 10.0, respectively.

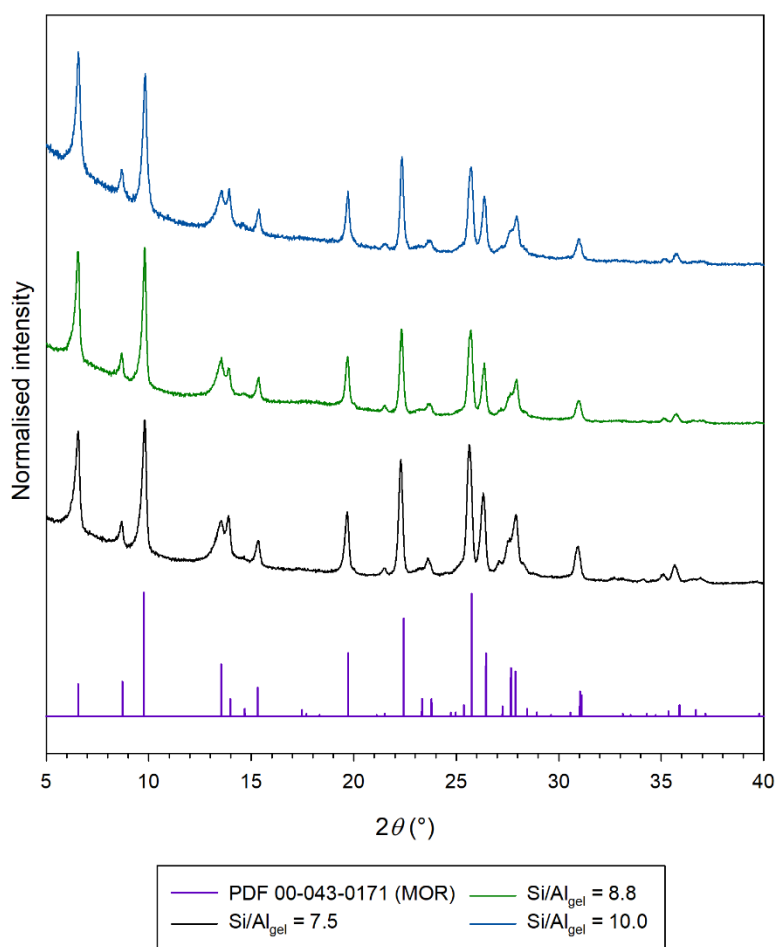


Figure 3.6. PXRD patterns for products of gels with colloidal silica as the silicon source.

Upon increasing the Si/Al ratio, the morphologies observed in the products also differ from those in the TEOS system (Figure 3.5). Mordenite particles produced from gels with Si/Al = 8.8 adopt disc-like morphologies with approximate diameters of 15  $\mu\text{m}$  and thicknesses between 5 – 10  $\mu\text{m}$ . Disc shaped particles are also produced from gels with Si/Al = 10.0, as well as much smaller particulate matter that

is also present in the sample. The discs with higher Si/Al are larger in size with diameters between 20 – 25  $\mu\text{m}$  and thicknesses between 10 – 15  $\mu\text{m}$  for discrete discs.

### 3.3.4 Colloidal Silica System: The Influence of Ethanol

In the TEOS system, the hydrolysis of TEOS produces ethanol. The influence of ethanol on the product morphology and composition in the colloidal silica system has been tested by adding different amounts of ethanol to gels with otherwise equivalent compositions. The Si/Al and Na/Al ratios measured for different amounts of ethanol added to the gel are presented in Table 3.3. PXRD patterns recorded on the samples are presented in Figure 3.7 and scanning electron micrographs in Figure 3.8.

Table 3.3. The amount of ethanol added, gel Si/Al ratios and product Si/Al and Na/Al ratios measured by XRF spectrometry.

Ethanol added (ml)	Si/Al gel	Measured Si/Al	Measured Na/Al
0	7.5	7.7(2)	0.44(2)
5	7.5	7.7(2)	0.53(2)
10	7.5	8.4(2)	0.74(2)
15	7.5	9.6(3)	0.83(3)

Adding 5 ml of ethanol to the gel does not change the product Si/Al ratio, but a small increase in the product Na/Al ratio is observed. Compared with products where the gel contains no ethanol, the product mostly constitutes smaller particles, and aggregates thereof, with fewer well-defined spherical particles. The addition of higher quantities of ethanol to the gel (10 ml), leads to increases in both the Si/Al and Na/Al ratios in the product, with further increases observed upon adding 15 ml of ethanol. As the ethanol content in the gel increases, the product PXRD patterns appear more crystalline, exhibiting sharper peaks compared with those produced from the system without ethanol. Polydisperse prismatic particles and aggregates are produced from gels containing both 10 ml and

15 ml of ethanol. The disc shaped particles observed upon increasing the gel Si/Al ratio in the colloidal silica system without ethanol in Section 3.3.3 are not observed, despite comparable product Si/Al ratios. Ultimately, the addition of ethanol in significant quantities (10 ml and 15 ml) to gels with an otherwise identical composition leads to an increase in the Si/Al and Na/Al ratios in the products, as well as causing a shift from spherical to prismatic particle morphology.

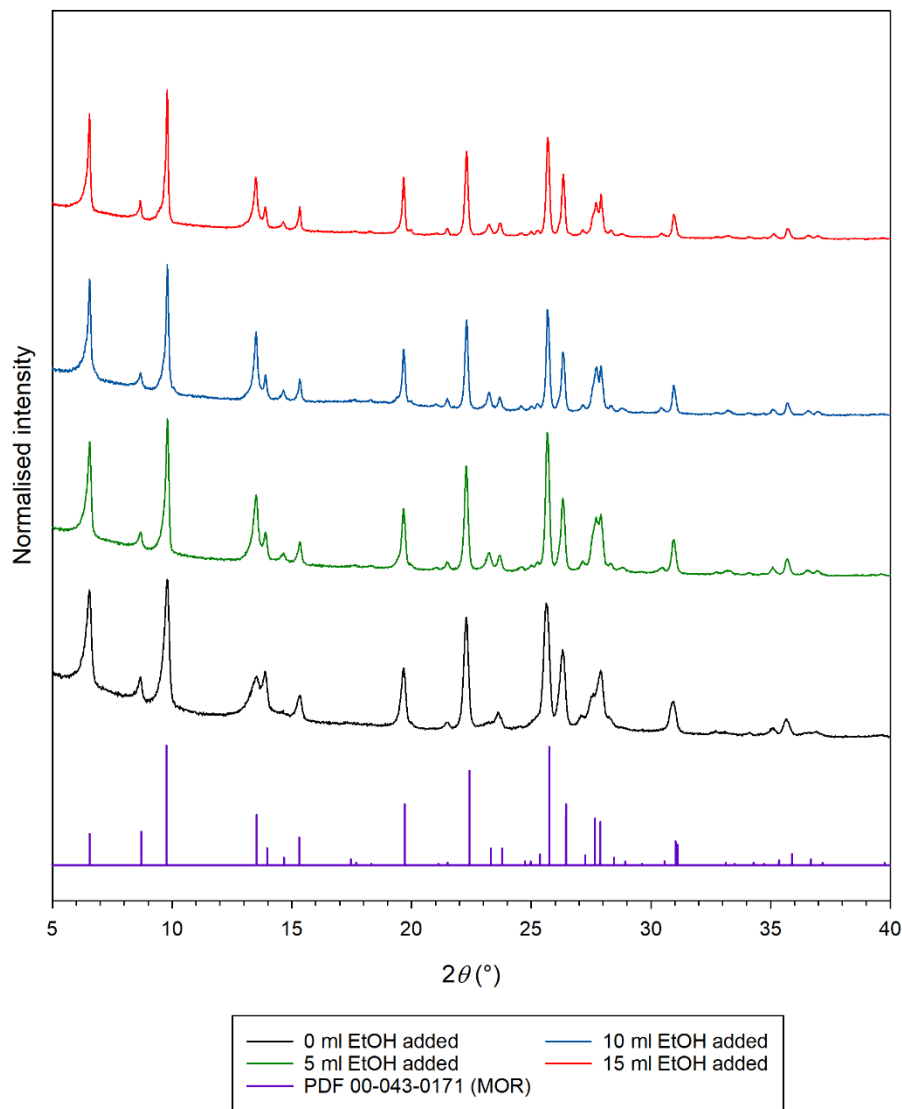


Figure 3.7. PXRD patterns for mordenite produced from the colloidal silica system with different ethanol contents (as labelled).

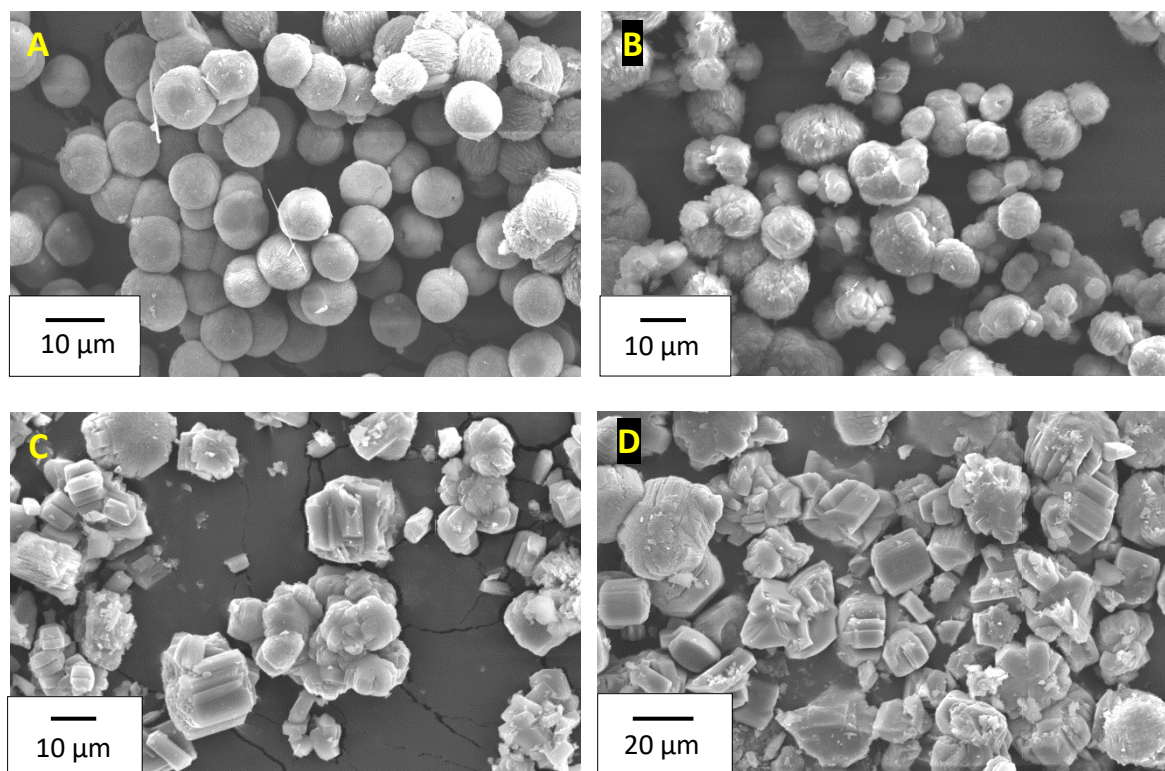


Figure 3.8. Scanning electron micrographs for mordenite produced from the colloidal silica system with (A) 0 ml, (B) 5 ml, (C) 10 ml and (D) 15 ml of ethanol added to the gel.

### 3.3.5 TEOS System: The Influence of Ethanol

The influence of ethanol on product composition and particle morphology has also been probed in the TEOS system. The Si/Al and Na/Al ratios measured for the products following the addition of 1 ml and 2 ml of ethanol to gels with otherwise equivalent compositions (Si/Al = 7.7) are listed in Table 3.4, along with the expected ethanol content in the gel considering both the ethanol produced by hydrolysis and that which has been added to the gel. In each case, only mordenite is produced and the addition of ethanol to the gel has little impact on the product PXRD pattern (Figure 3.9). Adding 1 ml of ethanol to the gel gives rise to a small increase in the product Si/Al ratio to 8.2(2); however, there is no change in the product Na/Al ratio, and the particles produced are principally microspheres, and aggregates thereof, as shown in Figure 3.10.

A significant increase in the product Na/Al ratio (0.68(3)) is observed upon adding 2 ml of ethanol to the gel. The product Si/Al ratio also increases but is equivalent within error to the Si/Al observed for

the product where only 1 ml of ethanol was added. The product resembles the intermediate morphology observed in products of gels with higher Si/Al ratios in Section 3.3.1 with microparticles that are oblong and disc shaped with rough edges.

Table 3.4. Gel Si/Al, measured Si/Al and Na/Al ratios, as well as ethanol added and expected ethanol content for products of the TEOS system.

Ethanol added (ml)	Expected ethanol content (ml)	Gel Si/Al	Measured Si/Al	Measured Na/Al
0	7.7	7.7	7.8(2)	0.45(3)
1	8.7	7.7	8.2(2)	0.45(2)
2	9.7	7.7	8.5(3)	0.68(3)

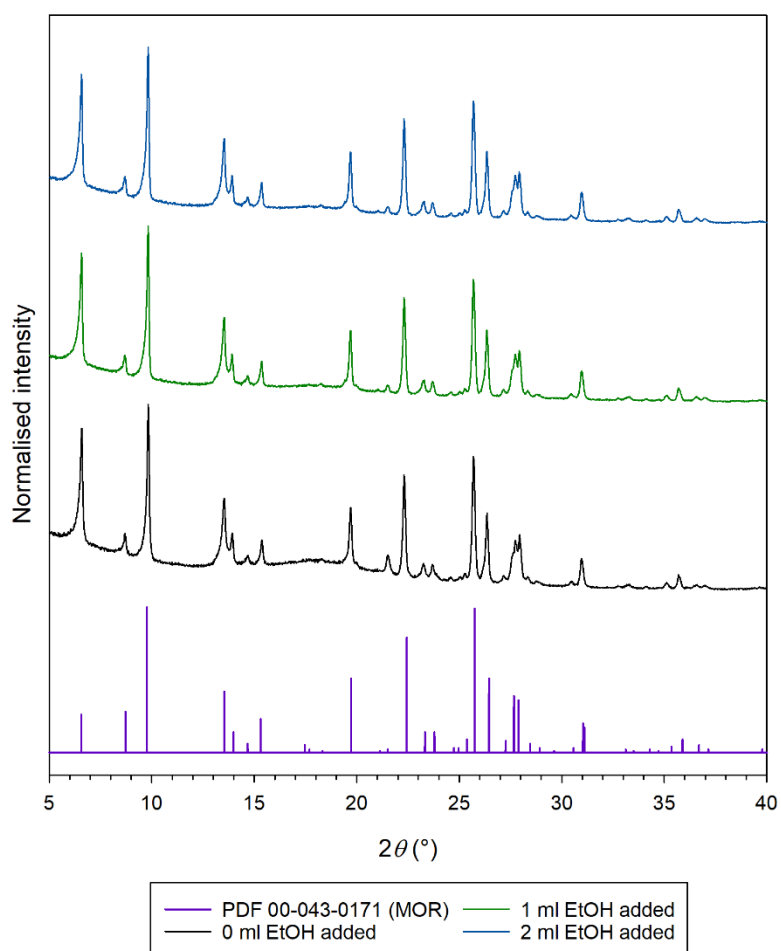


Figure 3.9. PXRD patterns of mordenite produced in the TEOS system with added ethanol content.

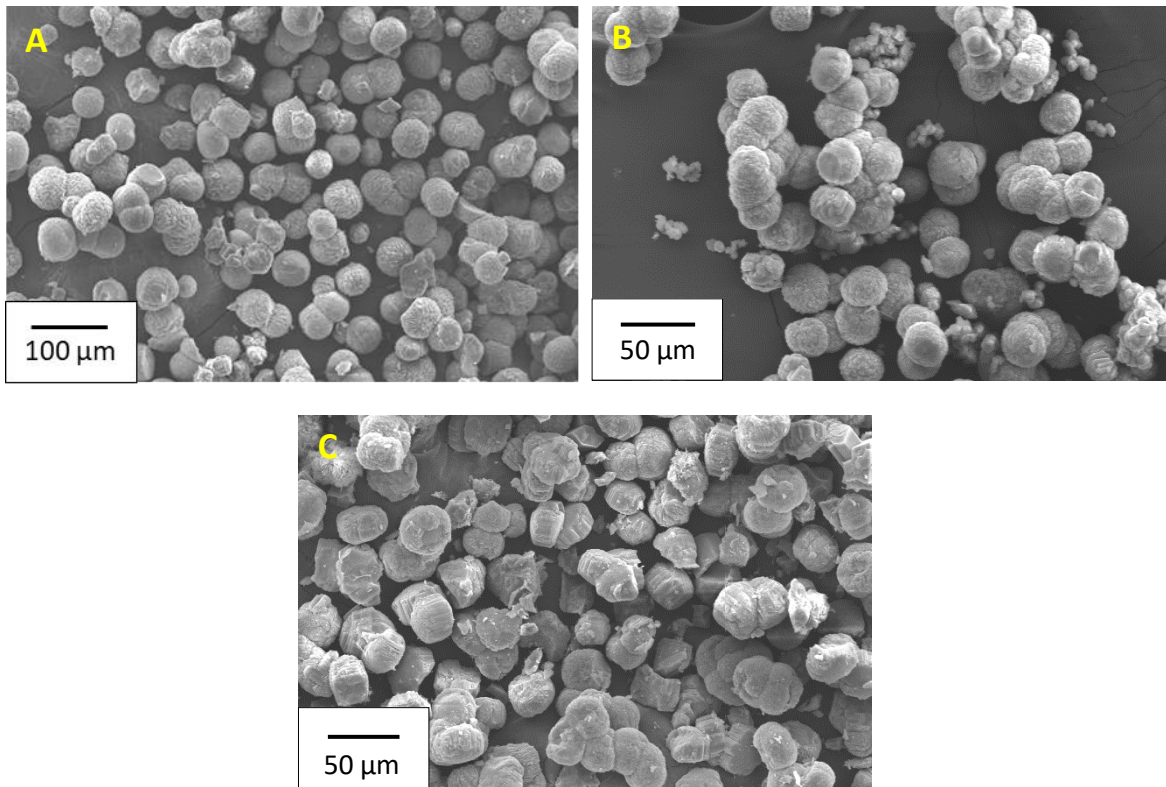


Figure 3.10. Scanning electron micrographs of mordenite produced from the TEOS system (gel Si/Al = 7.7) with (A) 0 ml, (B) 1 ml and (C) 2 ml of ethanol added.

It is clear from XRF analysis on mordenite, produced from both the TEOS and colloidal silica systems, that adding ethanol to the gel, in sufficient quantities, leads to an increase in the product Si/Al ratio relative to the Si/Al content of the gel, as well as an increase in the product Na/Al ratio. In turn, the particles produced may more closely resemble intermediate and prismatic morphologies, rather than the microspheres that would otherwise be expected from the gels containing no additional ethanol. Naturally, ethanol is produced in the hydrolysis of TEOS and the role of alcohols in producing prismatic and irregular-shaped particles has been determined previously.<sup>79</sup> It would appear ethanol alone can play a key role in governing the product composition and morphology, as demonstrated in the colloidal silica system in Section 3.3.4. Moreover, the different morphologies observed in the TEOS system upon increasing the gel Si/Al ratio in Section 3.3.1, compared with the colloidal silica system in Section 3.3.3, may be due to the absence of ethanol in the latter.

### 3.3.6 Sieving Efficacy

Significant quantities of intergrown aggregates are present in spherical mordenite samples, as depicted in Figure 3.11. In calcined samples, sintering occurs during heating to remove the intrapore  $\text{TEA}^+$ , further increasing the concentration of aggregates. The efficacy of sieving to remove aggregates, as well as to remove any fragments, has been evaluated by wet sieving a calcined spherical mordenite sample ( $\text{Si}/\text{Al} = 7.8(2)$ ;  $\text{Na}/\text{Al} = 0.45(3)$ ) with 25  $\mu\text{m}$  and 50  $\mu\text{m}$  test sieves using deionised water as an eluent. Scanning electron micrographs, in Figure 3.11, performed on the  $25 < x < 50 \mu\text{m}$  sieved fraction demonstrates sieving is effective in separating discrete microspheres from aggregates and fragments.

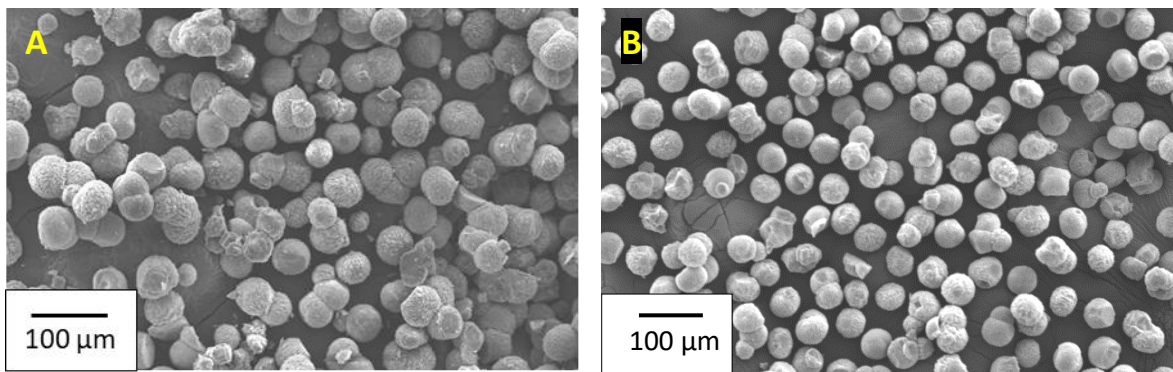


Figure 3.11. Scanning electron micrographs depicting (A) pre-sieved and uncalcined mordenite ( $\text{Si}/\text{Al} = 7.8(2)$ ) and (B) the calcined sample sieved between 25 and 50  $\mu\text{m}$ .

Diameters of distinct microspheres, whether discrete or part of aggregates, were measured using ImageJ software<sup>86</sup> for the spherical mordenite sample ( $\text{Si}/\text{Al} = 7.8(2)$ ;  $\text{Na}/\text{Al} = 0.45(3)$ ) prior to calcination and sieving. For 100 particles, the measured diameters spanned 24.9 – 50.1  $\mu\text{m}$  with mean diameter ( $\bar{x}$ ) = 40.0  $\mu\text{m}$  and standard deviation ( $\sigma$ ) = 5.3  $\mu\text{m}$ . Histograms of the measured diameters are presented in Figure 3.12, along with a kernel plot (the solid line), which estimates the probability density function of a random variable,<sup>87,88</sup> as calculated in SigmaPlot software.<sup>85</sup> Analysis on diameters in the sieved fraction (sample size = 100) reveals discrete microspheres span 38.4 – 54.6  $\mu\text{m}$ , with  $\bar{x} = 46.7 \mu\text{m}$  and  $\sigma = 3.8 \mu\text{m}$ . A particle size distribution for the sieved fraction is also present in Figure 3.12. While dispersity in the sample is reduced upon sieving, an increase in mean diameter is

observed, indicating discrete microspheres possess larger diameters than those which are present in intergrown aggregates.

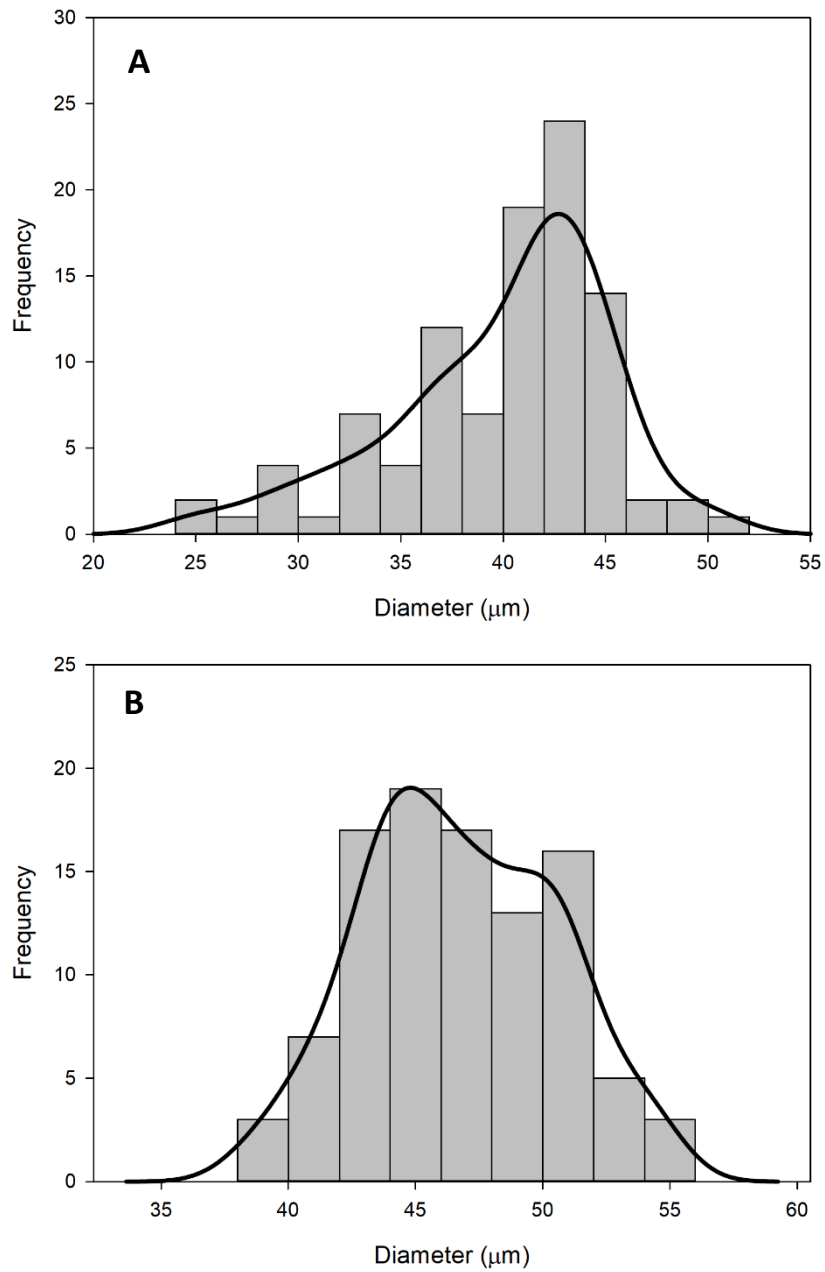


Figure 3.12. Particle size distributions for (A) unsieved mordenite and (B) the 25 < x < 50 μm fraction.

### 3.3.7 Gallium Uptake

As gallium-68 is a  $\beta^+$ -emitting isotope of interest, the affinity of a prismatic calcined mordenite sample (Si/Al = 9.5(3); Na/Al = 0.92(3)) for aqueous gallium(III) has been evaluated by batch adsorption experiments with gallium(III) sulfate solutions (2000 ppm Ga). In the calcined mordenite sample, the intrapore TEA<sup>+</sup> ions are no longer present as they break down upon calcination and instead charge balancing H<sup>+</sup> ions remain in place of the TEA<sup>+</sup> in the calcined product.<sup>52</sup> The gallium content in recovered products has been quantified by XRF spectrometry performed on loose powders and is reported as both Ga/Al ratios and the gallium weight fraction (wt%) measured in the samples. Significant gallium uptake is observed from solution by the calcined mordenite sample following an hour of contact at ambient temperature (Ga/Al = 0.36; 3.2 wt% Ga). PXRD patterns recorded on the mordenite sample and the gallium-loaded product, in Figure 3.13, show no significant difference or additional reflections following gallium loading. As a result, it is unlikely that gallium exists in the product as a crystalline phase that has precipitated from solution such as  $\alpha$ -GaOOH. Moreover, the gallium(III) sulfate solutions are significantly more acidic (pH = 2.95) than the ideal conditions for  $\alpha$ -GaOOH precipitation (pH > 4).<sup>31</sup>

Ion exchange between intrapore H<sup>+</sup> and aqueous Ga<sup>3+</sup> ions has been reported for both mordenite<sup>89</sup> and ZSM-5;<sup>90</sup> however, the calcined mordenite employed here contains mostly Na<sup>+</sup> intrapore cations (Na/Al = 0.92(3)). The total replacement of the intrapore protons in the calcined mordenite by ion exchange would lead to an approximate gallium loading, Ga/Al  $\approx$  0.02, that is much lower than the measured gallium loading, Ga/Al = 0.36. While some ion exchange between aqueous gallium and intrapore protons may occur, the predominant mode by which loading occurs cannot be ion exchange as the gallium loading measured is much greater than the ion-exchange capacity for gallium. Ion exchange between intrapore sodium and aqueous gallium is not viable;<sup>89,90</sup> indeed, there is no reduction in the sodium content in the zeolite following gallium loading.

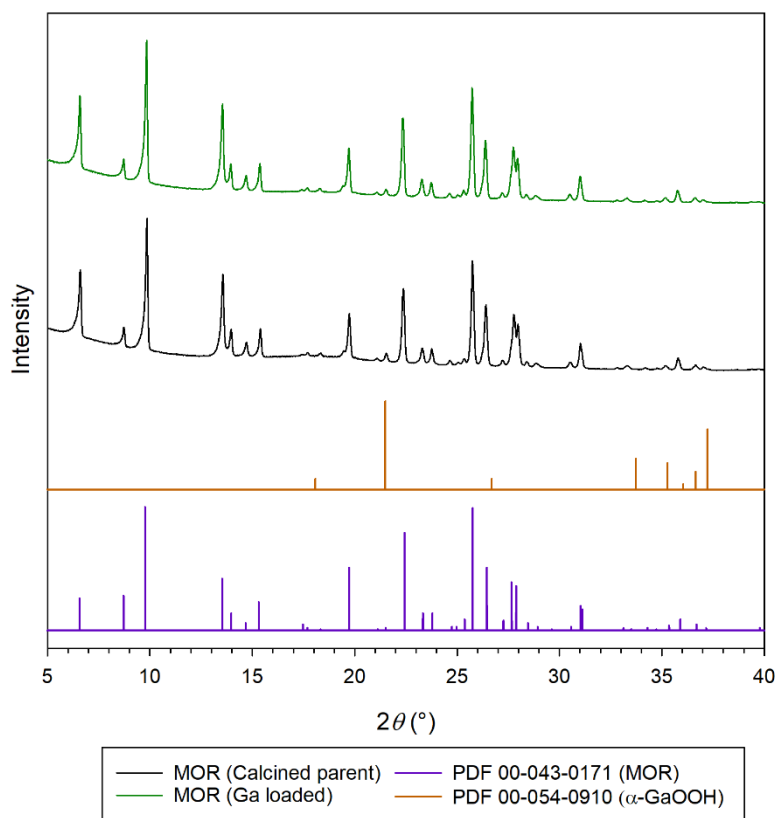


Figure 3.13. PXRD patterns of calcined mordenite prior to, and following, gallium loading.

The gallium loading attained by the uncalcined mordenite ( $\text{Ga}/\text{Al} = 0.07$ ; 0.81 wt% Ga) is lower than for the calcined sample ( $\text{Ga}/\text{Al} = 0.36$ ; 3.2 wt% Ga). The large  $\text{TEA}^+$  cations in the uncalcined mordenite are not exchangeable and inhibit diffusion into the zeolite pores.<sup>91</sup> Consequently, the gallium in the uncalcined mordenite could not have been loaded by ion exchange. The possibility of some gallium ion exchange occurring in the calcined system, but not in the uncalcined system, cannot be eliminated and may be partly responsible for the increased gallium loading measured in the former. Ultimately, it appears the most likely interaction between mordenite and aqueous gallium(III) ions leading to the observed gallium loadings is adsorption of gallium complexes or clusters onto the zeolite surface, as has been reported for gallium and other trivalent metals, such as iron(III).<sup>90,92-94</sup> The greater anticipated surface area of the calcined mordenite, compared with the uncalcined sample, is likely responsible for the significant difference in gallium loading observed between these species.

While the gallium(III) sulfate solutions (2000 ppm Ga) are mildly acidic (pH = 2.95), gallium-68 is eluted from generators using hydrochloric acid in the 0.05 – 1 M concentration range.<sup>5</sup> Gallium loadings attained from solutions with the pH adjusted by concentrated hydrochloric acid, with overall volume equivalent within error of solutions used in previous adsorption experiments, have been measured for prismatic calcined mordenite (Si/Al = 9.5(3); Na/Al = 0.92(3)). Lowering the pH to 2.5 leads to a reduction in the measured gallium loading (Ga/Al = 0.11; 0.9 wt% Ga) and further reducing the pH to both 2.0 and 1.0 leads to no detectable quantity of gallium in the products.

As outlined in Section 1.2, the predominant form of gallium expected in a solution with sulfate counter-anions at room temperature, and with pH  $\approx$  3, would be the hexaaquagallium(III) ion,  $[\text{Ga}(\text{H}_2\text{O})_6]^{3+}$ . A minor but detectable amount of gallium would be present as pentaquasulfatogallium(III) ions, i.e.  $[\text{Ga}(\text{H}_2\text{O})_5(\text{OSO}_3)]^+$ ,<sup>31</sup> whereas in chloride containing solutions,  $[\text{Ga}(\text{H}_2\text{O})_6]^{3+}$  exists in equilibrium with  $[\text{GaCl}_4]^-$  and multiple intermediate complexes containing both chloride and water ligands.<sup>34</sup> In order to establish the influence of gallium speciation on uptake from solutions by mordenite, the pH of gallium(III) sulfate solutions (2000 ppm Ga) were adjusted using sulfuric acid in experiments analogous to those outlined above. Upon reducing the pH to 2.5 with sulfuric acid, the gallium loading achieved also decreases (Ga/Al = 0.22; 1.8 wt% Ga) but to a lesser extent than solutions adjusted by hydrochloric acid. Further reducing the pH to both 2.0 and 1.0 leads to no discernible gallium loading, as in the case of solutions adjusted with hydrochloric acid. Reduced gallium uptake with decreasing pH in both systems may be caused by the greater concentration of protons relative to gallium(III) ions in solutions of lower pH, leading to competition between  $\text{H}^+$  and  $\text{Ga}^{3+}$  ions for surface sorption. At pH  $\approx$  3,  $\text{Ga}^{3+}$  is present in greater concentration than  $\text{H}^+$ ,  $4.7 \times 10^{-3}$  M and  $1 \times 10^{-3}$  M, respectively; however, at pH  $\leq$  2,  $\text{H}^+$  ions are in greater concentration than  $\text{Ga}^{3+}$ .

The interaction of aqueous gallate ions,  $[\text{Ga}(\text{OH})_4]^-$ , with mordenite has also been studied. Gallium(III) sulfate solutions (2000 ppm Ga) were adjusted to pH = 13 by the addition of sodium hydroxide. No detectable gallium uptake was observed for calcined mordenite (Si/Al = 9.5(3); Na/Al = 0.92(3)) from

the basic solution. Moreover, adjusting the pH with tetraethylammonium hydroxide rather than sodium hydroxide also leads to no discernible gallium uptake. The reduced affinity for gallate ions may be rationalised by Coulombic repulsion between the negative surface of the zeolite and the negative ions, rendering surface sorption unfavourable.

### 3.4 Conclusions

Mordenite microparticles with different morphologies, and diameters within the range of interest (5 – 50  $\mu\text{m}$ ), have been synthesised and the role of tetraethylammonium cations in governing particle morphology has been investigated. Of all observed morphologies, spherical particles possess the lowest product Na/Al ratios, so likely contain the most tetraethylammonium cations, whereas particles with prismatic morphologies contain comparatively little TEA<sup>+</sup>. It has also been demonstrated that the addition of ethanol to gels can give rise to more siliceous products with enhanced Na/Al ratios, as well as affecting the morphology of the particles produced.

Considering the desired application, the efficacy of sieving to control dispersity has been demonstrated. Moreover, appreciable gallium loadings on large particles of mordenite may be achieved by surface sorption from aqueous solutions; however, appreciable loadings only occur within a narrow pH range. While surface sorption occurs at pH  $\approx$  3.0, decreasing the pH to 2.0 leads to no detectable gallium loading. Moreover, in less acidic solutions (pH = 4 – 7), the precipitation of  $\alpha$ -GaOOH is expected.<sup>31</sup> Ultimately, acidic gallium-68 solutions eluted from germanium-68 generators would require a cautious pH adjustment prior to labelling mordenite particles; performing such a procedure while minimising exposure to the radioactive solution presents a practical challenge. Furthermore, the pH adjustment must be done in a timely manner to preserve as much activity as possible in the solution. While appreciable gallium loadings may be attained by mordenite from aqueous solutions; the narrow pH window within which loading occurs would present issues in

labelling the particles with gallium-68 solutions, and thus labelling with gallium-68 is ultimately unsuitable.

## CHAPTER 4: GROWING LARGE ZEOLITE CRYSTALS AND PARTICLES

### 4.1 Introduction

Large zeolite crystals may be synthesised by heating aluminosilicate gels containing triethanolamine ( $\text{N}(\text{C}_2\text{H}_4\text{OH})_3$ ) for periods of weeks, as first reported by Charnell for zeolites A and X.<sup>42</sup> The growth of large crystals from gels containing triethanolamine (TEOA) has been extended to other zeolites, including zeolite Y and analcime.<sup>95,96</sup> TEOA promotes crystal growth by complexing  $\text{Al}^{3+}$  ions, as confirmed by  $^{27}\text{Al}$  and  $^{13}\text{C}$  NMR experiments which have identified Al-TEOA complexes, as well as demonstrating there is no discernible quantity of aluminate ions present in the gels.<sup>97,98</sup> The complexation of  $\text{Al}^{3+}$  leads to a reduction in nucleation events in the gel, accordingly TEOA is often described as a “nucleation suppressing agent”.<sup>99</sup>

Reports on crystal growths from TEOA containing gels often focus on producing the largest crystals possible; the largest crystals of zeolites A ( $100\ \mu\text{m}$ ),<sup>42</sup> X ( $140\ \mu\text{m}$ ),<sup>42</sup> Y ( $125\ \mu\text{m}$ )<sup>95</sup> and analcime ( $180\ \mu\text{m}$ )<sup>96</sup> reportedly synthesised by this method all exceed the size range of interest for new PEPT tracers ( $5 - 50\ \mu\text{m}$ ). Nevertheless, well defined crystal morphologies are observed for zeolites A (cubic) and X (octahedral), and the large zeolite Y crystals are reported to adopt a spherical morphology.<sup>42,95</sup> The effect of crystallisation time on the particle sizes produced for zeolite A and X have been studied to determine if crystals within the desired size range can be produced. Further to this, the zeolite Y system reported by Ferchiche *et al.*<sup>95</sup> has also been investigated, particularly by studying the effect of changing the silicon source and lowering the crystallisation temperature. Through studying these effects on the gel system, a method for synthesising microspheres of the zeolite gmelinite (GME) with narrow dispersities has been developed.

## 4.2 Experimental

### 4.2.1 Large Zeolite A and X Crystal Growths

Large crystals of zeolite A and X were synthesised by a modification of the method first reported by Charnell.<sup>42</sup> In the preparation of large zeolite A crystals, anhydrous sodium aluminate (1.52 g) was dissolved in deionised water (13.3 ml), the solution was then filtered through a 0.45 µm polytetrafluoroethylene, PTFE, filter (Fisherbrand™). A separate solution of sodium silicate was prepared by dissolving sodium metasilicate pentahydrate (1.42 g) in deionised water (13.3 ml), this solution was then passed through a 0.45 µm filter before the addition of triethanolamine (4.29 g). The aluminate solution was added to the silicate solution then stirred vigorously for 30 minutes, after which the gel was divided into 3 equal volumes and placed in 15 ml capacity high-density polyethylene (HDPE) bottles. The gels were heated in a convection oven for 2 - 4 weeks at 85°C. Triethanolamine (> 99%) was obtained from Sigma-Aldrich, whereas technical grade sodium aluminate and sodium silicate pentahydrate were obtained from Fisher Chemical.

The procedure for zeolite X was identical to that for zeolite A, except 0.76 g of sodium aluminate was used instead of 1.52 g.

### 4.2.2 Zeolite Y Crystal Growths

A modification of the method reported by Ferchiche *et al.*<sup>95</sup> was used in “zeolite Y” growths. In this preparation, fumed silica (0.44 g, 0.58 g and 0.73 g for gels A1, A2 and A3, respectively) was added to deionised water (5 ml) in a 12 ml HDPE bottle, then aged at ambient temperature for 24 hours. An aluminate solution was prepared by dissolving anhydrous sodium aluminate (3.24 g) and sodium hydroxide (5.76 g) in deionised water (85 ml). The aluminate solution was then filtered through a 0.45 µm PTFE filter (Fisherbrand™). The weight of the filtered solution was measured and triethanolamine was added (1.52 g per 10 g of solution). The aluminate solution was then aged for

48 hours. Following aging, the aluminate solution (7.74 g) was added to the silica slurries, the mixture was then shaken manually for *ca.* 1 minute, followed by further homogenisation on a mechanical shaker for 10 minutes. The gels were then aged at room temperature for 9 days, followed by heating at 95°C for 32 days. The products were recovered by vacuum filtration, washed copiously with deionised water and dried overnight at 60°C. Triethanolamine (> 99%), sodium hydroxide (> 97%) and fumed silica were obtained from Sigma-Aldrich, and technical grade sodium aluminate was obtained from Fisher Chemical.

In instances where colloidal silica was employed instead of fumed silica, solutions were prepared by the addition of Ludox™ HS-40 colloidal silica (1.09 g, 1.45 g and 1.81 g for gels B1, B2 and B3, respectively) to deionised water (4.35 g, 4.13 g and 3.92 g for gels B1, B2 and B3, respectively). The synthesis then proceeded as described above for gels A1 – 3.

#### 4.2.3 The Synthesis of Gmelinite Microspheres

An aluminate solution was prepared by dissolving sodium aluminate (5.52 g) and sodium hydroxide (9.86 g) in deionised water (146 ml). After filtering through a 0.45 µm PTFE filter (Fisherbrand™), triethanolamine (24.50 g) was added to the aluminate solution. A silica solution was prepared by adding Ludox™ HS-40 colloidal silica (37.76 g) to deionised H<sub>2</sub>O (104 ml). The silica solution was added to the aluminate solution in a 500 ml HDPE bottle, then homogenised on a mechanical shaker for 15 minutes. Following homogenisation, the gel was divided into 10 ml portions and transferred to 15 ml HDPE bottles. The gels were then aged at ambient temperature for 9 days prior to heating at 85°C for 14 - 21 days. In instances where the gel was unaged, the bottled gels were heated at 85°C for 3 – 21 days. Following the desired heating time, the product was recovered by vacuum filtration, washed copiously with deionised water and dried overnight at 60°C. All re-agents were obtained from the same suppliers listed in Section 4.2.2.

#### 4.2.4 Powder X-ray Diffraction (PXRD)

PXRD was performed on a Bruker D8 Advance diffractometer, in reflection geometry, equipped with a Ni-filtered Cu  $K_{\alpha}$  X-ray source ( $\lambda = 1.5418 \text{ \AA}$ ) and fitted with a solid-state LynxEye position sensitive detector. PXRD patterns were recorded on finely ground samples mounted on silicon low background holders that were first covered in a thin layer of Vaseline. Scans were measured over the  $2\theta$  range  $4 - 60^{\circ}$  at a scan rate of  $0.04^{\circ} \text{ s}^{-1}$  with a  $0.02^{\circ}$  step-size. All reference PDF stick plots are derived from the appropriate entry in the ICDD PDF 4+ database.<sup>83</sup> All PXRD patterns were plotted in SigmaPlot.<sup>87</sup>

#### 4.2.5 Scanning Electron Microscopy (SEM)

Scanning electron micrographs were obtained on a JEOL 6060 microscope at an accelerating voltage of 20 keV and a working distance of *ca.* 13 mm. The imaged samples were mounted on graphite tape then sputter coated with a gold thin film, with an approximate thickness of 20 nm, prior to imaging. All particle sizes were measured using Image J software.<sup>86</sup>

#### 4.2.6 Sieving

Prior to sieving, samples were sonicated in deionised water for 5 minutes. Wet sieving was performed by passing the sonicated solution over a stainless steel VWR test sieve ( $25 \mu\text{m}$ ) using more deionised water (*ca.* 500 ml) as an eluent to aid passage through the sieve.

## 4.3 Results and Discussion

### 4.3.1 Large Zeolite A Crystals

Large crystals of zeolite A, within the size range of interest, have been synthesised following the crystal growth procedure reported by Charnell,<sup>42</sup> with the same gel composition at 85°C but with some modifications to the method. Notable changes to the method include the addition of TEOA to the aluminate solution following filtration rather than before; the use of HDPE bottles instead of glass and growing the crystals in a convection oven rather than a water bath. The effect of crystallisation time on the phase purity and the crystal sizes in the product were studied by heating gels with the same composition for 14, 21 and 28 days. PXRD patterns recorded on the products are displayed in Figure 4.1 along with a stick plot of a Na-A pattern, in each case all reflections correspond to those expected for zeolite A.

Scanning electron micrographs recorded on the samples are shown in Figure 4.2. In each sample, the crystals display cubic or pseudo-cubic morphologies over a wide range of particle sizes. In the discussion of the size of cubes, it is more intuitive to discuss particle size in terms of side length rather than diameter, though as other authors discuss “diameters” of cubic crystals, diameters are also presented, where the diameter is defined as the distance between a given vertex of the cube and the most distant vertex from it. Following crystal growth for 14 days, the cubic crystal side lengths span 3 – 16  $\mu\text{m}$ , equivalent to diameters of 5 – 28  $\mu\text{m}$ . Crystal growths for 21 and 28 days produce crystals with a similar range of particle sizes and little variation from those grown for 14 days, with side lengths between 3 – 18  $\mu\text{m}$  ( $d \approx 5 - 31 \mu\text{m}$ ) and 3 – 21  $\mu\text{m}$  ( $d \approx 5 - 36 \mu\text{m}$ ) observed for samples grown for 21 and 28 days, respectively. Ultimately, some larger crystals are observed upon increasing the crystal growth time, but overall little variation is observed in the particle sizes upon increasing the growing time of crystals from 14 to 21 or 28 days.

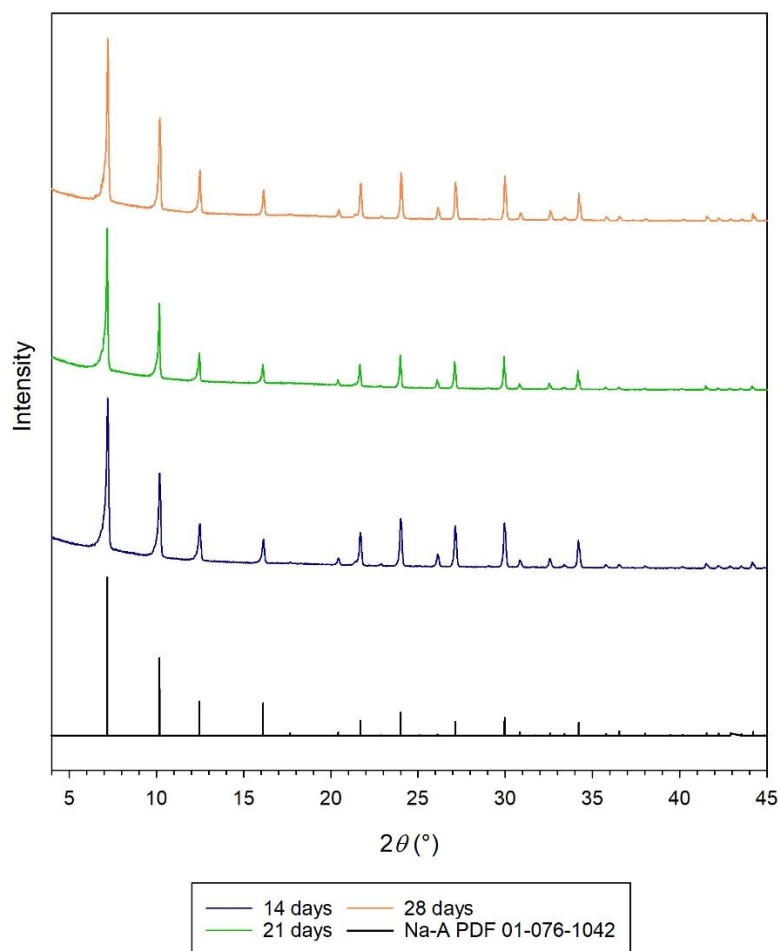


Figure 4.1. PXRD patterns of zeolite A crystals grown for 14, 21 and 28 days.

The efficacy of sieving to control dispersity was tested on zeolite A grown for 28 days by wet sieving with a 25  $\mu\text{m}$  test sieve, using deionised water as an eluent. Scanning electron micrographs recorded on the > 25  $\mu\text{m}$  fraction collected following sieving, in Figure 4.3, appear to show fewer small crystals ( $d < 25 \mu\text{m}$ ) than in the pre-sieved material, however, crystals with diameters below 25  $\mu\text{m}$  are still present. The presence of smaller crystals intimately associated with larger crystals may indicate some intergrowth preventing separation of these smaller crystals. Additionally, it is likely the larger crystals clog the apertures of the sieve during sieving, preventing adequate separation of all small crystals that would otherwise pass through the sieve apertures.

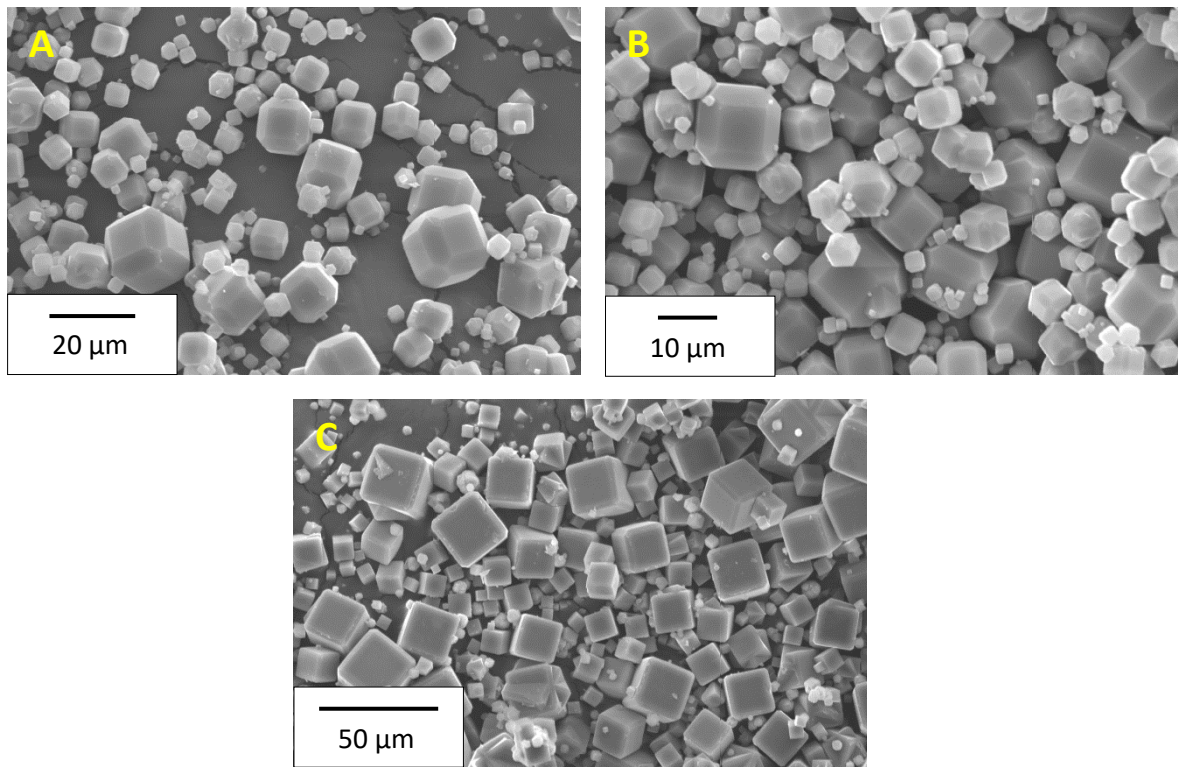


Figure 4.2. Scanning electron micrographs for zeolite A grown for (A) 14, (B) 21 and (C) 28 days.

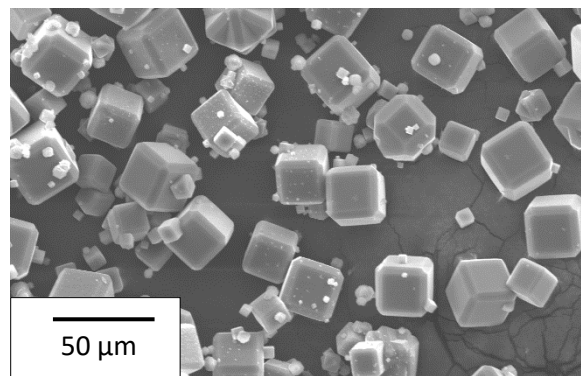


Figure 4.3. Scanning electron micrograph of the > 25 μm fraction of zeolite A grown for 28 days.

Ultimately, cubic or pseudo-cubic crystals of zeolite A with diameters in the size range of interest may be synthesised by a modification of the method first reported by Charnell.<sup>42</sup> Crystals produced by this method are polydisperse, though sieving is moderately effective in separating some, but not all, of the smaller particles from the sample.

### 4.3.2 Large Zeolite X Crystals

Large zeolite X crystals have been synthesised by the method reported by Charnell,<sup>42</sup> in an analogous manner to the large zeolite A crystals, in Section 4.3.1, at 85°C but with a different gel composition. The effect of time on crystal sizes and phase purity was also studied for zeolite X by growing crystals for 14, 21 and 28 days. PXRD patterns recorded on the products are presented in Figure 4.4 along with a stick plot of a reference Na-X pattern. In each pattern, the relative intensity of the 111 reflection at  $2\theta \approx 6.1^\circ$  is much greater than all other reflections compared with the relative intensities observed in the reference Na-X pattern (PDF 00-038-0237). In each pattern, additional low intensity peaks are present at  $2\theta \approx 7.1$ , 10.2 and  $12.5^\circ$  corresponding to zeolite A.

Scanning electron micrographs of zeolite X grown for 14, 21 and 28 days are presented in Figure 4.5. The crystals produced are principally octahedral, or pseudo-octahedral, as would be expected for zeolite X. In addition, cubic crystals are also present in all samples likely corresponding to the zeolite A responsible for the additional reflections in the PXRD patterns, most notably at  $2\theta \approx 7.1^\circ$ . In the sample grown for 28 days, there are also a significant amount of small spherical particles. Although no other discernible reflections are present in the PXRD pattern, the spherical particles are likely zeolite P (Section 6.3.3.1).

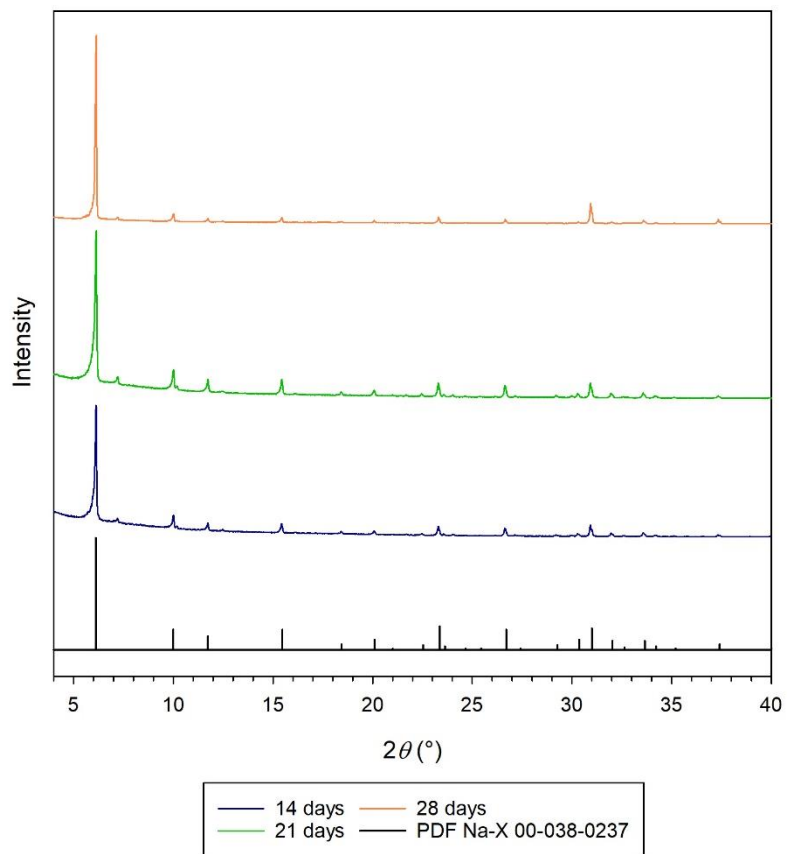


Figure 4.4. PXRD patterns for zeolite X grown for 14, 21 and 28 days.

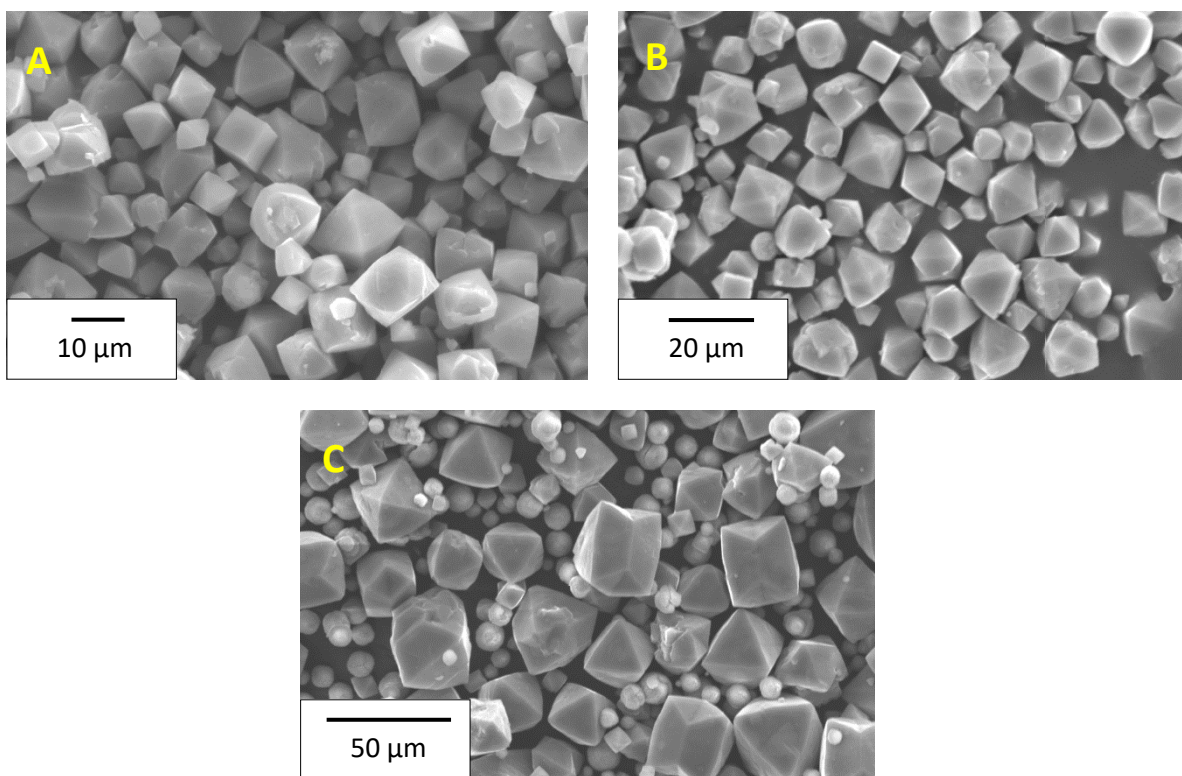


Figure 4.5. Scanning electron micrographs for zeolite X grown for (A) 14, (B) 21 and (C) 28 days.

The zeolite X crystals display a range of crystal habits as shown in Figure 4.6, including perfect octahedra (Fig 4.6A), intergrown octahedra (Fig. 4.6B) and some crystals which appear to be intergrown with cubic crystals (Fig. 4.6C). In each sample, the particles sizes of the zeolite X octahedra are polydisperse but much greater in size than those synthesised by conventional hydrothermal methods ( $d \approx 0.1 \mu\text{m}$ ).<sup>52</sup> In the sample grown for 14 days, the diameters of the octahedra span 8 - 20  $\mu\text{m}$ , where the diameter has been defined as the distance from one vertex to the furthest vertex in the octahedron. Similar diameters are present in the sample grown for 21 days ( $d = 10 - 25 \mu\text{m}$ ), whereas in the sample grown for 28 days greater diameters are also observed ( $d = 10 - 40 \mu\text{m}$ ).

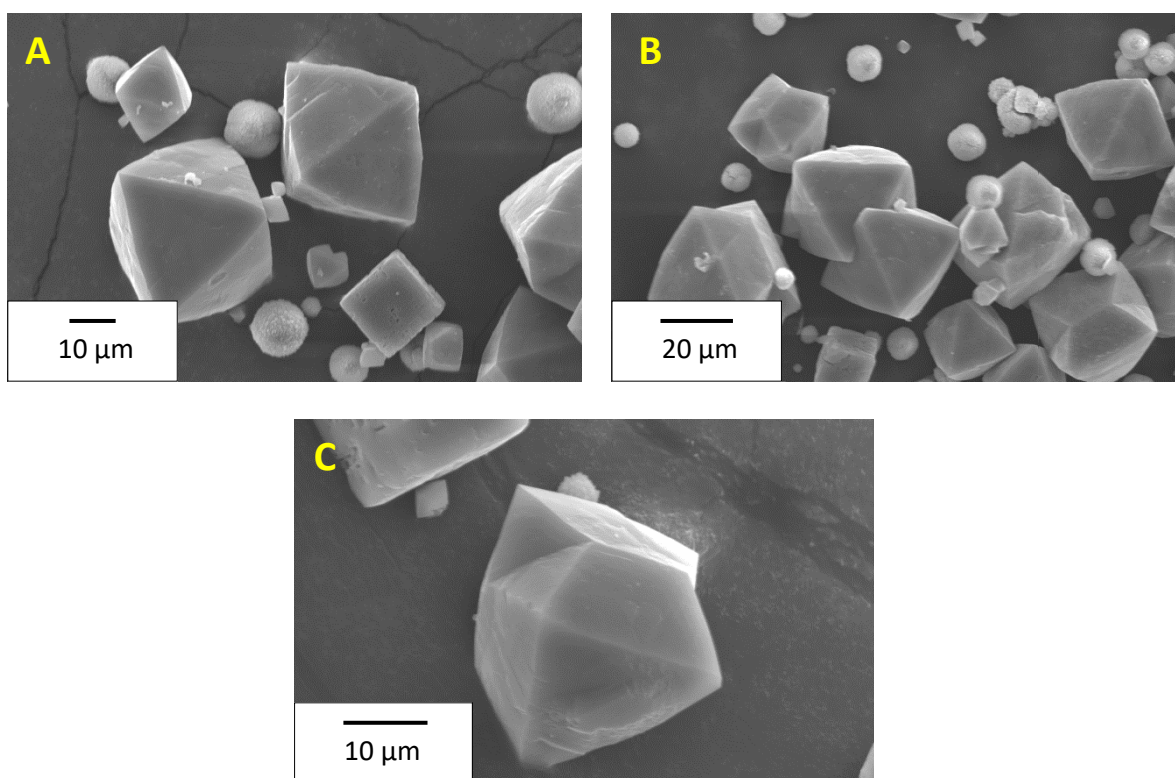


Figure 4.6. Scanning electron micrographs depicting the range of morphologies present in zeolite X samples grown for 28 days.

The efficacy of sieving to remove the spherical particles and smaller octahedra in samples of zeolite X grown for 28 days has been tested by wet sieving with a 25  $\mu\text{m}$  test sieve using deionised water as an eluent. A scanning electron micrograph of the  $> 25 \mu\text{m}$  fraction of sieved zeolite X (Figure 4.7) reveals

sieving appears to be effective in removing some spherical particles, as the frequency with which they are observed decreases. Nevertheless, some spherical particles remain in the > 25  $\mu\text{m}$  fraction likely due to large octahedra clogging the apertures during sieving. Sieving also appears to be successful in removing smaller octahedra, as few octahedra with diameters below *ca.* 25  $\mu\text{m}$  are present in micrographs of the sieved product.

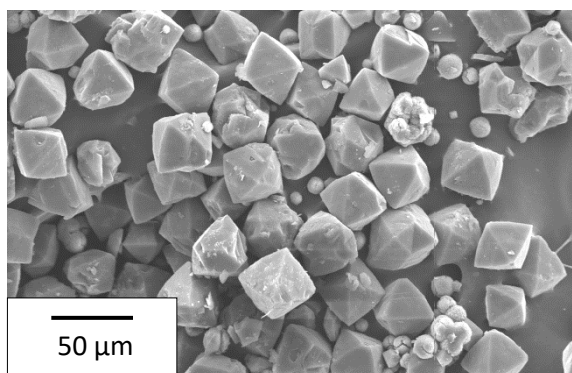


Figure 4.7. A scanning electron micrograph of the > 25  $\mu\text{m}$  fraction of zeolite X.

Ultimately, octahedra and similarly shaped crystals may be grown within the size range of interest by employing the Charnell method.<sup>42</sup> Growth for 28 days produces particles greater in size than those produced following 14 and 21 days, although all products are polydisperse. The efficacy of sieving to control dispersity and remove spherical impurities has been demonstrated for the largest crystals grown for 28 days, although some spherical particles and smaller octahedra remain in the product.

#### 4.3.3 Large Zeolite Y Crystals and the Associated Gel System

The growth of large spherical zeolite Y crystals with diameters spanning 60 – 120  $\mu\text{m}$ , from gels containing TEOA, was reported by Ferchiche *et al.*<sup>95</sup> The crystal growths reported by Ferchiche *et al.* have been studied, as well as the influence of replacing the silicon source, fumed silica, with colloidal silica. Gels with equivalent compositions to those reported with Si/Al = 2.6 (A1), 3.4 (A2) and 4.3 (A3)

were aged at ambient temperature for 9 days, after which they were heated at 95°C for 32 days.

Scanning electron micrographs of the products are presented in Figure 4.8.

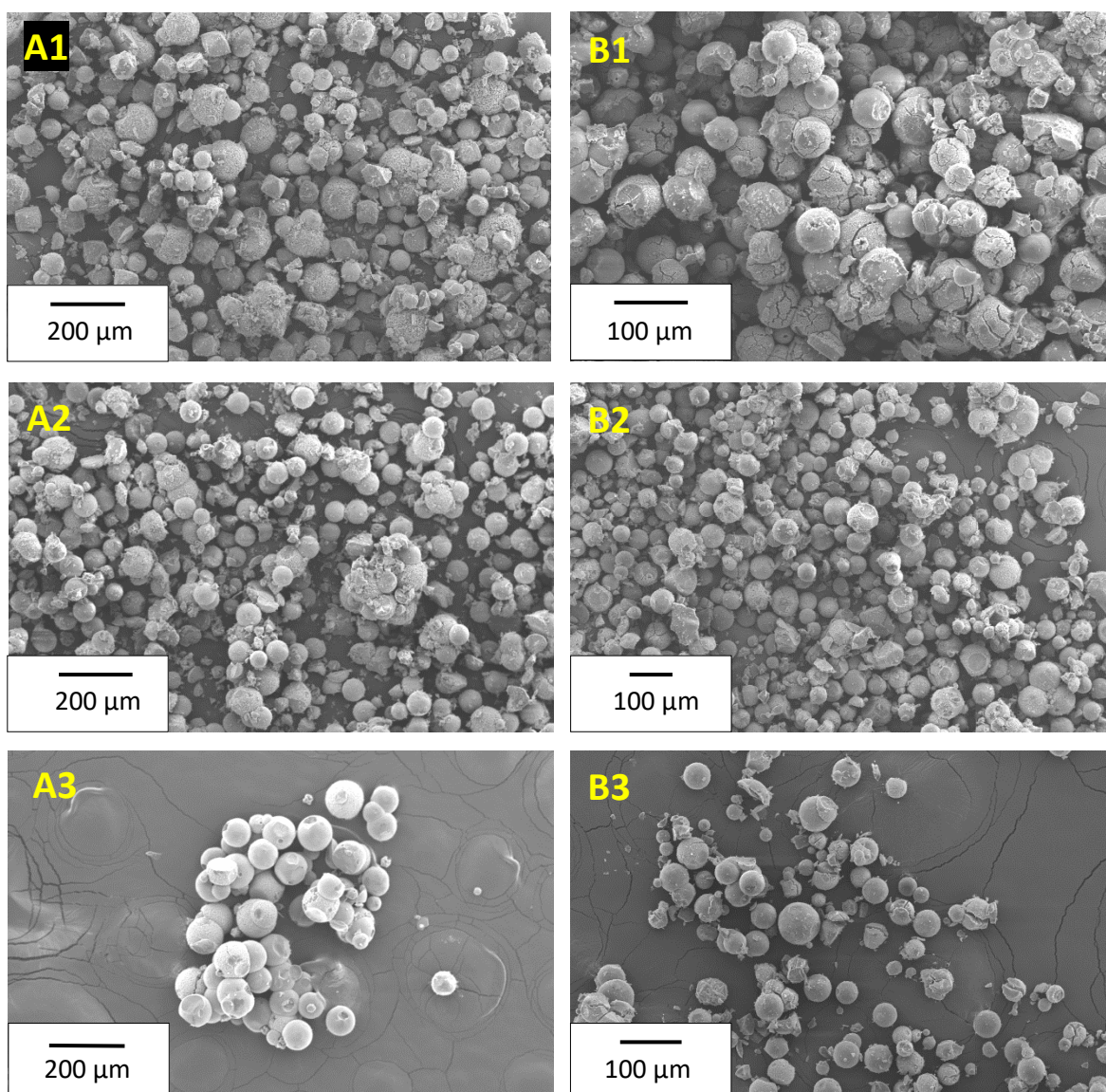


Figure 4.8. Scanning electron micrographs of A1, A2, A3, B1, B2 and B3, as labelled.

PXRD patterns recorded on the products along with appropriate stick plots are presented in Figure 4.9 for A1 and Figure 4.10 for A2 and A3. The PXRD pattern recorded for A1 shows principally zeolite Y is produced along with chabazite and zeolite P. The product contains particles with various shapes including spheres, octahedra and cubes, among much smaller particulate matter. The spherical particles produced are polydisperse with smaller ( $d = 20 - 60 \mu\text{m}$ ) and larger ( $d = 100 - 115 \mu\text{m}$ ) particle

size ranges present. This agrees reasonably well with the observations of Ferchiche *et al.* who reported mostly zeolite Y, with a sizeable zeolite P impurity, was produced from gels with the same Si/Al, however, the maximum sphere diameter reported was only 65  $\mu\text{m}$ .

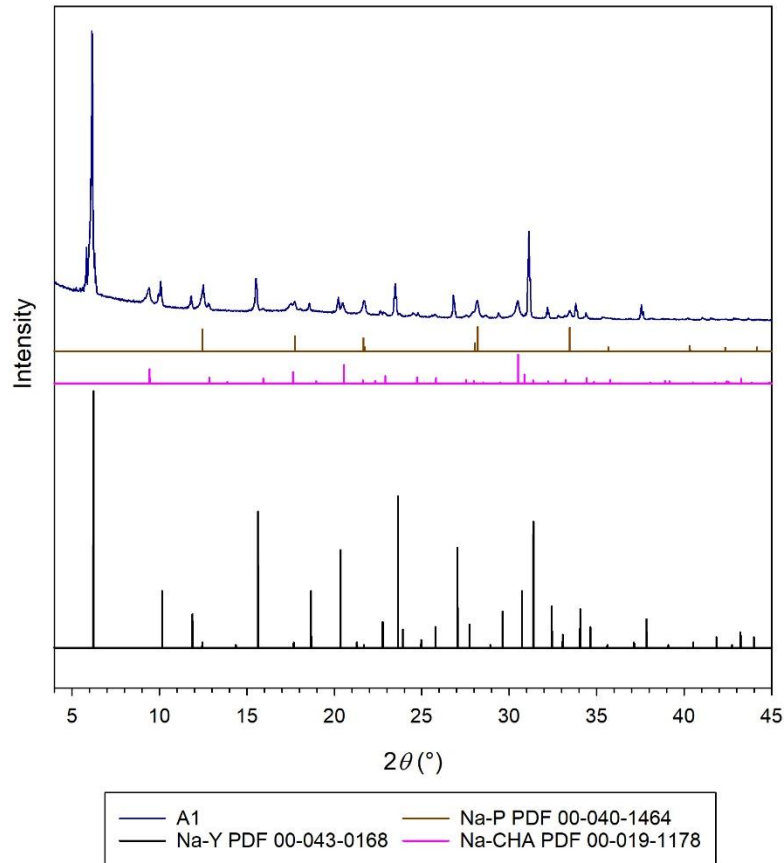


Figure 4.9. PXRD pattern of A1 and reference patterns for Na-Y, Na-CHA and Na-P.

Upon increasing the gel Si/Al ratio to 3.4 (A2) and 4.3 (A3), the composition of the products changes significantly. The PXRD pattern of A2 shows the product is mostly zeolite P and chabazite with some zeolite Y also produced, albeit with significantly reduced intensities compared with A1. Similarly, A3 also comprises mostly chabazite and zeolite P but with the relative intensity of zeolite P reflections increasing from those observed for A2. A2 principally comprises particles that are spheres, hemispheres or fragments of spheres among other smaller particulate matter; the spheres present possess diameters ( $d = 50 - 80 \mu\text{m}$ ) within a narrower range than observed in A1 samples. The largest particle diameters present in A2 ( $d \approx 80 \mu\text{m}$ ) agree well with those reported by Ferchiche *et al.*

( $d \approx 85 \mu\text{m}$ ), although it was reported the phase comprised a mixture of zeolite Y and zeolite P. A3 comprises mostly spherical aggregates with individual spherical components possessing diameters in the range  $d = 80 - 100 \mu\text{m}$ , and much less smaller particulate matter present than in A1 and A2. The largest diameter present ( $d = 100 \mu\text{m}$ ) is smaller than the reported value ( $d = 125 \mu\text{m}$ ).<sup>95</sup>

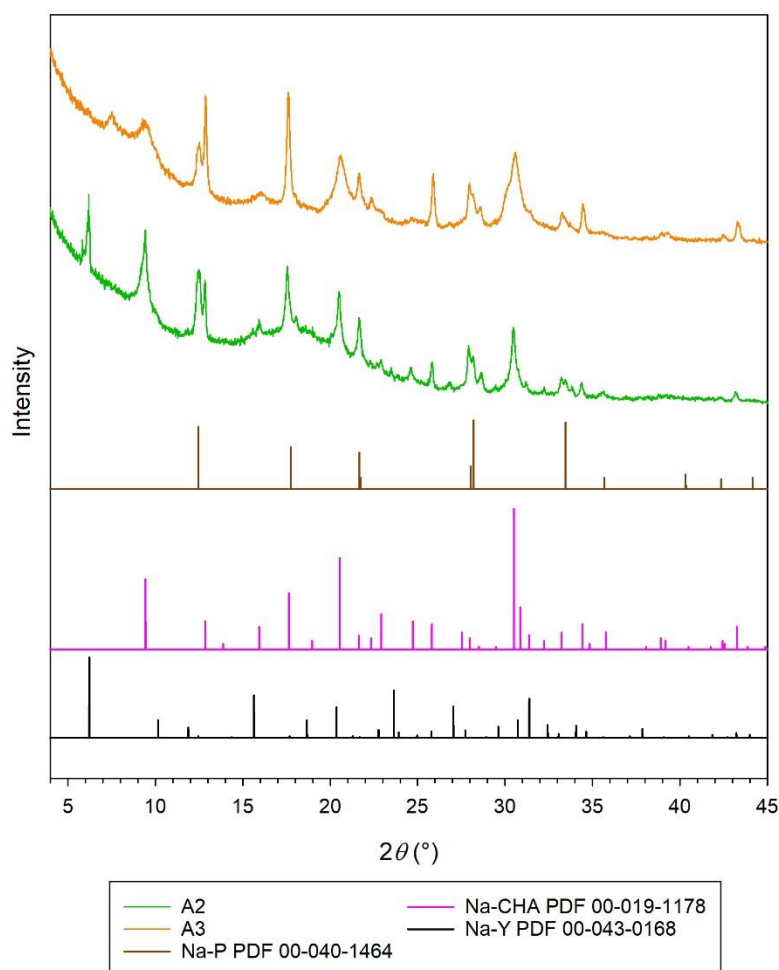


Figure 4.10. PXRD patterns of A2 and A3, and reference patterns of Na-P, Na-CHA and Na-Y.

Employing large quantities of fumed silica in syntheses presents challenges in handling owing to the low density of the material. In syntheses analogous to those described for A1, A2 and A3, the influence of substituting colloidal silica for fumed silica, while maintaining the overall water content of the gel equivalent, has been evaluated. PXRD patterns of products for gels with Si/Al ratios 2.6 (B1), 3.4 (B2) and 4.3 (B3) are presented in Figure 4.11. Scanning electron micrographs for B1, B2 and B3 are presented in Figure 4.8.

Upon substituting colloidal silica for fumed silica in gels with Si/Al = 2.6 (B1), zeolite Y is no longer the major phase present, rather the sample comprises both zeolite Y and zeolite P. While the phases present in B1 differ from A1, the particles produced are mostly spherical ( $d = 40 - 70 \mu\text{m}$ ) among smaller particulate matter, although the spheres produced appear fractured and friable in some cases.

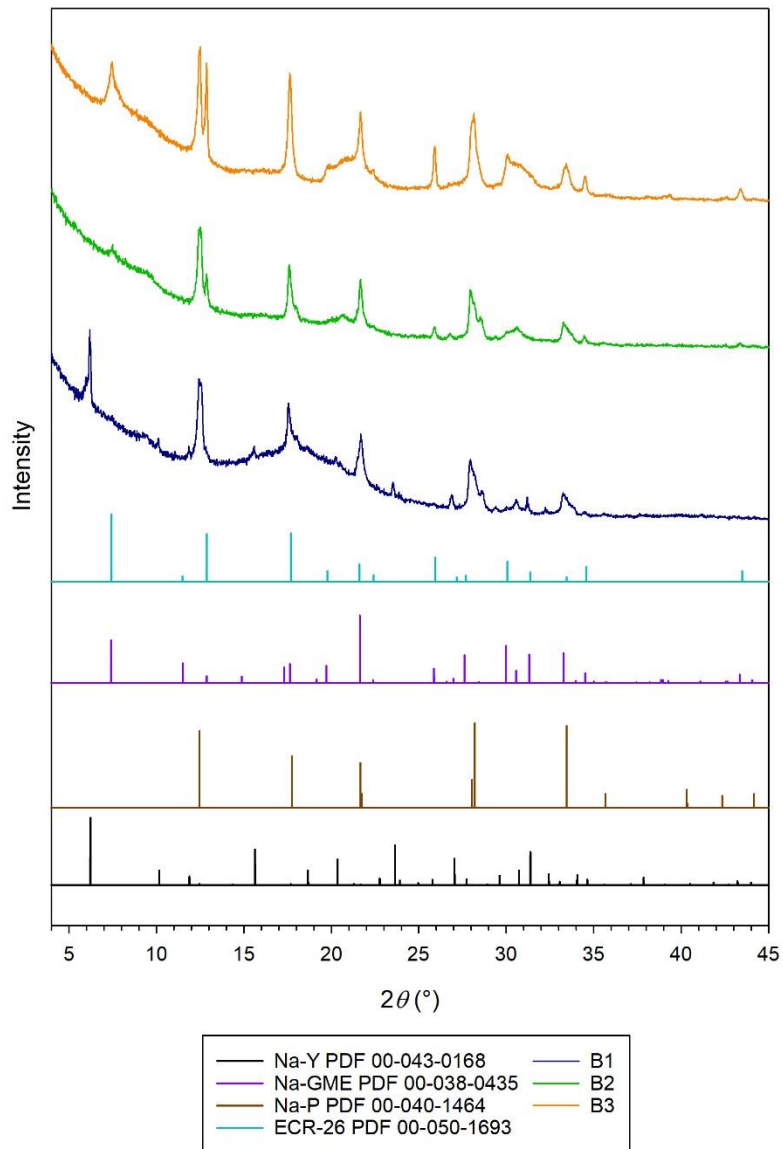


Figure 4.11. PXRD patterns for B1, B2 and B3, and reference patterns for Na-Y, Na-GME, Na-P and ECR-26.

As in the case of B1, the particles produced at Si/Al = 3.4 (B2) are chiefly spherical or spherical aggregates with similar sizes ( $d = 40 - 70 \mu\text{m}$ ). The product comprises mostly zeolite P and some

reflections attributable to gmelinite (GME), with no discernible zeolite Y reflections. B3 also comprises zeolite P and GME, though the reflections attributable to GME are more intense compared with those observed in B2. The relative intensities of gmelinite reflections in B3 are more similar to those observed for ECR-26, a gmelinite analogue containing some Fe<sup>III</sup> and Cr<sup>III</sup> framework substitutions,<sup>100</sup> than those observed for the regular aluminosilicate, as shown in Figure 4.11. Naturally, there are no isomorphous framework substitutions in the product B3 such as those in ECR-26. The product B3 principally comprises spherical particles ( $d = 25 - 80 \mu\text{m}$ ) among smaller fragments. Critically, the spheres in B3 appear less fractured and fragmented than those in B2 and B1, and therefore more suitable in the application of radiotracers.

#### 4.3.4 The Synthesis of Gmelinite Microspheres

Given the desired size range and mechanical integrity required for application as radiotracers, the most promising particles produced in Section 4.3.3 are synthesised in the preparations A3 and B3. The inherent disadvantages of handling large quantities of fumed silica renders B3 a more suitable method than A3. The influence of lowering the temperature from 95°C to 85°C, as well as the time over which the particles are grown was tested for the B3 gel composition with a modified experimental procedure (Section 4.2.3).

PXRD patterns recorded on the products of gels with the B3 composition heated at 85°C for 14 and 21 days are presented in Figure 4.12. In each case, the reflections present may be attributed to gmelinite, and as in the case of B3, the relative intensities more closely match those reported for ECR-26 than GME; this is highlighted in Figure 4.13 which shows the PXRD pattern for GME synthesised following 21 days along with stick plots of GME and ECR-26. In ECR-26, the most intense reflections are the 100 at  $2\theta = 7.4^\circ$ , 110 at  $2\theta = 12.9^\circ$  and 002 at  $2\theta = 17.6^\circ$ .<sup>100</sup> The 100 reflection is also intense in patterns of GME; however, the 110 and 002 reflections have lower relative intensities in GME compared with ECR-26. In contrast, the most intense reflection expected for GME (211 at  $2\theta = 21.6^\circ$ )

has a comparatively low relative intensity in ECR-26 patterns. In general,  $hk0$  or  $00l$  reflections are more intense in both the products and ECR-26, than in reported patterns for aluminosilicate gmelinite. Naturally, in the product there are no isomorphous substitutions for  $Al^{3+}$  such as those in ECR-26; however, the similar relative intensities may instead be an artefact from a similar crystal growth process. In layered materials such as clays, particles often grow by addition of atoms to  $(hk0)$  faces; these particles then adhere to one another in oriented attachment giving rise to growth in the  $[00l]$  direction.<sup>102</sup> While GME is not a structurally layered material in the way that clays are, platy crystals of GME have been observed in natural deposits, as well as spherical aggregates of twinned crystals.<sup>103</sup> It may be the case that crystal growth of GME microspheres is occurring in a similar manner to clays, giving rise to the observed preferred orientation in  $hk0$  and  $00l$  reflections.

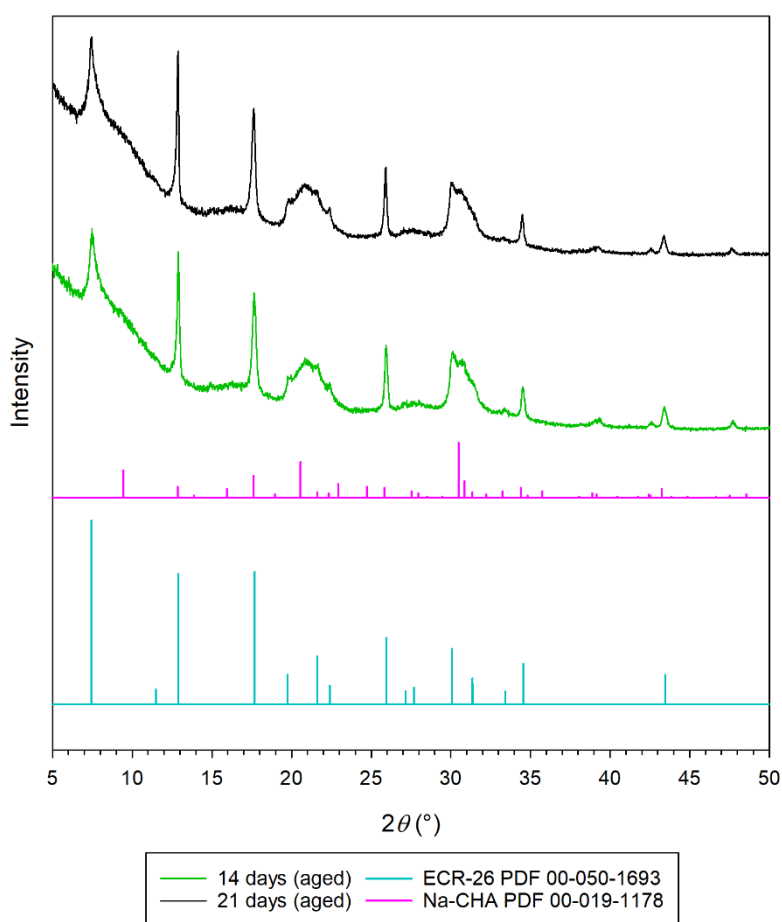


Figure 4.12. PXRD patterns of GME produced by heating for 14 and 21 days, and reference patterns of ECR-26 and Na-CHA.

The intergrowth of gmelinite and chabazite phases is observed widely in both natural and synthetic zeolite samples.<sup>104</sup> The presence of chabazite in the products cannot be eliminated as the two most intense reflections in chabazite PXRD patterns would occur at  $2\theta = 20.5^\circ$  and  $2\theta = 30.5^\circ$ , in the 2 regions of broad overlapping peaks, at  $2\theta \approx 20 - 23^\circ$  and  $2\theta \approx 30 - 32^\circ$ , in the product PXRD patterns.

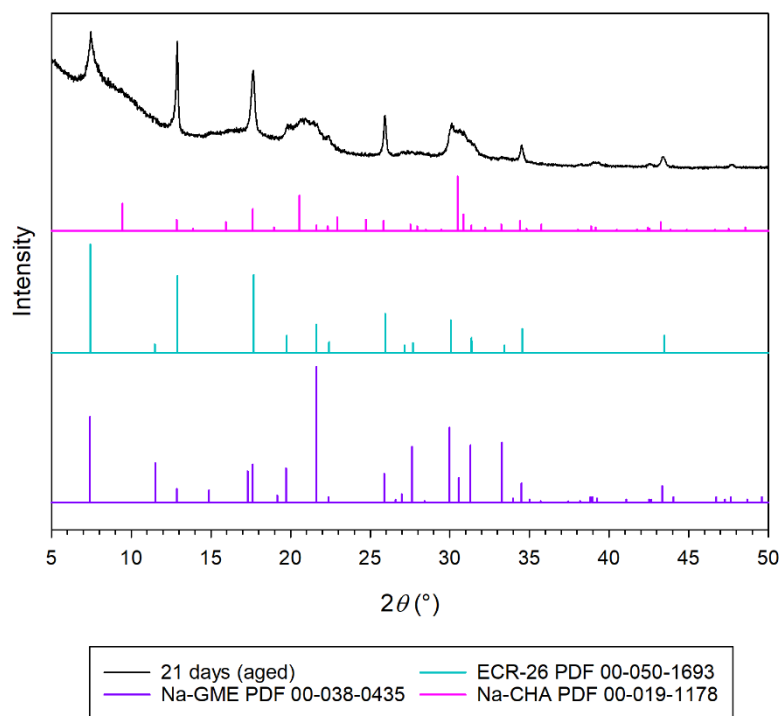


Figure 4.13. PXRD pattern of GME (21 days) and reference patterns of Na-GME, Na-CHA and ECR-26.

Scanning electron micrographs of the products of gels heated for 14 and 21 days, presented in Figure 4.14, show the particles produced are universally spherical in morphology with little intergrowth observed between particles in both cases. Statistical analysis on particle diameters, as measured using ImageJ software,<sup>86</sup> is presented in Table 4.1 and histograms for diameters in both samples are plotted in Figure 4.15, along with a kernel plot estimate of the particle size distribution calculated in SigmaPlot.<sup>85</sup> The histogram of particle diameters grown for 14 days attests that particles in the sample are relatively uniform in size with most diameters close to the mean (7.58  $\mu\text{m}$ ). In samples grown for 21 days, there are still many particles with diameters between 7 – 8  $\mu\text{m}$ , however,

larger particles up to 15  $\mu\text{m}$  are also present as demonstrated in the particle size distribution and by the greater mean diameter (8.64  $\mu\text{m}$ ).

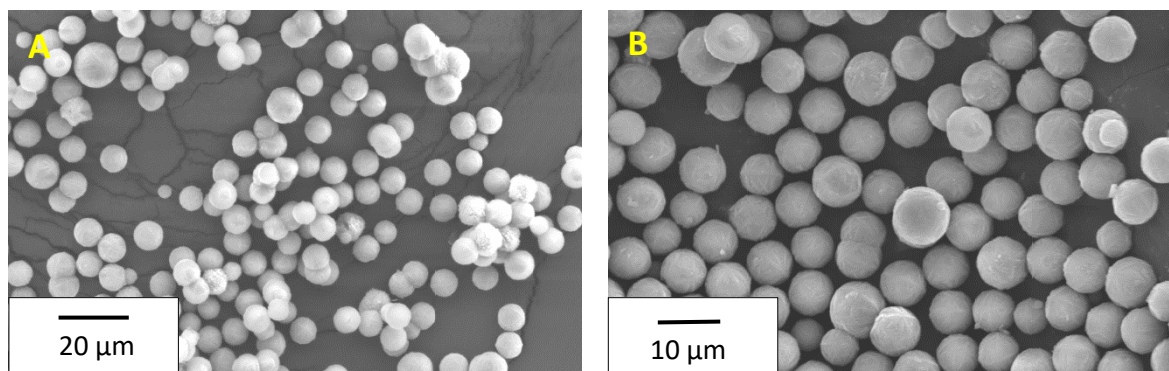


Figure 4.14. Scanning electron micrographs of GME synthesised following heating for (A) 14 and (B) 21 days.

Table 4.1. Statistical analysis of diameters for GME microspheres.

Heating duration (days)	Sample size	Mean diameter ( $\mu\text{m}$ )	Standard deviation ( $\mu\text{m}$ )
14	205	7.58	1.34
21	182	8.64	2.06

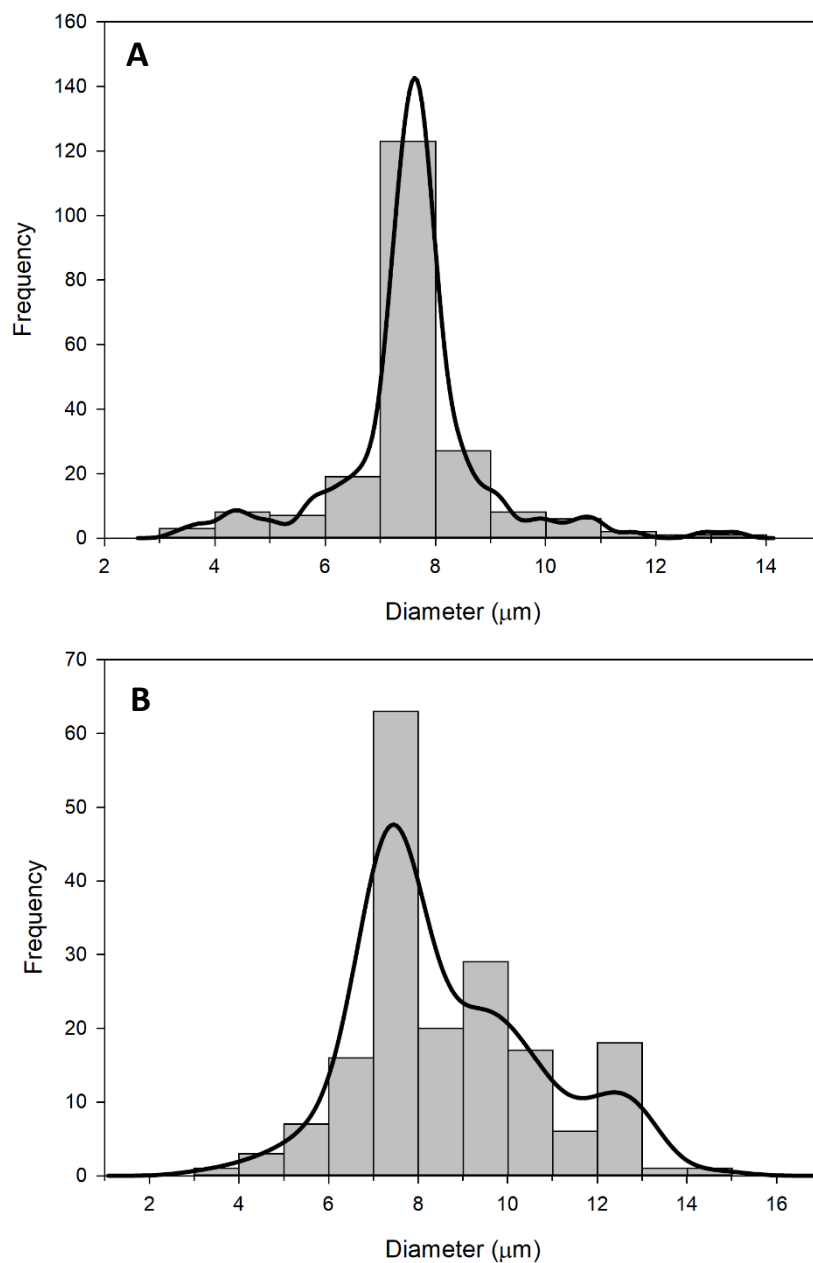


Figure 4.15. Particle size distribution of diameters of GME microspheres heated for (A) 14 days and (B) 21 days.

#### 4.3.5 Gmelinite Microspheres: The Role of Aging

The importance of aging the gel at ambient temperature prior to heating was investigated by directly heating the gel to 85°C following homogenisation, rather than aging at ambient temperature for 9 days. The products from unaged gels heated for 3, 5, 7, 14 and 21 days have been investigated by PXRD (Fig. 4.16) and SEM (Fig. 4.17). Following 3 days of heating, no microspheres are detected in the

product, nor are any discernible peaks present in the PXRD pattern. After 5 days, some microspheres are observed, however, the product still principally constitutes much smaller particulate matter. The PXRD pattern on the product heated for 5 days shows some small kinks in the background at  $2\theta \approx 13$ , 18 and  $26^\circ$  corresponding to the 110, 002 and 220 reflections of GME, respectively.

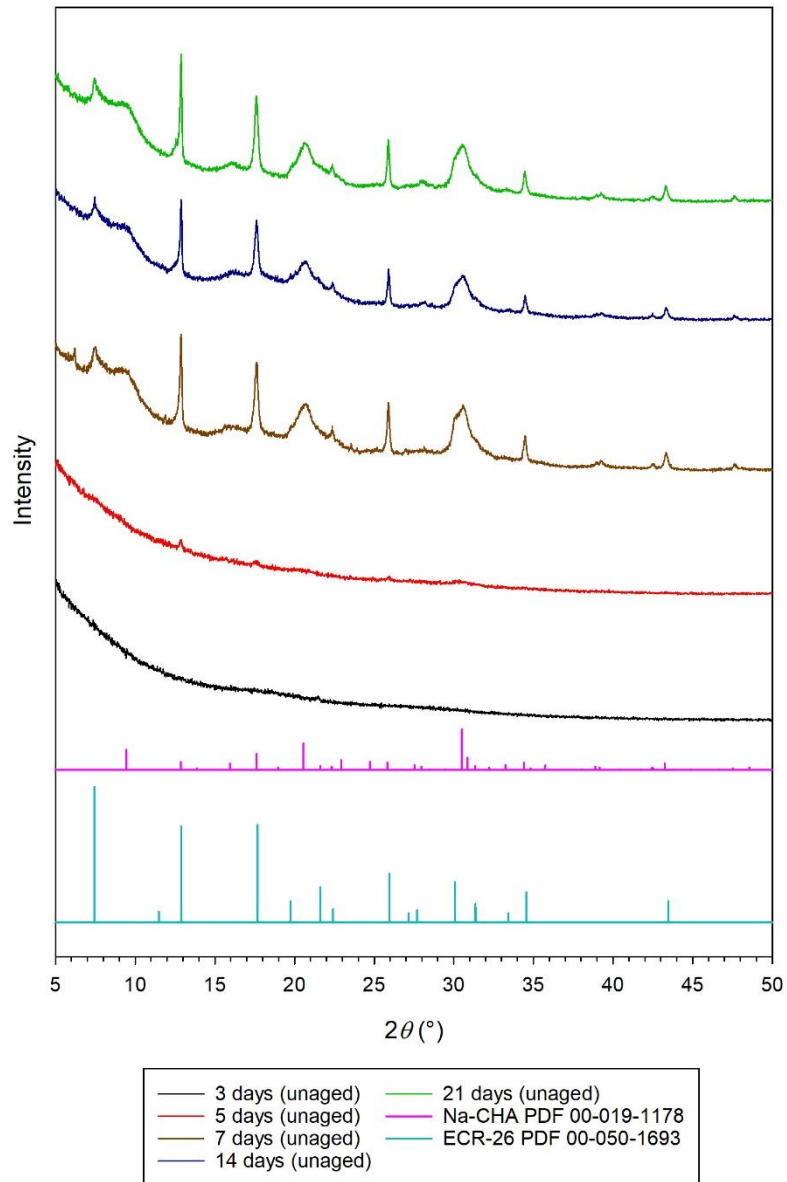


Figure 4.16. PXRD patterns of unaged gels heated for 3, 5, 7, 14 and 21 days, and reference patterns of CHA and ECR-26.

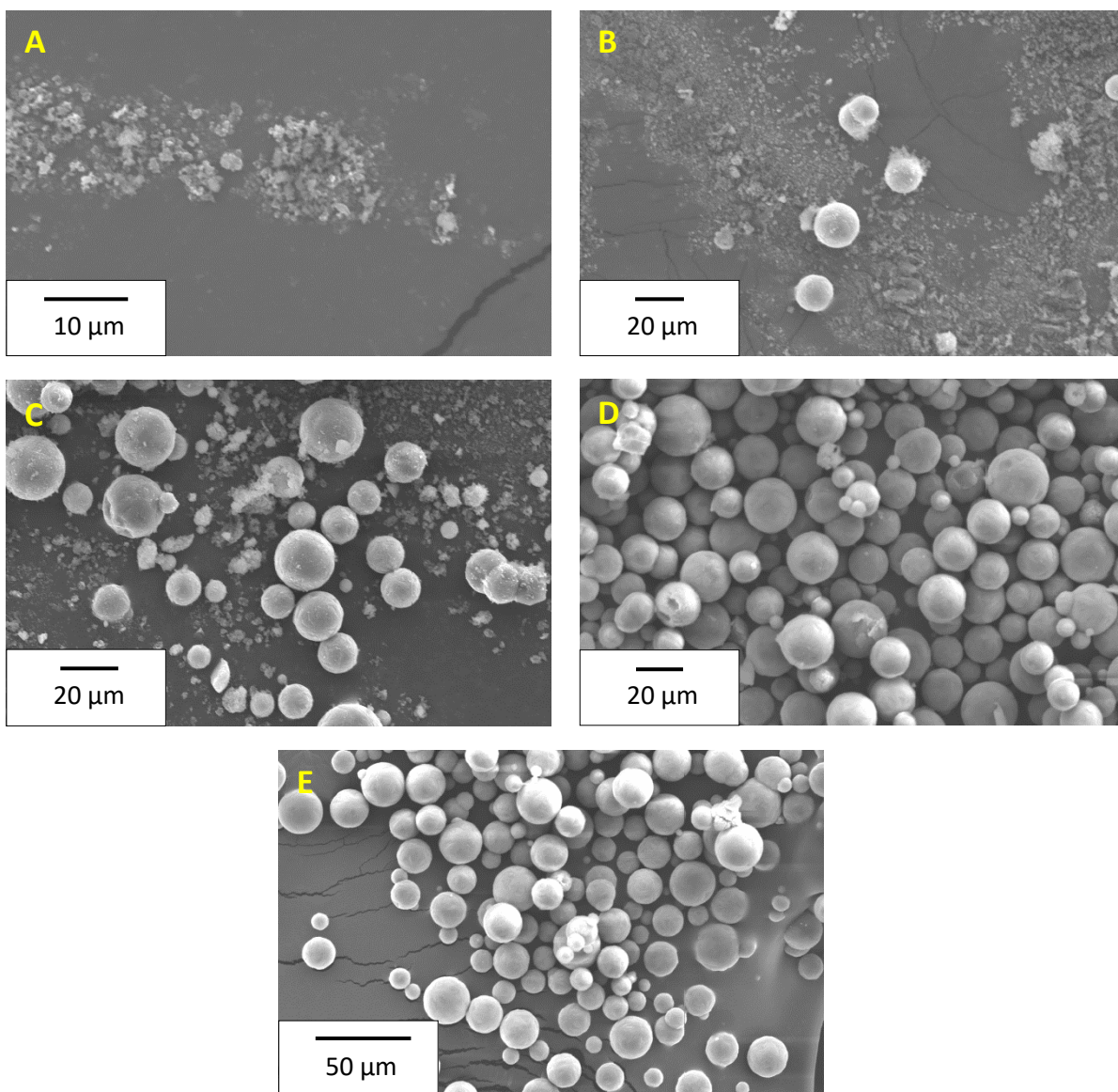


Figure 4.17. Scanning electron micrographs of products of unaged gels heated for (A) 3, (B) 5, (C) 7, (D) 14 and (E) 21 days.

Following heating for 7 days, the product principally constitutes microspheres with only a minor amount of the much smaller particulate matter previously observed. The PXRD pattern contains the GME reflections observed in aged samples; however, an additional small peak is also present at  $2\theta \approx 6^\circ$  which may correspond to the 111 reflection in zeolite Y. In the 2 areas with broad overlapping peaks in aged samples, at  $2\theta \approx 20 - 23$  and  $2\theta \approx 30 - 32^\circ$ , there are distinct peaks at  $2\theta \approx 20.5^\circ$  and  $2\theta \approx 30.5^\circ$  attributable to the 211 and 401 reflections of chabazite, respectively. Moreover, there is also a broad shoulder at  $2\theta \approx 9.5^\circ$  corresponding to the 101 reflection of chabazite. In samples heated for

14 and 21 days, there is no small peak at  $2\theta \approx 6^\circ$ , however, the remainder of the PXRD pattern resembles that recorded on the sample heated for 7 days with the gmelinite reflections along with the 3 broad chabazite peaks.

Statistical analysis on the diameters of the microspheres heated for 5, 7, 14 and 21 days are presented in Table 4.2. In each product of unaged gels, the microspheres are polydisperse, existing over a greater range of sizes than are observed for aged samples. Greater mean diameters are observed, as well as relatively high standard deviations attesting the heterogenous dispersity. Particle size distributions for the samples heated for 14 and 21 days are plotted in Figure 4.18.

Table 4.2. Statistical analysis of microspheres in products of unaged gels.

Heating duration (days)	Sample size	Mean diameter ( $\mu\text{m}$ )	Standard deviation ( $\mu\text{m}$ )
5	24	13.0	2.82
7	48	15.4	5.55
14	245	16.0	5.31
21	266	17.4	5.05

When the gels are not aged at ambient temperature prior to heating, a wider range of particle diameters are observed in the product compared with those produced from aged gels. The products of unaged gels contain distinct broad peaks attributable to chabazite, which are not observed in the products of aged gels. It has been previously noted that aging in zeolite Y gels increases the number of nucleation events, accelerating crystallisation kinetics and decreasing the product particle size.<sup>101</sup> This reasoning would rationalise the smaller diameters observed in aged products compared with those in unaged products.

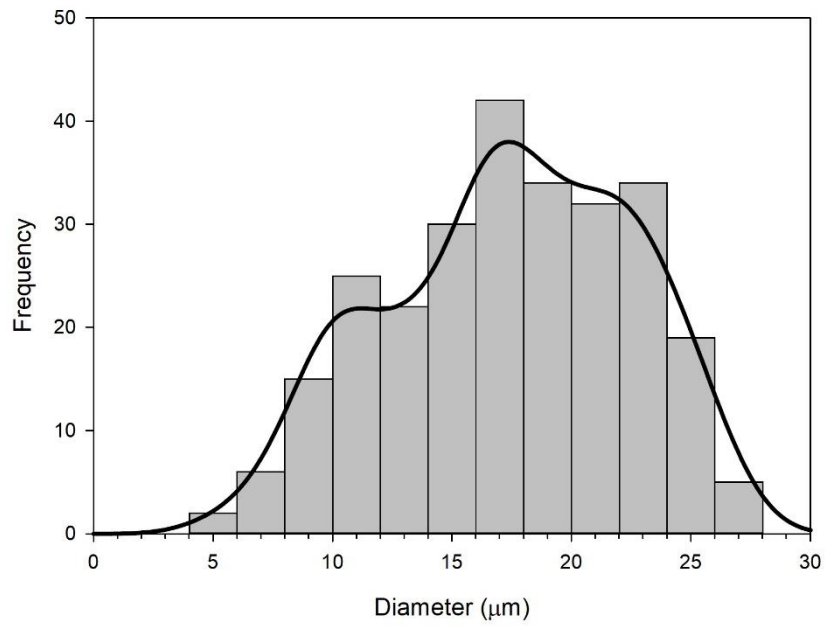
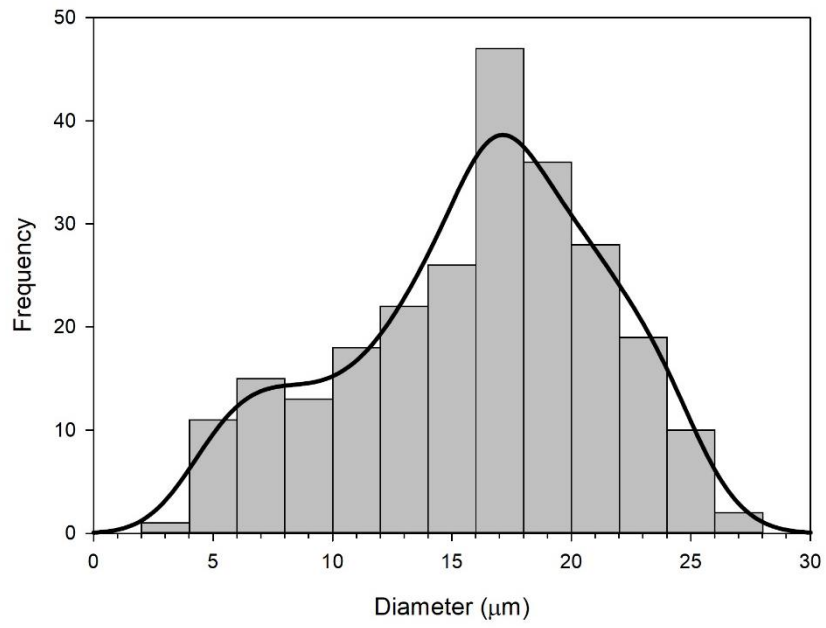


Figure 4.18. Particle size distributions for microspheres produced from unaged gels heated for 14 (top) and 21 (bottom) days.

#### 4.4 Conclusions

Large zeolite A and X crystals adopting chiefly cubic and octahedral morphologies, respectively, with diameters in the size range of interest (5 – 50  $\mu\text{m}$ ) may be synthesised by a modification of the Charnell method. Heating the gel for 4 weeks gives rise to the largest X crystals; however, in the case of zeolite A, no significant increase in crystal size is observed over the range 2 – 4 weeks. While samples are polydisperse, sieving is moderately effective in removing smaller crystals.

Gels reported to produce large spherical zeolite Y particles have been investigated, with most products containing polydisperse particles of various shapes including spheres. The spheres are mostly greater than 50  $\mu\text{m}$  in diameter, and in many cases appear friable so may not have the mechanical integrity required of a radiotracer. Heating gels with similar compositions at lower temperatures with some modifications to the method produces universally spherical particles with a relatively narrow range of diameters. The particles chiefly constitute the zeolite gmelinite, though some chabazite may also be present. The importance of aging the gel prior to heating has been established as when the gel is not aged, the products are polydisperse though still universally spherical.

### 5.1 Introduction

Previous studies on fluoride uptake by zeolites from aqueous solutions can generally be divided into two categories: studies where zeolites are evaluated as adsorbents for aqueous fluoride<sup>59,105-110</sup> and studies where fluoride is reacted with the zeolite to modify the properties of the surface for enhanced performance in catalytic applications.<sup>111-117</sup> In the former, the data presented is limited to uptake from dilute solutions measured by a fluoride ion-selective electrode (ISE) and the application of adsorption isotherms to equilibrium uptake data; post-treatment characterisation of the zeolite to determine the fluoride environment is not reported in any instance. By contrast in studies of the latter type, following treatment of the zeolite with concentrated fluoride solutions at elevated temperatures, <sup>19</sup>F MAS NMR spectroscopy is usually employed to identify the fluorine-containing moieties in the treated zeolite. In this chapter, the term defluoridation is applied to the sorption of fluoride from low concentration aqueous solutions. The term fluorination is applied to the reaction between zeolites and fluoride that results in a product that contains chemically bound fluorine.

The fluorination of zeolites to adapt surface properties typically involves heating a concentrated mineral acid solution, also containing NH<sub>4</sub>F and the zeolite, or related material, under reflux for between several hours and several days.<sup>111-114</sup> Alternatively, incipient wetness impregnation of the zeolite with NH<sub>4</sub>F solutions followed by heating the sample to 500°C has been used to introduce fluoride into ZSM-5 and Ce-exchanged zeolite Y.<sup>115,116</sup> In successfully fluorinated products, fluorine may be bonded to 4 or 5 co-ordinate silicon as evidenced by resonances at *ca.* -153 ppm and -145 ppm in <sup>19</sup>F MAS NMR spectra, respectively corresponding to [SiO<sub>3</sub>F] and [SiO<sub>4</sub>F] moieties.<sup>111-115,117</sup>

In some studies, fluorination is reported to occur by exchange of the hydroxide component in silanol moieties with fluoride. Infrared (IR) spectra performed under vacuum on Ti-MOR demonstrate a decrease in the intensity of hydroxide stretches attributed to silanol moieties following fluorination, supporting the proposed fluoride exchange mechanism.<sup>113</sup> The fluorination of Ce-Y, by the incipient

wetness impregnation method is also reported to proceed by the hydroxide exchange mechanism, as inferred from diminishing intensities in the hydroxyl stretches in IR spectra recorded following fluorination.<sup>116</sup> In contrast, the fluorination of ZSM-5 by incipient wetness impregnation followed by heat treatment is reported to occur by the addition of  $\text{H}^+\text{F}^-$  ion pairs across siloxane bonds. This alternate mechanism was inferred from an alleged increase in acid site density in the fluorinated derivative; however, in the reported acid site densities measured by  $\text{NH}_3$  adsorption, an increase upon fluorination was only observed for some samples, and in others the acid site density decreased.<sup>115</sup>

The zeolites treated in fluorination reactions typically possess relatively high Si/Al ratios, such as ZSM-5, or contain a heteroatom instead of aluminium such as titanium in Ti-MOR, reflecting the catalytic applications of the zeolites that are fluorinated.<sup>111,115</sup> In zeolite Y samples containing intrapore  $\text{H}^+$  ions (H-Y) treated with  $\text{NH}_4\text{F}$  solutions of varying concentrations at  $80^\circ\text{C}$ , four co-ordinate aluminium species containing fluoride,  $[\text{AlO}_3\text{F}]$ , corresponding to resonances at  $\delta_{\text{F}} \approx -173$  ppm in  $^{19}\text{F}$  MAS NMR spectra were identified by 2D NMR experiments.<sup>118</sup> In other studies, dealumination has been observed in zeolites treated with concentrated fluoride solutions under hydrothermal conditions.<sup>119,120</sup>

In a study that evaluated the efficacy of zeolites in defluoridation, fluoride uptake from 20 ppm solutions at ambient temperature was measured for natural samples of analcime, stilbite and clinoptilolite. Analcime demonstrated the highest fluoride uptake with lower uptakes for stilbite and clinoptilolite. The composition of the zeolites employed was not reported, thus the intrapore cations in each zeolite and the framework Si/Al ratios were not known. The fluoride uptake was attributed to reactivity with non-zeolite aluminium in “detrital material” present in the sample, a postulate for which no supporting evidence was provided.<sup>105</sup> In an earlier study, fluoride uptake for natural stilbite from wide ranging fluoride concentrations (5 – 280 ppm  $\text{F}^-$ ) was demonstrated with greater uptake for stilbite containing intrapore  $\text{Ca}^{2+}$  compared with the Na-form. Optimal uptake in the pH range 3 – 4 was also demonstrated, as well as that the presence of chloride in solution inhibits fluoride uptake.<sup>106</sup>

Another study focusing on defluoridation by a natural stilbite (STI) containing intrapore  $\text{Ca}^{2+}$  and  $\text{Na}^+$  reported that ion exchange of  $\text{Na}^+$  for  $\text{NH}_4^+$  led to enhanced fluoride uptake. Enhanced uptake for Ca/ $\text{NH}_4$ -STI was attributed to “connectivity defects” introduced to the zeolite upon ion exchange, a definition of a “connectivity defect” and an explanation of how fluoride might interact with one was not provided. Fluoride uptake by Ca/Na-STI is ascribed to ion exchange between aqueous  $\text{Na}^+$  and intrapore  $\text{Ca}^{2+}$  leading to the precipitation of  $\text{CaF}_2$ ; however, no experimental evidence is provided to support that  $\text{CaF}_2$  precipitation or “connectivity defects” are responsible for the observed defluoridation.<sup>107</sup>

In other studies, fluoride uptake is reported on zeolites modified by surface sorption of complexes containing trivalent cations, such as  $\text{Fe}^{3+}$ ,  $\text{La}^{3+}$  and  $\text{Al}^{3+}$ . Efficacy in defluoridation was reported for a natural stilbite sample modified with  $\text{Fe}^{3+}$ ; equilibrium uptake data was fitted to adsorption isotherms and good agreement to the Langmuir isotherm was observed.<sup>108</sup> Uptake from 10 – 80 ppm fluoride solutions by synthetic zeolite Y modified with surface sorbed  $\text{Al}^{3+}$  and  $\text{La}^{3+}$ -complexes has also been reported. Equilibrium fluoride uptake data for  $\text{Al}^{3+}$  and  $\text{La}^{3+}$ -modified Y was fitted to various adsorption isotherm models, including the Freundlich and Dubinin-Radushkevitch (DR) equations to which good agreement between the models and experimental data was found. Characteristic adsorption energies ( $E_c$ ) for fluoride uptake by the modified zeolites were calculated from the gradient in DR fits. The magnitude of  $E_c$  indicated fluoride adsorption proceeded by chemisorption for  $\text{Al}^{3+}$ -modified Y and physisorption for  $\text{La}^{3+}$ -modified Y.<sup>109</sup> The same authors have also demonstrated  $\text{Al}^{3+}$ -modified zeolites A and X also chemisorb fluoride from solution, albeit with lower fluoride loadings.<sup>59</sup> It is believed fluoride uptake by zeolites modified with trivalent cations (M) occurs by substitution of fluoride for hydroxide ions in M-OH moieties within surface bound complexes.<sup>59,108</sup>

Though uncommon, reported studies into defluoridation by zeolites typically either evaluate the efficacy of fluoride uptake by a natural zeolite sample or a zeolite modified by surface sorption of trivalent metal-containing complexes. In studies on defluoridation by natural zeolites, little attention

is paid to understanding the mechanistic aspects of the process or which zeolite specific parameters may affect uptake; consequently, this has led authors to make unevidenced postulations on how fluoride interacts with the zeolite.

A comprehensive study has been undertaken into fluoride uptake by zeolite Y containing different intrapore cations to develop an understanding of how defluoridation by zeolites occurs. Equilibrium fluoride loadings have been measured by a fluoride ISE and adsorption isotherms have been applied to this data. Further to this, the post-fluoride treated zeolite has been characterised by techniques including MAS NMR spectroscopy to determine the local fluoride environment, a plausible mechanism for the reaction and how this is affected by the presence of different intrapore cations.

## 5.2 Experimental

### 5.2.1 NH<sub>4</sub>-Y, Na-Y and H-Y

Na-Y was obtained from Sigma-Aldrich (product 334448). NH<sub>4</sub>-zeolite Y (NH<sub>4</sub>-Y) was obtained from Alfa-Aesar (product 45863). H-Y was produced by calcination of NH<sub>4</sub>-Y at 550°C in air in a muffle furnace for 5 hours.

### 5.2.2 Synthesis of Dealuminated NH<sub>4</sub>-Y

Following the method first reported by Kerr,<sup>121</sup> dealuminated NH<sub>4</sub>-Y was produced by adding NH<sub>4</sub>-Y (3.34 g) to a slurry of ethylenediaminetetraacetic acid, H<sub>4</sub>EDTA, (1.60 g) in deionised water (50 ml). The zeolite-H<sub>4</sub>EDTA slurry was stirred vigorously at ambient temperature for 6 hours. The dealuminated zeolite was then recovered by vacuum filtration, washed copiously with deionised water and dried at 60°C overnight.

### 5.2.3 Preparation of $M_x(NH_4)_{1-2x}-Y$ and $M_xNa_{1-2x}-Y$ by Ion Exchange

Solutions of divalent metals (0.25 M) were made by dissolving the appropriate mass of the nitrate salt in deionised water (50 ml); the form of the nitrate salt, masses dissolved to make 0.25 M solutions (50 ml) and re-agent suppliers are listed in Table 5.1. The zeolite,  $NH_4-Y$  or  $Na-Y$ , (0.50 g) was added to the 0.25 M metal nitrate solution (50 ml) then placed in a Memmert WNB14 water bath equipped with a shaking attachment and shaken laterally at approximately 110 shakes per minute for 24 hours at 60°C. Following 24 hours and cooling to room temperature, the ion-exchanged zeolites were recovered by vacuum filtration, washed copiously with deionised water and dried overnight at 60°C.

Table 5.1. Metal salts, suppliers and masses used to make 0.25 M solutions.

Ion	Salt	Mass (g)	Supplier
$Mg^{2+}$	$Mg(NO_3)_2 \cdot 6H_2O$	3.21	Sigma Aldrich, 99%
$Ca^{2+}$	$Ca(NO_3)_2 \cdot 4H_2O$	2.95	Acros Organics, 99%
$Sr^{2+}$	$Sr(NO_3)_2$	2.65	Alfa Aesar, 99%
$Ba^{2+}$	$Ba(NO_3)_2$	3.27	Sigma Aldrich, 99%
$Cu^{2+}$	$Cu(NO_3)_2 \cdot 2.5H_2O$	2.91	Sigma Aldrich, 98%

### 5.2.4 Batch Fluoride Adsorption Measurements

Sodium fluoride solutions in the desired concentration range, 5 – 60 ppm  $F^-$ , were made by dilution of the appropriate volume of 1000 ppm  $F^-$  ( $1 \text{ g L}^{-1}$ ) NaF solution (Hanna Instruments, HI70701L) with deionised water in polypropylene volumetric flasks. Approximately 0.100 g of zeolite, weighed accurately to 3 decimal places, was added to the NaF solution (20 ml) of desired concentration in a polypropylene vessel (capacity = 60 ml, diameter = 28 mm). The solution and zeolite were added to a Memmert WNB14 water bath equipped with a shaking attachment and shaken laterally at approximately 110 shakes per minute for 24 hours at the specified temperature. Following 24 hours, 15 ml of the supernatant solution was decanted and added to 3 ml of TISAB-II buffer (Hanna

Instruments, HI401005L). The potential of the solution (mV) was measured with a calibrated fluoride ion-selective electrode (Cole Parmer) connected to a Hanna Instruments HI 3222 processor, calibrated across the range 1 – 100 ppm F<sup>-</sup> with standards (1, 10 and 100 ppm F<sup>-</sup>) made by serial dilution of 1000 ppm F<sup>-</sup> NaF solution. In instances where solution concentrations exceeding 100 ppm F<sup>-</sup> were measured, an additional 1000 ppm F<sup>-</sup> standard was also employed such that the probe was calibrated across the concentration range 1 - 1000 ppm F<sup>-</sup>. Standards were also measured in a 5:1 volume mixture with TISAB-II buffer. Solution fluoride concentrations were calculated from the appropriate calibration curve. Calibrant and analyte solutions were stirred while measured to ensure accurate readings. A blank measurement was employed for all analyte solutions of a given concentration to adjust for any adsorption to the vessel.

Equilibrium fluoride loadings ( $q_e$ ) per gram of the initial zeolite material (mg F<sup>-</sup> g<sup>-1</sup>) were calculated by Equation 5.1, in which  $c_0$  and  $c_e$  are the initial and equilibrium fluoride concentrations (mg L<sup>-1</sup>), respectively, as measured by a calibrated fluoride ISE. The term  $\rho$  in Equation 5.1 is calculated by Equation 5.2, where  $m$  is the initial mass of the zeolite (g) and  $v$  is the volume of the solution (L).

$$q_e = \frac{(c_0 - c_e)}{\rho} \quad (\text{Eq. 5.1})$$

$$\rho = m/v \quad (\text{Eq. 5.2})$$

#### 5.2.5 Batch Fluoride Adsorption Measurements for ICP-OES

Batch fluoride measurements for ICP-OES analysis of the supernatant solutions were performed in the manner described above in Section 5.2.4 with the following changes. Sodium fluoride solutions were made spanning the concentration range 5 – 60 ppm F<sup>-</sup> by dilution of 1000 ppm F<sup>-</sup> (1 g L<sup>-1</sup>) NaF solution (Hanna Instruments, HI70701L) with ultrapure water. Approximately 0.150 g of either zeolite H-Y or NH<sub>4</sub>-Y, weighed accurately to 3 decimal places, was added to each NaF solution of a given

concentration (30 ml). After 24 hours in the shaking water bath at 25°C, solutions were filtered through a 0.22 µm filter (Fisherbrand™). Aliquots of the filtered solution (15 ml) were added to TISAB-II buffer (3 ml); the fluoride concentration was then measured as described in Section 5.2.4. Separate aliquots of the filtered analyte solution (9.71 ml) were diluted and acidified by the addition of ultrapure 67 wt% HNO<sub>3</sub> solution (0.29 ml) supplied by VWR (Normatom®), rendering the final analyte solution 2 wt% HNO<sub>3</sub>.

#### 5.2.6 Preparation of Acidic Fluoride Solutions

1:1 HNO<sub>3</sub>:NaF solutions, in the range 5 – 60 ppm F<sup>-</sup>, were prepared by dilution of the appropriate amount of 1000 ppm F<sup>-</sup> (1 g L<sup>-1</sup>) NaF solution (Hanna Instruments, HI70701L) with deionised water, where the required amount of 0.1 M HNO<sub>3</sub> to render the final solution 1:1 HNO<sub>3</sub>:NaF was added during dilution (e.g. for a 250 ml solution with a 20 ppm F<sup>-</sup> concentration, 2.60 ml of 0.1 M HNO<sub>3</sub> was added during dilution). Batch adsorption experiments with Na-Y proceeded as described in Section 5.2.4 with the 1:1 HNO<sub>3</sub>:NaF solutions.

The pH adjustment of 60 ppm F<sup>-</sup> NaF solutions (100 ml) to pH 3.0, 3.5 and 4.1 was done by dropwise addition of 0.1 M HNO<sub>3</sub>. The pH was monitored by a HI1131 pH electrode coupled with a Hanna pH 211 Microprocessor pH meter.

#### 5.2.7 Powder X-ray Diffraction (PXRD)

PXRD was performed on a Bruker D8 Advance diffractometer, in reflection geometry, equipped with a Ni-filtered Cu K<sub>α</sub> X-ray source ( $\lambda = 1.5418 \text{ \AA}$ ) and fitted with a solid-state LynxEye position sensitive detector. PXRD patterns were recorded on finely ground samples mounted on silicon low background holders that were first covered in a thin layer of Vaseline. Unless otherwise stated in the discussion, scans were measured over the  $2\theta$  range 4 – 60° at a scan rate of 0.04° s<sup>-1</sup> with a 0.02° step-size. Phase

matching was performed in Bruker EVA software linked to the PDF 4+ database. All PDF stick plots are derived from the appropriate entry in the ICDD PDF 4+ database.<sup>83</sup> Lattice constants have been determined from unit cell refinements using Chekcell software,<sup>84</sup> based on peak positions identified in Bruker EVA software. All PXRD patterns were plotted in SigmaPlot.<sup>85</sup>

#### 5.2.8 X-ray Fluorescence Spectrometry (XRF)

XRF spectrometry was performed on a Bruker S8 Tiger spectrometer. All samples were measured as loose powders mounted on Mylar<sup>®</sup> film for the maximum 18-minute data collection time. Quantitative results were obtained from Bruker SPECTRA<sup>plus</sup> software.  $K_{\alpha}$  emission lines were used to quantify all elements, except for Sr, Ba and Cu which were instead quantified from  $L_{\alpha}$  emission lines. Elemental weight fractions for each sample measured by XRF spectrometry may be found in Appendix 5.

#### 5.2.9 Scanning Electron Microscopy (SEM)

Scanning electron micrographs were obtained on a Phillips XL30 ESEM FEG microscope at an accelerating voltage of 20 keV and a working distance of 10 mm. The imaged samples were mounted on graphite tape then sputter coated with a gold thin film, with a 20 nm approximate thickness, prior to imaging. All particle measurements were performed using ImageJ software.<sup>86</sup>

#### 5.2.10 Magic-Angle Spinning Nuclear Magnetic Resonance Spectroscopy (MAS NMR)

All NMR spectra were recorded by staff at the Solid-state NMR service at Durham University. Silicon-29 MAS NMR spectra were acquired using a Varian VNMRS spectrometer operating at 79.44 MHz for silicon, with a 6 mm MAS probe at a spin rate of approximately 6 kHz. Direct excitation spectra were obtained following a 90° pulse (4.3  $\mu$ s pulse duration and 12.7 ms acquisition time) and a recycle delay

of 240 s.  $^{29}\text{Si}\{^1\text{H}\}$  CP MAS NMR spectra were recorded using a 10 ms contact time and 1 s recycle delay. Chemical shifts in the  $^{29}\text{Si}$  MAS NMR spectra are referenced to tetramethylsilane ( $\text{SiMe}_4$ ). The framework Si/Al ratio of zeolite H-Y was calculated from deconvoluted integrals ( $I_{\text{Si}(n\text{Al})}$ ) for assigned peaks ( $\text{Si}(n\text{Al})$ ) by Equation 5.3.

$$\text{Si/Al} = \frac{\sum I_{\text{Si}(n\text{Al})}}{\sum 0.25nI_{\text{Si}(n\text{Al})}} \quad (\text{Eq. 5.3})$$

Fluorine-19 MAS NMR spectra were acquired using a Bruker Avance III HD spectrometer operating at 376.48 MHz, with a 3.2 mm MAS probe at a spin rate of 20 kHz. A rotor-synchronised Hahn-echo pulse sequence was employed to produce a flat baseline, as is standard practice when measuring  $^{19}\text{F}$  MAS NMR spectra to eliminate phasing errors which would otherwise contribute to background intensity.<sup>122</sup> The Hahn-echo pulse sequence comprised a pulse at angle ( $\pi/2$ ), followed by a delay ( $\tau_1$ ), then a further pulse at angle ( $\pi$ ) followed by another delay ( $\tau_2$ ), where  $\pi = 180^\circ$ ,  $\tau_1 = 45 \mu\text{s}$  and  $\tau_2 = 40 \mu\text{s}$ . The pulses at  $90^\circ$  and  $180^\circ$  lasted 3  $\mu\text{s}$  and 6  $\mu\text{s}$ , respectively. Chemical shifts in the  $^{19}\text{F}$  MAS NMR spectra were referenced to  $\text{CFCl}_3$ . All MAS NMR spectra were recorded at ambient temperature.

#### 5.2.11 Inductively Coupled Plasma Optical Emission Spectroscopy (ICP-OES)

ICP-OES analysis of Na concentrations was performed on a PerkinElmer OES Optima 8000 spectrometer. Calibrants, with concentrations 0.1, 1, 5, 10 and 100 ppm, were made by dilution of 1000 ppm Na standard solution (Centripur™) with ultrapure water. Ultrapure 67 wt%  $\text{HNO}_3$  solution (0.29 ml), supplied by VWR (Normatom®), was added to each calibrant solution (9.71 ml), such that each calibrant was acidified to ca. 2 wt%  $\text{HNO}_3$ , the same extent as the analyte solutions. A representative blank solution of ultrapure water (9.71 ml) was also acidified by addition of ultrapure 67 wt%  $\text{HNO}_3$  solution (0.29 ml).

### 5.2.12 Adsorption Isotherms

An introduction to adsorption isotherms, and their utility in understanding adsorption processes, is presented in Section 2.1.3. The Langmuir, Freundlich, Temkin and Dubinin-Radushkevitch (DR) isotherm equations and their linear forms as applied in this chapter, and as commonly applied to adsorption at the solid-liquid interface, are presented in Table 2.1.<sup>56,57</sup> The adsorption potential ( $\epsilon$ ) in the DR isotherm may be calculated by either Equation 2.10 or 2.11; in the DR isotherms plotted in this study the adsorption potential has been calculated using Equation 2.11.<sup>57,58</sup> The adsorbate solubility ( $c_s$ ) used in Equation 2.11 was calculated at each temperature employed using the equation presented by Reynolds and Belsher,<sup>123</sup> then converted to ppm F<sup>-</sup>. The adsorbate solubility values used are: 18803 ppm F<sup>-</sup> at 25°C and 19621 ppm F<sup>-</sup> at 40°C. The characteristic adsorption energy ( $E_c$ ) may be derived from the Dubinin-Radushkevitch constant ( $K$ ) by the relationship in Equation 2.12.<sup>59</sup> Linear regression analysis to determine  $R^2$ , the gradient and y-intercept for each plot was performed in Sigmaplot software.<sup>85</sup>

## 5.3 Results Part 1: Fluoride Uptake in H-Y, NH<sub>4</sub>-Y and Na-Y

### 5.3.1 Zeolite Characterisation

The influence of intrapore cation on fluoride uptake by the zeolite has been probed for zeolite Y containing Na<sup>+</sup> (Na-Y), NH<sub>4</sub><sup>+</sup> (NH<sub>4</sub>-Y) and H<sup>+</sup> (H-Y) intrapore cations. Commercially available Na-Y and NH<sub>4</sub>-Y were used in this study, whereas H-Y was synthesised by calcining NH<sub>4</sub>-Y in air at 550°C for 5 hours. PXRD patterns recorded for each zeolite, presented in Figure 5.1, demonstrate that each material is phase pure, containing only peaks attributable to zeolite Y. Table 5.2 contains the unit cell parameter and volumes derived from unit cell refinements by Chekcell,<sup>84</sup> which first indexed the pattern in the expected space group *Fd-3m*. Table 5.2 also presents bulk Si/Al ratios determined by XRF spectrometry, coupled with the associated error in the last figure expressed parenthetically. The bulk Si/Al ratio of Na-Y, NH<sub>4</sub>-Y and H-Y are all in agreement within error.

Table 5.2. Unit cell parameters, volumes and bulk Si/Al ratios for H-Y, NH<sub>4</sub>-Y and Na-Y.

	$a$ (Å)	$V$ (Å <sup>3</sup> )	Si/Al
NH <sub>4</sub> -Y	24.59(1)	14,869(18)	2.8(1)
H-Y	24.53(1)	14,724(18)	2.7(1)
Na-Y	24.71(1)	15,088(19)	2.7(1)

Synthesising H-Y by calcination of NH<sub>4</sub>-Y often leads to dealumination of the framework and subsequent formation of extra-framework aluminium species which remain within the zeolite pores.<sup>124</sup> Naturally, the extra-framework aluminium species contribute to the bulk Si/Al ratio of H-Y derived by XRF spectrometry. The <sup>29</sup>Si MAS NMR spectrum recorded for H-Y and deconvoluted integrals for assigned peaks are presented in Table 5.3 and Figure 5.2, respectively; a framework Si/Al ratio of 4.73 was calculated from the deconvoluted integrals, by Equation 5.2 in Section 5.2.10. The framework Si/Al ratio calculated from NMR attests that considerable extra-framework aluminium is present in the pores, as the bulk Si/Al ratio for H-Y (Si/Al = 2.7) is much lower.

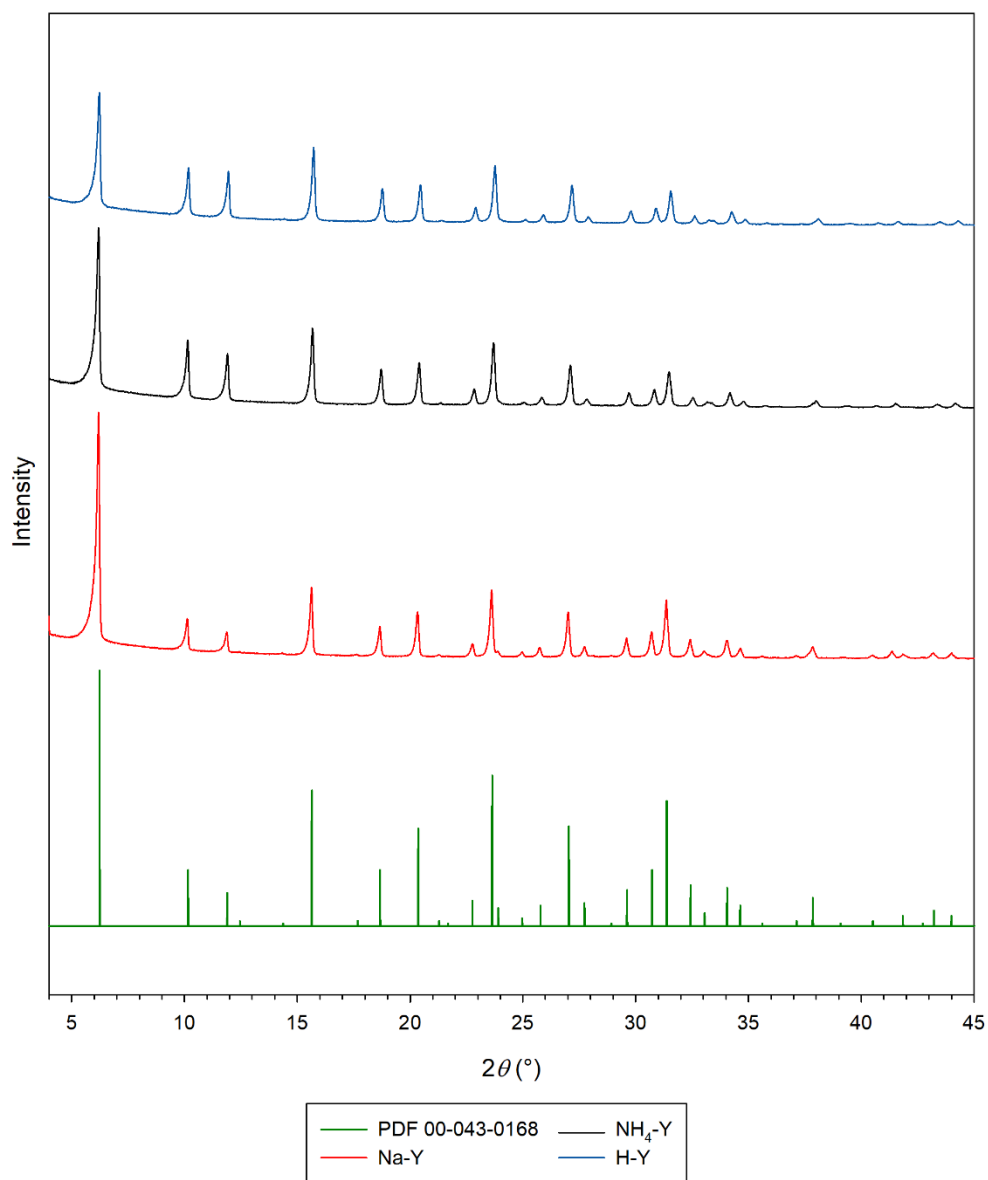


Figure 5.1. PXRD patterns of Na-Y (red), NH<sub>4</sub>-Y (black) and H-Y (blue), compared with a reference Na-Y pattern, PDF 00-043-0168 (green).

Table 5.3. Chemical shifts, relative peak areas and assignments for peaks in the <sup>29</sup>Si MAS NMR spectrum of H-Y.

$\delta$ (ppm)	Relative peak area (%)	Assignment
-106.8	45.2	Si(0Al)
-101.9	35.9	Si(1Al)
-97.0	16.9	Si(2Al)
-90.2	2.0	Si(3Al)

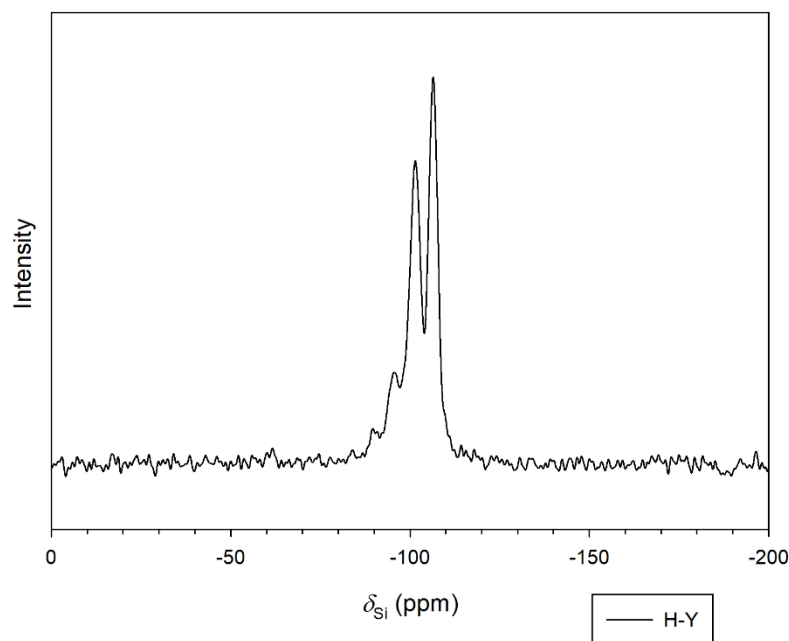


Figure 5.2.  $^{29}\text{Si}$  MAS NMR spectrum of H-Y.

SEM was employed to determine the particle sizes of the zeolite Y crystals used in this study; scanning electron micrographs of  $\text{NH}_4\text{-Y}$ , H-Y and Na-Y are presented in Figure 5.3.  $\text{NH}_4\text{-Y}$  comprises mostly aggregates of intergrown particles with irregular morphologies, although some discrete particles are also present in the sample. The larger discrete particles possess diameters in the range 0.9 – 1.3  $\mu\text{m}$ , whereas the smaller discrete particles have diameters between 0.3 – 0.6  $\mu\text{m}$ . Similarly, H-Y comprises discrete particles with similar diameters to the larger particles in  $\text{NH}_4\text{-Y}$  (0.9 – 1.3  $\mu\text{m}$ ). Aggregates are also present in H-Y, however, the individual intergrown particles within aggregates are less well defined, likely caused by sintering during calcination. In general, the particle morphology of Na-Y is similar to  $\text{NH}_4\text{-Y}$  and H-Y, however, the crystals are slightly larger. The largest crystals in the Na-Y sample have diameters between 1.3 - 1.8  $\mu\text{m}$ , whereas the smaller particles in the sample are between 0.6 – 0.9  $\mu\text{m}$ .

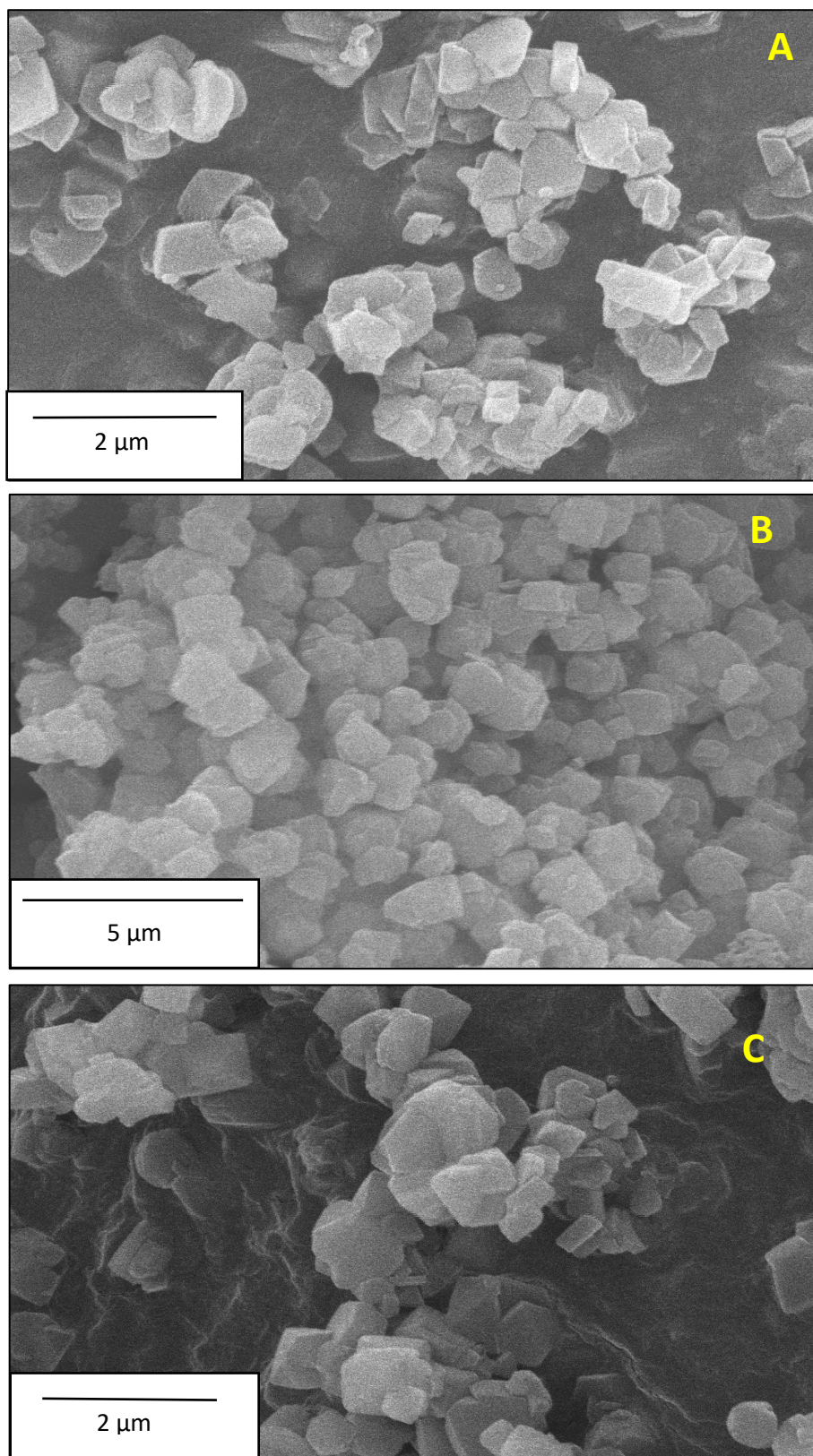


Figure 5.3. Scanning electron micrographs of (A) NH<sub>4</sub>-Y, (B) Na-Y and (C) H-Y.

### 5.3.2 Fluoride Loadings

Equilibrium fluoride loadings from low concentration sodium fluoride solutions (5 – 60 ppm F<sup>-</sup>) achieved by the zeolites, H-Y, NH<sub>4</sub>-Y and Na-Y, under isothermal conditions are plotted in Figure 5.4 as a function of the initial solution fluoride concentration. As described in Section 5.2.4, the zeolite samples were added to fluoride solutions, in the given concentration range, in a 0.10 g:20 ml mass to solution ratio and agitated laterally for 24 hours in a shaking water bath. The aqueous fluoride concentrations of the supernatant solution, following separation from the zeolite and addition of TISAB-II buffer, were measured with a fluoride ion-selective electrode calibrated across the range 1 – 100 ppm F<sup>-</sup>. Fluoride loadings from solution were calculated from Equation 5.1 in Section 5.2.4. The contact time for all solutions with the zeolite was 24 hours, loadings measured following 48 and 72 hours show negligible variation from those measured after 24 hours indicating that equilibrium is achieved by 24 hours of contact between the zeolite and solution.

The range of fluoride concentrations employed in this study, 5 – 60 ppm F<sup>-</sup>, was selected as fluoride uptake from low concentration solutions is of interest. Both H-Y and NH<sub>4</sub>-Y recorded high uptakes from 1 and 2 ppm F<sup>-</sup> solutions corresponding to between 70 - 90% of the total fluoride present; however, the resulting equilibrium fluoride concentrations are low and the relative error in the values is too great (5 – 10%) to accurately determine the concentration. The lower limit of detection for fluoride ion-selective electrodes (0.02 ppm) causes the high relative error in the measurement of solutions with concentrations below 0.5 ppm.<sup>73</sup> In contrast, the relative error in measurements from 5 ppm F<sup>-</sup> solutions with the same proportion of fluoride removed are much lower (*ca.* 1%), as the equilibrium fluoride concentration is greater. Uptake from solutions with concentrations below 5 ppm F<sup>-</sup> are not considered due to inaccuracies introduced by equilibrium concentrations approaching the lower limit of detection for fluoride ion-selective electrodes.

Changing the intrapore cation gives rise to markedly different equilibrium fluoride loadings across the concentration range (5 – 60 ppm F<sup>-</sup>). No detectable fluoride uptake is measured for Na-Y indicating

negligible fluoride adsorption on this zeolite. In contrast, fluoride uptake is observed for both H-Y and NH<sub>4</sub>-Y across the same concentration range under the same conditions, plotted in Figure 5.4. The fluoride loadings achieved by H-Y are greater than NH<sub>4</sub>-Y from solutions with the same concentration; moreover, loadings for both zeolites increase upon increasing the temperature from 25°C to 40°C.

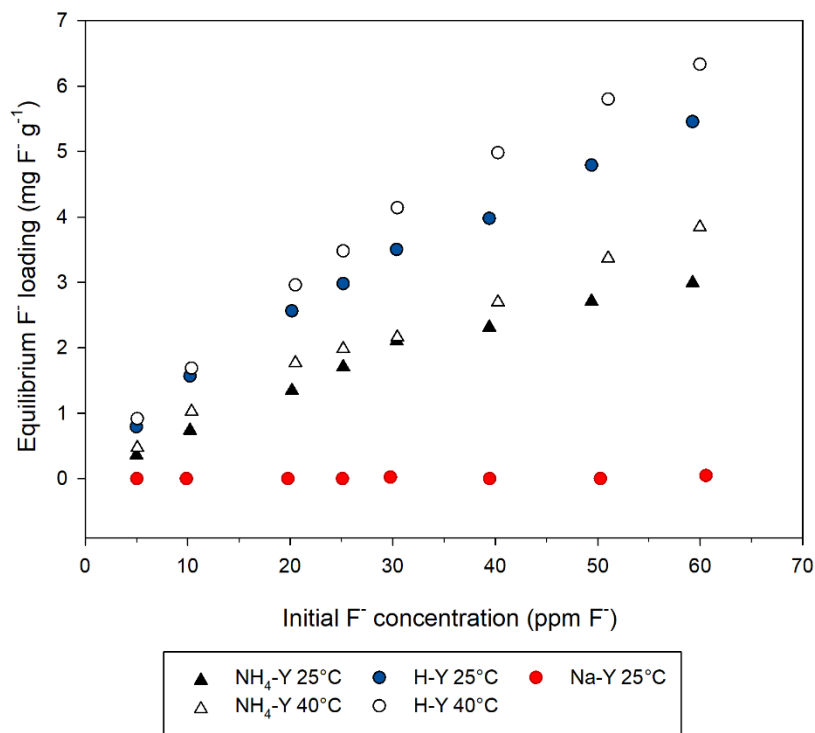


Figure 5.4. A plot of equilibrium fluoride loading ( $\text{mg F}^- \text{g}^{-1}$ ), by zeolites H-Y, NH<sub>4</sub>-Y and Na-Y, at different temperatures as a function of initial fluoride concentration ( $\text{ppm F}^-$ ).

### 5.3.3 The Role of Protons

While substantial fluoride uptake is observed for H-Y and NH<sub>4</sub>-Y, negligible uptake under the same conditions is observed for Na-Y. The NH<sub>4</sub>-Y and Na-Y employed possess similar particle sizes and bulk Si/Al ratios; the only obvious characteristic difference between the two zeolites is the nature of the intrapore cation. Unlike Na-Y, the intrapore cations in NH<sub>4</sub>-Y and H-Y are Brønsted acids; it would appear these acidic cations are critical to the interaction occurring between the zeolite and aqueous fluoride. While ammonium is a relatively weak Brønsted acid under standard aqueous conditions, the

acidity of the ion may be increased provided conducive conditions with a sufficient thermodynamic driving force for dissociation.<sup>125</sup> Ammonium ions are herein described as Brønsted acidic cations, in reference not to the dissociation of ammonium ions in aqueous solution, but to highlight that ammonium is a potential source of protons.

Measurement of the Na<sup>+</sup> concentrations in supernatant solutions by ICP-OES, following 24 hours of contact with the zeolite, confirms ion exchange is occurring between aqueous Na<sup>+</sup> ions and intrapore NH<sub>4</sub><sup>+</sup> or H<sup>+</sup> ions, in the case of NH<sub>4</sub>-Y and H-Y, respectively. Figure 5.5 presents a plot of equilibrium ion loading (mol g<sup>-1</sup>), for both fluoride and sodium, by each zeolite at 25°C as a function of initial fluoride concentration (ppm F<sup>-</sup>), where fluoride concentrations were determined by a fluoride ion-selective electrode and sodium concentrations were determined by ICP-OES of the same supernatant solutions; lines join the data points to add clarity in areas where they are proximal. The plot clearly shows that at each concentration for each zeolite, a higher sodium concentration is exchanged into the zeolite than the fluoride concentration that is adsorbed to it, hence the concentration of H<sup>+</sup> or NH<sub>4</sub><sup>+</sup> ions released by ion exchange is greater than the amount of fluoride adsorbed. Consequently, a stoichiometric equivalence of H<sup>+</sup> or NH<sub>4</sub><sup>+</sup> ions migrates to the surface upon ion exchange, where they may participate in the adsorption of aqueous fluoride onto the zeolite surface.

The pH of the NaF solutions employed are near-neutral, and decrease slightly over the concentration range, ranging from pH = 6.9 for 5 ppm F<sup>-</sup> NaF to pH = 6.7 for 60 ppm F<sup>-</sup> NaF. Consequently, the concentration of free H<sup>+</sup> ions in solution is significantly lower than the fluoride concentration. At 5 ppm F<sup>-</sup>, the fluoride concentration is 2000 times greater than the free H<sup>+</sup> concentration inferred from the measured pH (i.e. [F<sup>-</sup>]/[H<sup>+</sup>] = 2000), increasing further at 60 ppm F<sup>-</sup> to [F<sup>-</sup>]/[H<sup>+</sup>] = 15,000. Therefore, the only available stoichiometric source of protons to participate in a reaction between aqueous fluoride and the zeolite framework are the intrapore H<sup>+</sup> or NH<sub>4</sub><sup>+</sup> ions released from H-Y and NH<sub>4</sub>-Y, respectively, upon ion exchange with Na<sup>+</sup>.

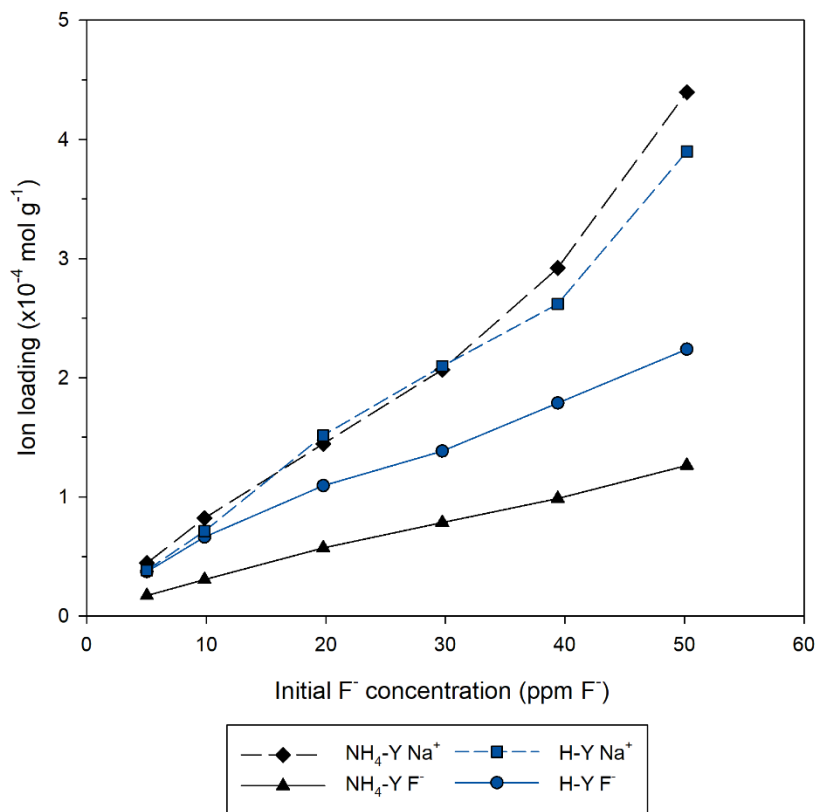


Figure 5.5. A plot of equilibrium ion loading ( $\text{mol g}^{-1}$ ,  $\text{Na}^+$  or  $\text{F}^-$ ), by each zeolite at  $25^\circ\text{C}$  as a function of initial fluoride concentration ( $\text{ppm F}^-$ ).

The influence of protons on fluoride uptake has been further demonstrated by measuring fluoride loadings from acidic solutions. The pH of 60 ppm  $\text{F}^-$  NaF solutions were reduced to 4.1, 3.5 and 3.0 by the addition of 0.1 M  $\text{HNO}_3$ ; fluoride loadings from these solutions by Na-Y, H-Y and  $\text{NH}_4$ -Y at  $25^\circ\text{C}$  were measured and the results are plotted in Figure 5.6. An increase in fluoride loading is observed for all zeolites upon lowering the pH from 6.7 to 4.1, with a further increase in loading upon reducing the pH to 3.5. In the case of  $\text{NH}_4$ -Y and Na-Y, a yet higher fluoride loading may be achieved at pH = 3.0; however, the fluoride loading attained for H-Y decreases upon lowering the pH from 3.5 to 3.0. Critically, fluoride uptake is observed for Na-Y in acidic media but not in near neutral solutions (pH = 6.7).

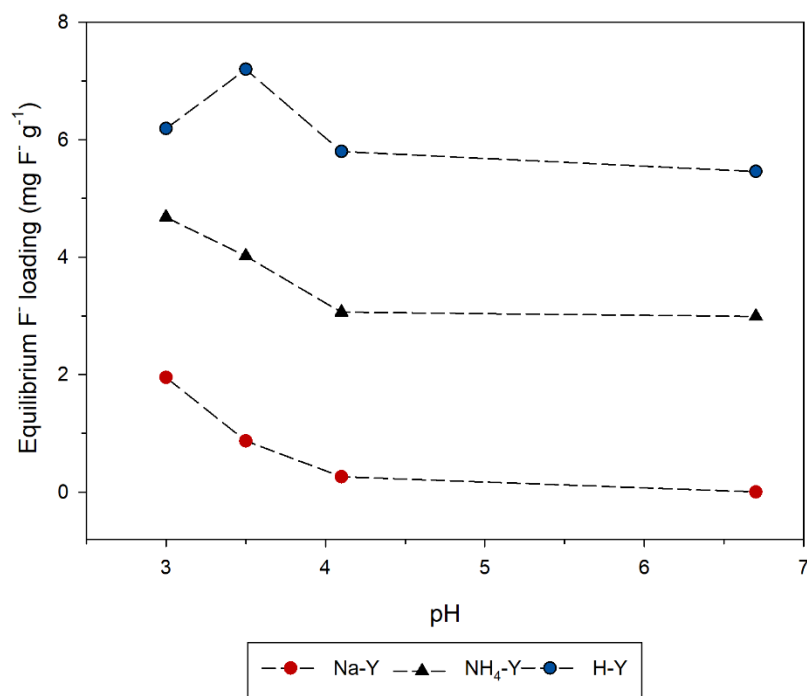


Figure 5.6. A plot of fluoride loading as a function of initial solution pH for zeolites H-Y, NH<sub>4</sub>-Y and Na-Y from 60 ppm F<sup>-</sup> solutions at 25°C.

Equilibrium fluoride loadings achieved by Na-Y measured from 1:1 NaF:HNO<sub>3</sub> solutions, that span the concentration range 5 – 60 ppm F<sup>-</sup>, are plotted in Figure 5.7, as well as the loadings measured from unadjusted NaF solutions for comparison. Quantifiable fluoride uptake by Na-Y in the presence of a stoichiometric equivalence of protons further supports the critical role that protons play in the sorption of fluoride from solution by zeolites, as no fluoride sorption is measured for the same zeolite under near-neutral conditions (pH = 6.7). The increase in fluoride loadings achieved by zeolites H-Y and NH<sub>4</sub>-Y under acidic conditions also lends further support for the critical role of protons. The nature of fluoride sorption has been further studied by applying adsorption isotherms to uptake data and probing the local environment in fluorinated zeolites with <sup>19</sup>F MAS NMR spectroscopy.

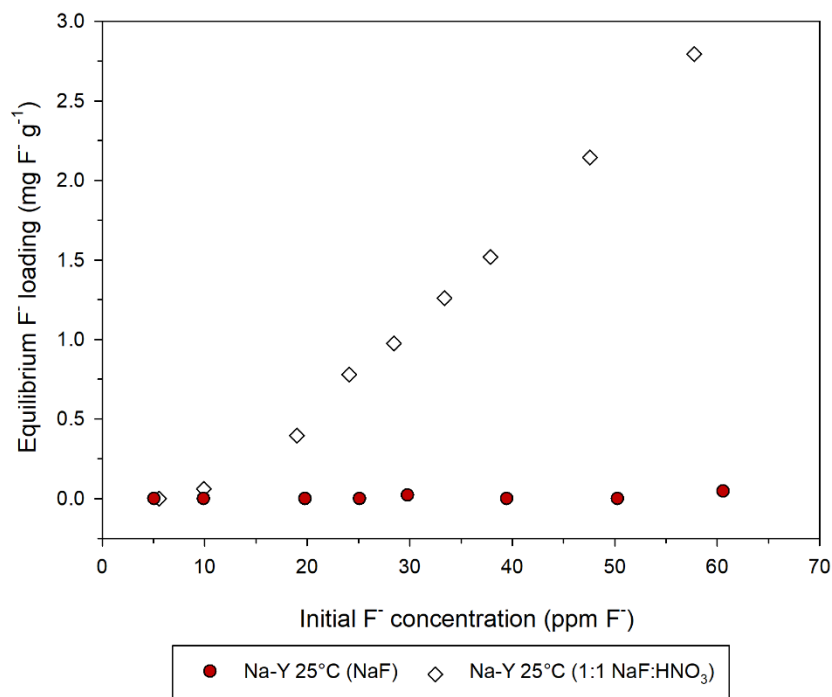


Figure 5.7. A plot of equilibrium fluoride loadings attained by Na-Y from 1:1 NaF:HNO<sub>3</sub> solutions as a function of initial fluoride concentration.

#### 5.3.4 H-Y and NH<sub>4</sub>-Y: Adsorption Isotherms

Equilibrium fluoride loadings ( $q_e$ ) and concentrations ( $c_e$ ), across the initial concentration range 5 – 60 ppm F<sup>-</sup>, for H-Y and NH<sub>4</sub>-Y at different temperatures have been fitted to the linear forms of the Freundlich, Langmuir, Temkin and Dubinin-Radushkevitch (DR) isotherms. The linear and non-linear forms of these equations as applied here, and as commonly applied to adsorption at the solid-liquid interface, are listed in Table 2.1 in Section 2.1.3. Additional information on the derivation of isotherm parameters may be found in Section 5.2.12. Fitting to the Langmuir, Temkin and Freundlich isotherms was tested as each models the influence of adsorbate-adsorbate interactions differently. Adsorbate-adsorbate interactions are not accounted for in the Langmuir model, by contrast in the Temkin isotherm the heat of adsorption decays linearly with increasing loading, and in the Freundlich isotherm the decay is assumed to be exponential rather than linear.<sup>57</sup> Fitting to the Dubinin-Radushkevitch

isotherm was also tested as the free energy of sorption may be calculated from the gradient which may provide greater insight into the nature of adsorption taking place.<sup>59</sup>

The results of fitting adsorption data for both H-Y and NH<sub>4</sub>-Y, at both 25 and 40°C, to the Freundlich, Temkin and Langmuir isotherms are summarised in Table 5.4, which contains  $R^2$  for each linear regression analysis and the Freundlich isotherm parameters ( $n$  and  $K_F$ ). Plots of fits to the Langmuir, Temkin and Freundlich isotherms are presented in Figures 5.8, 5.9 and 5.10, respectively. In general, despite reasonable  $R^2$  values ( $R^2 > 0.92$ ) that may indicate a good fit to the Temkin and Langmuir models, qualitative inspection of the plots shows a clear non-linear distribution of data points and these models are therefore a poor representation of the adsorptive process taking place.

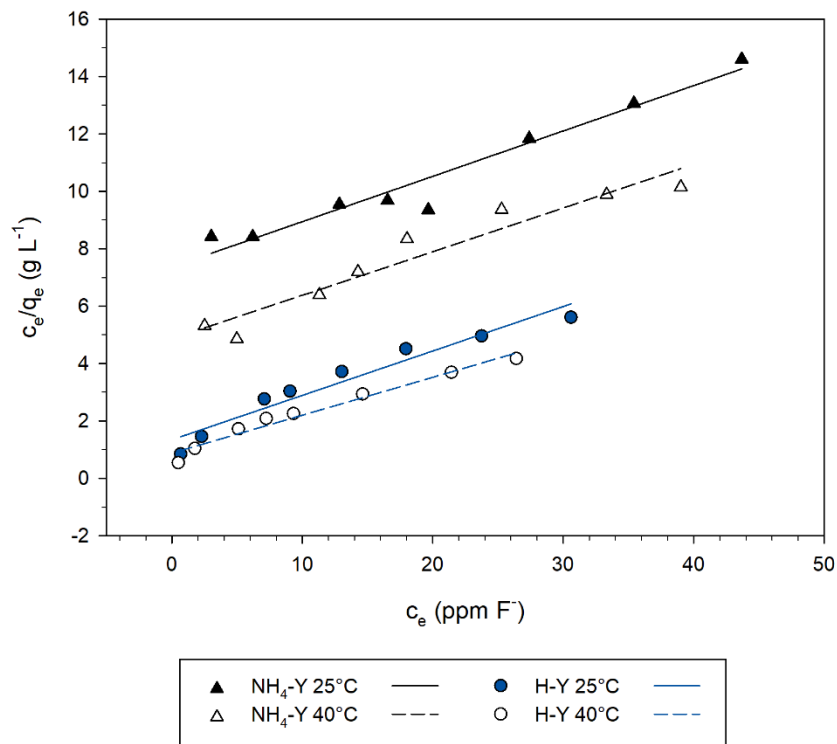


Figure 5.8. Langmuir plots for H-Y and NH<sub>4</sub>-Y at 25 and 40°C.

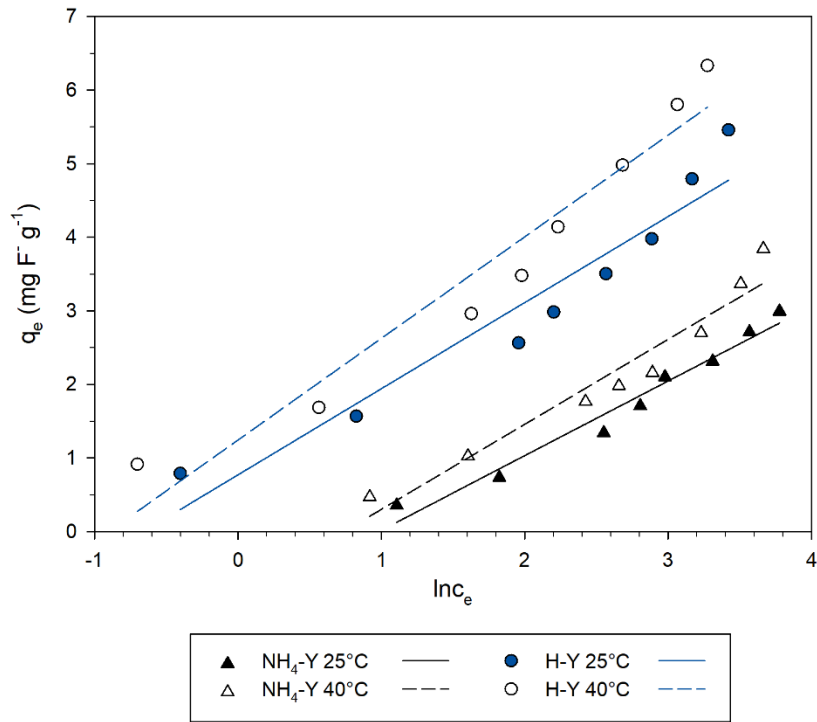


Figure 5.9. Temkin plots for H-Y and NH<sub>4</sub>-Y at 25 and 40°C.

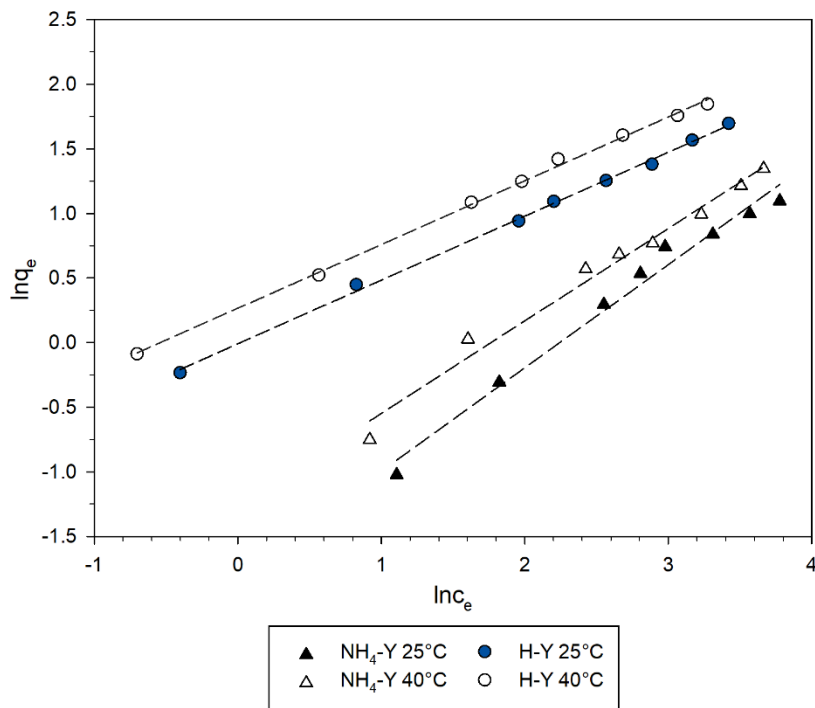


Figure 5.10. Freundlich plots for H-Y and NH<sub>4</sub>-Y at 25 and 40°C.

Table 5.4. Isotherm parameters and  $R^2$  for fits of equilibrium fluoride uptake data for H-Y and NH<sub>4</sub>-Y to the Freundlich, Temkin and Langmuir isotherms. The units of  $K_F$  are (mg g<sup>-1</sup>)/(mg L<sup>-1</sup>)<sup>n</sup>.

Zeolite	Temp. (°C)	Freundlich			Temkin	Langmuir
		$R^2$	$K_F$	$n$	$R^2$	$R^2$
H-Y	25	0.998	0.99	0.495	0.923	0.943
	40	0.998	1.31	0.494	0.940	0.970
NH <sub>4</sub> -Y	25	0.982	0.17	0.800	0.968	0.950
	40	0.982	0.28	0.716	0.939	0.931

Fitting adsorption data for both H-Y and NH<sub>4</sub>-Y, at both temperatures, to the Freundlich isotherm results in good fits, with  $R^2 > 0.98$  in all cases. The adsorption co-efficient,  $K_F$ , increases with the strength of adsorption, whereas the exponent,  $n$ , is a measure of favourability which decreases with increasing favourability. A trend is observed in both  $K_F$  and  $n$  values, where H-Y at 40°C has the greatest value of  $K_F$  and the lowest value of  $n$ , indicating adsorption is the most favourable in this case. This is followed by H-Y at 25°C, then NH<sub>4</sub>-Y at 40°C, and finally NH<sub>4</sub>-Y at 25°C which has the highest  $n$  and lowest  $K_F$  value. Based on the isotherm parameters of the Freundlich model, the strength of adsorption, and favourability of the process, appears to be greater for H-Y than NH<sub>4</sub>-Y, and increases for both upon raising the temperature from 25°C to 40°C.

Good fits to the linear DR equation are observed for both zeolites at each temperature, with  $R^2 > 0.988$  in each case (plots presented in Figure 5.11 and isotherm parameters and  $R^2$  values from the fits are tabulated in Table 5.5). Although data was fitted to the DR equation with the adsorption potential ( $\epsilon$ ) in the form presented in Equation 2.11, if the form of the adsorption potential in Equation 2.10 is used instead, the gradient,  $R^2$  and y-intercept obtained from linear regression analysis are all equivalent, to 3 significant figures, to those observed for Equation 2.11.

Table 5.4.  $R^2$ , isotherm parameters and  $E_c$  for fits to the linear Dubinin-Radushkevitch equation.

Zeolite	Temperature (°C)	$R^2$	$E_c$ (kJ mol <sup>-1</sup> )	$K$ (x10 <sup>-3</sup> mol <sup>2</sup> /kJ <sup>2</sup> )	$V_0/V_m$
H-Y	25	0.995	10.2	4.83	17.2
	40	0.997	10.9	4.24	21.8
NH <sub>4</sub> -Y	25	0.992	7.5	8.85	24.0
	40	0.989	8.5	7.00	23.4

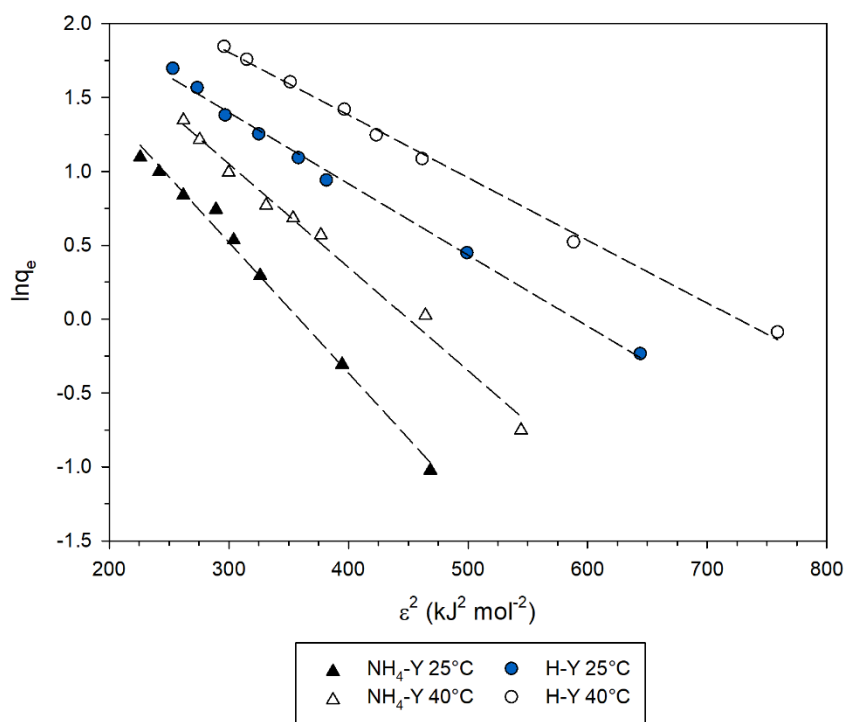


Figure 5.11. Plot of adsorption data fitted to the linear DR equation for H-Y and NH<sub>4</sub>-Y.

The DR isotherm is arguably the most informative model commonly applied to adsorption from solution as it permits the accurate determination of the free energy of sorption ( $E_c$ ), also termed the characteristic adsorption energy, providing good fits are observed. The magnitude of  $E_c$  is often used to determine the strength and nature of adsorption occurring. In instances where  $E_c < 8$  kJ mol<sup>-1</sup>, adsorption is attributed to physical adsorption; in contrast, values in the range  $8 < E_c < 16$  kJ mol<sup>-1</sup> are often ascribed to chemical adsorption.<sup>59</sup> The values of  $E_c$  calculated from the gradient ( $K$ ) by the

relationship,  $E_c = 2K^{-0.5}$ , are presented in Table 5.5. The magnitude of  $E_c$  for H-Y, at both 25 and 40°C, indicates chemisorption is the dominant mode of adsorption taking place, intimating a chemical bond is being formed between fluoride and the zeolite H-Y.

The free energy of sorption,  $E_c$ , for NH<sub>4</sub>-Y at 40°C (8.5 kJ mol<sup>-1</sup>) indicates chemisorption is taking place; however, at 25°C the value of  $E_c$  for NH<sub>4</sub>-Y (7.5 kJ mol<sup>-1</sup>) falls below 8 kJ mol<sup>-1</sup>, which by convention demarcates physical and chemical adsorption. Although the magnitude of  $E_c$  indicates fluoride interacts by physisorption to NH<sub>4</sub>-Y at 25°C, as chemisorption appears to occur at 40°C for the same adsorbent, 2 different interactions occurring separated by a narrow temperature range seems infeasible. Indeed, solid state NMR of NH<sub>4</sub>-Y fluorinated at 25°C, detailed later (Section 5.3.5, Figure 5.13), shows fluoride reacts with, and forms a chemical bond to, the zeolite framework. Ultimately, the 8 kJ mol<sup>-1</sup> value should be viewed as a guideline and the value of  $E_c$  at 25°C reflects the lower favourability of the reaction at lower temperatures, rather than a weaker interaction with the adsorbent.

### 5.3.5 <sup>19</sup>F MAS NMR spectroscopy

<sup>19</sup>F MAS NMR spectroscopy has been employed to determine the chemical environment of fluoride ions in fluorinated H-Y and NH<sub>4</sub>-Y, herein referred to as H-Y(F) and NH<sub>4</sub>-Y(F), respectively. To enhance the fluoride content in the zeolites analysed by MAS NMR, H-Y(F) and NH<sub>4</sub>-Y(F) were fluorinated by contact with 200 ppm F<sup>-</sup> NaF solutions for 24 hours at 25°C. Fluoride loadings of 29 and 20 mg F<sup>-</sup> g<sup>-1</sup> were measured for H-Y and NH<sub>4</sub>-Y, respectively, by a fluoride ISE calibrated across the range 1 – 1000 ppm F<sup>-</sup>.

The <sup>19</sup>F MAS NMR spectra for H-Y(F) (Figure 5.12) and NH<sub>4</sub>-Y(F) (Figure 5.13) contain 3 distinct resonances at  $\delta_F \approx -119, -153$  and  $-176$  ppm. The spectrum for H-Y(F) was recorded at spin rates of 20 and 18 kHz to differentiate centrebands from spinning sidebands, as centrebands do not change

position with changing spin rate unlike spinning sidebands. Upon changing the spin rate, the 3 resonances at  $\delta_F \approx -119$ ,  $-153$  and  $-176$  ppm did not change position; however, signal in the spectrum recorded both upfield from  $-180$  ppm and downfield from  $-115$  ppm fluctuated with differing spin rate, indicating that all intensity outside the range  $-115$  to  $-180$  ppm is produced by spinning sidebands. The spectra recorded at each spin rate may be found in Appendix 2.

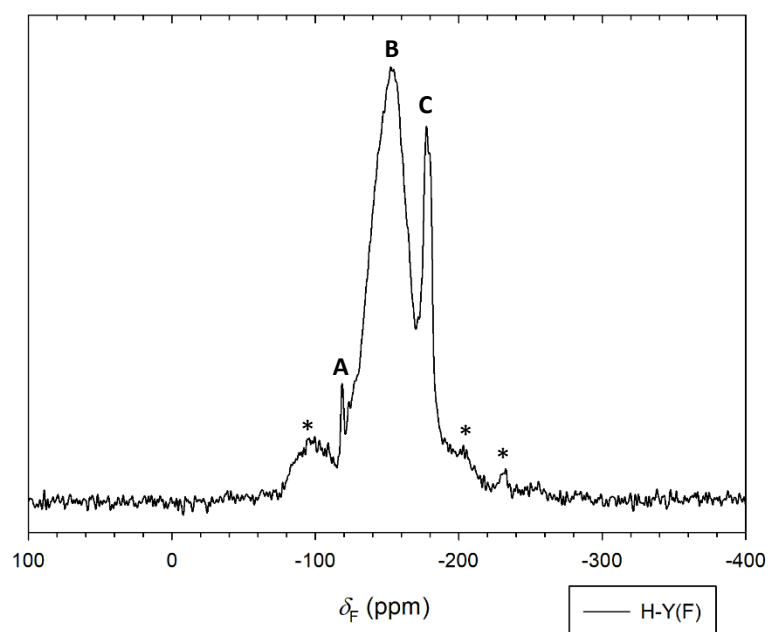


Figure 5.12.  $^{19}\text{F}$  MAS NMR spectrum for H-Y(F). Spinning sidebands are indicated by a \*.

Resonances in  $^{19}\text{F}$  MAS NMR spectra associated with  $[\text{SiO}_3\text{F}]$  groups in zeolites, and related materials, often occur at a chemical shift between  $-151$  to  $-153$  ppm.<sup>111-114,117</sup> The same moiety produces a resonance slightly downfield in amorphous silicas at  $\delta_F \approx -146$  ppm. Cross polarisation experiments have validated the assignment of this peak to  $[\text{SiO}_3\text{F}]$  groups.<sup>126</sup> In the  $^{19}\text{F}$  MAS NMR spectra recorded on both H-Y(F) and  $\text{NH}_4\text{-Y(F)}$ , the resonances labelled **B** at  $\delta_F \approx -153$  ppm are most likely produced by  $[\text{SiO}_3\text{F}]$  groups.

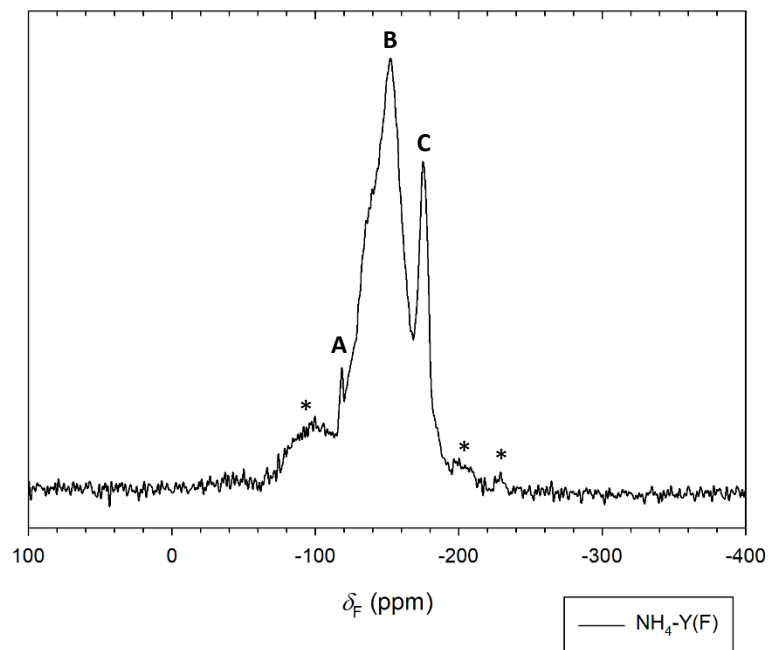


Figure 5.13.  $^{19}\text{F}$  MAS NMR spectrum for  $\text{NH}_4\text{-Y(F)}$ . Spinning sidebands are indicated by a \*.

Five co-ordinate species containing a Si-F bond,  $[\text{SiO}_4\text{F}]$ , in fluorinated zeolites, or in zeolites synthesised in fluoride media, produce resonances at  $\delta_{\text{F}} \approx -145$  ppm in  $^{19}\text{F}$  MAS NMR spectra. A resonance at this chemical shift could be masked by the broad  $[\text{SiO}_3\text{F}]$  resonance in both fluorinated zeolites, H-Y(F) and  $\text{NH}_4\text{(F)}$ . In the  $^{29}\text{Si}$  MAS NMR spectrum of H-Y(F), Figure 5.2, no discernible intensity is present in the region where resonances for five co-ordinate silicon would be anticipated, at chemical shifts in the range -125 to -150 ppm.<sup>127</sup> Moreover, in  $^{29}\text{Si}\{^1\text{H}\}$  CP MAS NMR performed on  $\text{NH}_4\text{-Y(F)}$ , detailed later in Section 5.3.6 and Figure 5.15, there are also no peaks in the region expected for five co-ordinate silicon. While there are no peaks in the  $^{29}\text{Si}$  MAS NMR spectra of the fluorinated zeolites in the region that would correspond to five co-ordinate silicon, this may be because the population of silicon in the environment is too low to give rise to a discernible signal. Ultimately, it is unclear if the  $[\text{SiO}_4\text{F}]$  moiety is present in H-Y(F) and  $\text{NH}_4\text{(F)}$ .

Peak **B** has an asymmetric profile in both spectra. Peak fitting indicates there may be an additional resonance at  $\delta_{\text{F}} \approx -135$  ppm in both spectra (Appendix 2); however, this does not account for all the observed peak asymmetry. Discussions on the possible origins of a resonance at  $\delta_{\text{F}} \approx -135$  ppm are presented later in Section 5.4.5. Asymmetry in the profile of the resonance at  $\delta_{\text{F}} \approx -153$  ppm may be

indicative of multiple signals in the region giving rise to one unresolved peak. Several signals resulting from  $[\text{SiO}_3\text{F}]$  moieties could be expected in the  $^{19}\text{F}$  MAS NMR spectra on account of the four observed silicon environments in the  $^{29}\text{Si}$  MAS NMR spectra of both H-Y (Fig. 5.2) and  $\text{NH}_4\text{-Y}$  (Fig. 5.15, Section 5.3.6).

Resonances with the same chemical shift as the peaks labelled **C** at  $\delta_{\text{F}} \approx -176$  ppm have been observed in a previous study on H-Y fluorinated by incipient wetness impregnation followed by high temperature treatment.  $^{27}\text{Al}$  NMR experiments, including 2D NMR, in the study demonstrated the resonance was produced by fluorine atoms bonded to 4 co-ordinate aluminium atoms, i.e.  $[\text{AlO}_3\text{F}]$ .<sup>118</sup> Resonances **C** at  $\delta_{\text{F}} \approx -176$  ppm in both H-Y(F) and  $\text{NH}_4\text{-Y(F)}$  may therefore be assigned to  $[\text{AlO}_3\text{F}]$  species in the fluorinated zeolites.

The low intensity resonances labelled **A** at  $\delta_{\text{F}} \approx -119$  ppm in both the H-Y(F) and  $\text{NH}_4\text{-Y(F)}$  spectra occur at a chemical shift often associated with fluoride ions within zeolite pores, but not within a cage, and charge compensated by an intrapore cation.<sup>117,118,128,129</sup> In  $^{19}\text{F}$  NMR spectra, aqueous fluoride in sodium fluoride solutions produces a resonance at  $\delta_{\text{F}} \approx -122$  ppm,<sup>130</sup> similar to the chemical shift observed for fluoride within zeolite pores, and unsurprising as the anticipated environment of both would comprise hydrated fluoride ions. The charge on each intrapore fluoride anion must be compensated by an additional intrapore cation which would be expected to migrate simultaneously into the framework with the fluoride anion.

In  $^{19}\text{F}$  MAS NMR spectra recorded on fluorinated zeolites and related materials, peaks within the range -122 to -130 ppm may be attributed to fluoride in hexafluorosilicate anions,  $\text{SiF}_6^{2-}$ , produced by desilication of the zeolite.<sup>111-113</sup> Hexafluorosilicates produce a resonance at  $\delta_{\text{Si}} \approx -189$  ppm in  $^{29}\text{Si}$  MAS NMR spectra,<sup>131</sup> yet there is no intensity in this region in the  $^{29}\text{Si}$  MAS NMR spectrum of H-Y (Figure 5.2) and the  $^{29}\text{Si}\{^1\text{H}\}$  CP MAS NMR spectrum of  $\text{NH}_4\text{-Y}$  (Figure 5.15). Moreover, the solubility of  $(\text{NH}_4)_2\text{SiF}_6$  and  $\text{Na}_2\text{SiF}_6$  are sufficiently high that if any were produced, it would be soluble and likely not remain in the solid product following washing during recovery.<sup>132</sup> Ultimately, it is unlikely that the peaks at

$\delta_F \approx -119$  ppm in the  $^{19}\text{F}$  MAS NMR spectra of both H-Y(F) and  $\text{NH}_4\text{-Y(F)}$  are caused by hexafluorosilicate anions.

The dominant resonances in the  $^{19}\text{F}$  MAS NMR spectra of H-Y(F) and  $\text{NH}_4\text{-Y(F)}$  may be assigned to  $[\text{SiO}_3\text{F}]$  and  $[\text{AlO}_3\text{F}]$  moieties in the zeolite. The presence of these moieties following fluorination further supports that fluoride interacts by “chemical adsorption”, reacting with the zeolite framework, as indicated previously by adsorption energies derived from fitting to the Dubinin-Radushkevitch isotherm. Indeed, the presence of these environments in  $\text{NH}_4\text{-Y(F)}$ , fluorinated at  $25^\circ\text{C}$  confirms that chemisorption is occurring despite the lower than expected  $E_c$  value. It appears the presence of extra-framework aluminium species within H-Y do not affect the interaction between the zeolite and fluoride, as the  $^{19}\text{F}$  MAS NMR spectra for both H-Y(F) and  $\text{NH}_4\text{-Y(F)}$  contain the same resonances. Peak fitting indicates a further resonance may be present in both spectra at  $\delta_F \approx -135$  ppm. Fluorine-19 MAS NMR has also revealed the migration of small quantities of NaF ion-pairs into the zeolite, as evidenced by the resonance attributed to intrapore fluoride anions.

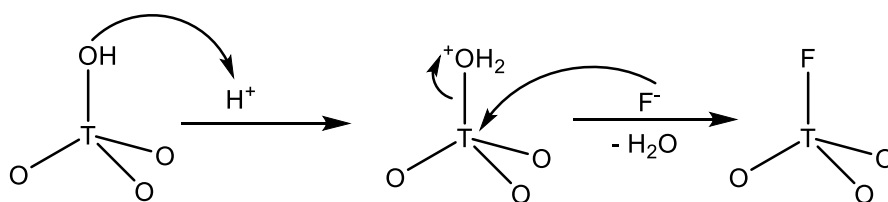
### 5.3.6 Fluorination Mechanism

Assignments in the MAS NMR spectra of H-Y(F) and  $\text{NH}_4\text{-Y(F)}$  indicate that fluoride reacts with the zeolite framework to form  $[\text{SiO}_3\text{F}]$  and  $[\text{AlO}_3\text{F}]$  moieties. The acid mediated fluorination of zeolite frameworks to produce these moieties may proceed by two plausible mechanisms, illustrated in Figure 5.14. Mechanism 1 depicts the substitution of fluoride at surface hydroxyl groups (either silanol or aluminol) proceeding by the protonation of the hydroxyl group to produce a more favourable “leaving group” in an E1 type elimination of water, enabling fluoride to form a bond to silicon or aluminium. A subtle difference in the by-product would arise depending on if the acid source is a  $\text{H}^+$  or  $\text{NH}_4^+$  ion. In the case of  $\text{H}^+$ , the proton is consumed in the formation of water, the only by-product in this instance. In contrast when the acid source is  $\text{NH}_4^+$ , aqueous  $\text{NH}_3$  is a further by-product in addition to water. The reaction could be considered to produce ammonium hydroxide; however, the

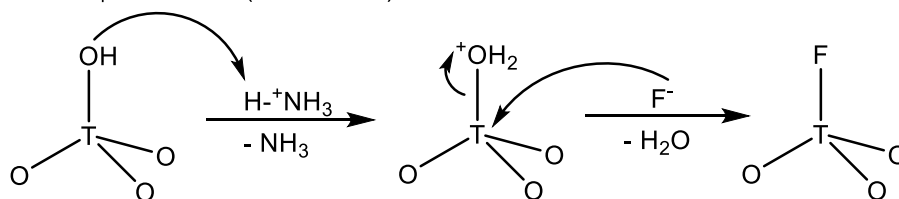
position of equilibrium in solutions of ammonium hydroxide favours ammonia and water with very few free hydroxide and ammonium ions present.<sup>125</sup> The production of  $\text{NH}_4^+$  in the reaction would render  $\text{NH}_4^+$  catalytic in the fluorination reaction; however the very low concentrations of  $\text{NH}_4^+$  expected in solution compared with  $\text{NH}_3$  would limit the ability of  $\text{NH}_4^+$  to participate in further fluorination reactions.

### Mechanism 1

$\text{H}^+$ -mediated (T = Si or Al)



$\text{NH}_4^+$ -mediated (T = Si or Al)



### Mechanism 2

(T = Si or Al)

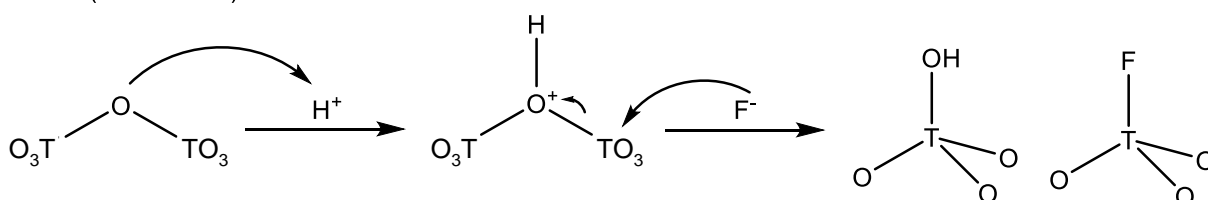


Figure 5.14. Proposed mechanisms for the fluorination of zeolite frameworks.

Alternatively, the addition of  $\text{H}^+\text{F}^-$  ion-pairs across T-O-T bonds could also lead to fluorination of the framework as illustrated in mechanism 2 in Figure 5.14. There are 2 critical differences in the products of mechanism 1 and 2. Firstly, mechanism 2 would be destructive to the framework, whereas mechanism 1 would not. Secondly, mechanism 1 would lead to a commensurate decrease in surface hydroxyl moieties with increasing fluoride loading. In contrast, the reaction proceeding by mechanism

2 would lead to a corresponding increase in T-OH concentration with increasing fluoride loading. This distinction may be exploited to determine which mechanism is occurring by employing  $^{29}\text{Si}\{^1\text{H}\}$  cross-polarised MAS NMR (CP MAS NMR) to analyse the fluorinated zeolites. An introduction to the working principles of CP MAS NMR spectroscopy is given in Section 2.2.4.4. A background to the interpretation of  $^{29}\text{Si}$  MAS NMR spectra recorded on zeolites and the associated nomenclature for discussing chemical environments may be found in Section 2.2.4.5.

In the  $^{29}\text{Si}$  MAS NMR spectra of zeolites,  $\text{Q}^3 \text{Si}(n\text{Al})$  resonances typically appear at a chemical shift a few ppm downfield of the corresponding  $\text{Q}^4 \text{Si}(n\text{Al})$  resonance; consequently,  $\text{Q}^3 \text{Si}(n-1\text{Al})$  resonances often appear co-incident with  $\text{Q}^4 \text{Si}(n\text{Al})$  resonances.<sup>70</sup> In  $^{29}\text{Si}\{^1\text{H}\}$  CP MAS NMR, magnetisation is transferred from the  $^1\text{H}$  nuclei in the silanol moieties, and intrapore water molecules, to the  $^{29}\text{Si}$  nuclei, enhancing the signal. As silanol moieties are bonded to  $\text{Q}^3$  silicon, with the exception of geminal silanol moieties, the intensity of  $\text{Q}^3$  silicon resonances are enhanced in  $^{29}\text{Si}\{^1\text{H}\}$  CP MAS NMR spectra. As all resonances assigned to  $\text{Q}^4 \text{Si}(n\text{Al})$ , except  $\text{Si}(0\text{Al})$ , will also have some  $\text{Q}^3 \text{Si}(n-1\text{Al})$  contribution, comparing changes in peak intensity in  $^{29}\text{Si}\{^1\text{H}\}$  CP MAS NMR spectra between the parent material and fluorinated derivative may intimate by which mechanism the reaction proceeds. Figure 5.15 depicts the  $^{29}\text{Si}\{^1\text{H}\}$  CP MAS NMR spectra of  $\text{NH}_4\text{-Y}$  and  $\text{NH}_4\text{-Y}(\text{F})$ , where intensity has been normalised such that the intensities of the  $\text{Si}(0\text{Al})$  peaks are equivalent in both spectra to allow comparisons on differing intensities in the other peaks. Peak positions of the assigned resonances in the  $^{29}\text{Si}\{^1\text{H}\}$  CP MAS NMR spectra are tabulated in Table 5.6. A decrease in the intensity of the  $\text{Si}(1\text{Al})$  and  $\text{Si}(2\text{Al})$  peaks is apparent for  $\text{NH}_4\text{-Y}(\text{F})$ , compared with the parent material  $\text{NH}_4\text{-Y}$ , indicating the silanol concentration decreases following fluorination, and therefore the reaction proceeds by mechanism 1, the substitution of fluoride at surface T-OH moieties.

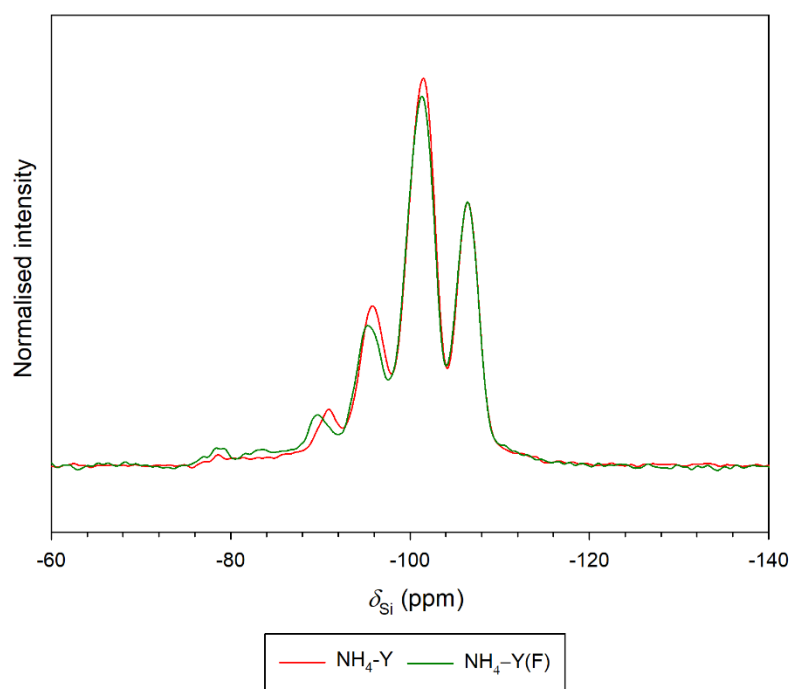


Figure 5.15. Normalised  $^{29}\text{Si}\{^1\text{H}\}$  CP MAS NMR spectra for  $\text{NH}_4\text{-Y}$  and  $\text{NH}_4\text{-Y(F)}$ .

Table 5.6. Chemical shifts for peaks in the  $^{29}\text{Si}\{^1\text{H}\}$  CP MAS NMR spectra for  $\text{NH}_4\text{-Y}$  and  $\text{NH}_4\text{-Y(F)}$ .

$\text{Q}^4$ peak assignment	$\delta_{\text{Si}}$ (ppm) for $\text{NH}_4\text{-Y}$	$\delta_{\text{Si}}$ (ppm) for $\text{NH}_4\text{-Y(F)}$
Si(0Al)	-106.5	-106.5
Si(1Al)	-101.5	-101.4
Si(2Al)	-95.9	-95.3
Si(3Al)	-91.0	-89.7

$^{29}\text{Si}\{^1\text{H}\}$  CP MAS NMR spectra were recorded for H-Y and H-Y(F), however, there was no significant difference in the peak intensities upon cross-polarisation. The spectra may be found in Appendix 2. The higher concentration of silanol functional groups in H-Y, caused by dealumination during heat treatment, compared with  $\text{NH}_4\text{-Y}$  would render the changes in intensity much smaller upon cross-polarisation. Accordingly, the technique may become insufficiently sensitive for the changes in silanol concentration to be discernible. It is assumed given that reactivity between H-Y and  $\text{NH}_4\text{-Y}$  with aqueous fluoride produces the same fluoride environments, the mechanism by which fluoride reacts is also the same in zeolite H-Y.

### 5.3.7 Na-Y in 1:1 NaF:HNO<sub>3</sub> Solutions: Adsorption Isotherms

Adsorption isotherms have been applied to the equilibrium fluoride uptake data collected for Na-Y in 1:1 NaF:HNO<sub>3</sub> solutions over the range 20 – 60 ppm F<sup>-</sup> at 25°C; fits to the Temkin, Freundlich and Dubinin-Radushkevitch isotherms are presented in Figures 5.16, 5.17 and 5.18, respectively. A poor fit to the Langmuir isotherm (Appendix 1) is observed over the concentration range with  $R^2 = 0.686$ . In contrast, reasonably good fits are observed for the Temkin ( $R^2 = 0.968$ ), Freundlich ( $R^2 = 0.973$ ) and Dubinin-Radushkevitch ( $R^2 = 0.978$ ) isotherms. In calculating  $\epsilon$  for the DR isotherm, it was assumed that the solubility of sodium fluoride is equivalent under these conditions to the solubility in deionised water.

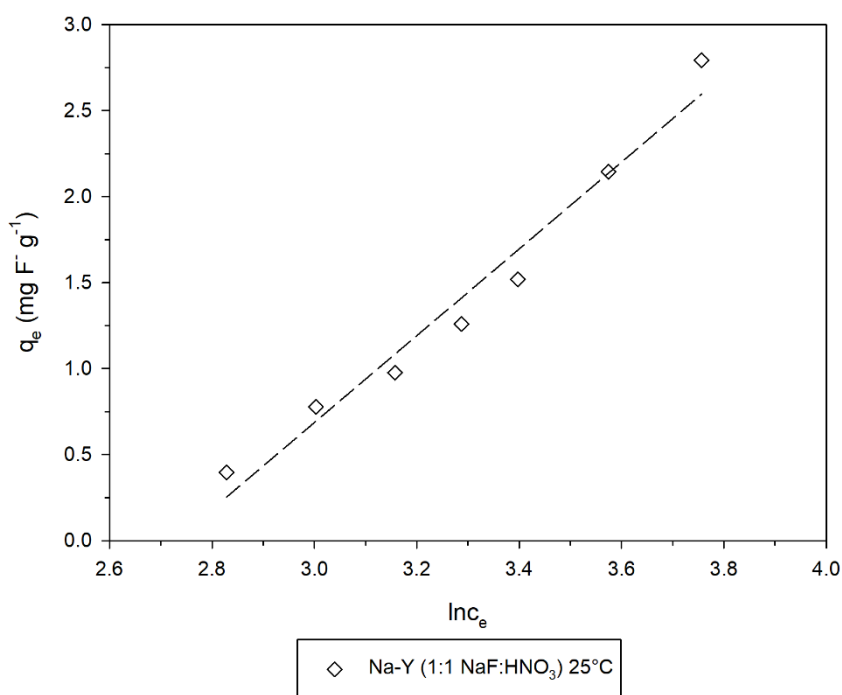


Figure 5.16. Temkin plot for Na-Y in 1:1 NaF:HNO<sub>3</sub>.

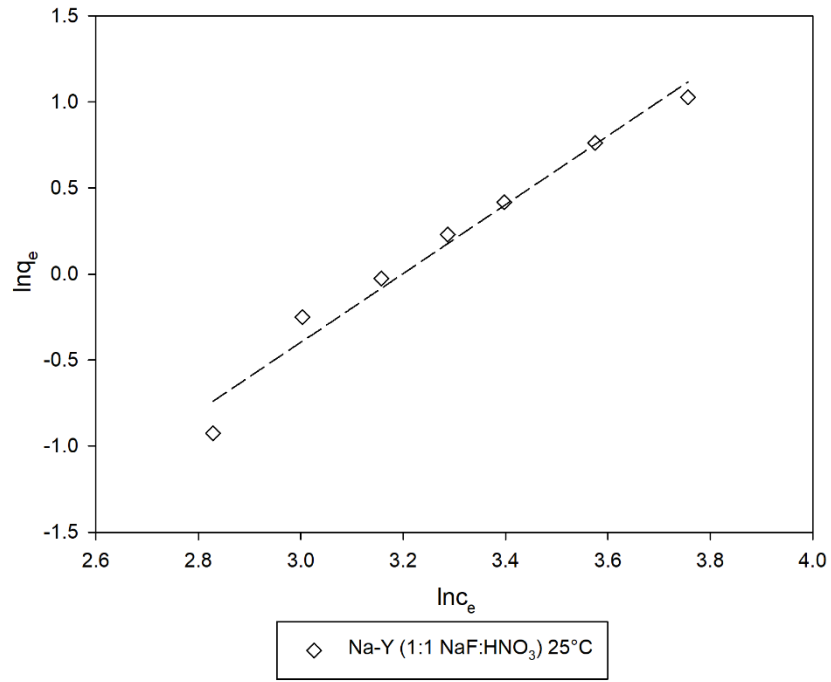


Figure 5.17. Freundlich plot for Na-Y in 1:1 NaF:HNO<sub>3</sub>.

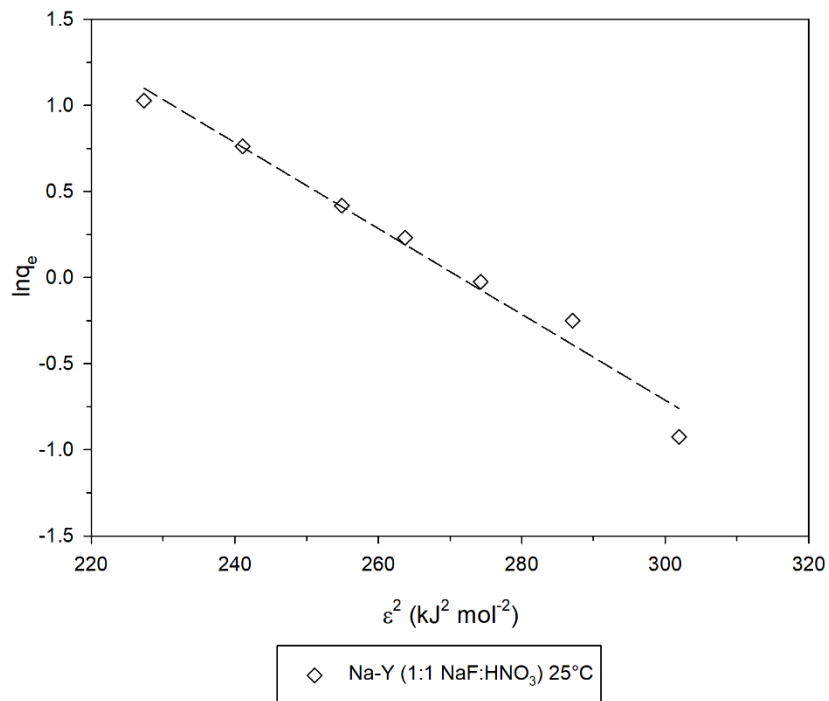


Figure 5.18. DR plot for Na-Y in 1:1 NaF:HNO<sub>3</sub>.

The characteristic adsorption energy calculated from the DR equation ( $4.4 \text{ kJ mol}^{-1}$ ) and the Freundlich isotherms parameters,  $n$  (2.00) and  $K_f$  ( $1.66 \times 10^{-2}$ ), all indicate the reaction between fluoride and Na-Y is much less favourable, under these conditions, compared with fluoride sorption by zeolites H-Y and  $\text{NH}_4\text{-Y}$  from pure NaF solutions. The value of the exponent,  $n > 1$ , indicates adsorption is “unfavourable”;<sup>56</sup> the thermodynamic interpretation of unfavourable adsorption is that adsorption is not spontaneous but requires work to be done in order to occur.<sup>57</sup> While there is a stoichiometric equivalent of protons in each solution, the lower favourability may be caused by a difference in the interaction between the zeolite surface and the aqueous protons in 1:1 NaF:HNO<sub>3</sub> solutions, compared with the  $\text{H}^+$  or  $\text{NH}_4^+$  ions released following ion exchange from H-Y or  $\text{NH}_4\text{-Y}$ , respectively. Critically, in the former case a proton must first be adsorbed to the surface before the reaction may proceed, whereas in the latter case the  $\text{H}^+$  or  $\text{NH}_4^+$  will migrate into the surface layers, following ion exchange, from which it may either desorb or remain adsorbed to the surface where it can mediate the reaction between the zeolite framework and fluoride ion.

The adsorption of a proton from solution, and the associated counter anion, would have an inherent entropic and enthalpic cost to the system. A reduction in entropy would result from the limited motional freedom of a surface-adsorbed proton compared with the antecedent hydronium ion ( $\text{H}_3\text{O}^+$ ) in solution. Moreover, the enhanced solvation energy of the hydronium ion ( $\text{H}_3\text{O}^+$ ), relative to a water molecule in solution, would be lost upon adsorption to the hydrated surface. Ultimately, work must be done to overcome the energetic barrier and enable proton adsorption to occur. In fluoride adsorption by H-Y and  $\text{NH}_4\text{-Y}$  from NaF solutions, proton adsorption is not necessary, as a result there is no energy barrier to the reaction as in the case of fluoride adsorption to Na-Y in 1:1 NaF:HNO<sub>3</sub> solutions. Ultimately, this may rationalise the lower characteristic adsorption energy, much lower Freundlich constant and greater exponent observed in fluoride adsorption on Na-Y from 1:1 NaF:HNO<sub>3</sub> solutions compared with values for H-Y and  $\text{NH}_4\text{-Y}$  from NaF solutions.

### 5.3.8 Conclusions

NH<sub>4</sub>-Y and H-Y exhibit reactivity with aqueous fluoride, whereas Na-Y does not. The importance of a proton source in mediating the fluorination reaction between the zeolite and fluoride has been established. Moreover, by applying adsorption isotherms to equilibrium fluoride uptake data and employing <sup>19</sup>F MAS NMR spectroscopy to probe the local environment, it has been determined that fluoride reacts with the framework forming 4 co-ordinate fluorine-containing species, [SiO<sub>3</sub>F] and [AlO<sub>3</sub>F]. A minor amount of fluoride is also present as intrapore anions, suggesting the migration of some Na<sup>+</sup>F<sup>-</sup> ion-pairs into the zeolite. <sup>29</sup>Si{<sup>1</sup>H} CP MAS NMR spectra have been used to differentiate between two plausible mechanisms for the fluorination reaction in NH<sub>4</sub>-Y, intimating the reaction proceeds by substitution of fluoride at surface hydroxyl groups, the same mechanism by which fluorination is reported to proceed in hydrothermal and high temperature treatments, as inferred in those reports by IR spectroscopy.<sup>113,116</sup>

Findings on the fluorination of zeolite frameworks have important implications on the potential application of zeolites in defluoridation, as the environmental remediation of excess aqueous fluoride from solutions with typical concentrations 20 - 50 ppm F<sup>-</sup> is desirable.<sup>59,105</sup> Here, the efficacy of H<sup>+</sup> and NH<sub>4</sub><sup>+</sup>-bearing zeolite Y in fluoride uptake from solutions in this concentration range has been demonstrated. In addition, the fluorination of zeolites under mild conditions, 25°C and 200 ppm F<sup>-</sup> solutions, has achieved significant fluoride loadings (2 – 3 wt%) for zeolites containing acidic intrapore cations. These conditions achieve comparable fluoride loadings with fluorinated zeolites prepared for catalytic applications,<sup>111-116</sup> yet under significantly milder and safer conditions.

## 5.4 Results Part 2: Fluoride Uptake in $M_x(NH_4)_{1-2x}Y$ and $M_xNa_{1-2x}Y$

### 5.4.1 Introduction

The influence of the intrapore cation on zeolite fluorination has been further studied for zeolite-Y containing divalent intrapore cations. Divalent cations possess greater charge density than monovalent cations, and the presence of divalent cations within channels lowers the overall cation concentration, therefore increasing accessibility to guest species. Fluoride uptake has been studied in zeolite-Y species,  $NH_4Y$  and  $NaY$ , partially ion-exchanged with divalent cations,  $M_xNa_{1-2x}Y$  and  $M_x(NH_4)_{1-2x}Y$ , where  $M = Mg^{2+}, Ca^{2+}, Sr^{2+}, Ba^{2+}$  and  $Cu^{2+}$ . Divalent cations such as  $Co^{2+}$  and  $Ni^{2+}$  have not been studied, as the harmful and negative environmental effects associated with these species may negate any beneficial applications in the removal of aqueous fluoride.

### 5.4.2 Characterisation

The partially exchanged zeolites,  $M_xNa_{1-2x}Y$  and  $M_x(NH_4)_{1-2x}Y$ , were prepared by batch ion exchange experiments with 0.25 M solutions of the appropriate metal nitrate at 60°C for 24 hours (described in Section 5.2.3).  $M_xNa_{1-2x}Y$  and  $M_x(NH_4)_{1-2x}Y$  have been characterised by PXRD and XRF spectrometry. Unit cell parameters and volumes for  $M_xNa_{1-2x}Y$  and  $M_x(NH_4)_{1-2x}Y$  species, calculated by a unit cell refinement in Chekcell<sup>84</sup> assuming the  $Fd-3m$  space group, are presented in Table 5.7. PXRD patterns are presented in Figures 5.19 and 5.20 for  $M_x(NH_4)_{1-2x}Y$  and  $M_xNa_{1-2x}Y$  species, respectively.

M/Al and Si/Al ratios, with errors in parenthesis, measured by XRF spectrometry are presented in Table 5.7 for the  $M_x(NH_4)_{1-2x}Y$  species, the  $x$  in the general formula for each species has been directly inferred from the M/Al ratio measured. M/Al, Si/Al and Na/Al ratios for  $M_xNa_{1-2x}Y$  are also presented in Table 5.7, the cation occupancies  $(2(M/Al) + Na/Al)$  measured for each  $M_xNa_{1-2x}Y$  species fall in the range 1.05 – 1.13, greater than the ideal value of 1.0, indicating the error in the values is greater than the errors calculated by the software that are presented in parenthesis. The value for Na-Y (Na/Al = 1.1(1)) is also inflated compared with the expected value of 1.0. While the values of M/Al and Na/Al

are greater than the maximum possible cation occupancy, the M/Al and Na/Al values have been used directly in the descriptive  $M_xNa_{1-2x}Y$  formulae.

Table 5.7. Lattice constants, volumes and compositional ratios for  $M_xNa_{1-2x}Y$  and  $M_x(NH_4)_{1-2x}Y$ .

Zeolite	$a$ (Å)	$V$ (Å <sup>3</sup> )	M/Al	Si/Al	Na/Al
NH <sub>4</sub> -Y	24.59(1)	14,869(18)	-	2.8(1)	-
Mg <sub>0.15</sub> (NH <sub>4</sub> ) <sub>0.70</sub> -Y	24.515(6)	14,733(11)	0.15(1)	2.7(1)	-
Ca <sub>0.17</sub> (NH <sub>4</sub> ) <sub>0.66</sub> -Y	24.57(1)	14,833(18)	0.17(1)	2.7(1)	-
Sr <sub>0.14</sub> (NH <sub>4</sub> ) <sub>0.72</sub> -Y	24.531(8)	14,762(4)	0.14(1)	2.6(1)	-
Ba <sub>0.21</sub> (NH <sub>4</sub> ) <sub>0.58</sub> -Y	24.61(2)	14,905(37)	0.21(1)	2.6(1)	-
Cu <sub>0.24</sub> (NH <sub>4</sub> ) <sub>0.52</sub> -Y	24.56(2)	14,814(37)	0.24(2)	2.8(1)	-
Na-Y	24.71(1)	15,088(19)	-	2.7(1)	1.1(1)
Mg <sub>0.37</sub> Na <sub>0.39</sub> -Y	24.71(1)	15,088(17)	0.37(2)	2.7(1)	0.39(4)
Ca <sub>0.46</sub> Na <sub>0.14</sub> -Y	24.69(2)	15,051(38)	0.46(2)	2.7(1)	0.14(3)
Sr <sub>0.45</sub> Na <sub>0.18</sub> -Y	24.72(2)	15,106(37)	0.45(2)	2.8(1)	0.18(3)
Ba <sub>0.33</sub> Na <sub>0.44</sub> -Y	24.69(1)	15,051(18)	0.33(2)	2.5(1)	0.44(4)
Cu <sub>0.41</sub> Na <sub>0.29</sub> -Y	24.73(1)	15,124(18)	0.41(2)	2.5(1)	0.29(3)

There are several factors inherent to the ion-exchanged products which may contribute to the additional error, and lower accuracy, observed in their quantitative analysis by XRF spectrometry. As outlined in Section 2.2.2, the accuracy of quantitative results is compromised in samples containing elements with disparate fluorescence yields.<sup>64</sup> As the fluorescence yield of an element is proportional to the atomic number, the influence of disparate fluorescence yields on accuracy will be most pronounced in the strontium and barium-exchanged zeolites. Additional sample-dependent factors that may give rise to error in the M/Al ratios and the overall intrapore cation concentrations include the possible occurrence of divalent metal ion complex adsorption on the zeolite surface, and the occurrence of “over exchange” phenomena, i.e. the exchange, or formation, of intrapore species containing the divalent metal ion but that carry a charge less than the charge on the cation (e.g. [Sr(OH)]<sup>+</sup>).<sup>133,134</sup> The extent to which surface adsorption and “over exchange” phenomena contribute to the observed results is unknown.

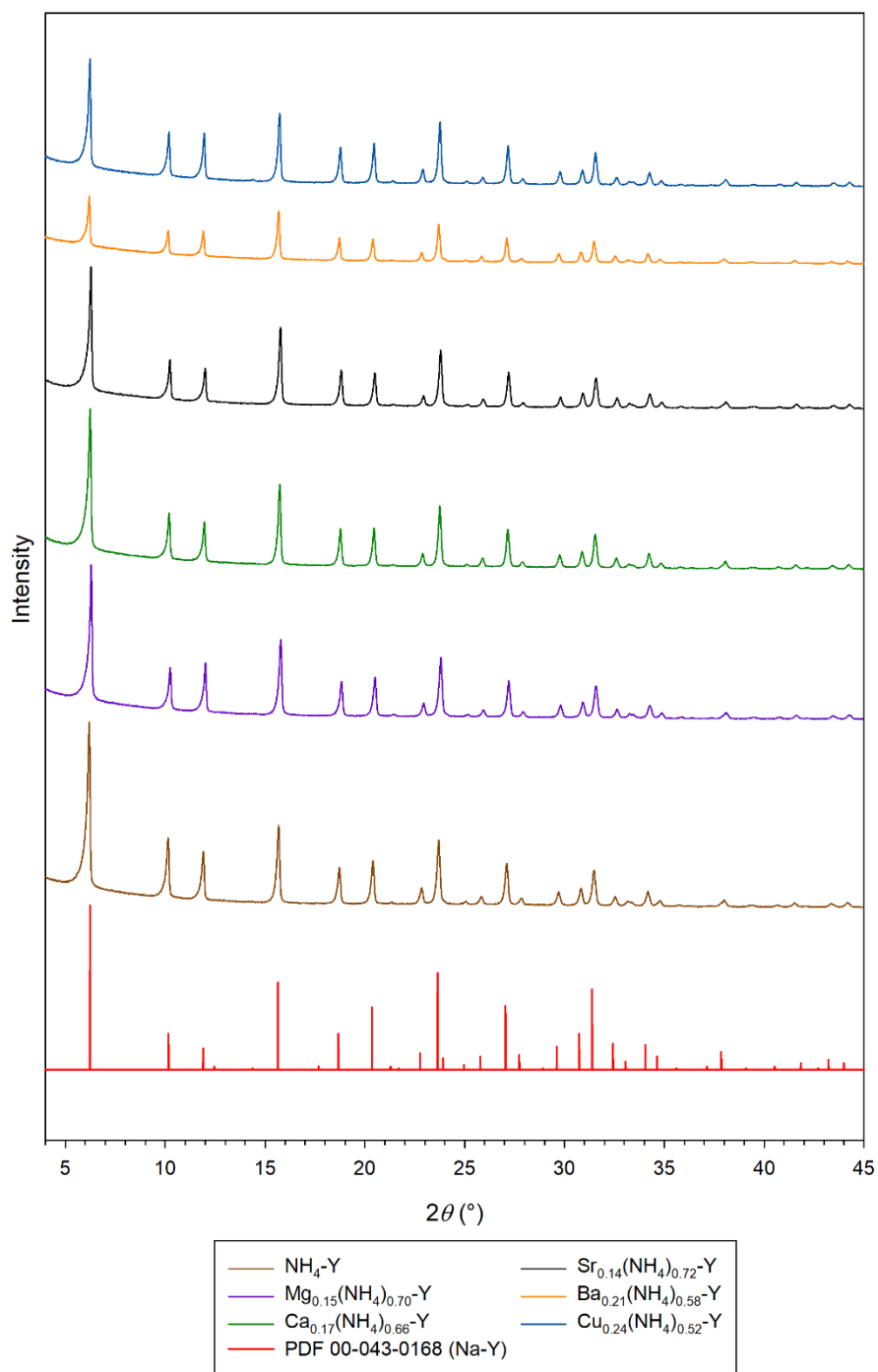


Figure 5.19. PXRD patterns of  $\text{M}_x(\text{NH}_4)_{1-2x}\text{-Y}$  species and a reference Na-Y pattern.

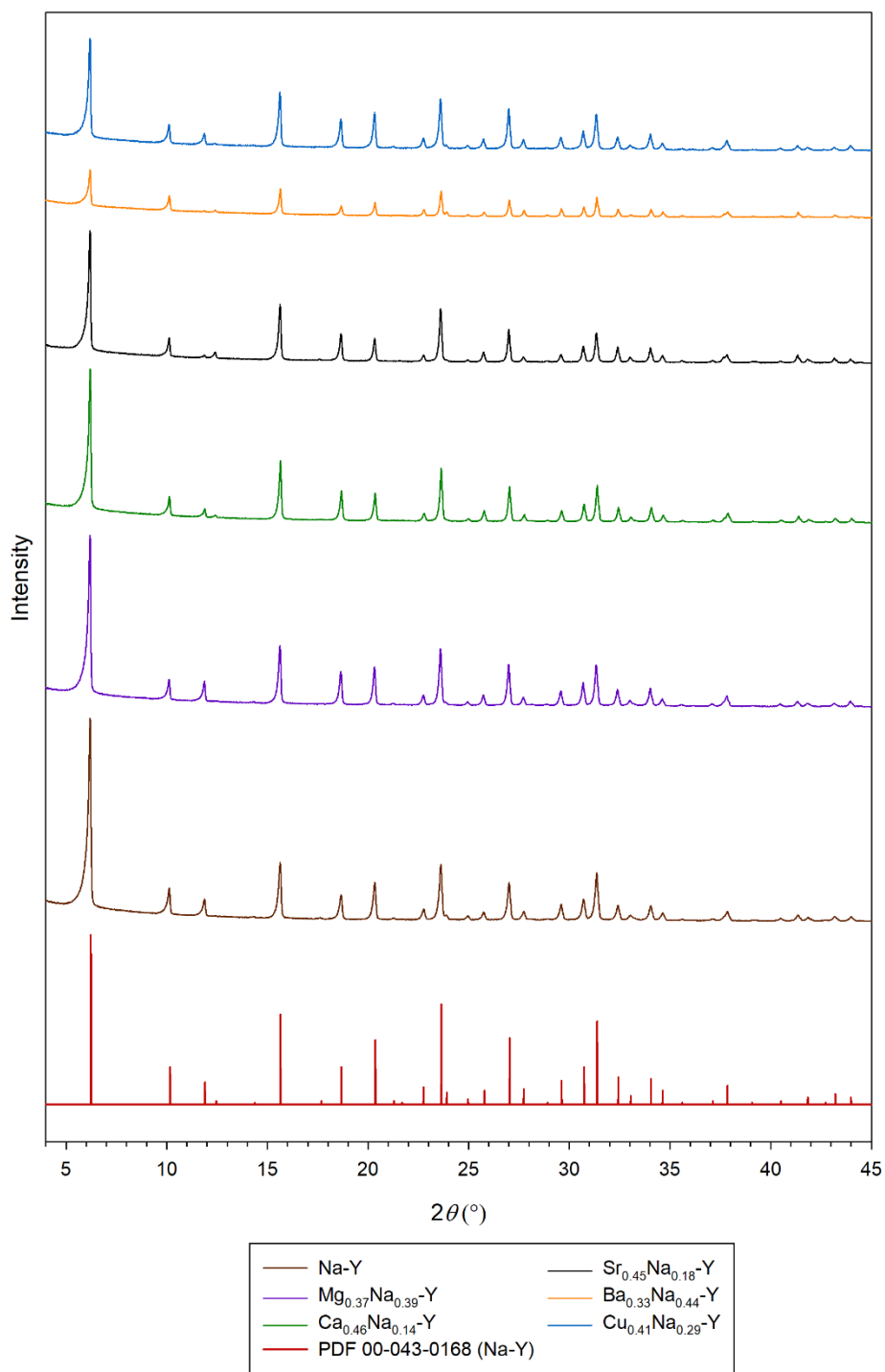


Figure 5.20. PXRD patterns for  $\text{M}_x\text{Na}_{1-2x}\text{-Y}$  species and a reference Na-Y pattern.

A contraction of the unit cell is observed upon the introduction of  $Mg^{2+}$  and  $Sr^{2+}$  into  $NH_4$ -Y, whereas a less significant contraction is observed upon introducing  $Ca^{2+}$  and  $Cu^{2+}$ ; the latter contraction is within the confidence interval of the lattice constant of the parent material,  $NH_4$ -Y. A significant reduction in relative peak intensities are observed in the PXRD pattern recorded on  $Ba_{0.21}(NH_4)_{0.58}$ -Y compared with the parent material. The reduced relative intensities may be ascribed to increased X-ray absorption and Compton scattering, owing to the presence of barium.<sup>63</sup> Higher loadings of the divalent metal upon ion exchange are observed for Na-Y compared with  $NH_4$ -Y. Upon ion exchange with  $Mg^{2+}$  and  $Cu^{2+}$ , few changes in relative intensities are observed in the PXRD patterns compared with the parent material, Na-Y. Ion exchange with  $Ca^{2+}$  and  $Sr^{2+}$  leads to growth in the relative intensity of the 222 reflection at  $2\theta = 12.4^\circ$ , and for  $Sr_{0.45}Na_{0.18}$ -Y the relative intensity of the 311 reflection at  $2\theta = 11.8^\circ$  diminishes significantly. As in the case of  $NH_4$ -Y, ion exchange with  $Ba^{2+}$  leads to a significant reduction in the observed peak intensities.

#### 5.4.3 $M_x(NH_4)_{1-2x}$ -Y: Fluoride Loadings

Equilibrium fluoride loadings ( $q_e$ ) attained across the concentration range (5 - 60 ppm F<sup>-</sup>) at 25°C for  $M_x(NH_4)_{1-2x}$ -Y are plotted in Figure 5.21, for M = Mg, Ca and Sr, and Figure 5.22 for M = Ba and Cu; for comparison loadings measured for the parent material,  $NH_4$ -Y, are also plotted in both figures. In all cases, the partial exchange of a divalent cation into the zeolite leads to enhanced equilibrium fluoride loadings achieved across the entire concentration range. The greatest loadings are attained by  $Ca_{0.17}(NH_4)_{0.66}$ -Y, followed by  $Sr_{0.14}(NH_4)_{0.72}$ -Y, then  $Cu_{0.24}(NH_4)_{0.52}$ -Y and finally similar loadings are attained for both  $Mg_{0.15}(NH_4)_{0.70}$ -Y and  $Ba_{0.21}(NH_4)_{0.58}$ -Y. Analogous plots for equilibrium loadings at 40°C are plotted in Fig. 5.23 and Fig. 5.24 and demonstrate modest increases in loading upon increasing temperature.

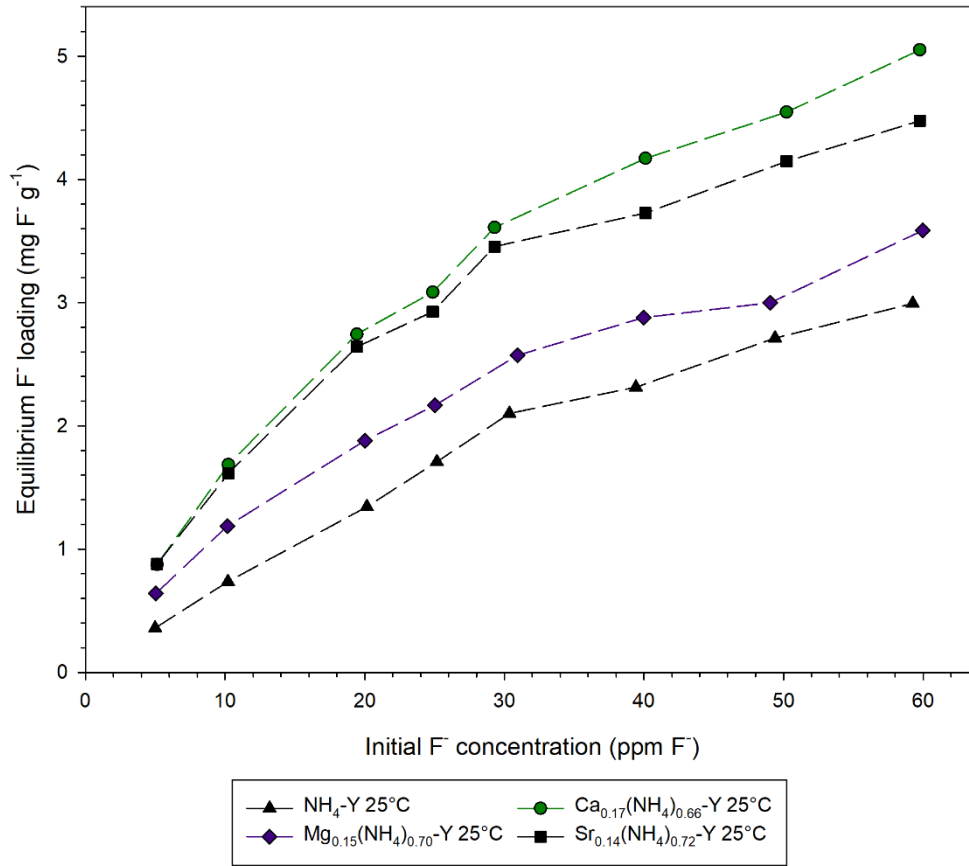


Figure 5.21. Equilibrium fluoride loadings achieved for  $M_x(NH_4)_{1-2x}-Y$  species at 25°C, where  $M = Mg^{2+}$ ,  $Ca^{2+}$  or  $Sr^{2+}$ , as a function of initial fluoride concentration.

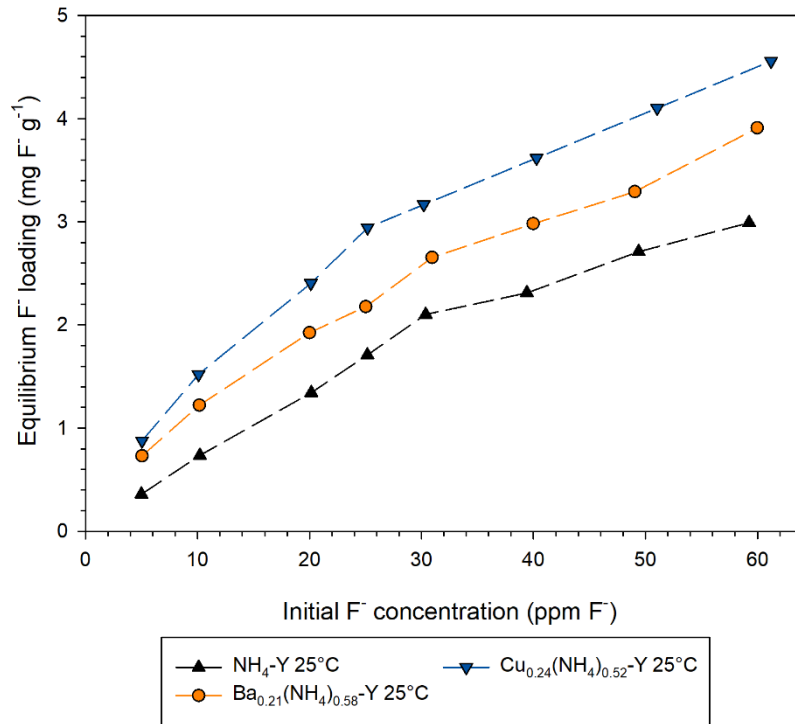


Figure 5.22. Equilibrium fluoride loadings achieved for  $M_x(NH_4)_{1-2x}-Y$  species at 25°C, where  $M = Cu^{2+}$  or  $Ba^{2+}$ , as a function of initial fluoride concentration.

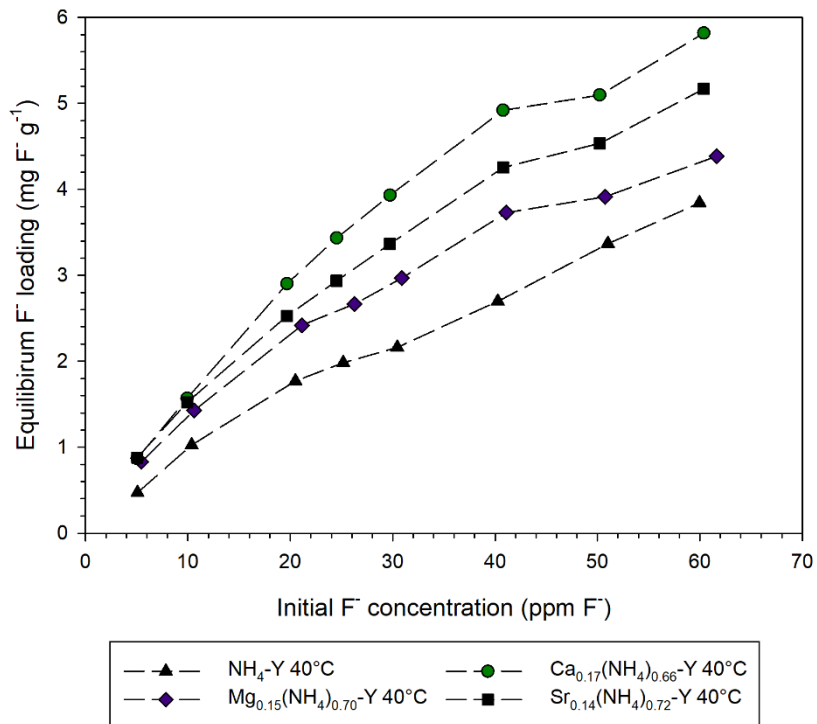


Figure 5.23. Equilibrium fluoride loadings achieved for  $M_x(NH_4)_{1-2x}-Y$  species at 40°C, where  $M = Mg^{2+}$ ,  $Ca^{2+}$  or  $Sr^{2+}$ , as a function of initial fluoride concentration.

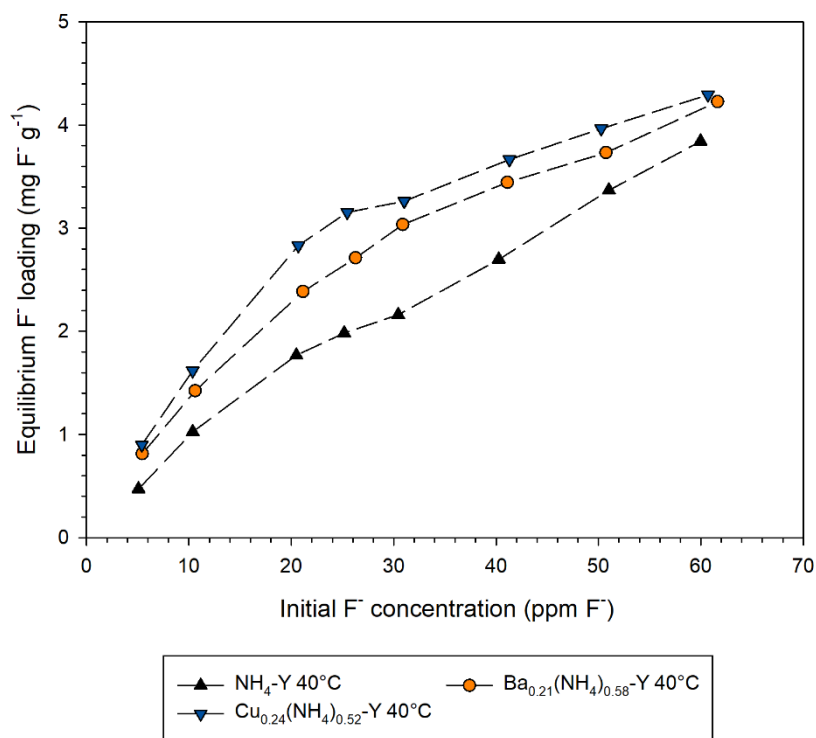


Figure 5.24. Equilibrium fluoride loadings achieved for  $M_x(\text{NH}_4)_{1-2x}\text{-Y}$  species at 40°C, where  $M = \text{Cu}^{2+}$  or  $\text{Ba}^{2+}$ , as a function of initial fluoride concentration.

#### 5.4.4 $M_x(\text{NH}_4)_{1-2x}\text{-Y}$ : Adsorption Isotherms

Equilibrium fluoride uptake data for  $M_x(\text{NH}_4)_{1-2x}\text{-Y}$  zeolites, at 25 and 40°C, have been fitted to the Freundlich, Langmuir, Temkin and Dubinin-Radushkevitch (DR) adsorption isotherms. The  $R^2$  values from linear regression analysis are presented in Table 5.8 for fits to the Freundlich, Langmuir and Temkin isotherms, in addition to Freundlich isotherm parameters. In general, poor fits are observed to the Temkin and Langmuir isotherms with a non-linear distribution of data points, reflected in the  $R^2$  values. Plots for the Langmuir and Temkin isotherms may be found in Appendix 1.

In general, good fits to the Freundlich isotherm are observed with  $R^2 > 0.98$  in all instances except for  $\text{Cu}_{0.24}(\text{NH}_4)_{0.52}\text{-Y}$  at 40°C ( $R^2 = 0.969$ ); the Freundlich fits are plotted in Figures 5.25 ( $\text{Mg}_{0.15}(\text{NH}_4)_{0.70}\text{-Y}$  and  $\text{Ca}_{0.17}(\text{NH}_4)_{0.66}\text{-Y}$ ), 5.26 ( $\text{Sr}_{0.14}(\text{NH}_4)_{0.72}\text{-Y}$ ), 5.27 ( $\text{Ba}_{0.21}(\text{NH}_4)_{0.58}\text{-Y}$ ) and 5.28 ( $\text{Cu}_{0.24}(\text{NH}_4)_{0.52}\text{-Y}$ ). For all  $M_x(\text{NH}_4)_{1-2x}\text{-Y}$  species examined, values for the exponent ( $n$ ) are lower than the values for  $\text{NH}_4\text{-Y}$  and values for the Freundlich constant ( $K_F$ ) are greater than the corresponding values for  $\text{NH}_4\text{-Y}$ , both

demonstrating the adsorption of fluoride is more favourable for the  $M_x(NH_4)_{1-2x}-Y$  species compared with the parent material ( $NH_4-Y$ ).

Applying the linear DR equation to equilibrium uptake data for  $M_x(NH_4)_{1-2x}-Y$  leads to good agreement in all instances, with  $R^2 > 0.987$  for each species at both temperatures. DR plots at each temperature are presented in Figures 5.29 ( $Mg_{0.15}(NH_4)_{0.70}-Y$  and  $Ca_{0.17}(NH_4)_{0.66}-Y$ ), 5.30 ( $Sr_{0.14}(NH_4)_{0.72}-Y$ ), 5.31 ( $Ba_{0.21}(NH_4)_{0.58}-Y$ ) and 5.32 ( $Cu_{0.24}(NH_4)_{0.52}-Y$ );  $R^2$ ,  $E_c$  and isotherm parameters,  $K$  and  $V_o/V_m$ , for each plot are collated in Table 5.9. In each instance where a divalent cation has been partially exchanged into  $NH_4-Y$ , the characteristic fluoride sorption energy is greater at 25°C than the value for the parent material,  $NH_4-Y$  ( $E_c = 7.5 \text{ kJ mol}^{-1}$ ). In the most modest increase, the characteristic adsorption energy for  $Mg_{0.15}(NH_4)_{0.70}-Y$  ( $E_c = 10.0 \text{ kJ mol}^{-1}$ ) is  $2.5 \text{ kJ mol}^{-1}$  greater than for  $NH_4-Y$ . Greater  $E_c$  values are attained for the other  $M_x(NH_4)_{1-2x}-Y$  species with the highest observed for  $Ca_{0.17}(NH_4)_{0.66}-Y$  and  $Sr_{0.14}(NH_4)_{0.72}-Y$ , with  $E_c = 11.9 \text{ kJ mol}^{-1}$  for both species.

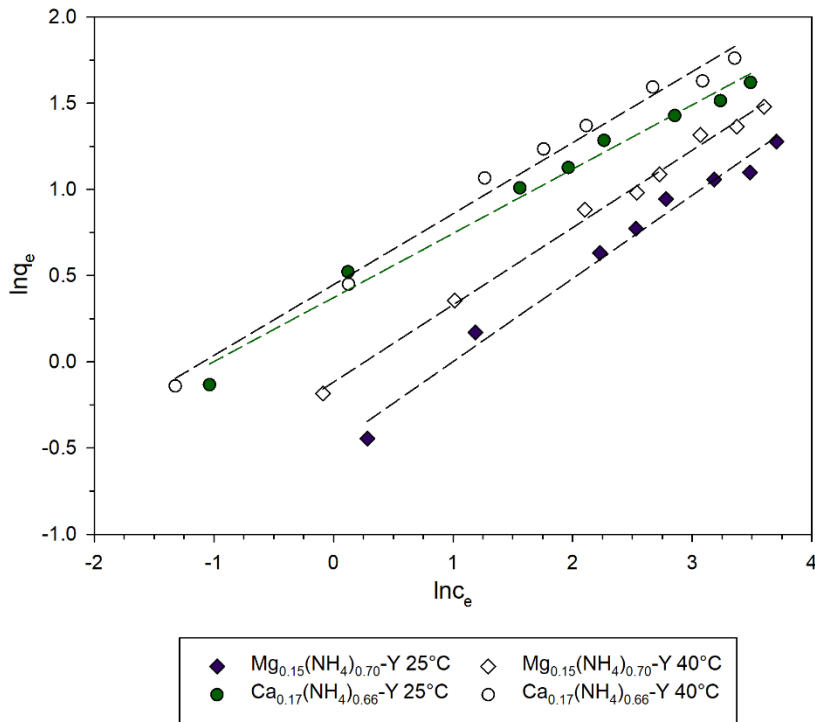


Figure 5.25. Freundlich plots for  $Mg_{0.15}(NH_4)_{0.70}-Y$  and  $Ca_{0.17}(NH_4)_{0.66}-Y$  at 25°C and 40°C.

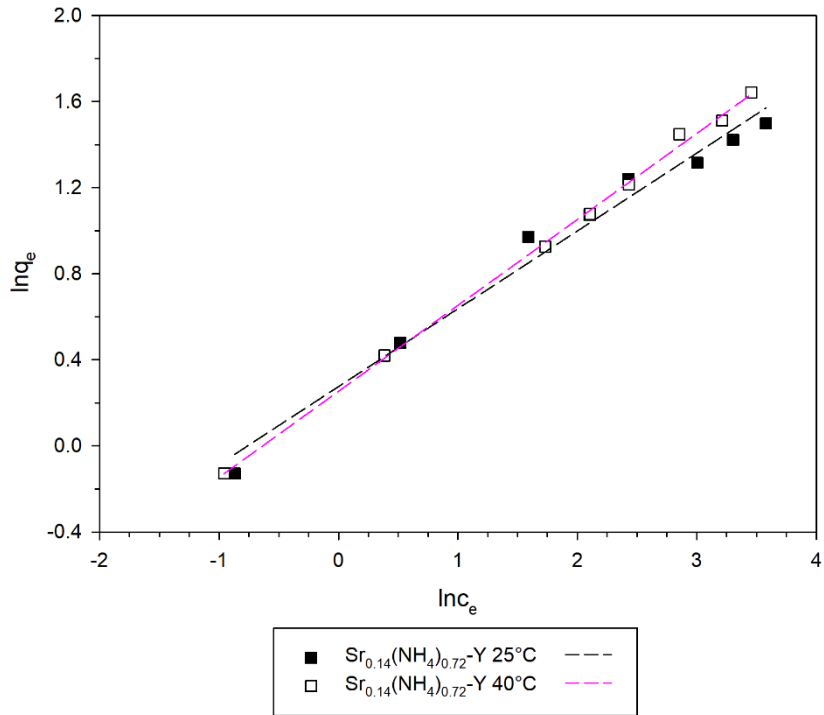


Figure 5.26. Freundlich plots for  $\text{Sr}_{0.14}(\text{NH}_4)_{0.72}\text{-Y}$  at 25°C and 40°C.

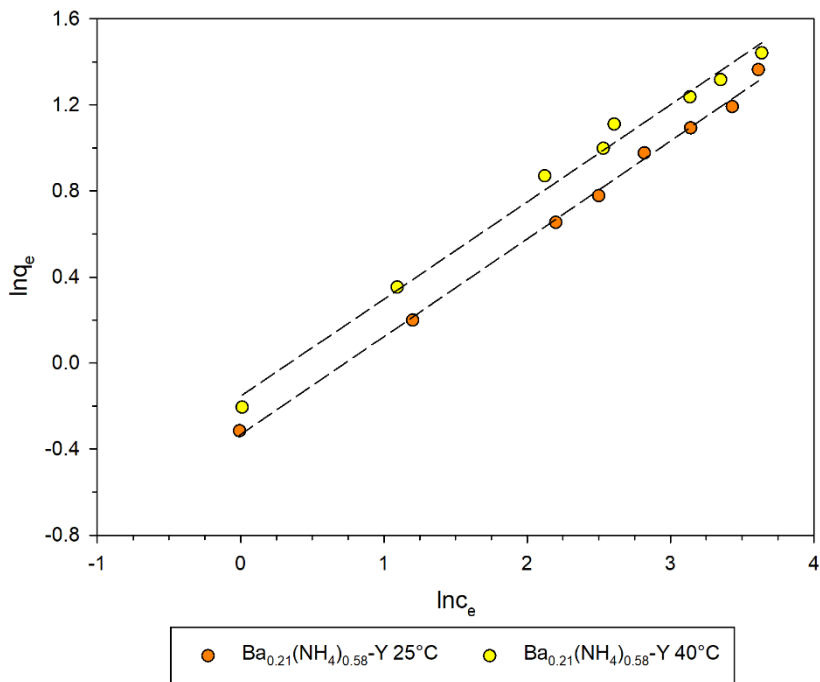


Figure 5.27. Freundlich plots for  $\text{Ba}_{0.21}(\text{NH}_4)_{0.58}\text{-Y}$  at 25°C and 40°C.

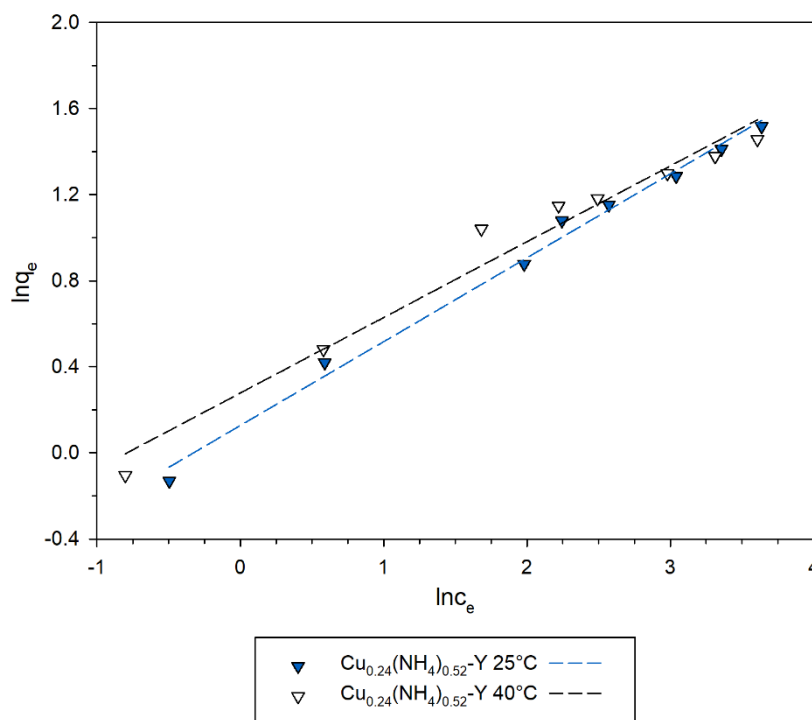


Figure 5.28. Freundlich plots for  $\text{Cu}_{0.24}(\text{NH}_4)_{0.52}\text{-Y}$  at 25°C and 40°C.

Table 5.8.  $R^2$  for fits to the Freundlich, Temkin and Langmuir isotherms, and Freundlich isotherm parameters, for  $\text{M}_x(\text{NH}_4)_{1-2x}\text{-Y}$  and  $\text{NH}_4\text{-Y}$ . The units of  $K_F$  are  $(\text{mg g}^{-1})/(\text{mg L}^{-1})^n$ .

Zeolite	Temp. (°C)	Freundlich			Temkin	Langmuir
		$R^2$	$K_F$	$n$	$R^2$	$R^2$
$\text{NH}_4\text{-Y}$	25	0.982	0.17	0.800	0.968	0.950
	40	0.982	0.28	0.716	0.939	0.931
$\text{Mg}_{0.15}(\text{NH}_4)_{0.70}\text{-Y}$	25	0.982	0.62	0.717	0.971	0.976
	40	0.995	0.89	0.449	0.952	0.967
$\text{Ca}_{0.17}(\text{NH}_4)_{0.66}\text{-Y}$	25	0.983	1.45	0.373	0.980	0.914
	40	0.988	1.57	0.412	0.964	0.985
$\text{Sr}_{0.14}(\text{NH}_4)_{0.72}\text{-Y}$	25	0.981	1.32	0.362	0.985	0.867
	40	0.998	1.29	0.400	0.932	0.964
$\text{Ba}_{0.21}(\text{NH}_4)_{0.58}\text{-Y}$	25	0.998	0.72	0.455	0.925	0.947
	40	0.991	0.86	0.452	0.975	0.982
$\text{Cu}_{0.24}(\text{NH}_4)_{0.52}\text{-Y}$	25	0.992	1.14	0.390	0.967	0.978
	40	0.969	1.32	0.352	0.989	0.993

For each  $M_x(\text{NH}_4)_{1-2x}\text{-Y}$  species, increasing the temperature from 25 to 40°C leads to an increase in  $E_c$ . For the alkaline earth ion-exchanged zeolites, the greatest increase upon raising the temperature is observed for  $\text{Mg}_{0.15}(\text{NH}_4)_{0.70}\text{-Y}$ , increasing 1.1  $\text{kJ mol}^{-1}$  to 11.1  $\text{kJ mol}^{-1}$ . The increase in  $E_c$  for  $\text{Ba}_{0.21}(\text{NH}_4)_{0.58}\text{-Y}$  is smaller (0.6  $\text{kJ mol}^{-1}$ ), consequently it has the lowest  $E_c$  of the  $M_x(\text{NH}_4)_{1-2x}\text{-Y}$  species examined at 40°C. The characteristic adsorption energies for  $\text{Ca}_{0.17}(\text{NH}_4)_{0.66}\text{-Y}$  and  $\text{Sr}_{0.14}(\text{NH}_4)_{0.72}\text{-Y}$  increase only slightly from the values at 25°C to 12.0  $\text{kJ mol}^{-1}$  and 12.1  $\text{kJ mol}^{-1}$ , respectively. The most significant increase in the characteristic adsorption energy upon increasing the temperature is observed for  $\text{Cu}_{0.24}(\text{NH}_4)_{0.52}\text{-Y}$  (1.3  $\text{kJ mol}^{-1}$ ), leading to the greatest  $E_c$  of all  $M_x(\text{NH}_4)_{1-2x}\text{-Y}$  species examined at 40°C.

Table 5.9.  $R^2$ , isotherm parameters and  $E_c$  for fits to the linear Dubinin-Radushkevitch equation for  $M_x(\text{NH}_4)_{1-2x}\text{-Y}$ .

Zeolite	Temperature (°C)	$R^2$	$E_c$ ( $\text{kJ mol}^{-1}$ )	$K$ ( $\times 10^{-3} \text{ mol}^2/\text{kJ}^2$ )	$V_0/V_m$
$\text{Mg}_{0.15}(\text{NH}_4)_{0.70}\text{-Y}$	25	0.993	10.0	5.04	11.32
	40	0.995	11.1	4.07	12.67
$\text{Ca}_{0.17}(\text{NH}_4)_{0.66}\text{-Y}$	25	0.995	11.9	3.55	12.16
	40	0.995	12.0	3.45	15.83
$\text{Sr}_{0.14}(\text{NH}_4)_{0.72}\text{-Y}$	25	0.994	11.9	3.51	10.65
	40	0.992	12.1	3.41	12.57
$\text{Ba}_{0.21}(\text{NH}_4)_{0.58}\text{-Y}$	25	0.989	10.4	4.60	10.59
	40	0.997	11.0	4.15	13.20
$\text{Cu}_{0.24}(\text{NH}_4)_{0.52}\text{-Y}$	25	0.996	11.4	3.84	11.04
	40	0.988	12.7	3.11	10.16

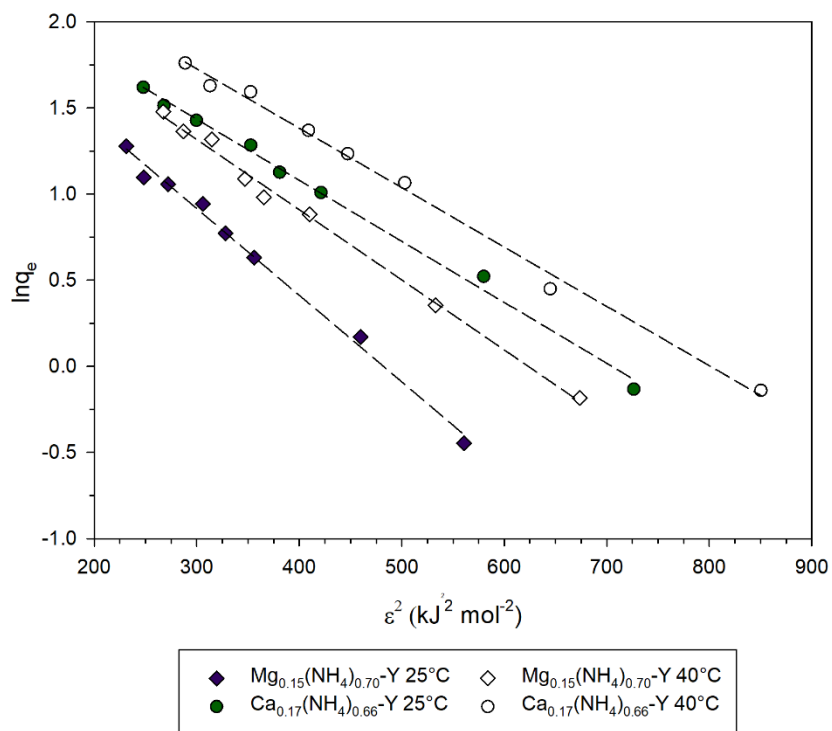


Figure 5.29. DR plots for  $\text{Mg}_{0.15}(\text{NH}_4)_{0.70}\text{-Y}$  and  $\text{Ca}_{0.17}(\text{NH}_4)_{0.66}\text{-Y}$  at 25°C and 40°C.

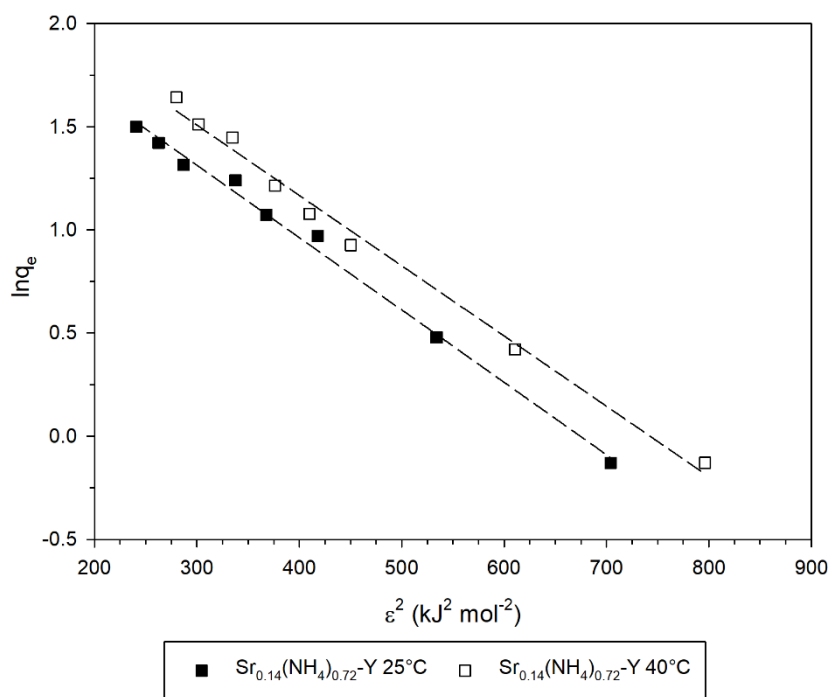


Figure 5.30. DR plots for  $\text{Sr}_{0.14}(\text{NH}_4)_{0.72}\text{-Y}$  at 25°C and 40°C.

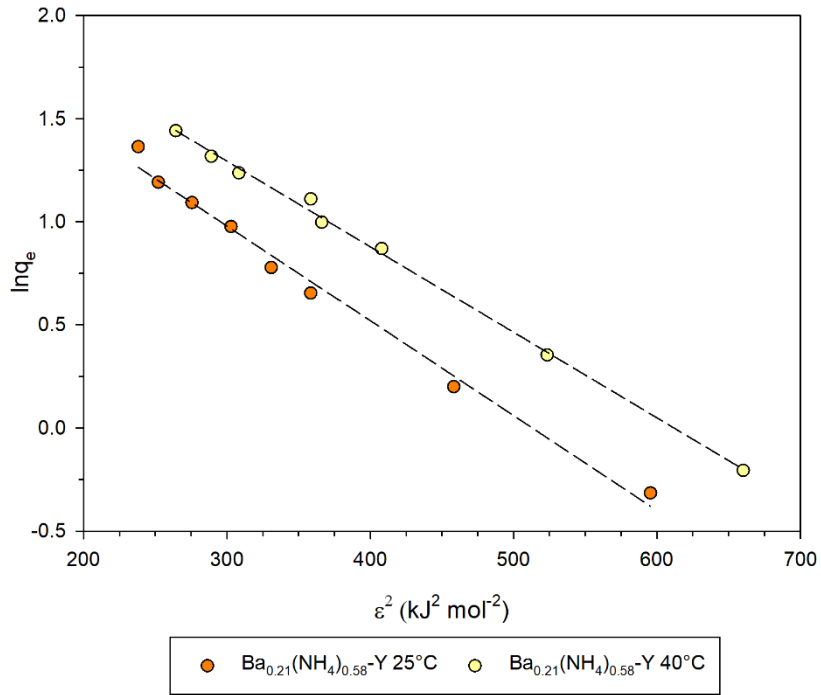


Figure 5.31. DR plots for  $\text{Ba}_{0.21}(\text{NH}_4)_{0.58}\text{-Y}$  at 25°C and 40°C.

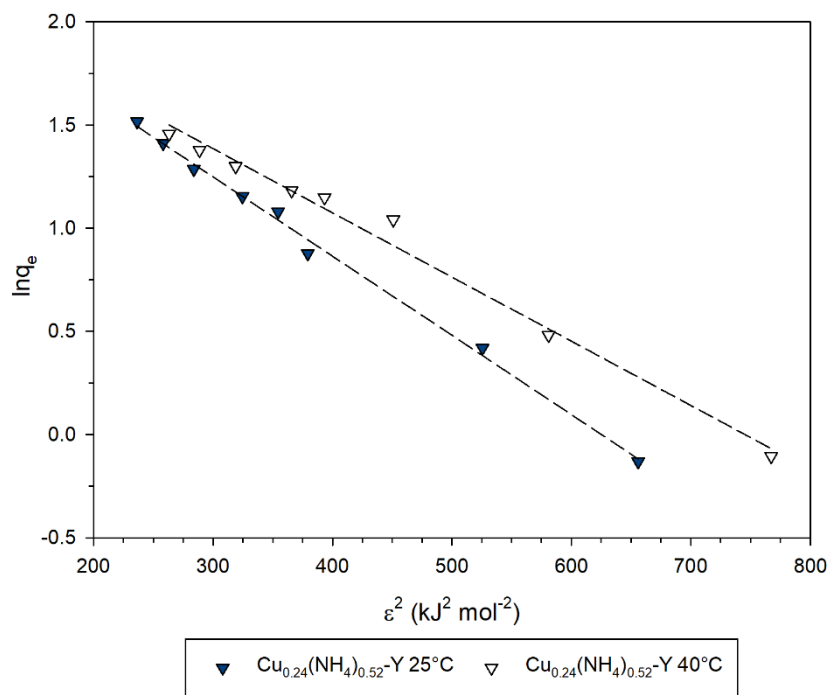


Figure 5.32. DR plots for  $\text{Cu}_{0.24}(\text{NH}_4)_{0.52}\text{-Y}$  at 25°C and 40°C.

#### 5.4.5 $M_x(\text{NH}_4)_{1-2x}\text{-Y}$ : $^{19}\text{F}$ MAS NMR spectroscopy

Fluorine-19 MAS NMR spectra recorded on  $M_x(\text{NH}_4)_{1-2x}\text{-Y}$  species, treated with 60 ppm  $\text{F}^-$  NaF solutions for 24 hours at 25°C, are presented in Figures 5.33 ( $\text{Mg}_{0.15}(\text{NH}_4)_{0.70}\text{-Y}$ ), 5.34 ( $\text{Ca}_{0.17}(\text{NH}_4)_{0.66}\text{-Y}$ ), 5.35 ( $\text{Sr}_{0.14}(\text{NH}_4)_{0.72}\text{-Y}$ ), 5.36 ( $\text{Ba}_{0.21}(\text{NH}_4)_{0.58}\text{-Y}$ ) and 5.37 ( $\text{Cu}_{0.24}(\text{NH}_4)_{0.52}\text{-Y}$ ). Approximate chemical shifts for the resonances **1** – **4** as labelled in each spectrum are listed in Table 5.10. The spectra recorded on  $\text{NH}_4\text{-Y}$  partially exchanged with alkaline earth metals (Mg, Ca, Sr and Ba) resemble the spectrum for the fluorinated parent material ( $\text{NH}_4\text{-Y(F)}$ ), all containing the same 3 peaks at similar chemical shifts within the range -115 to -180 ppm, with some spinning sidebands outside this range, in addition to the appearance of a new resonance at  $\delta_{\text{F}} \approx -136$  ppm in most spectra.

The  $[\text{SiO}_3\text{F}]$  resonance which dominates the  $\text{NH}_4\text{-Y(F)}$  spectrum at  $\delta_{\text{F}} \approx -153$  ppm (resonance **B**) is also present in the fluorinated alkaline earth ion-exchanged zeolites (resonance **3**), occurring at chemical shifts between 3 – 8 ppm downfield of resonance **B**, reflecting deshielding of the fluorine nuclei caused by the higher charge density of the divalent intrapore cations. The resonance attributed to  $[\text{AlO}_3\text{F}]$  at  $\delta_{\text{F}} \approx -176$  ppm in the  $\text{NH}_4\text{-Y(F)}$  spectrum (resonance **C**) is also present in the fluorinated alkaline earth ion-exchanged zeolites (resonance **4**); the resonance also occurs at chemical shifts between 3 – 8 ppm downfield of the corresponding resonance in the  $\text{NH}_4\text{-Y(F)}$  spectrum, for analogous reasons to the shifting of resonance **3**. In each instance, the relative intensity of the  $[\text{AlO}_3\text{F}]$  peak appears to be reduced compared with the corresponding intensity in the  $\text{NH}_4\text{-Y(F)}$  spectrum. The origin of this diminished intensity is not clear. In the  $^{19}\text{F}$  MAS NMR spectra recorded on the fluorinated alkaline earth ion-exchanged zeolites, resonance **1** at  $\delta_{\text{F}} \approx -119$  ppm corresponds to resonance **A** in the  $\text{NH}_4\text{-Y(F)}$  spectrum and is therefore attributed to the intrapore fluoride environment (Section 5.3.5).

A further resonance is observed at  $\delta_{\text{F}} \approx -136$  ppm (resonance **2**) in the spectra of all fluorinated alkaline earth ion-exchanged zeolites. While there is no distinct maximum at  $\delta_{\text{F}} \approx -136$  ppm in the  $\text{Ca}_{0.17}(\text{NH}_4)_{0.66}\text{-Y(F)}$  spectrum, peak fitting demonstrates there is a resonance at this chemical shift (Appendix 2). Peak fitting performed on the fluorinated parent material,  $\text{NH}_4\text{-Y(F)}$ , also indicated the

likely presence of a resonance at  $\delta_F \approx -136$  ppm (Section 5.3.5 and Appendix 2). The environment responsible for the resonance at  $\delta_F \approx -136$  ppm, therefore, appears to occur in fluorinated  $\text{NH}_4\text{-Y}$ , albeit with a lower relative population compared with in the fluorinated  $\text{M}_x(\text{NH}_4)_{1-2x}\text{-Y}$  species. The origin of resonance **2** is unclear.

Table 5.10. Approximate chemical shifts for resonances **1** - **4** in  $^{19}\text{F}$  MAS NMR spectra recorded on fluorinated  $\text{M}_x(\text{NH}_4)_{1-2x}\text{-Y}$ .

Zeolite	$\delta_F$ (ppm)			
	<b>1</b>	<b>2</b>	<b>3</b>	<b>4</b>
$\text{Mg}_{0.15}(\text{NH}_4)_{0.70}\text{-Y}$	-118	-137	-150	-174
$\text{Ca}_{0.17}(\text{NH}_4)_{0.66}\text{-Y}$	-118	-134	-145	-167
$\text{Sr}_{0.14}(\text{NH}_4)_{0.72}\text{-Y}$	-118	-136	-144	-168
$\text{Ba}_{0.21}(\text{NH}_4)_{0.58}\text{-Y}$	-118	-136	-144	-166
$\text{Cu}_{0.24}(\text{NH}_4)_{0.52}\text{-Y}$	-	-135	-147	-172

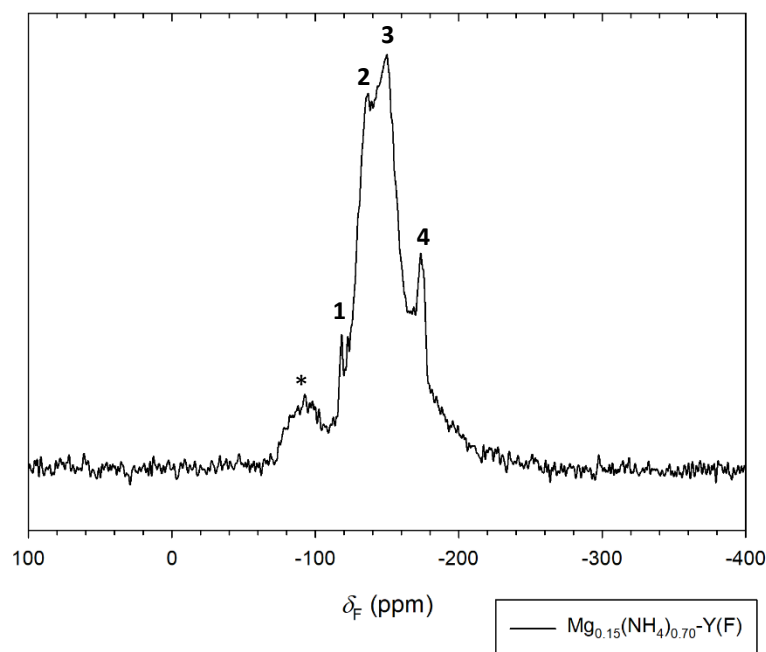


Figure 5.33.  $^{19}\text{F}$  MAS NMR spectrum of fluorinated  $\text{Mg}_{0.15}(\text{NH}_4)_{0.70}\text{-Y}$ . Spinning sidebands are indicated by a \*.

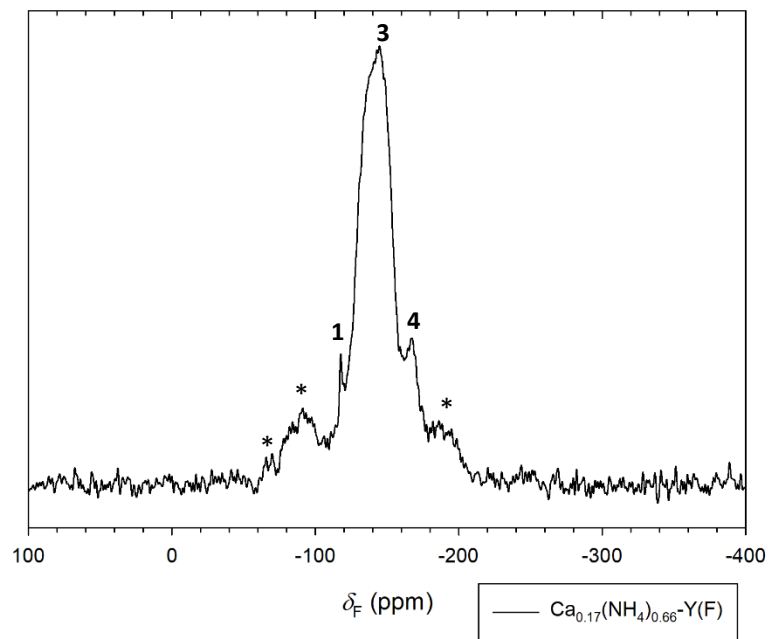


Figure 5.34.  $^{19}\text{F}$  MAS NMR spectrum of fluorinated  $\text{Ca}_{0.17}(\text{NH}_4)_{0.66}\text{-Y}$ . Spinning sidebands are indicated by a \*.

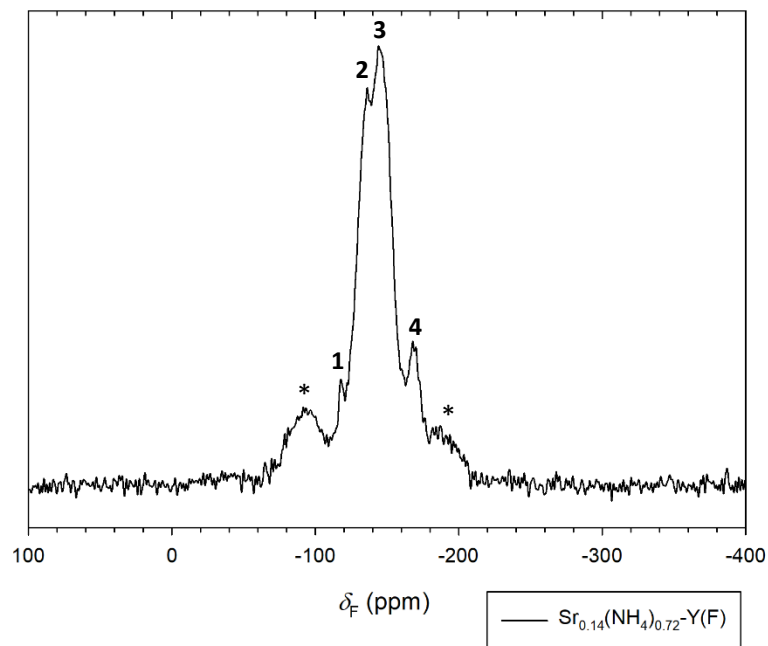


Figure 5.35.  $^{19}\text{F}$  MAS NMR spectrum of fluorinated  $\text{Sr}_{0.14}(\text{NH}_4)_{0.72}\text{-Y}$ . Spinning sidebands are indicated by a \*.

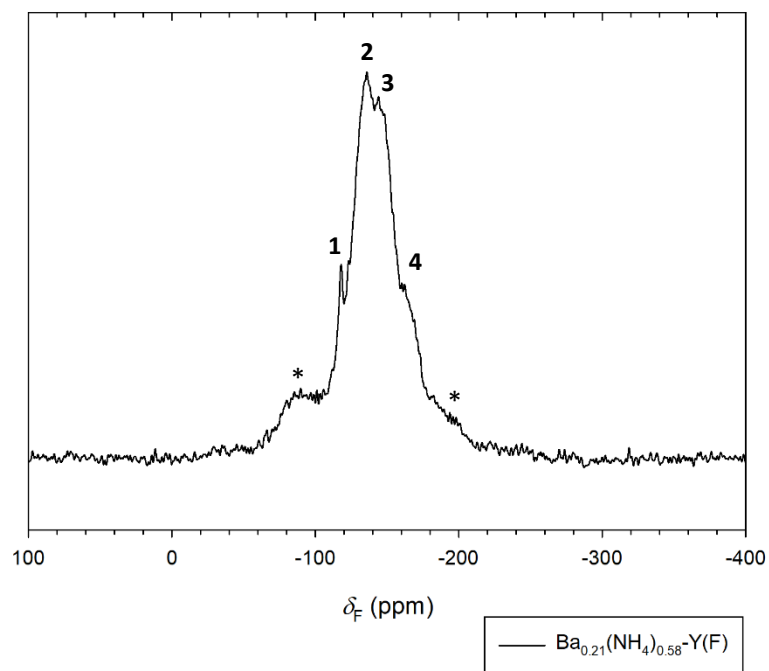


Figure 5.36.  $^{19}\text{F}$  MAS NMR spectrum of fluorinated  $\text{Ba}_{0.21}(\text{NH}_4)_{0.58}\text{-Y}$ . Spinning sidebands are indicated by a \*.

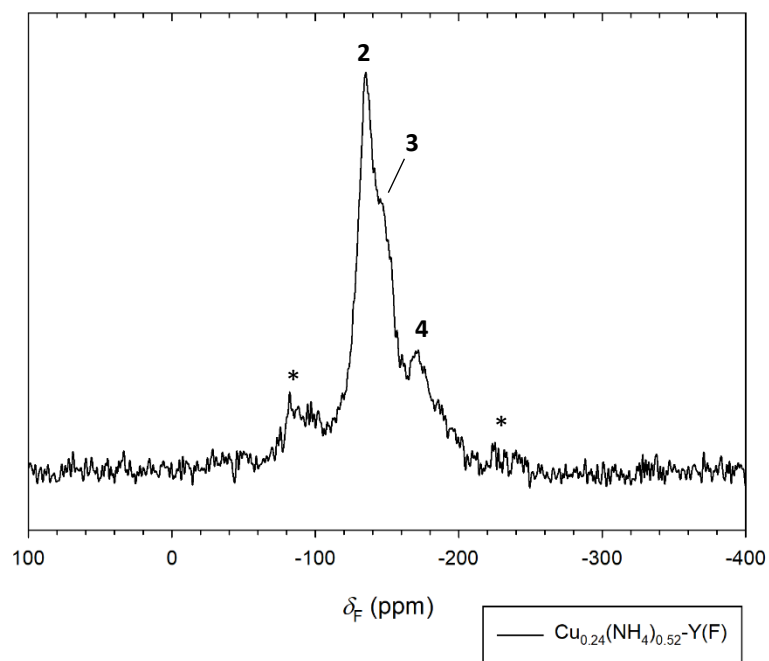


Figure 5.37.  $^{19}\text{F}$  MAS NMR spectrum of fluorinated  $\text{Cu}_{0.24}(\text{NH}_4)_{0.52}\text{-Y}$ . Spinning sidebands are indicated by a \*.

There are some clear differences exhibited in the  $^{19}\text{F}$  MAS NMR spectrum recorded on fluorinated  $\text{Cu}_{0.24}(\text{NH}_4)_{0.52}\text{-Y}$  compared with the fluorinated alkaline earth ion-exchanged zeolites. The spectrum is dominated by resonance **2**, the unassigned peak, with a shoulder at  $\delta_{\text{F}} \approx -146$  ppm corresponding to resonance **3**, the  $[\text{SiO}_3\text{F}]$  environment. Resonance **4** corresponding to the  $[\text{AlO}_3\text{F}]$  environment is also present at  $\delta_{\text{F}} \approx -171$  ppm, albeit with low intensity.

Differences in the experimental conditions under which  $\text{Cu}_{0.24}(\text{NH}_4)_{0.52}\text{-Y}$  was prepared, compared with the alkaline earth ion-exchanged zeolites, may be pertinent to the differences in the relative populations of resonances in the  $^{19}\text{F}$  MAS NMR spectrum of fluorinated  $\text{Cu}_{0.24}(\text{NH}_4)_{0.52}\text{-Y}$  compared with the spectra of other divalent metal ion-exchanged zeolites. Copper(II) ions are more polarising in aqueous solution than alkaline earth metal ions. Accordingly, copper(II) solutions are significantly more acidic than solutions of alkaline earth metal ions with the same concentration and counter-anion. The pH values measured for 0.25 M  $\text{M}(\text{NO}_3)_2$  solutions, where M = Mg, Ca, Sr and Ba, fall within the range 5 to 6. In contrast, the value pH = 3.41 was measured for a 0.25 M  $\text{Cu}(\text{NO}_3)_2$  solution. The enhanced acidity could lead to two significant effects at the zeolite surface during contact with the solution. Firstly, dealumination may occur at this pH value, producing more surface silanol moieties in close proximity on the surface.<sup>137</sup> Secondly,  $\text{H}^+$ -ion exchange between aqueous protons and intrapore ammonium ions may occur during treatment with the acidic copper(II) nitrate solution. While there is no discernible difference in the Si/Al ratios measured by XRF spectrometry on the parent material,  $\text{NH}_4\text{-Y}$ , and the copper(II) exchanged derivative,  $\text{Cu}_{0.24}(\text{NH}_4)_{0.52}\text{-Y}$ , this may be because the technique, as applied, is insufficiently sensitive to detect the change in Si/Al ratio upon dealumination. Some dealumination occurring during treatment with the copper(II) nitrate solution is, therefore, possible. Moreover, it is not possible to determine to what extent  $\text{H}^+$ -ion exchange into the zeolite has occurred. The origin of resonance **2**, observed at  $\delta_{\text{F}} \approx -136$  ppm, is unclear. If present in the  $\text{M}_x(\text{NH}_4)_{1-2x}\text{-Y}$  species, resonances for  $[\text{SiO}_4\text{F}]$  moieties would be expected at  $\delta_{\text{F}} \approx -136$  ppm, approximately 10 ppm downfield of the  $[\text{SiO}_3\text{F}]$  resonances. Silicon-29 MAS NMR spectra recorded on fluorinated  $\text{Sr}_{0.14}(\text{NH}_4)_{0.72}\text{-Y}$  and

$\text{Cu}_{0.24}(\text{NH}_4)_{0.52}\text{-Y}$ , Figures 5.38 and 5.39, respectively, show no intensity in the region where five co-ordinate silicon resonances would be expected, between -125 and -150 ppm. It could be argued that the population of silicon in a five co-ordinate environment would be too low to give rise to a discernible peak in the  $^{29}\text{Si}$  MAS NMR spectra; however, if all the fluoride adsorbed by  $\text{Cu}_{0.24}(\text{NH}_4)_{0.52}\text{-Y}$  were bonded to silicon in  $[\text{SiO}_4\text{F}]$  moieties, this would correspond to *ca.* 2% of all silicon atoms within the zeolite present as  $[\text{SiO}_4\text{F}]$  moieties. While the  $^{19}\text{F}$  MAS NMR spectrum for  $\text{Cu}_{0.24}(\text{NH}_4)_{0.52}\text{-Y}$  demonstrates the presence of  $[\text{SiO}_3\text{F}]$  and  $[\text{AlO}_3\text{F}]$ , it is dominated by resonance **2**, thus if most fluoride were present in a five co-ordinate environment, a discernible corresponding peak would be anticipated in the  $^{29}\text{Si}$  MAS NMR spectrum. Ultimately, the absence of such a peak renders  $[\text{SiO}_4\text{F}]$  moieties unlikely to be responsible for resonance **2**.

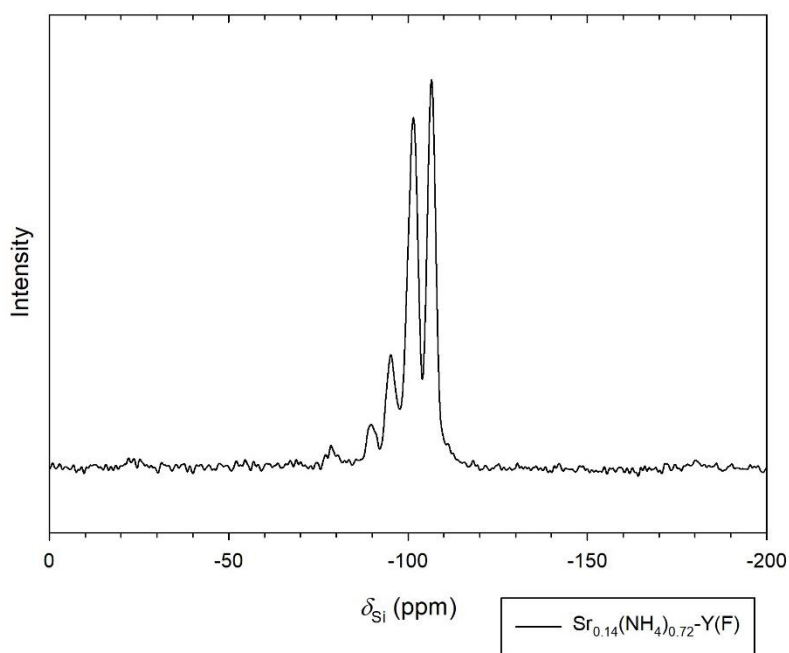


Figure 5.38.  $^{29}\text{Si}$  MAS NMR spectrum of fluorinated  $\text{Sr}_{0.14}(\text{NH}_4)_{0.72}\text{-Y}$ .

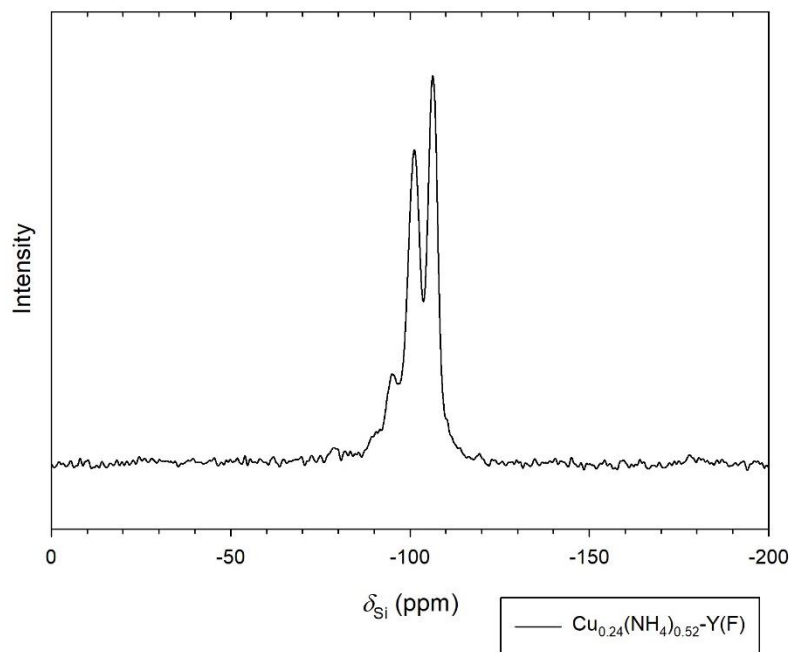


Figure 5.39.  $^{29}\text{Si}$  MAS NMR spectrum of fluorinated  $\text{Cu}_{0.24}(\text{NH}_4)_{0.52}\text{-Y}$ .

Hexafluorosilicate anions are most commonly observed at chemical shifts near to the unassigned peak,  $\delta_{\text{F}} \approx -129$  ppm; however, hexafluorosilicate ions are unlikely to be responsible for resonance **2**, as there is no corresponding peak present at  $\delta_{\text{Si}} \approx -189$  ppm in the  $^{29}\text{Si}$  MAS NMR spectra recorded on  $\text{Sr}_{0.14}(\text{NH}_4)_{0.72}\text{-Y(F)}$  and  $\text{Cu}_{0.24}(\text{NH}_4)_{0.52}\text{-Y(F)}$ .<sup>131</sup> The invariance of the chemical shift with changing intrapore cation makes an environment bonding directly to the divalent cation unlikely, as changes in the effective nuclear charge of the cations would significantly affect the chemical shift of an associated fluoride ion upon changing the cation.<sup>135</sup> Moreover, the likely presence of this environment in fluorinated  $\text{NH}_4\text{-Y}$  further supports that an environment directly bonded to a divalent metal ion is not responsible for the resonance.

A resonance at  $\delta_{\text{F}} \approx -135$  ppm has been observed in fluorinated derivatives previously, but the responsible moiety was not identified.<sup>111,113</sup> The  $[\text{SiO}_2\text{F}_2]$  moiety was put forward in each study as a candidate responsible for the resonance. For fluorination to proceed by the established mechanism,  $[\text{SiO}_2\text{F}_2]$  moieties could only be produced by substitution of fluoride for both hydroxide components

of geminal silanol moieties (i.e.  $[\text{SiO}_2(\text{OH})_2]$ ). If some dealumination occurs in the production of  $\text{Cu}_{0.24}(\text{NH}_4)_{0.52}\text{-Y}$ , the concentration of geminal silanol moieties may increase, relative to the parent material, upon extrication of aluminium from sites neighbouring  $[\text{SiO}_3(\text{OH})]$  functionalities. While  $\text{Cu}_{0.24}(\text{NH}_4)_{0.52}\text{-Y}$  may possess an increased population of geminal silanol moieties, the concentration of geminal silanol moieties would not increase upon partial ion-exchange with alkaline earth metal ions, as the solutions are insufficiently acidic for any degree of dealumination to occur. As the geminal silanol concentration would not increase following ion exchange to produce the alkaline earth containing  $\text{M}_x(\text{NH}_4)_{1-2x}\text{-Y}$  species, the divalent ions must preferentially promote fluorination at geminal silanol moieties in zeolites for  $[\text{SiO}_2\text{F}_2]$  groups to be responsible for resonance **2**.

A new theoretical assignment is that neighbouring or proximal  $[\text{SiO}_3\text{F}]$  groups may give rise to resonance **2**. The presence of  $[\text{SiO}_3\text{F}]$  groups in close proximity could cause deshielding of the fluorine nuclei leading to the  $[\text{SiO}_3\text{F}]$  resonances occurring at a less negative chemical shift than is typically observed. If sufficiently close, fluoride atoms bonded to the framework could exert Coulombic repulsion on one another through space, serving to distort the electron cloud and subsequently affect the shielding of the fluorine nuclei. Furthermore, the presence of fluorine substituents on neighbouring silicon atoms in the framework could lead to increased polarity of the Si-F bonds, deshielding the fluorine nuclei through inductive effects. Comparable downfield shifts (*ca.* 10 ppm) are observed in  $^{19}\text{F}$  NMR spectra upon the introduction of fluorine substituents at neighbouring carbon atoms in fluoroalkanes.<sup>136</sup> Ultimately, both  $[\text{SiO}_2\text{F}_2]$  and proximal  $[\text{SiO}_3\text{F}]$  functional groups are credible candidates that could be responsible for resonance **2**.

While peak fitting indicates the presence of a resonance at  $\delta_{\text{F}} \approx -135$  ppm in the  $^{19}\text{F}$  MAS NMR spectrum of fluorinated  $\text{NH}_4\text{-Y}$ , the relative population of the resonance is significantly increased in spectra of the fluorinated  $\text{M}_x(\text{NH}_4)_{1-2x}\text{-Y}$  species. The divalent cations must, therefore, promote fluorination at functionalities that produce the moiety responsible for resonance **2**. If either  $[\text{SiO}_2\text{F}_2]$  or proximal  $[\text{SiO}_3\text{F}]$  moieties are responsible for the resonance, the question of how the divalent cations promote

reactivity at geminal silanol or proximal silanol groups, respectively, is raised. It is surmised that a divalent cation on the zeolite surface may co-ordinate the fluoride ion prior to the reaction, bringing the fluoride ion into close proximity to silanol moieties that may neighbour the divalent cation, allowing a reactive intermediate to form more readily. A divalent cation in a fixed position on the surface could promote reactivity at two or more proximal silanol groups, if present. The same argument is applicable to how a divalent cation could promote reactivity at near geminal silanol moieties. In the absence of a divalent cation, reactivity at silanol groups is expected to be random, therefore, accounting for the lower population of the resonance in the  $\text{NH}_4\text{-Y(F)}$  spectrum. Moreover, Coulombic repulsion incurred by proximal fluoride ions may reduce the instances of  $[\text{SiO}_2\text{F}_2]$  or proximal  $[\text{SiO}_3\text{F}]$  formation in the absence of a divalent cation. Naturally, the assignment of the resonance to either  $[\text{SiO}_2\text{F}_2]$  or proximal  $[\text{SiO}_3\text{F}]$  moieties, and how divalent cations may promote reactivity at them, remains only a theory unless empirically proven.

If resonance **2** is caused by either proximal  $[\text{SiO}_3\text{F}]$  or  $[\text{SiO}_2\text{F}_2]$  moieties, the increased relative population of the resonance in the spectrum of fluorinated  $\text{Cu}_{0.24}(\text{NH}_4)_{0.52}\text{-Y}$ , compared with the other fluorinated  $\text{M}_x(\text{NH}_4)_{1-2x}\text{-Y}$  species, may be rationalised by the different conditions under which  $\text{Cu}_{0.24}(\text{NH}_4)_{0.52}\text{-Y}$  was produced. As outlined previously, the increased acidity of the copper(II) nitrate solution, compared with the alkaline earth solutions, may lead to both dealumination of the framework and some  $\text{H}^+$ -ion exchange. The former would lead to an increased proportion of both geminal silanol and proximal silanol moieties on the zeolite surface, reactivity at which would produce  $[\text{SiO}_2\text{F}_2]$  and proximal  $[\text{SiO}_3\text{F}]$  moieties, respectively. Ultimately, this would rationalise the increased relative population of resonance **2** in the spectrum of fluorinated  $\text{Cu}_{0.24}(\text{NH}_4)_{0.52}\text{-Y}$ , compared with the spectra of other fluorinated  $\text{M}_x(\text{NH}_4)_{1-2x}\text{-Y}$  species.

The fluorine environments observed in fluorinated alkaline earth ion-exchanged zeolites correspond to those observed in  $\text{NH}_4\text{-Y(F)}$ , demonstrating the presence of  $[\text{SiO}_3\text{F}]$  and  $[\text{AlO}_3\text{F}]$  moieties, as well as intrapore fluoride anions. An additional resonance, of uncertain origin, is also present in the spectra

of fluorinated  $M_x(\text{NH}_4)_{1-2x}\text{-Y}$  species, which peak fitting indicates may also be present in  $\text{NH}_4\text{-Y(F)}$ , albeit with a lower population. In fluorinated  $\text{Cu}_{0.24}(\text{NH}_4)_{0.52}\text{-Y}$ , the fluorine is principally present in the environment responsible for the unassigned resonance, with comparatively minor amounts present as  $[\text{SiO}_3\text{F}]$  and  $[\text{AlO}_3\text{F}]$  moieties. Critically, while higher fluoride loadings and increased characteristic adsorption energies are observed for  $M_x(\text{NH}_4)_{1-2x}\text{-Y}$  species compared with the parent material ( $\text{NH}_4\text{-Y}$ ), there is no evidence that the divalent metal cations directly co-ordinate the fluoride ions. It would appear the presence of divalent cations promotes the fluorination of zeolites without directly co-ordinating the fluoride ions. A full understanding of how divalent cations promote the reaction is hindered by the unknown identity of the moiety responsible for the unassigned resonance in the  $^{19}\text{F}$  MAS NMR spectra of the fluorinated zeolites.

It was reported in a study on defluorination by a natural Ca/Na-STI sample that ion exchange between intrapore  $\text{Ca}^{2+}$  and aqueous  $\text{Na}^+$  followed by precipitation of  $\text{CaF}_2$  was responsible for the observed fluoride uptake.<sup>107</sup> Fluorine-19 MAS NMR spectra recorded on alkaline earth metal exchanged zeolites ( $M_x(\text{NH}_4)_{1-2x}\text{-Y}$ ) contain no resonance corresponding to  $\text{MF}_2$  species, which would be expected at -107 ( $\text{CaF}_2$ ), -83.2 ( $\text{SrF}_2$ ), -196 ( $\text{MgF}_2$ ) and -11.2 ppm ( $\text{BaF}_2$ ).<sup>135</sup> All  $\text{MF}_2$  species corresponding to the alkaline earth metal-containing zeolites, except  $\text{CaF}_2$ , have a greater solubility than the highest fluoride concentration employed in these studies. As a result ion exchange between aqueous  $\text{Na}^+$  and intrapore  $M^{2+}$  could not give rise to  $\text{MF}_2$  precipitation in these systems.<sup>132</sup> In the case of  $\text{CaF}_2$ , precipitation could occur from solutions with concentrations greater than 7 ppm  $\text{F}^-$ , provided a stoichiometric equivalence of  $\text{Ca}^{2+}$  were present in solution. There is no evidence to support the presence of  $\text{CaF}_2$  in the  $^{19}\text{F}$  MAS NMR spectrum of  $\text{Ca}_{0.17}(\text{NH}_4)_{0.66}\text{-Y(F)}$  as there is no resonance at  $\delta_{\text{F}} \approx -107$  ppm; moreover, in a PXRD pattern recorded on  $\text{Ca}_{0.17}(\text{NH}_4)_{0.66}\text{-Y(F)}$  (Fig. 5.40) there is no intensity where reflections corresponding to  $\text{CaF}_2$  would be expected. Fig. 5.40 presents the PXRD patterns for fluorinated  $\text{Ca}_{0.17}(\text{NH}_4)_{0.66}\text{-Y}$ ,  $\text{Mg}_{0.15}(\text{NH}_4)_{0.70}\text{-Y}$  and  $\text{Sr}_{0.14}(\text{NH}_4)_{0.72}\text{-Y}$ , recorded across the  $2\theta$  range 25 – 50° at a scan rate of  $0.02^\circ \text{ s}^{-1}$ , along with stick plots corresponding to PDF patterns for  $\text{CaF}_2$ ,

SrF<sub>2</sub> and MgF<sub>2</sub>. Ultimately, there is no evidence to support the postulation that precipitation of MF<sub>2</sub> species is responsible for fluoride uptake in M<sub>x</sub>(NH<sub>4</sub>)<sub>1-2x</sub>-Y.

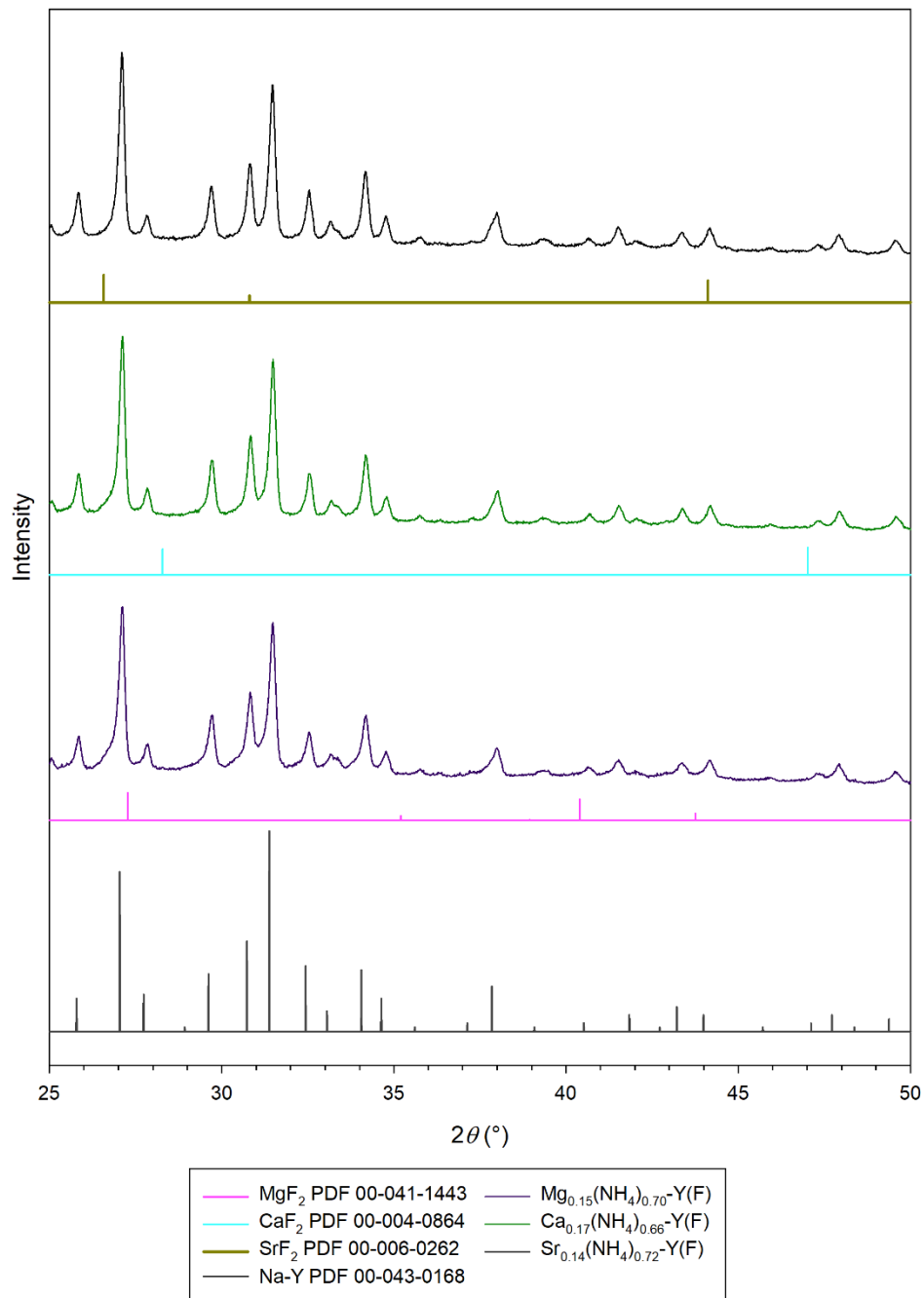


Figure 5.40. PXRD patterns for Mg<sub>0.15</sub>(NH<sub>4</sub>)<sub>0.70</sub>-Y, Ca<sub>0.17</sub>(NH<sub>4</sub>)<sub>0.66</sub>-Y(F) and Sr<sub>0.14</sub>(NH<sub>4</sub>)<sub>0.72</sub>-Y, along with PDF stick plots for Na-Y, MgF<sub>2</sub>, CaF<sub>2</sub> and SrF<sub>2</sub>.

The Si/Al, M/Al and Na/Al ratios in the zeolites, M<sub>x</sub>(NH<sub>4</sub>)<sub>1-2x</sub>-Y, following treatment with 60 ppm F<sup>-</sup> for 24 hours have been determined by XRF spectrometry (Table 5.11). The M/Al ratios are all within error

of those determined for the material prior to fluorination, indicating that negligible ion exchange between aqueous  $\text{Na}^+$  and  $\text{M}^{2+}$  occurs. The Na/Al values demonstrate incorporation of sodium into the zeolite in all cases. Ion exchange between aqueous sodium and intrapore ammonium would provide a proton source at the surface allowing the reaction to proceed in an analogous manner to that observed for the parent material. The incorporation of sodium into the zeolites further supports observations in the NMR spectra that indicate the interaction between the zeolite and fluoride principally occurs in the same manner for both  $\text{NH}_4\text{-Y}$  and  $\text{M}_x(\text{NH}_4)_{1-2x}\text{-Y}$ , where M is an alkaline earth metal.

Table 5.11. Compositional data for  $\text{M}_x(\text{NH}_4)_{1-2x}\text{-Y}$  fluorinated at 25°C with 60 ppm  $\text{F}^-$ .

Zeolite	Temperature (°C)	Si/Al	Na/Al	M/Al
$\text{NH}_4\text{-Y}$	25	2.7(1)	0.14(2)	-
	40	2.7(1)	0.13(2)	-
$\text{Mg}_{0.15}(\text{NH}_4)_{0.70}\text{-Y}$	25	2.8(1)	0.10(2)	0.15(1)
	40	2.8(1)	0.09(3)	0.13(1)
$\text{Ca}_{0.17}(\text{NH}_4)_{0.66}\text{-Y}$	25	2.7(1)	0.08(3)	0.18(1)
	40	2.6(1)	0.06(2)	0.19(1)
$\text{Sr}_{0.14}(\text{NH}_4)_{0.72}\text{-Y}$	25	2.8(1)	0.10(3)	0.15(1)
	40	2.6(1)	0.06(2)	0.17(1)
$\text{Ba}_{0.21}(\text{NH}_4)_{0.58}\text{-Y}$	25	2.7(1)	0.14(2)	0.19(1)
	40	2.6(1)	0.07(3)	0.22(1)
$\text{Cu}_{0.24}(\text{NH}_4)_{0.52}\text{-Y}$	25	2.9(1)	0.07(2)	0.22(1)
	40	2.9(1)	0.07(2)	0.22(1)

#### 5.4.6 $M_xNa_{1-2x}Y$ : Fluoride Loadings

Equilibrium fluoride loadings were measured for  $M_xNa_{1-2x}Y$  (where  $M = Mg^{2+}, Ca^{2+}, Sr^{2+}, Ba^{2+}$  and  $Cu^{2+}$ ) at 25°C from 20 ppm  $F^-$  NaF solutions. The concentration 20 ppm  $F^-$  was selected because as the concentration increases, the change in concentration per each 0.1 mV step recorded by the fluoride ISE also increases. As the absolute error in measurements at higher concentrations is greater, in systems where the difference between the initial and final concentration is small but both values are relatively high, there is a greater relative error in the measurement, consequently there is greater sensitivity to more subtle changes at lower concentrations. The concentration 20 ppm  $F^-$  was selected as greater loadings are observed compared with at lower concentrations, but the relative error is smaller than at higher concentrations.

Equilibrium fluoride loadings ( $q_e$ ) for  $M_xNa_{1-2x}Y$  and  $M_x(NH_4)_{1-2x}Y$  from 20 ppm  $F^-$  solutions are listed in Table 5.12. Despite higher divalent metal contents in  $M_xNa_{1-2x}Y$  species compared with  $M_x(NH_4)_{1-2x}Y$ , equilibrium loadings for  $M_xNa_{1-2x}Y$ , where  $M$  is an alkaline earth cation, are much lower than the analogous  $M_x(NH_4)_{1-2x}Y$  species, with equilibrium loadings for  $M_xNa_{1-2x}Y$  corresponding to between 2.6 – 6.3% of the loadings attained for  $M_x(NH_4)_{1-2x}Y$ . As the pH of the fluoride solutions are near neutral (pH = 6.8) and there is no proton source, this further supports the essential role of protons in mediating fluoride uptake in the divalent substituted zeolites.

While the fluoride loadings achieved for  $M_xNa_{1-2x}Y$  species are low compared with the loadings for  $M_x(NH_4)_{1-2x}Y$  under the same conditions, there is still detectable fluoride uptake for  $M_xNa_{1-2x}Y$  which is not observed for the parent compound Na-Y under the same conditions. As there is no proton source in the  $M_xNa_{1-2x}Y$  species, where  $M$  is an alkaline earth metal, the only fluoride environment observed in these  $M_x(NH_4)_{1-2x}Y$  species that would be anticipated in the  $M_xNa_{1-2x}Y$  analogues is the intrapore fluoride environment. The presence of this environment in  $M_xNa_{1-2x}Y$ , but not in Na-Y, may be rationalised by the greater accessibility to the pores afforded by lower intrapore cation

concentrations, allowing the migration of Na<sup>+</sup>F<sup>-</sup> ion pairs into the framework. Intrapore free fluoride being responsible for the observed uptake in M<sub>x</sub>Na<sub>1-2x</sub>-Y remains supposition, however, as NMR experiments have not been performed on fluorinated M<sub>x</sub>Na<sub>1-2x</sub>-Y species due to the low fluoride content and long experiment durations required to obtain informative spectra.

A higher equilibrium loading is observed for Cu<sub>0.41</sub>Na<sub>0.29</sub>-Y than the partially alkaline earth ion-exchanged M<sub>x</sub>Na<sub>1-2x</sub>-Y species, with  $q_e$  for Cu<sub>0.41</sub>Na<sub>0.29</sub>-Y corresponding to 14% of  $q_e$  for Cu<sub>0.24</sub>(NH<sub>4</sub>)<sub>0.52</sub>-Y. As previously noted, the significantly higher acidity of copper(II) solutions compared with alkaline earth metal solutions may lead to some degree of H<sup>+</sup>-ion exchange in the preparation of copper(II)-exchanged zeolites. If some degree of H<sup>+</sup>-ion exchange occurs concomitantly with Cu<sup>2+</sup>-ion exchange, this would lead to a source of protons in Cu<sub>0.41</sub>Na<sub>0.29</sub>-Y which may in turn participate in fluorination reactions, rationalising the enhanced fluoride loading attained for Cu<sub>0.41</sub>Na<sub>0.29</sub>-Y compared with other M<sub>x</sub>Na<sub>1-2x</sub>-Y species.

Table 5.12. Equilibrium fluoride loadings achieved by M<sub>x</sub>Na<sub>1-2x</sub>-Y and M<sub>x</sub>(NH<sub>4</sub>)<sub>1-2x</sub>-Y from 20 ppm F<sup>-</sup> NaF solutions at 25°C.

M	$q_e$ (M <sub>x</sub> Na <sub>1-2x</sub> -Y) (mg g <sup>-1</sup> )	$q_e$ (M <sub>x</sub> (NH <sub>4</sub> ) <sub>1-2x</sub> -Y) (mg g <sup>-1</sup> )	% $q_e$ (M <sub>x</sub> Na <sub>1-2x</sub> -Y)/ $q_e$ (M <sub>x</sub> (NH <sub>4</sub> ) <sub>1-2x</sub> -Y)
Mg	0.11	1.88	5.9
Ca	0.14	2.74	5.1
Sr	0.07	2.64	2.6
Ba	0.12	1.92	6.3
Cu	0.34	2.41	14.1

#### 5.4.7 Conclusions

Partial ion exchange of divalent alkaline earth cations (Mg<sup>2+</sup>, Ca<sup>2+</sup>, Sr<sup>2+</sup> and Ba<sup>2+</sup>) into NH<sub>4</sub>-Y leads to enhanced fluoride loadings achieved and an increase in the characteristic adsorption energy in all cases, compared with the parent material (NH<sub>4</sub>-Y). In contrast, there is little change in the fluoride

uptake measured for the divalent cation exchanged forms of Na-Y compared with the parent material, with comparatively low uptake observed for all  $M_xNa_{1-2x}$ -Y species. Fluorine-19 MAS NMR spectroscopy reveals no direct M-F bonds are formed in fluorinated alkaline earth metal-containing zeolites, nor are  $MF_2$  species precipitated, rather the reaction appears to proceed in the same manner as for  $NH_4$ -Y evidenced by resonances attributable to the  $[SiO_3F]$ ,  $[AlO_3F]$  and intrapore fluoride environments. An additional resonance of unknown origin is also present at  $\delta_F \approx -136$  ppm in the  $^{19}F$  MAS NMR spectra. It has been postulated that the resonance is produced by either  $[SiO_2F_2]$  or proximal  $[SiO_3F]$  moieties with the downfield shift possibly caused by both through space Coulombic repulsion between proximal fluorine atoms and inductive effects leading to deshielding of the fluorine nuclei. A theory has been put forward for how divalent cations could promote fluoride reactivity at geminal or proximal silanol moieties, however, the assignment remains unproven. Ultimately, it appears the  $H^+$ -mediated mechanism for fluorination is also responsible for the observed uptake in  $M_x(NH_4)_{1-2x}$ -Y species. As there is no evidence to suggest that the divalent ion directly co-ordinates fluoride, the presence of the divalent ion nevertheless increases the loading and characteristic adsorption energy for the process, therefore promoting fluoride uptake in the zeolites.

The partial exchange of  $Cu^{2+}$  into  $NH_4$ -Y leads to enhanced fluoride loadings and characteristic adsorption energies, as in the case of the alkaline earth ion-exchanged zeolites. In contrast to the alkaline earth ion-exchanged zeolites, the  $^{19}F$  MAS NMR spectrum recorded on  $Cu_{0.24}(NH_4)_{0.52}$ -Y demonstrates fluoride principally resides in the unassigned environment that produces resonances at  $\delta_F \approx -136$  ppm. The spectrum also contains lower intensity resonances attributed to both  $[SiO_3F]$  and  $[AlO_3F]$  moieties. There is no evidence in the  $^{19}F$  MAS NMR spectrum for direct co-ordination of fluorine to  $Cu^{2+}$ . The different distribution of fluoride environments present in fluorinated  $Cu_{0.24}(NH_4)_{0.52}$ -Y may be an artefact from the acidity of the copper(II) nitrate solution employed in the ion exchange process, perhaps giving rise to dealumination, increasing the number of proximal and geminal silanol moieties on the zeolite surface.

The promotion of the fluorination reaction by the divalent cations raises the question: in what way does the cation promote the reaction with respect to the mechanism? It is possible that the promotion of the reaction by a divalent cation is partly caused by the lower overall intrapore cation concentration and higher charge density of the cation in the partially exchanged zeolites, compared with the parent material, increasing pore accessibility to fluoride permitting access to more surface hydroxyl sites and favourability by enhanced Coulombic attraction. Moreover, divalent ions residing on the surface may serve to co-ordinate fluoride ions in reactive intermediates, lowering the energy of the intermediate and increasing favourability of the process by bringing the fluoride ions into close proximity to surface hydroxyl sites, as postulated in Section 5.4.5.

### 5.5 Results Part 3: Fluoride Uptake in Dealuminated NH<sub>4</sub>-Y

#### 5.5.1 Introduction

The impact of dealumination in NH<sub>4</sub>-Y by H<sub>4</sub>EDTA, ethylenediaminetetraacetic acid, on fluoride uptake has been investigated. H<sub>4</sub>EDTA extricates Al<sup>3+</sup> from zeolite frameworks as soluble [NH<sub>4</sub>AlEDTA] complexes, in the case of NH<sub>4</sub>-Y, leading to the formation of hydroxyl nests in the dealuminated zeolite products, as illustrated in Figure 5.41.<sup>121,137</sup> Dealuminated NH<sub>4</sub>-Y, (D)-NH<sub>4</sub>-Y, was prepared by action of H<sub>4</sub>EDTA on NH<sub>4</sub>-Y in aqueous slurries at ambient temperature, as described in Section 5.2.4.

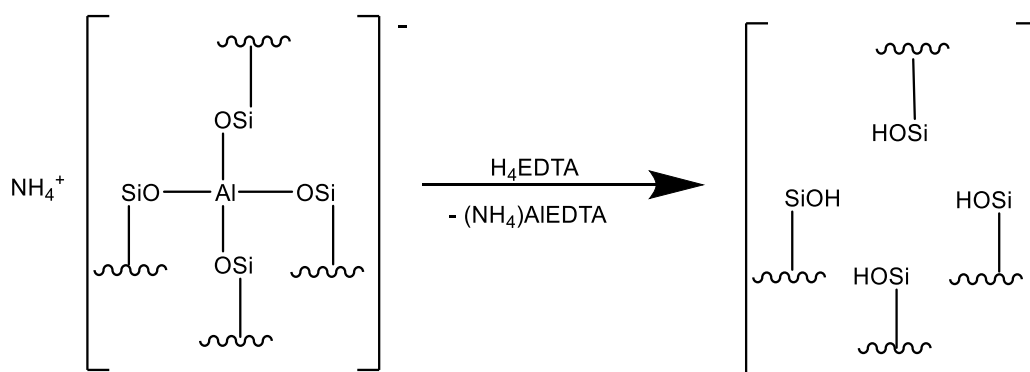


Figure 5.41. Schematic representation of the dealumination of NH<sub>4</sub>-Y and the formation of silanol nests.

### 5.5.2 Characterisation

(D)-NH<sub>4</sub>-Y has a greater Si/Al ratio (Si/Al = 4.9(2)) than the parent material NH<sub>4</sub>-Y (Si/Al = 2.6(1)), as measured by XRF spectrometry, attesting dealumination has occurred. PXRD demonstrates a significant decrease in crystallinity occurs upon dealumination (Figure 5.42); the intensity of the 331 reflection at  $2\theta = 15.7^\circ$  for (D)-NH<sub>4</sub>-Y is just 16% of the intensity observed for NH<sub>4</sub>-Y. While there are no additional peaks, a shoulder on the 111 reflection at  $2\theta \approx 6 - 7^\circ$  is present reflecting sample heterogeneity. The shoulder likely corresponds to (111) planes in areas on the zeolite surface where more dealumination has occurred than in the rest of the sample, giving rise to local contractions in interplanar spacings, reflecting contractions in unit cells with increasing dealumination. A unit cell refinement of indexed peaks in the PXRD pattern gives  $a = 24.46(1) \text{ \AA}$  and  $V = 14,634(18) \text{ \AA}^3$ . A scanning electron micrograph of (D)-NH<sub>4</sub>-Y (Fig. 5.43) demonstrates no significant change in morphology or particle size upon dealumination compared with the parent material NH<sub>4</sub>-Y (Fig. 5.3).

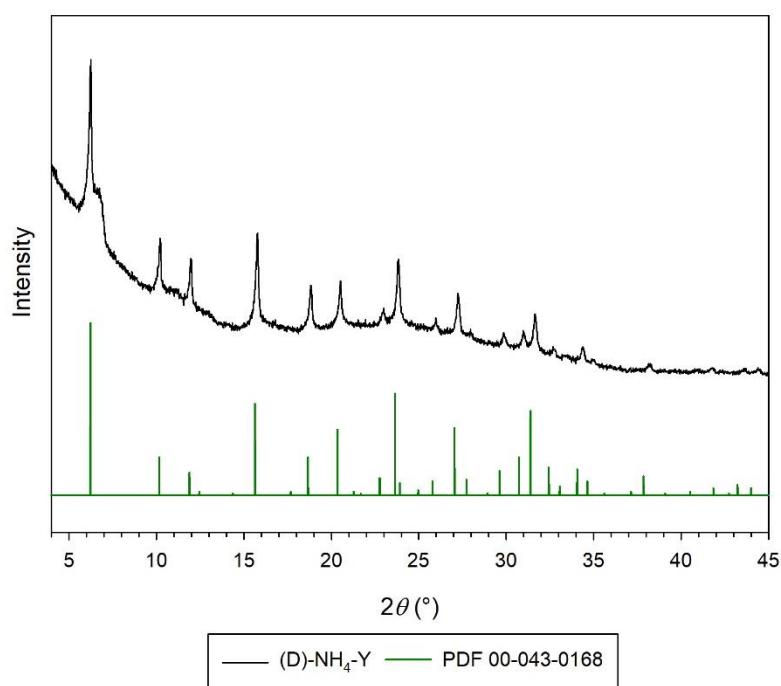


Figure 5.42. PXRD pattern for (D)-NH<sub>4</sub>-Y and a reference pattern for Na-Y (PDF 00-043-0168).

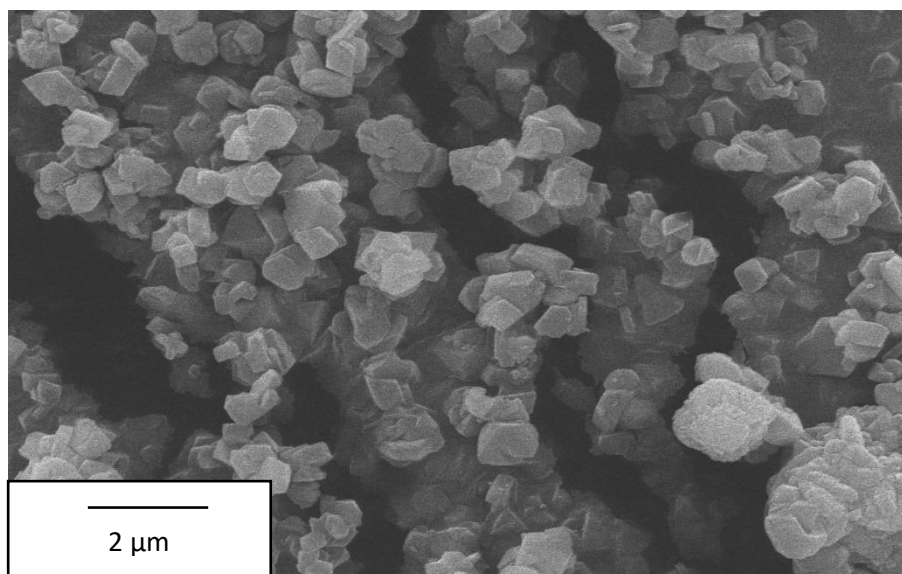


Figure 5.43. Scanning electron micrograph of (D)-NH<sub>4</sub>-Y.

### 5.5.3 Fluoride Loadings and Adsorption Isotherms

A significant increase in fluoride loadings achieved by (D)-NH<sub>4</sub>-Y is observed compared with the parent material at both 25°C and 40°C, plotted in Figures 5.44 and 5.45, respectively. Fitting to the Temkin, Langmuir and Freundlich isotherms has been tested for equilibrium uptake data,  $R^2$  values for each fit and isotherm parameters for the Freundlich isotherm are listed in Table 5.13 along with the corresponding values for the parent material, NH<sub>4</sub>-Y. Despite reasonable  $R^2$  values for the Temkin and Langmuir isotherms, a non-linear distribution of data points is observed qualitatively in the corresponding plots (Appendix 1). Excellent agreement to the Freundlich isotherm is observed for fluoride uptake by (D)-NH<sub>4</sub>-Y at both temperatures, as plotted in Figure 5.46. An increase in  $K_F$  and a decrease in  $n$  compared with the parent material attest that fluoride adsorption is more favourable for (D)-NH<sub>4</sub>-Y than NH<sub>4</sub>-Y.

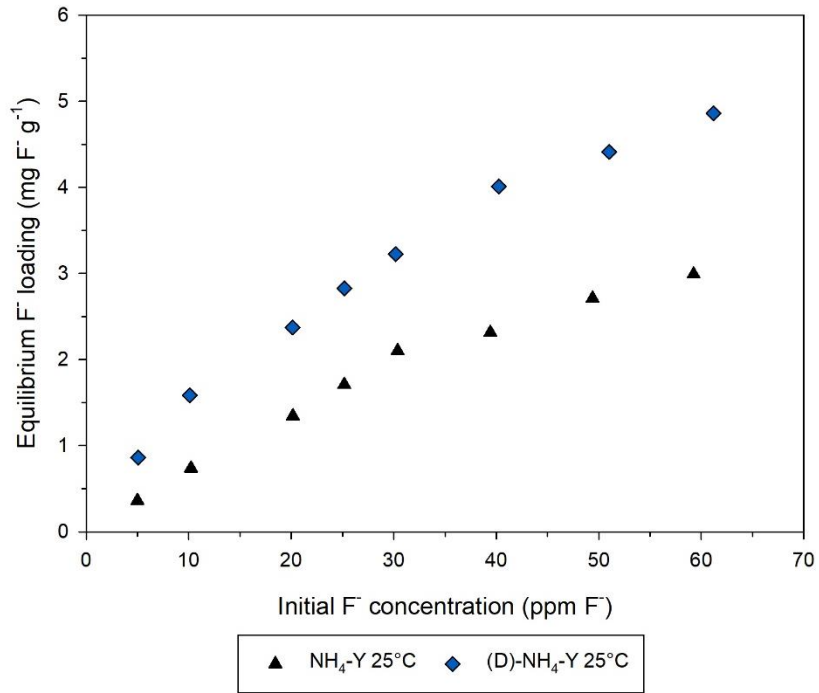


Figure 5.44. Equilibrium fluoride loadings attained for (D)-NH<sub>4</sub>-Y and NH<sub>4</sub>-Y at 25°C as a function of initial fluoride concentration.

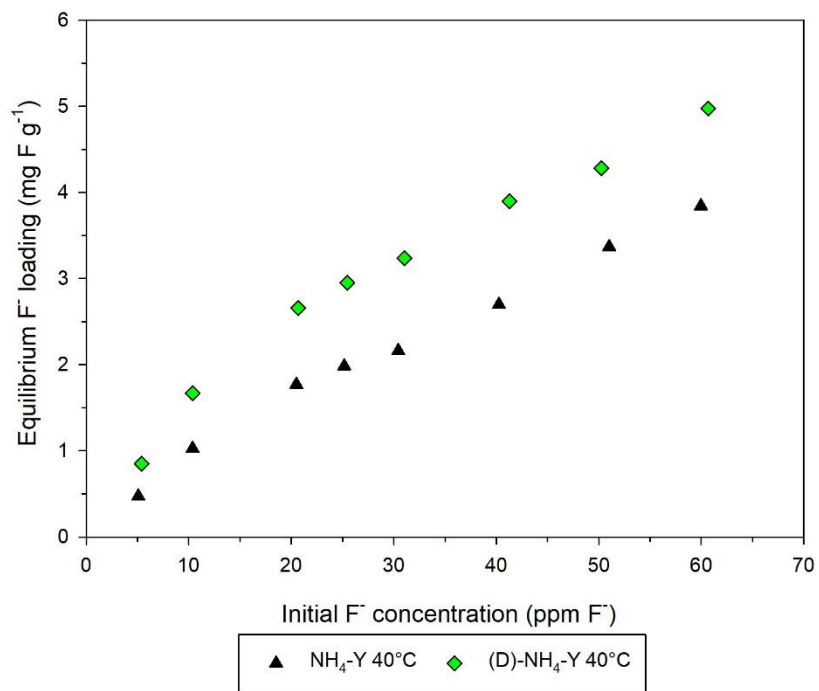


Figure 5.45. Equilibrium fluoride loadings attained for (D)-NH<sub>4</sub>-Y and NH<sub>4</sub>-Y at 40°C as a function of initial fluoride concentration.

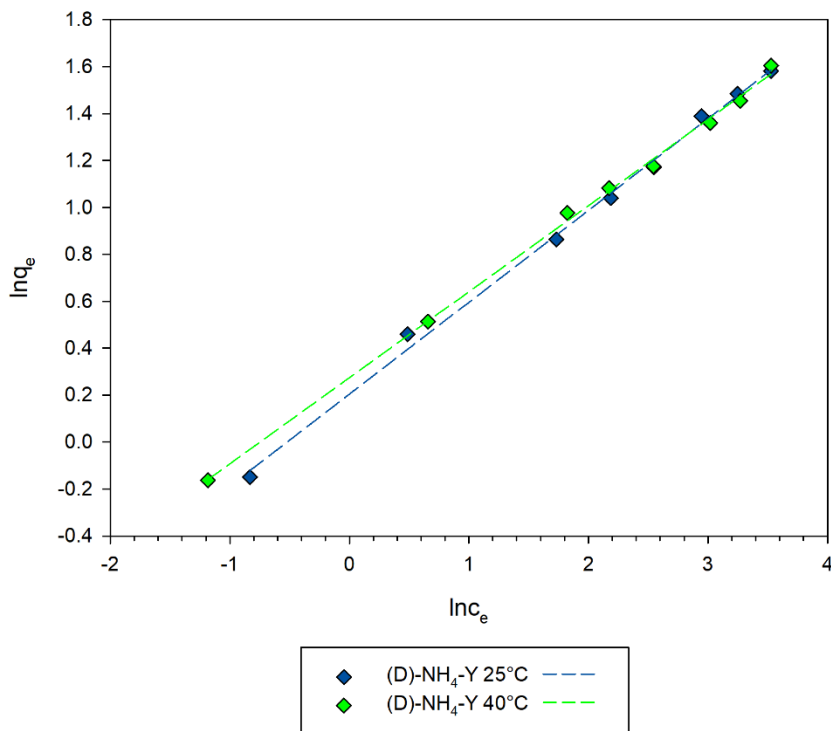


Figure 5.46. Freundlich plots for (D)-NH<sub>4</sub>-Y at 25 and 40°C.

Table 5.13.  $R^2$  for fits to the Temkin, Langmuir and Freundlich isotherms, and Freundlich isotherm parameters, for (D)-NH<sub>4</sub>-Y and NH<sub>4</sub>-Y at 25 and 40°C. The units of  $K_F$  are  $(\text{mg g}^{-1})/(\text{mg L}^{-1})^n$ .

Zeolite	Temp. (°C)	Freundlich			Temkin	Langmuir
		$R^2$	$K_F$	$n$	$R^2$	$R^2$
NH <sub>4</sub> -Y	25	0.982	0.17	0.800	0.968	0.950
	40	0.982	0.28	0.716	0.939	0.931
(D)-NH <sub>4</sub> -Y	25	0.997	1.23	0.392	0.938	0.966
	40	0.998	1.32	0.367	0.930	0.962

Fitting fluoride adsorption data for (D)-NH<sub>4</sub>-Y to the DR isotherm results in good agreement with the model at both temperatures, plots are presented in Figure 5.47 and  $R^2$  values and isotherm parameters for both plots are presented in Table 5.14. A substantial increase in the characteristic fluoride adsorption energy ( $E_C$ ) occurs following dealumination, with  $E_C$  increasing by 4.1 kJ mol<sup>-1</sup> compared to the parent material at 25°C and increasing by 4.3 kJ mol<sup>-1</sup> at 40°C.

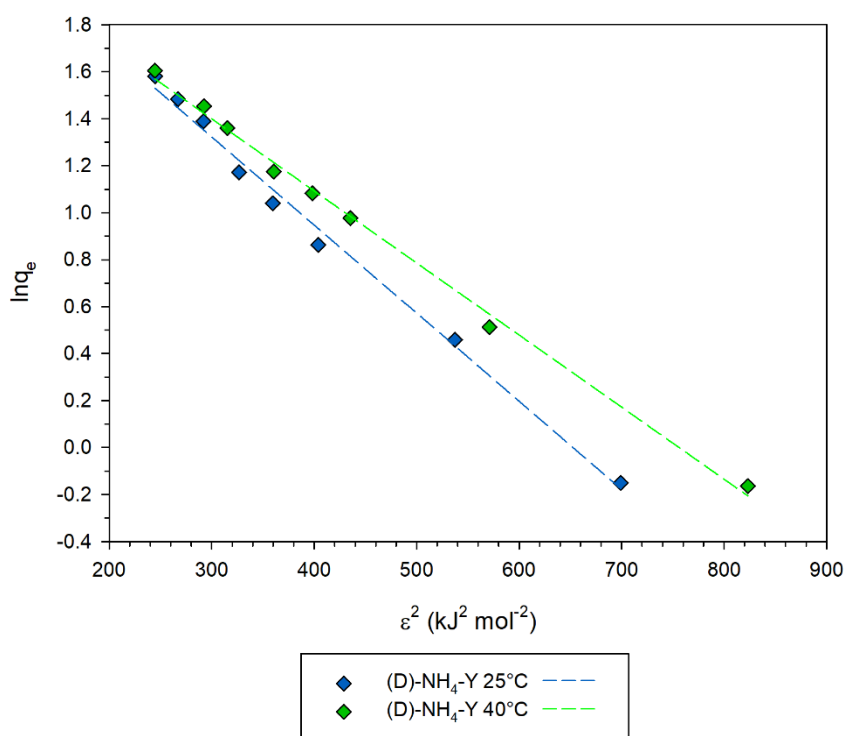


Figure 5.47. DR plots for (D)-NH<sub>4</sub>-Y at 25 and 40°C.

Table 5.14.  $R^2$ , isotherm parameters and  $E_c$  for fits to the DR isotherm for (D)-NH<sub>4</sub>-Y and NH<sub>4</sub>-Y at 25 and 40°C.

Zeolite	Temperature (°C)	$R^2$	$E_c$ (kJ mol <sup>-1</sup> )	$K$ (x10 <sup>-3</sup> mol <sup>2</sup> /kJ <sup>2</sup> )	$V_0/V_m$
NH <sub>4</sub> -Y	25	0.992	7.5	8.85	24.0
	40	0.989	8.5	7.00	23.4
(D)-NH <sub>4</sub> -Y	25	0.993	11.6	3.75	11.6
	40	0.996	12.8	3.07	10.0

#### 5.5.4 <sup>19</sup>F MAS NMR spectroscopy

The <sup>19</sup>F MAS NMR spectrum recorded on (D)-NH<sub>4</sub>-Y (Figure 5.48), fluorinated at 25°C with 60 ppm F<sup>-</sup>, exhibits 4 distinct resonances at  $\delta_F \approx -123, -136, -162$  and  $-176$  ppm, with intensity outside of this range caused by spinning sidebands, rather than fluorine environments in the material. The resonance labelled **iv** at  $\delta_F \approx -176$  ppm in the fluorinated (D)-NH<sub>4</sub>-Y spectrum corresponds to [AlO<sub>3</sub>F], observed in

fluorinated  $\text{NH}_4\text{-Y}$  at the same chemical shift. The resonance labelled **i** at  $\delta_{\text{F}} \approx -123$  ppm is within the range reported for the intrapore fluoride environment. The shift in resonance **i** from  $\delta_{\text{F}} \approx -119$  ppm in  $\text{NH}_4\text{-Y(F)}$  may be attributed to differences in intrapore cation concentration and local mesoporosity introduced by the heterogenous dealumination of the framework, consequently affecting the intrapore environment.<sup>118</sup> The origin of the sharp resonance **iii** at  $\delta_{\text{F}} \approx -162$  ppm is unknown.

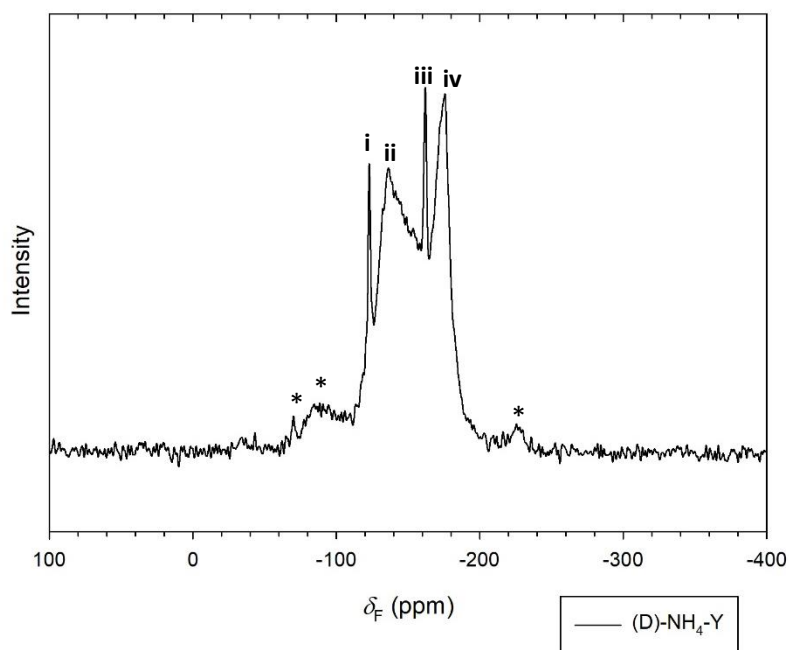


Figure 5.48.  $^{19}\text{F}$  MAS NMR spectrum of fluorinated (D)- $\text{NH}_4\text{-Y}$ .

Interestingly, despite the anticipated increase of silanol functionalities in (D)- $\text{NH}_4\text{-Y}$  relative to  $\text{NH}_4\text{-Y}$  caused by dealumination, there is no distinct resonance at  $\delta_{\text{F}} \approx -153$  ppm where the  $[\text{SiO}_3\text{F}]$  resonance is observed in the parent material. There is a resonance at  $\delta_{\text{F}} \approx -136$  ppm, however, akin to those observed in the  $^{19}\text{F}$  MAS NMR spectra recorded on fluorinated  $\text{M}_x(\text{NH}_4)_{1-2x}\text{-Y}$  species. In Section 5.4.5, it was theorised that this resonance is caused by either  $[\text{SiO}_2\text{F}_2]$  or proximal  $[\text{SiO}_3\text{F}]$  species, shifted downfield due to inductive effects and Coulombic repulsion. An increased density of geminal silanol or proximal silanol groups, such as those in silanol nests, would be anticipated following dealumination by  $\text{H}_4\text{EDTA}$ . In turn, an increase in the amount of both  $[\text{SiO}_2\text{F}_2]$  and proximal  $[\text{SiO}_3\text{F}]$  species would be expected from substitution of fluoride at geminal and proximal silanol moieties,

respectively. The observation of this resonance in fluorinated (D)-NH<sub>4</sub>-Y provides support for the theorised assignment of resonances at  $\delta_F \approx -136$  ppm in <sup>19</sup>F MAS NMR spectra to either [SiO<sub>2</sub>F<sub>2</sub>] or proximal [SiO<sub>3</sub>F] species. This will remain supposition, however, unless empirically proven.

#### 5.5.5 Conclusions

Dealumination of NH<sub>4</sub>-Y by treatment with H<sub>4</sub>EDTA leads to an increase in fluoride loadings attained compared with the parent material under the probed conditions. Good agreement is observed to both the Freundlich and DR isotherms for (D)-NH<sub>4</sub>-Y with the characteristic fluoride sorption energy indicating adsorption is significantly more favourable for (D)-NH<sub>4</sub>-Y compared with NH<sub>4</sub>-Y. Fluorine-19 MAS NMR spectroscopy has revealed the presence of [AlO<sub>3</sub>F] and intrapore fluoride environments in fluorinated (D)-NH<sub>4</sub>-Y, as well as an environment which may be caused by either [SiO<sub>2</sub>F<sub>2</sub>] or proximal [SiO<sub>3</sub>F] species.

### 5.6 Overall Conclusions

The interaction between zeolites and aqueous fluoride in dilute solutions has been studied revealing a greater mechanistic understanding of the fluorination reaction that occurs. The essential role of a Brønsted acid in mediating the fluorination of zeolite frameworks has been established. The Brønsted acid may be an intrapore cation such as NH<sub>4</sub><sup>+</sup> or H<sup>+</sup>, released upon ion exchange with aqueous Na<sup>+</sup> permitting participation in the fluorination reaction. The fluorination of zeolite frameworks at low temperatures (25°C) from low concentration solutions (5 – 60 ppm F<sup>-</sup>) leading to the formation of [SiO<sub>3</sub>F] and [AlO<sub>3</sub>F] species has been demonstrated. Moreover, <sup>29</sup>Si{<sup>1</sup>H} CP MAS NMR studies indicate the reaction proceeds by substitution of fluoride at surface hydroxyl moieties.

Partial ion exchange of divalent cations (Mg<sup>2+</sup>, Ca<sup>2+</sup>, Sr<sup>2+</sup>, Ba<sup>2+</sup> and Cu<sup>2+</sup>) into NH<sub>4</sub>-Y gives rise to enhanced fluoride loadings compared with the parent material, as well as greater characteristic

fluoride adsorption energies. Critically, the reaction appears to proceed by the same  $H^+$ -mediated substitution at surface hydroxyl moieties in  $M_x(NH_4)_{1-2x}-Y$  species. The promotion of fluorination is not completely understood owing to an unassigned resonance in the  $^{19}F$  MAS NMR spectra; however, some possible explanations for this peak have been discounted. A theory has been put forward that this peak is caused by either  $[SiO_2F_2]$  or proximal  $[SiO_3F]$  moieties, adequately explaining the chemical shift and how population of this environment may be promoted by divalent cations. Dealumination of  $NH_4-Y$ , by treatment with  $H_4EDTA$ , also gives rise to enhanced fluoride loadings and characteristic adsorption energies; however, incomplete assignment of the  $^{19}F$  MAS NMR spectrum hinders a greater understanding of why this occurs.

Ultimately, for the first time defluoridation phenomena from low concentration solutions by zeolites have been studied by  $^{19}F$  MAS NMR spectroscopy, determining that fluoride reacts with the framework, establishing the fluorine environments produced in the zeolite and the mechanism by which the reaction likely proceeds. The implications are significant for defluoridation as high loadings may be achieved from solutions provided an acid is present, which can be delivered by *in situ* ion exchange with acidic intrapore cations. Moreover, there are also significant implications on the preparation of fluorinated zeolites for catalytic applications. The conventional hydrothermal treatments with concentrated acids appear superfluous, as the desirable fluorine-containing motif  $[SiO_3F]$  - which reduces the Brønsted acidity of zeolites hence favourably adapting the surface properties - can be produced exclusively with no  $[SiO_4F]$  or  $[SiF_6]$  formation, achieving high fluoride loadings (2 – 3 wt%) from low concentration (200 ppm  $F^-$ ) solutions at 25°C. Furthermore, the enhanced understanding of the fluorination reaction, and how this may be promoted by the presence of alkaline earth cations or through zeolite dealumination, has informed strategies for enhancing  $^{18}F^-$  loadings attained by large zeolite crystals for application as radiotracers in positron imaging techniques.

## CHAPTER 6: ENHANCING FLUORIDE UPTAKE IN LARGE ZEOLITE PARTICLES THROUGH POST-SYNTHETIC MODIFICATIONS

### 6.1 Introduction

Large particles, or crystals, of various zeolites with different morphologies and diameters in the range of interest (5 – 50  $\mu\text{m}$ ) have been synthesised, as detailed in Chapters 3 and 4. In order to apply a particle as a tracer in the positron imaging technique, PEPT, sufficient activity must be imparted on the particle by labelling with a  $\beta^+$ -emitting isotope. The most commonly applied  $\beta^+$ -emitting isotopes are  $^{18}\text{F}$  ( $t_{1/2} = 110$  min), produced by irradiation of water using a cyclotron, and  $^{68}\text{Ga}$  ( $t_{1/2} = 68$  min), eluted from  $^{68}\text{Ge}$  generators, as detailed in Section 1.2. In Section 3.3.7, it was established for mordenite that surface sorption of gallium from aqueous solutions is possible; however, given the disparity between the optimal pH conditions for adsorption and the acidity of gallium-68 solutions as eluted from generators, labelling with gallium-68 is not viable for large mordenite particles. Moreover, the solutions eluted from generators are sufficiently acidic to dissolve lower Si/Al zeolites of which large particles have been synthesised, such as zeolites A, X and GME.<sup>138</sup>

As labelling with gallium-68 is not viable, imparting sufficient activity on zeolite particles by reaction with fluorine-18 would be advantageous. Reactivity between the zeolite Y framework and aqueous fluoride in dilute solutions was studied in Chapter 5, revealing the essential role of protons in mediating the reaction, as well as the promoting effect of divalent intrapore cations. Dealumination of the zeolite Y framework also increased fluoride loadings and the fluoride adsorption energies calculated for the zeolite. In this chapter, the influence of post-synthetic modifications to enhance fluoride uptake in large particles of zeolites A, X, gmelinite (GME) and mordenite (MOR) have been examined. Both ion exchange with divalent cations ( $\text{Ca}^{2+}$ ,  $\text{Sr}^{2+}$ ,  $\text{Cu}^{2+}$  and  $\text{Ba}^{2+}$ ) and dealumination have been employed, where possible, as well as surface sorption of iron(III) ions which has previously been shown to enhance fluoride uptake in zeolites.<sup>108</sup> In zeolites where iron(III) modification or dealumination are not possible, viz. zeolites A and X, the influence of appropriate treatments on the

morphology and crystallinity of the particles has been evaluated, demonstrating why these post-synthetic modifications are unsuitable.

The production of  $^{18}\text{F}$  by irradiation of water with a  $^3\text{He}$  beam, or  $^{18}\text{O}$  enriched water ( $[^{18}\text{O}]\text{H}_2\text{O}$ ) with a proton beam, leads to the formation of aqueous fluoride ions from oxygen atoms that previously constituted water molecules. The only possible counter cation for the fluoride anion produced is a proton released in the dissociation of the water molecule upon the nuclear reaction forming fluorine-18. Consequently, fluorine-18 solutions are produced as dilute solutions of hydrofluoric acid.<sup>30</sup> Accordingly, in studies on fluoride uptake by large zeolite particles, 1:1  $\text{NaF}:\text{HNO}_3$  solutions have been employed to simulate fluorine-18 solutions produced at cyclotrons. As the lower limit of detection for fluoride ion-selective electrodes is  $0.02 \text{ ppm F}^-$  ( $20 \text{ ppb F}^-$ ),<sup>73</sup> the concentration of fluoride solutions from which uptake has been evaluated ( $5 - 60 \text{ ppm F}^-$ ) is much greater than the concentration of as produced  $^{18}\text{F}$  solutions (*ca.*  $0.16 - 0.19 \text{ ppb F}^-$ ).<sup>8</sup> Nevertheless, valid conclusions may still be drawn on the relative affinities of materials for fluoride under the same conditions, influencing which post-synthetic modifications are best utilised for each zeolite to enhance fluoride loadings.

## 6.2 Experimental

### 6.2.1 Zeolite Syntheses

Each of the zeolites employed in this chapter were prepared by scaled-up versions of syntheses described previously in Chapters 3 and 4. All products match the compositions, particle sizes and morphologies observed for the products of previous syntheses; accordingly, a discussion of the characterisation of these products is not repeated in the discussion. PXRD patterns and scanning electron micrographs recorded on the products of scaled-up syntheses may be found in Appendix 3.

#### 6.2.1.1 Large Zeolite A Crystals

Large crystals of zeolite A were synthesised by a modification of the method first reported by Charnell,<sup>42</sup> as described in Section 4.2.1. In the scaled-up preparation, anhydrous sodium aluminate (10.57 g) was dissolved in deionised water (94 ml). The solution was then filtered through a 0.45 µm PTFE filter (Fisherbrand™) prior to the addition of triethanolamine (14.93 g). A separate solution of sodium silicate was prepared by dissolving sodium metasilicate pentahydrate (9.86 g) in deionised water (94 ml). The silicate solution was also passed through a 0.45 µm filter before the addition of triethanolamine (14.93 g). The aluminate solution was added to the silicate solution in a 250 ml HDPE bottle, then manually shaken for 2 – 3 minutes before further homogenisation on a mechanical shaker for 30 minutes. The gel was then heated in a convection oven for 28 days at 85°C. The product was recovered by vacuum filtration, washed copiously with deionised water and dried overnight at 60°C. Triethanolamine (> 99%) was obtained from Sigma-Aldrich, whereas technical grade sodium aluminate and sodium silicate pentahydrate were obtained from Fisher Chemical.

#### 6.2.1.2 Large Zeolite X Crystals

The procedure for zeolite X was identical to that for zeolite A described above in 6.2.1.1, except 5.28 g of sodium aluminate was used instead of 10.57 g.

#### 6.2.1.3 GME Microspheres

An aluminate solution was prepared by dissolving sodium aluminate (4.49 g) and sodium hydroxide (7.89 g) in deionised water (88.5 ml). After filtering through a 0.45 µm PTFE filter (Fisherbrand™), triethanolamine (19.58 g) was added to the aluminate solution. A silica solution was prepared by adding Ludox™ HS-40 colloidal silica (38.02 g) to deionised H<sub>2</sub>O (88.5 ml). The silica solution was added to the aluminate solution in a 250 ml HDPE bottle, then manually shaken for 2 – 3 minutes before

further homogenisation on a mechanical shaker for 30 minutes. Following homogenisation, the gel was then aged at ambient temperature for 9 days prior to heating at 85°C for 21 days. The product was recovered by vacuum filtration, washed copiously with deionised water and dried overnight at 60°C. Triethanolamine (> 99%), sodium hydroxide (> 97%) and Ludox™ HS-40 colloidal silica were obtained from Sigma-Aldrich and technical grade sodium aluminate was obtained from Fisher Chemical.

#### 6.2.1.4 Mordenite Microparticles

Mordenite was synthesised according to a modification of the preparation reported by Mao *et al.*,<sup>43</sup> in which tetraethyl orthosilicate, TEOS, (23.6 ml) was added to deionised water (27.8 ml) with stirring; the pH of the solution was then adjusted to 1.0 by the addition of 2 M hydrochloric acid. The pH was monitored with a HI1131 pH electrode connected to a pH 211 microprocessor pH meter (Hanna Instruments). The resulting solution was stirred at ambient temperature for 24 hours. A second solution was made by dissolving sodium hydroxide (2.78 g) and aluminium sulfate hexadecahydrate (3.75 g) in deionised water (55.5 ml), followed by addition of 35 wt% aqueous tetraethylammonium hydroxide, TEAOH, solution (6.11 ml). The hydrolysed TEOS was then added to the second solution with vigorous stirring and homogenised for a further 30 minutes. The resulting gel was aged for 24 hours at ambient temperature, following which the residual ethanol from the hydrolysis, expelled from the gel by syneresis, was decanted. The gel was then placed in a Parr® Teflon™-lined stainless-steel autoclave with a 125 ml capacity and heated at 170°C for 96 hours. The product was recovered by vacuum filtration, washed with deionised water and dried overnight at 60°C. Tetraethyl orthosilicate (> 98%) and sodium hydroxide (> 97%) were obtained from Sigma-Aldrich, technical grade aluminium sulfate hexadecahydrate was obtained from Fisher Chemical and the 35 wt% tetraethylammonium hydroxide aqueous solution was obtained from Alfa Aesar. The 2 M HCl solution was made by dilution of analytical re-agent grade 37 wt% hydrochloric acid obtained from Fisher Chemical.

## 6.2.2 Fluoride Adsorption Measurements

1:1 HNO<sub>3</sub>:NaF solutions, in the concentration range 5 – 60 ppm F<sup>-</sup>, were prepared by dilution of the appropriate amount of 1000 ppm F<sup>-</sup> (1 g L<sup>-1</sup>) NaF solution (Hanna Instruments) with deionised water, where the required amount of 0.1 M HNO<sub>3</sub> to render the final solution 1:1 HNO<sub>3</sub>:NaF was added during dilution (e.g. for a 250 ml solution with a 20 ppm F<sup>-</sup> concentration, 2.60 ml of 0.1 M HNO<sub>3</sub> was added during dilution, and for a 250 ml solution with a 60 ppm F<sup>-</sup> concentration, 7.90 ml of 0.1 M HNO<sub>3</sub> was added). The 0.1 M HNO<sub>3</sub> solution was produced by serial dilution from analytical re-agent grade 67 wt% nitric acid obtained from Fisher Chemical.

Approximately 0.100 g of zeolite, weighed accurately to 3 decimal places, was added to the 1:1 NaF:HNO<sub>3</sub> solution (20 ml) of desired concentration in a polypropylene vessel (capacity = 60 ml, diameter = 28 mm). The solution and zeolite were added to a Memmert WNB14 water bath equipped with a shaking attachment and shaken laterally at approx. 110 shakes per minute for 24 hours at 25°C. Following 24 hours, 15 ml of supernatant solution was decanted and added to 3 ml of TISAB-II buffer (Hanna Instruments). The potential of the solution (mV) was measured with a calibrated fluoride ion-selective electrode (Cole Parmer) connected to a Hanna Instruments HI 3222 processor, calibrated across the range 1 – 100 ppm F<sup>-</sup> with standards (1, 10 and 100 ppm F<sup>-</sup>) made by serial dilution of 1000 ppm F<sup>-</sup> NaF solution. Standards were also measured in a 5:1 volume mixture with TISAB-II buffer. Solution fluoride concentrations were calculated from the appropriate calibration curve. Calibrant and analyte solutions were stirred while measured to ensure accurate readings. A blank measurement was employed for all analyte solutions of a given concentration to adjust for any adsorption to the vessel. Equilibrium fluoride loadings ( $q_e$ ) per gram of the initial zeolite material (mg F<sup>-</sup> g<sup>-1</sup>) were calculated by Equation 6.1, in which  $c_0$  and  $c_e$  are the initial and equilibrium fluoride concentrations (mg L<sup>-1</sup>), respectively, as measured by a calibrated fluoride ISE. The term  $\rho$  in Equation 6.1 is calculated by Equation 6.2, where  $m$  is the initial mass of the zeolite (g) and  $v$  is the volume of the solution (L).

$$q_e = \frac{(c_0 - c_e)}{\rho} \quad (\text{Eq. 6.1})$$

$$\rho = m/v \quad (\text{Eq. 6.2})$$

### 6.2.3 Post-Synthetic Modifications

#### 6.2.3.1 Ion Exchange

Solutions of divalent metals (0.25 M) were made by dissolving the appropriate mass of the nitrate salt in deionised water (50 ml); the form of the nitrate salt, masses dissolved to make 0.25 M solutions (50 ml) and re-agent suppliers are listed in Table 6.1. A portion of zeolite A, X, GME or MOR (0.50 g) was added to the desired 0.25 M metal nitrate solution (50 ml) then placed in a Memmert WNB14 water bath equipped with a shaking attachment and shaken laterally at approximately 110 shakes per minute for 24 hours at 60°C. Following 24 hours and cooling to room temperature, the ion-exchanged zeolites were recovered by vacuum filtration, washed copiously with deionised water and dried overnight at 60°C.

Table 6.1. Metal salts, suppliers and masses to make 0.25 M solutions.

Ion	Salt	Mass (g)	Supplier
Ca <sup>2+</sup>	Ca(NO <sub>3</sub> ) <sub>2</sub> ·4H <sub>2</sub> O	2.95	Acros Organics, 99%
Sr <sup>2+</sup>	Sr(NO <sub>3</sub> ) <sub>2</sub>	2.65	Alfa Aesar, 99%
Ba <sup>2+</sup>	Ba(NO <sub>3</sub> ) <sub>2</sub>	3.27	Sigma Aldrich, 99%
Cu <sup>2+</sup>	Cu(NO <sub>3</sub> ) <sub>2</sub> ·2.5H <sub>2</sub> O	2.91	Sigma Aldrich, 98%

For Cu<sup>2+</sup>-ion exchange, 0.25 M solutions were employed to produce Cu<sup>2+</sup> ion-exchanged MOR and GME. In the case of zeolites A and X, precipitation of Cu<sub>2</sub>(NO<sub>3</sub>)(OH)<sub>3</sub> (monoclinic, *P*2<sub>1</sub>, *a* = 5.6 Å, *b* = 6.1 Å, *c* = 6.9 Å, *β* = 94.7°) was observed following treatment with 0.25 M Cu(NO<sub>3</sub>)<sub>2</sub> solutions.<sup>139</sup> Reducing the Cu(NO<sub>3</sub>)<sub>2</sub> concentration to 0.025 M and 0.01 M for zeolites X and A, respectively,

prevented  $\text{Cu}_2(\text{NO}_3)(\text{OH})_3$  precipitation, producing only the  $\text{Cu}^{2+}$ -exchanged zeolite. PXRD patterns recorded on zeolite A and X treated with 0.25 M  $\text{Cu}(\text{NO}_3)_2$  may be found in Appendix 4.

#### 6.2.3.2 Iron(III) Modification

Mordenite was modified with surface sorbed iron(III) by placing mordenite (0.40 g) in a 0.25 M iron(III) nitrate solution (40 ml), prepared by dissolving iron(III) nitrate nonahydrate (4.00 g) in deionised water (40 ml). The mordenite-containing iron(III) solution was then placed in a Memmert WNB14 water bath equipped with a shaking attachment and shaken laterally at approximately 110 shakes per minute for 24 hours at 60°C. Following 24 hours and cooling to room temperature, the zeolite was recovered by vacuum filtration, washed copiously with deionised water and dried overnight at 60°C.

In the case of zeolites A, X and GME, the zeolites (0.40 g) were added to 0.01 M, 0.025 M and 0.25 M  $\text{Fe}(\text{NO}_3)_3$  solutions (40 ml) and treated analogously to mordenite, as described above. The 0.01 M and 0.025 M solutions were prepared by dissolving 0.16 g and 0.40 g of iron(III) nitrate nonahydrate, respectively, in deionised water (40 ml). In the case of GME and MOR, the products following treatment with iron(III)-containing solutions were yellow in colour, whereas for zeolites A and X the products were brown. Iron(III) nitrate nonahydrate (> 98%) was obtained from Alfa Aesar.

#### 6.2.3.3 EDTA Treatments

GME microspheres were dealuminated by treatment with ethylenediaminetetraacetic acid,  $\text{H}_4\text{EDTA}$ , following the method first reported by Kerr<sup>121</sup> for the dealumination of Na-Y. GME microspheres (3.34 g) were added to a slurry of  $\text{H}_4\text{EDTA}$  (1.60 g) in deionised water (50 ml) and stirred vigorously at ambient temperature for 6 hours. The dealuminated zeolite was then recovered by vacuum filtration, washed copiously with deionised water and dried at 60°C. Ethylenediaminetetraacetic acid (99%) was obtained from Alfa Aesar.

In EDTA treatments of large zeolite A and X crystals, the zeolite (0.68 g) was added to H<sub>4</sub>EDTA (0.28 – 0.56 g) in deionised water (10 ml) and stirred vigorously at ambient temperature for 4 hours. In products prefixed with the label E1, the slurry contained 0.28 g of H<sub>4</sub>EDTA; in products prefixed with the labels E2, E3 and E4, the H<sub>4</sub>EDTA content in the slurry was 0.37 g, 0.46 g and 0.56 g, respectively. The products were recovered by vacuum filtration, washed copiously with deionised water and dried overnight at 60°C. For zeolite A, yields of the treatments were: E1 (0.64 g), E2 (0.56 g), E3 (0.39 g) and E4 (0.20 g). For zeolite X, yields were: E1 (0.62 g), E2 (0.57 g), E3 (0.41 g) and E4 (0.29 g).

#### 6.2.3.4 Attempts to Dealuminate Mordenite

A calcined mordenite sample (2.50 g) was added to a 6 M hydrochloric acid solution (50 ml) and refluxed for 24 hours. Following cooling, the supernatant solution was decanted before the product was recovered by vacuum filtration, washed copiously with deionised water and dried overnight at 60°C. The 6 M hydrochloric acid solution was prepared by dilution of analytical re-agent grade 37 wt% hydrochloric acid.

### 6.2.4 Instruments

#### 6.2.4.1 Powder X-ray Diffraction (PXRD)

PXRD was performed on a Bruker D8 Advance diffractometer, in reflection geometry, equipped with a Ni-filtered Cu K<sub>α</sub> X-ray source ( $\lambda = 1.5418 \text{ \AA}$ ) and fitted with a solid-state LynxEye position sensitive detector. PXRD patterns were recorded on finely ground samples mounted on silicon low background holders that were first covered in a thin layer of Vaseline. Scans were measured over the  $2\theta$  range 4 – 60°, or 5 – 60° for mordenite samples, at a scan rate of  $0.04^\circ \text{ s}^{-1}$  with a  $0.02^\circ$  step-size. Phase matching was performed in Bruker EVA software linked to the PDF 4+ database. All reference PDF pattern stick plots are derived from the appropriate entry in the ICDD PDF 4+ database.<sup>83</sup> Lattice

constants have been determined by unit cell refinements using Chekcell software,<sup>84</sup> based on peak positions identified in Bruker EVA software. The space groups *Fm-3c*, *Fd-3m* and *Cmcm* were assumed for the zeolites A, X and mordenite, respectively. All PXRD patterns were plotted in SigmaPlot.<sup>85</sup>

In some instances, stated where appropriate in the discussion, PXRD patterns were instead recorded on a Bruker D2 diffractometer, in reflection geometry, equipped with a Fe-filtered Co  $K_{\alpha}$  X-ray source ( $\lambda = 1.7902 \text{ \AA}$ ) and fitted with a LynxEye position sensitive detector. Finely ground samples were also mounted on silicon low background holders, however, without the aid of Vaseline. Scans were measured over the  $2\theta$  range  $6 - 70^{\circ}$  at a scan rate of  $0.04^{\circ} \text{ s}^{-1}$  with a  $0.02^{\circ}$  step-size.

#### 6.2.4.2 X-ray Fluorescence Spectrometry (XRF)

XRF spectrometry was performed on a Bruker S8 Tiger spectrometer. All samples were measured as loose powders mounted on Mylar<sup>®</sup> film for the maximum 18-minute data collection time. Quantitative results were obtained from SPECTRA<sup>plus</sup> software.  $K_{\alpha}$  emission lines were used to quantify all elements, except for Sr, Ba and Cu which were instead quantified from  $L_{\alpha}$  emission lines. Elemental weight fractions for each sample measured by XRF spectrometry may be found in Appendix 5.

#### 6.2.4.3 Scanning Electron Microscopy (SEM)

Scanning electron micrographs were obtained on a JEOL 6060 microscope at an accelerating voltage of 20 keV and a working distance of *ca.* 13 mm. The imaged samples were mounted on graphite tape then sputter coated with a gold thin film, with a 20 nm approximate thickness, prior to imaging.

### 6.2.5 Adsorption isotherms

The Langmuir, Freundlich, Temkin and Dubinin-Radushkevitch adsorption isotherms, as applied in this chapter, may be found in Table 2.1 in Section 2.1.3. Isotherm parameters and  $R^2$  values have been derived from linear regression analysis in Sigmaplot software.<sup>85</sup> Details on the derivation of characteristic adsorption energies may be found in Section 5.2.12.

## 6.3 Results and Discussion

### 6.3.1 Gmelinite Microspheres

#### 6.3.1.1 Fluoride Uptake by Na-GME Microspheres

Fluoride uptake by Na-GME microspheres has been studied from 20 ppm  $F^-$  1:1 NaF:HNO<sub>3</sub> solutions, following 1 hour of contact time between the zeolite and solution, as the rapid uptake of fluoride is important in labelling PEPT tracers to impart as much activity as possible on the particle, as well as following 24 hours of contact time to determine the equilibrium fluoride loading. Following an hour of contact time, a fluoride loading of 0.57 mg  $F^- g^{-1}$  was measured, equivalent to removal of 15% of the fluoride present in the starting solution under these conditions. Following 24 hours of contact time, an equivalent fluoride loading was measured, 0.57 mg  $F^- g^{-1}$ , with no discernible variation from the loading attained following an hour, indicating equilibrium is rapidly reached for the fluorination of Na-GME microspheres.

#### 6.3.1.2 Dealumination

Dealumination of Na-GME microspheres has been achieved by treatment with a H<sub>4</sub>EDTA slurry. A significant increase in the Si/Al ratio to 4.0(2) for the dealuminated product ((D)-Na-GME) from 2.2(1)

in the parent material has been measured by XRF spectrometry, attesting dealumination has occurred. A slight reduction in crystallinity is observed following dealumination, as shown in PXRD patterns of the parent material, Na-GME, and the dealuminated product, (D)-Na-GME, in Figure 6.1. Following dealumination, most microspheres appear the same as in the parent material, although some are cracked and split into two loosely connected hemispheres, as shown in Figure 6.2.

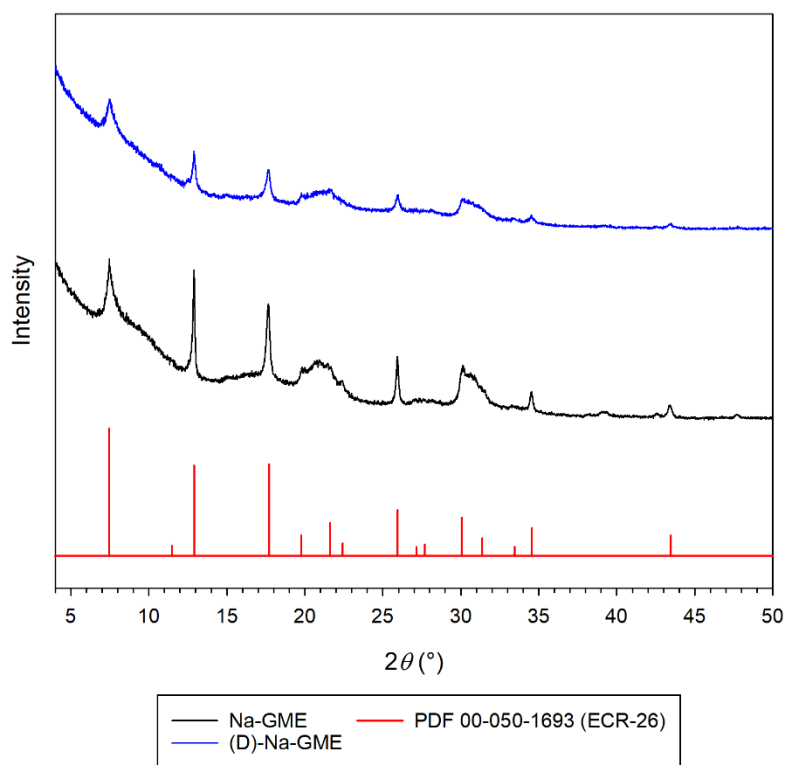


Figure 6.1. PXRD patterns of Na-GME and (D)-Na-GME, dealuminated Na-GME.

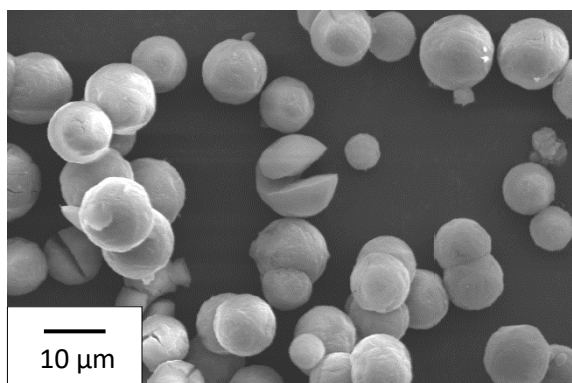


Figure 6.2. A scanning electron micrograph of dealuminated Na-GME.

Fluoride loadings attained from 1:1 NaF:HNO<sub>3</sub> solutions are significantly greater for (D)-Na-GME than for the parent material, Na-GME. From 20 ppm F<sup>-</sup> solutions, a 1.07 mg F<sup>-</sup> g<sup>-1</sup> loading is achieved by (D)-Na-GME following an hour of contact, corresponding to removal of 31% of the total fluoride content in solution. Following 24 hours of contact, a 4.24 mg F<sup>-</sup> g<sup>-1</sup> loading is attained, equivalent to removal of 98% of the solution fluoride content. The loadings achieved following 1 and 24 hours of contact time for (D)-Na-GME are significantly greater than those measured for Na-GME, 0.57 mg F<sup>-</sup> g<sup>-1</sup>, following both 1 and 24 hours of contact, although (D)-Na-GME appears to be slower to reach equilibrium than the parent material.

#### 6.3.1.3 Iron(III) Modification

GME microspheres may be modified by iron(III) surface sorption from treatments with 0.01 M and 0.025 M iron(III) nitrate solutions. Following treatment with a 0.01 M iron(III) nitrate solution, analysis by XRF spectrometry demonstrates a moderate iron loading in the product, 0.38(2) wt% Fe (corresponding to 0.54(2) wt% Fe<sub>2</sub>O<sub>3</sub> and Fe/Al = 0.02). The Si/Al ratio of the iron(III)-loaded product is 2.3(1), within error of the Si/Al ratio in the parent material 2.2(1), indicating no dealumination has occurred despite the acidity of the iron(III) solution (pH = 2.39). Upon iron loading from 0.01 M iron(III) nitrate solutions, no discernible change is observed in the scanning electron micrograph (Figure 6.3) and the PXRD pattern (Figure 6.4) recorded on the product. Treatment with a 0.025 M iron(III) nitrate solution leads to enhanced iron loadings in the product, 0.76(2) wt% Fe (equivalent to 1.08(2) wt% Fe<sub>2</sub>O<sub>3</sub> and Fe/Al = 0.05). An increase in the product Si/Al to 3.0(1) is observed following treatment with 0.025 M iron(III) nitrate indicating some dealumination has occurred, owing to the increased acidity of the solution (pH = 2.10). Scanning electron micrographs following treatment with 0.025 M iron(III) nitrate solutions show no change in the appearance of the product (Fig. 6.3); however, the PXRD pattern following treatment shows a significant reduction in crystallinity (Fig. 6.4), likely caused by dealumination. Products of treatments with both 0.01 M and 0.025 M iron(III) nitrate solutions are

yellow in colour, supporting the presence of surface sorbed hydroxo-containing iron(III) species on the zeolite surface.<sup>138</sup>

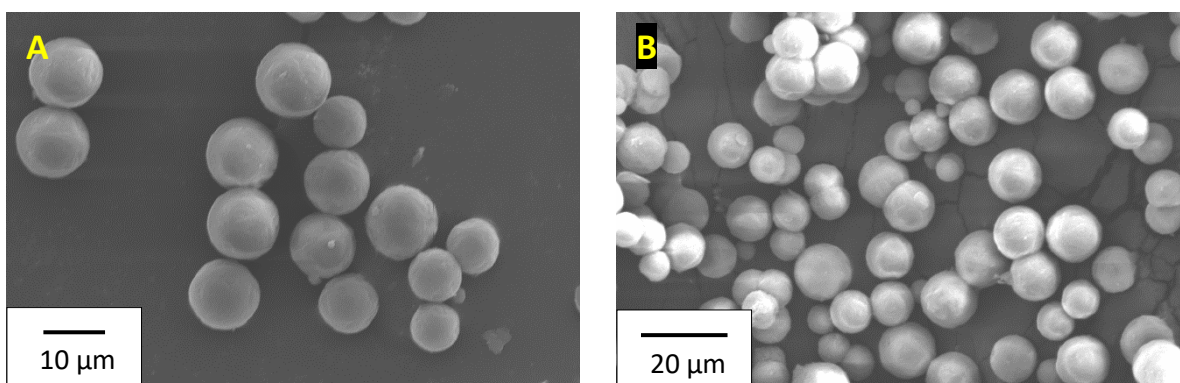


Figure 6.3. Scanning electron micrographs of GME microspheres treated with (A) 0.01 M and (B) 0.025 M  $\text{Fe}(\text{NO}_3)_3$  solutions.

Following 1 hour of contact with a 20 ppm  $\text{F}^-$  1:1 NaF:HNO<sub>3</sub> solution, fluoride loadings of 0.84 mg  $\text{F}^- \text{g}^{-1}$  are measured for  $\text{Fe}^{\text{III}}$ -loaded Na-GME produced from both 0.01 M and 0.025 M solutions, despite the higher iron content in the latter case. The loadings are equivalent to removal of 24% of the fluoride content in solution. Following 24 hours of contact, fluoride loadings of 1.61 mg  $\text{F}^- \text{g}^{-1}$  and 1.72 mg  $\text{F}^- \text{g}^{-1}$  are measured for  $\text{Fe}^{\text{III}}$ -loaded Na-GME produced from 0.01 M and 0.025 M solutions, respectively. While greater iron loadings may be attained from treatment with 0.025 M  $\text{Fe}(\text{NO}_3)_3$  solutions compared with 0.01 M, no difference in the fluoride loading attained following an hour of contact is observed, and only a small increase in equilibrium fluoride loading is attained for the zeolite with higher iron loading. Iron loading increases both the fluoride loadings attained following an hour and 24 hours of contact with the solution compared with the parent material; however, iron loading is less efficacious than dealumination in improving fluoride loadings on gmelinite microspheres. Critically, no fragmentation of microspheres is observed upon iron loading, such as those observed upon dealumination, rendering the iron-loaded microspheres more suitable for application as PEPT tracers, despite the lower fluoride loadings.

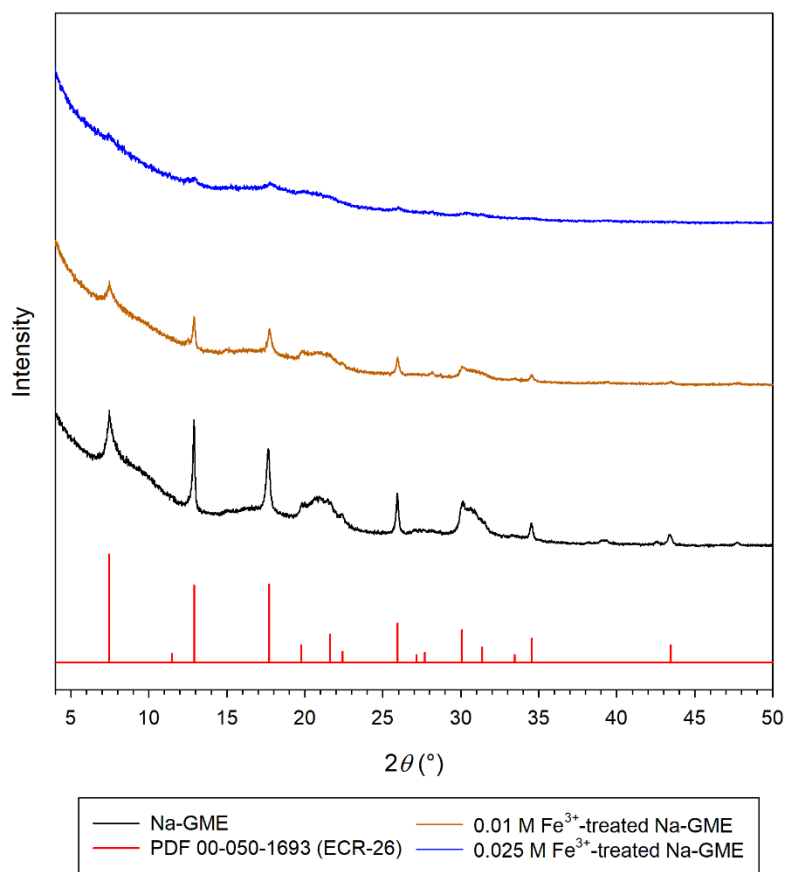


Figure 6.4. PXRD patterns recorded on GME microspheres treated with 0.01 M and 0.025 M  $\text{Fe}(\text{NO}_3)_3$  solutions, as well as the parent material.

#### 6.3.1.4 Divalent Metal Ion Exchange

Ion exchange between aqueous divalent cations ( $\text{Ca}^{2+}$ ,  $\text{Sr}^{2+}$ ,  $\text{Ba}^{2+}$  and  $\text{Cu}^{2+}$ ) and Na-GME microspheres has been achieved by batch ion exchange experiments at  $60^\circ\text{C}$  with 0.25 M solutions of the divalent cation. XRF spectrometry performed on the exchanged products attest ion exchange has occurred in each instance. Si/Al, Na/Al and M/Al ratios measured on the products are given in Table 6.2, where M is the appropriate divalent metal. In all cases, a high replacement of Na is observed, with 84% of  $\text{Na}^+$  exchanged for  $\text{Ca}^{2+}$  in the lowest instance. In each case except barium, the total intrapore cation content ( $2(\text{M}/\text{Al}) + \text{Na}/\text{Al}$ ) is within error of the expected value (1.0). For barium, no detectable sodium content was measured in the product; however, the Ba/Al ratio, 0.63(4), is greater than the theoretical maximum value, 0.50, permitted for complete ion exchange. The inflated value is likely caused by

issues inherent to the quantitative analysis of samples containing elements with disparate fluorescence yields by XRF spectrometry, as described in Section 2.2.2.<sup>64</sup> Additional factors that may contribute to error, and reduced accuracy, in the results include the possible occurrence of “over exchange” phenomena, and adsorption of divalent metal ion complexes on the zeolite surface, as outlined in Section 5.4.2.<sup>133,134</sup>

Table 6.2. Si/Al, Na/Al and M/Al ratios measured for ion-exchanged GME microspheres.

	Si/Al	Na/Al	M/Al
Na-GME	2.2(1)	1.1(1)	-
Ca-GME	2.1(1)	0.15(3)	0.42(3)
Sr-GME	2.2(1)	0.07(2)	0.46(3)
Ba-GME	2.1(1)	0.00	0.63(4)
Cu-GME	2.2(1)	0.04(1)	0.49(3)

PXRD patterns recorded on the divalent cation exchanged GME samples are presented in Figure 6.5. While too few distinct reflections occur in each pattern to reliably determine the unit cell parameters, significant qualitative changes in the PXRD patterns occur upon ion exchange. In PXRD patterns of Sr-GME and Ba-GME, the 110 reflection expected at  $2\theta = 12.9^\circ$  is not present. Reflections in the PXRD pattern of Ba-GME have low relative intensities compared with the parent material, as is observed upon barium ion exchange into zeolites Y (Section 5.4.2), X<sup>140</sup> and A,<sup>141</sup> owing to increased X-ray absorption and Compton scattering by barium atoms.<sup>63</sup> In Ca-GME, the 110 reflection is present, but the intensity is reduced relative to the 002 reflection compared with the relative intensities of the peaks in the parent material. In contrast, the intensity of the 110 reflection relative to the 002 reflection in Cu-GME increases compared with the relative intensities in the parent material.

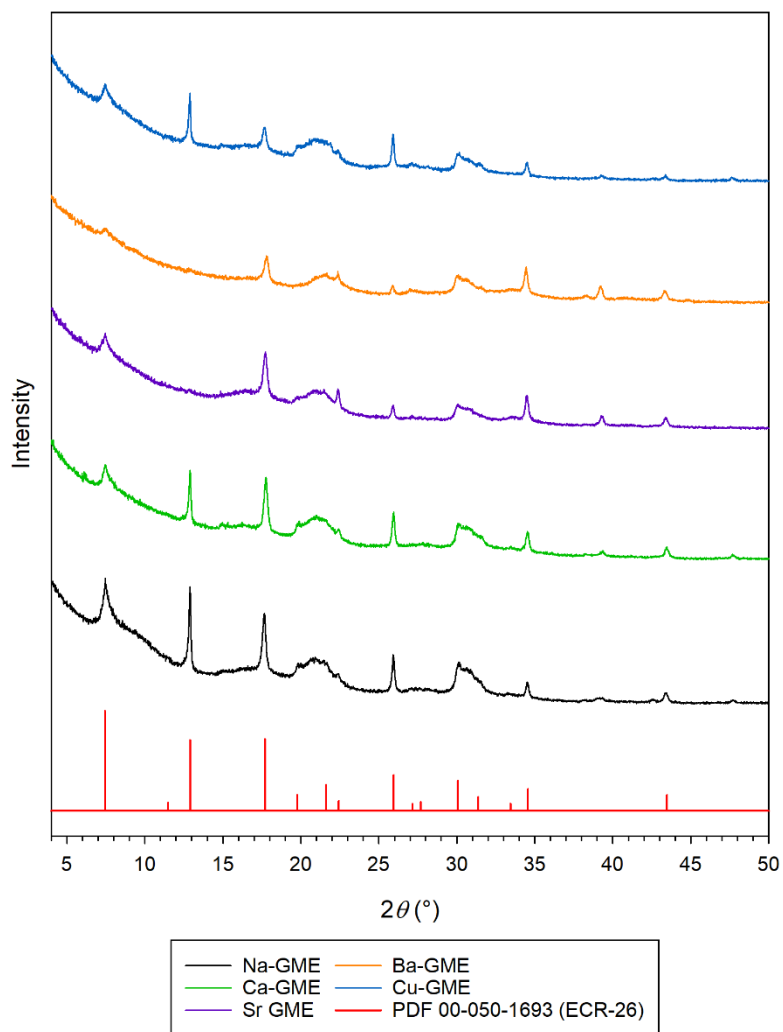


Figure 6.5. PXRD patterns recorded on Na-GME and divalent metal ion-exchanged products.

Table 6.3. Fluoride loadings attained following an hour ( $q(60 \text{ min})$ ) and at equilibrium ( $q_e$ ) for both Na-GME and divalent ion-exchanged derivatives.

	$q(60 \text{ min})$ ( $\text{mg F}^- \text{ g}^{-1}$ )	Fluoride removed after 60 min (%)	$q_e$ ( $\text{mg F}^- \text{ g}^{-1}$ )	Fluoride removed after 24 hours (%)
Na-GME	0.57	15	0.57	15
Ca-GME	0.76	20	0.83	22
Sr-GME	0.64	18	0.73	20
Ba-GME	0.69	19	0.79	20
Cu-GME	0.33	6	0.82	21

Fluoride loadings, and the percentage of fluoride removed from solution, by divalent cation exchanged GME following both an hour and 24 hours of contact are presented in Table 6.3. In all cases except Cu-GME, greater fluoride loadings are attained following an hour of contact compared with the parent material, and only moderate increases in fluoride loading upon extending the contact time to 24 hours are observed. While the presence of copper(II) appears to reduce the fluoride loading attained following an hour of contact, the equilibrium fluoride loading for Cu-GME is greater than that for the parent material and comparable with other divalent metal-exchanged GME species. The greatest fluoride loading attained following an hour of contact is observed for Ca-GME ( $0.76 \text{ mg F}^- \text{ g}^{-1}$ ); however, this is lower than the loading attained for Fe<sup>III</sup>-modified Na-GME ( $0.84 \text{ mg F}^- \text{ g}^{-1}$ ) under the same conditions.

#### 6.3.1.5 Adsorption Isotherms

Equilibrium fluoride loadings have been measured from 1:1 NaF:HNO<sub>3</sub> solutions at 25°C across the concentration range 5 - 60 ppm F<sup>-</sup> for Ca-GME and Fe<sup>III</sup>-loaded Na-GME, loaded by treatment with a 0.01 M iron(III) nitrate solution (0.38(2) wt% Fe), as plotted in Figure 6.6. Equilibrium fluoride loadings have also been measured for Na-GME and (D)-Na-GME from 1:1 NaF:HNO<sub>3</sub> solutions at 25°C with concentrations spanning 20 – 60 ppm F<sup>-</sup> (also plotted in Figure 6.6). Loadings from solutions below 20 ppm F<sup>-</sup> are negligible for Na-GME. In contrast, high equilibrium fluoride loadings are measured for (D)-Na-GME from solutions with concentrations less than 20 ppm F<sup>-</sup>, giving rise to supernatant solutions with low concentrations approaching the lower limit of detection of the fluoride ISE, resulting in errors that are too great to accurately report the fluoride loading.<sup>73</sup>

Equilibrium fluoride uptake data for Na-GME, Ca-GME, Fe<sup>III</sup>-loaded Na-GME and (D)-Na-GME have each been fitted to the linear Freundlich, Temkin, Langmuir and Dubinin-Radushkevitch (DR) isotherms, with  $R^2$  values from linear regression analysis, as well as appropriate isotherm constants,

presented in Table 6.4. Reasonably good fits are observed for all species to the Freundlich isotherm (Figure 6.7), including (D)-Na-GME which qualitatively indicates an acceptable fit despite the relatively low  $R^2$  value (0.958). Acceptable fits are also observed for all species ( $R^2 > 0.96$ ) to the Dubinin-Radushkevitch isotherm (Figure 6.8). Except for Na-GME, qualitatively poor fits are observed for all other species to the Temkin isotherm (Figure 6.9), including (D)-Na-GME despite an acceptable  $R^2$  value (0.971). Poor fits are also observed to the Langmuir isotherm for all species except (D)-Na-GME; the Langmuir plot for (D)-Na-GME is presented in Figure 6.10, whereas the other Langmuir plots may be found in Appendix 1.

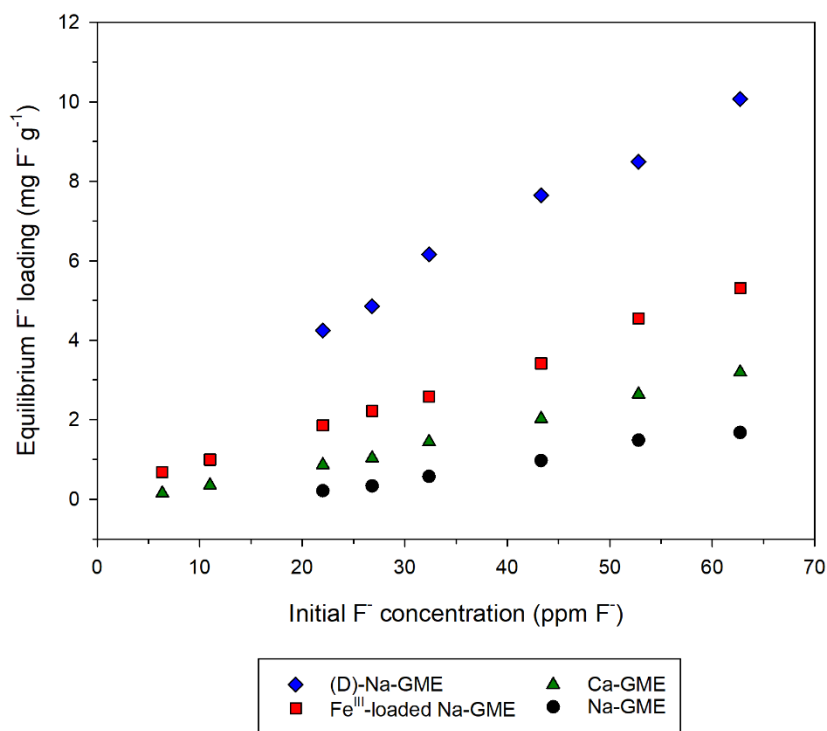


Figure 6.6. Equilibrium fluoride loadings plotted as a function of initial fluoride concentration for Na-GME, Ca-GME, Fe<sup>III</sup>-loaded Na-GME and (D)-Na-GME.

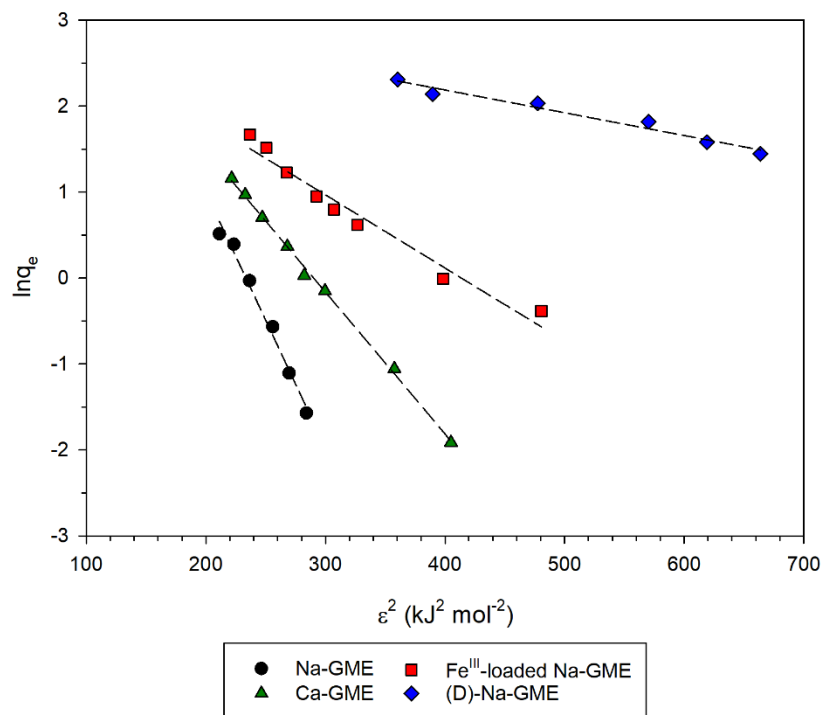


Figure 6.7. Dubinin-Radushkevitch plots for Na-GME, Ca-GME, Fe<sup>III</sup>-loaded Na-GME and (D)-Na-GME.

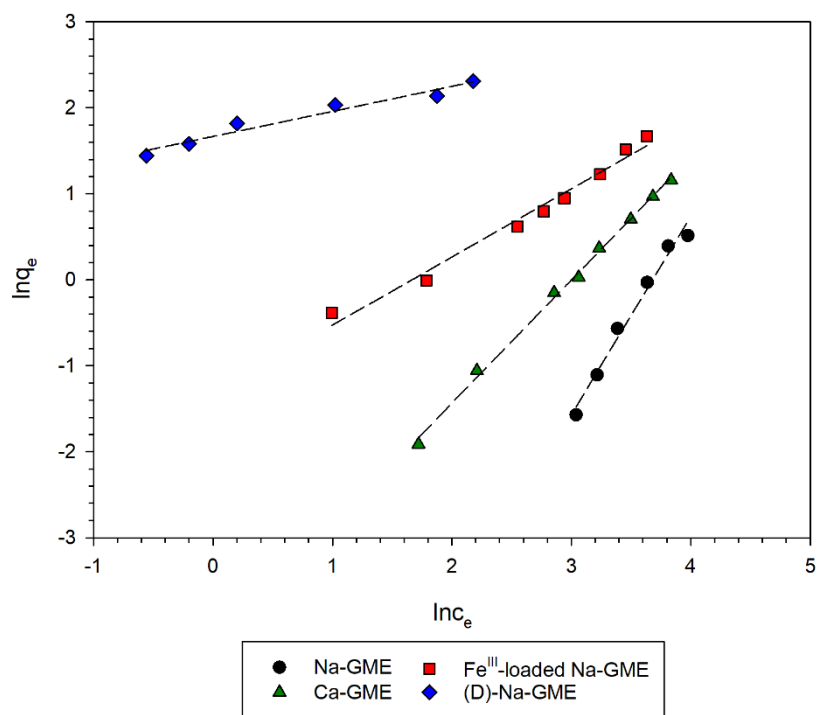


Figure 6.8. Freundlich plots for Na-GME, Ca-GME, Fe<sup>III</sup>-loaded Na-GME and (D)-Na-GME.

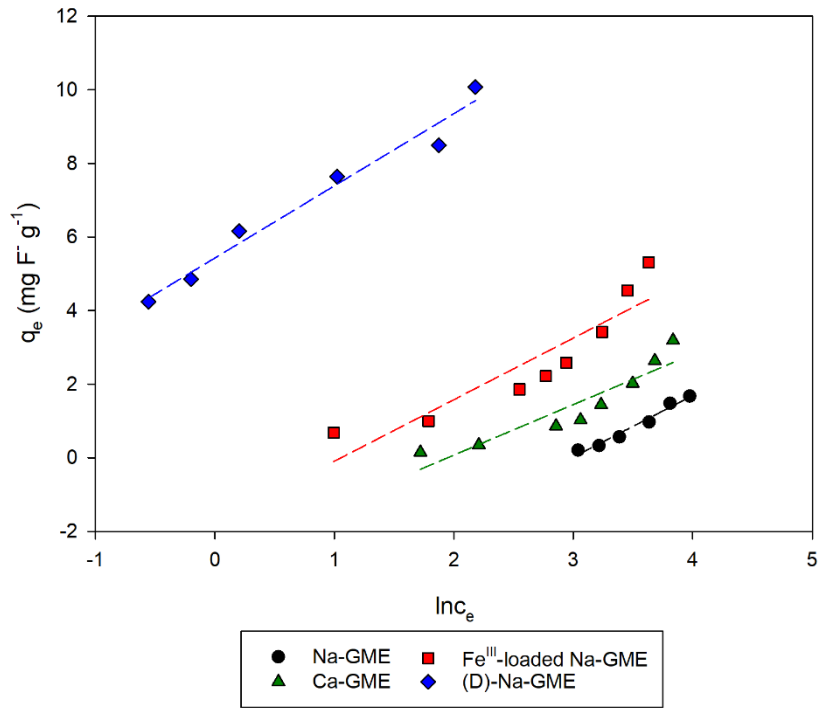


Figure 6.9. Temkin plots for Na-GME, Ca-GME, Fe<sup>III</sup>-loaded Na-GME and (D)-Na-GME.

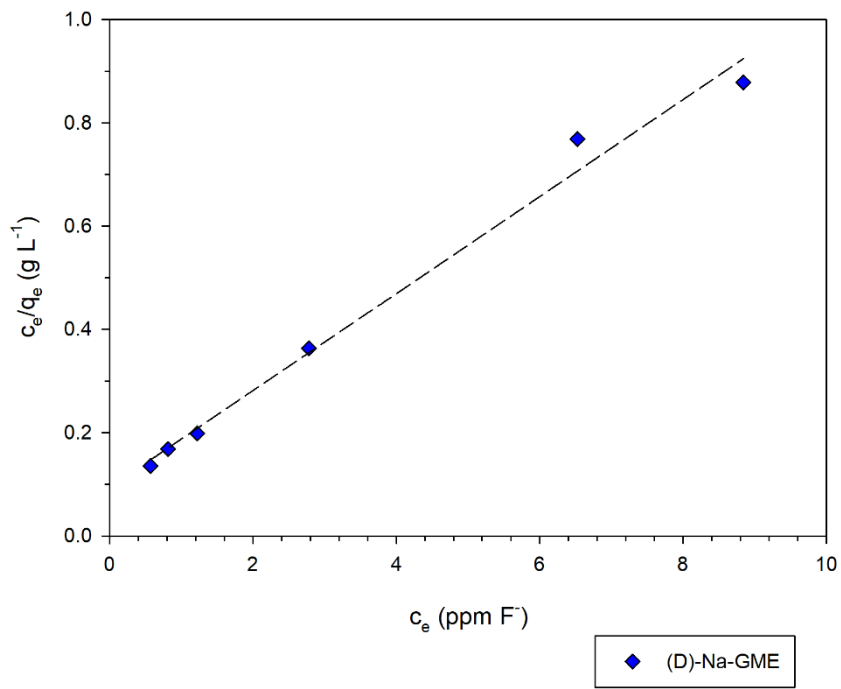


Figure 6.10. Langmuir plot for (D)-Na-GME.

Table 6.4.  $R^2$ , isotherm parameters and derived terms for fits to the listed isotherms for Na-GME, Ca-GME, Fe<sup>III</sup>-loaded Na-GME and (D)-Na-GME.

Isotherm		Na-GME	D-Na-GME	Fe <sup>III</sup> -loaded Na-GME	Ca-GME
Freundlich	$R^2$	0.982	0.958	0.980	0.997
	$K_F$ ((mg g <sup>-1</sup> )/(mg L <sup>-1</sup> ) <sup>n</sup> )	2 x 10 <sup>-4</sup>	5.30	0.27	0.01
	$n$	2.31	0.29	0.83	1.43
DR	$R^2$	0.986	0.967	0.964	0.998
	$E_C$ (kJ mol <sup>-1</sup> )	4.1	13.9	7.7	5.5
	$K$ (x10 <sup>-3</sup> mol <sup>2</sup> kJ <sup>-2</sup> )	29.8	2.6	8.5	16.5
Temkin	$R^2$	0.975	0.971	0.830	0.733
	$A_T$ (L g <sup>-1</sup> )	19.9	1.20	-	-
	$b_T$ (kJ mol <sup>-1</sup> )	1.48	4.99	-	-
Langmuir	$R^2$	0.798	0.988	0.458	0.860

Significant differences in  $K_F$  and  $n$  values are observed for the species examined. The exceptionally low  $K_F$  and high  $n$  values observed for Na-GME indicate low favourability for the reaction with the zeolite, as was observed for fluorination of Na-Y from 1:1 NaF:HNO<sub>3</sub> solutions (Section 5.3.7). Freundlich isotherm parameters for Ca-GME also indicate low favourability; however, a lower  $n$  and greater  $K_F$  value are observed for Ca-GME compared with Na-GME, indicating the reaction with Ca-GME is more favourable. Much greater  $K_F$  and lower  $n$  values are observed for Fe<sup>III</sup>-loaded Na-GME, and critically  $n < 1$  indicating a favourable process. Values indicating an even more favourable process are observed for (D)-Na-GME.

The trend in favourability based on Freundlich isotherm parameters is reflected in the characteristic adsorption energies,  $E_C$ , calculated from  $K$  in DR plots. The lowest  $E_C$  values is observed for Na-GME (4.1 kJ mol<sup>-1</sup>), comparable with the value for Na-Y (4.4 kJ mol<sup>-1</sup>), observed under the same conditions (Section 5.3.7). In Chapter 5, the essential role of protons in the fluorination of zeolites frameworks was established; however, the values of isotherm parameters that are indicative of energetic

favourability, including the characteristic sorption energy, varied greatly depending on whether the proton source was an intrapore cation or was present in solution. The unfavourable nature of adsorption in acidic media indicates fluorination is not a spontaneous process, and therefore requires work to be done for the reaction to occur.<sup>55</sup> It is postulated that the work that must be done is the adsorption of the proton from solution, as an adsorbed proton is less energetically favourable than a free proton in solution, considering both enthalpic and entropic arguments.

The characteristic sorption energy increases for Ca-GME ( $5.5 \text{ kJ mol}^{-1}$ ), but the value is significantly below  $8 \text{ kJ mol}^{-1}$ , the conventional lower bound of energies attributed to chemisorption.<sup>57</sup> The lower value for Ca-GME can again be related to arguments for low favourability of the fluorination reaction in acidic media, as outlined in Section 5.3.7 and above. The value of  $E_c$  observed for Fe<sup>III</sup>-loaded Na-GME ( $7.7 \text{ kJ mol}^{-1}$ ) is close to the lower bound of energies attributable to chemisorption, the mode of fluoride adsorption expected for iron(III)-modified zeolites.<sup>59,108</sup> The  $E_c$  value calculated for (D)-Na-GME ( $13.9 \text{ kJ mol}^{-1}$ ) resides within the range conventionally expected for chemical adsorption,  $8 - 16 \text{ kJ mol}^{-1}$ . The increased  $E_c$  value, and thus favourability, for the reaction between fluoride and (D)-Na-GME is ascribed to the increased density of silanol moieties on the surface of the dealuminated zeolite, permitting greater reactivity between the zeolite and fluoride.

#### 6.3.1.6 Conclusions

Dealumination, iron(III) surface sorption and ion exchange with divalent metal cations all successfully enhance fluoride loadings attained by GME microspheres, both at equilibrium and following an hour of contact with acidic fluoride solutions. The greatest fluoride loadings are obtained for dealuminated Na-GME, followed by iron(III)-treated Na-GME and finally Ca ion-exchanged GME, reflecting trends in favourability observed in Freundlich isotherm parameters and characteristic sorption energies calculated from fits to the Dubinin-Radushkevitch isotherm. While (D)-Na-GME shows excellent defluoridation capabilities in acidic fluoride solutions, fragmentation of GME microspheres upon

dealumination may compromise the mechanical integrity of the particle in applications involving attrition. Accordingly, iron(III) surface sorption is the most promising treatment for enhancing fluoride loadings in GME microspheres while also preserving the spherical morphology and mechanical integrity of the particle, the latter being essential for application as a tracer in positron imaging techniques. Nevertheless, (D)-Na-GME shows promise as a material for defluoridation applications as the relatively large particle sizes are desirable in vessels such as columns, often used in water treatments.

### 6.3.2 Mordenite

#### 6.3.2.1 Fluoride Uptake by Mordenite and Iron(III) Modification

Following 1 hour of contact between a calcined mordenite sample ( $\text{Na}/\text{Al} = 0.54(3)$ ;  $\text{Si}/\text{Al} = 8.6(3)$ ) and 20 ppm  $\text{F}^-$  1:1  $\text{NaF}:\text{HNO}_3$  solution, no discernible fluoride loading occurs. Following 24 hours, a relatively low fluoride loading,  $0.32 \text{ mg F}^- \text{ g}^{-1}$ , is attained, corresponding to removal of 9% of the fluoride present in solution. Iron(III) modification by treatment with 0.25 M iron(III) nitrate at  $60^\circ\text{C}$  for 24 hours gives rise to a product that is yellow in colour but with a relatively low iron loading measured by XRF spectrometry,  $0.12(1) \text{ wt\% Fe}$  (corresponding to  $0.17(1) \text{ wt\% Fe}_2\text{O}_3$  and  $\text{Fe}/\text{Al} = 0.02$ ). There is no discernible difference in PXRD patterns of the original calcined mordenite and the iron(III)-loaded derivative (Figure 6.11); moreover, no additional reflections corresponding to a crystalline iron(III)-containing phase are present. Iron(III)-loading would not be expected to influence the mordenite unit cell parameters and in agreement with this expectation, any variation in the lattice constants following iron(III)-loading, listed in Table 6.5, are within the appropriate confidence interval ( $\pm 3(\text{standard error})$ ). Despite the relatively low iron loading, iron(III)-modification increases the fluoride loadings attained compared with the parent material. Following 1 hour of contact with a 20 ppm  $\text{F}^-$  1:1  $\text{NaF}:\text{HNO}_3$  solution, a loading of  $0.34 \text{ mg F}^- \text{ g}^{-1}$  is measured, corresponding to removal of 9% of the

fluoride from solution. Increasing the contact time to 24 hours leads to an increased fluoride loading, 1.16 mg F<sup>-</sup> g<sup>-1</sup>, corresponding to removal of 42% of the fluoride in solution.

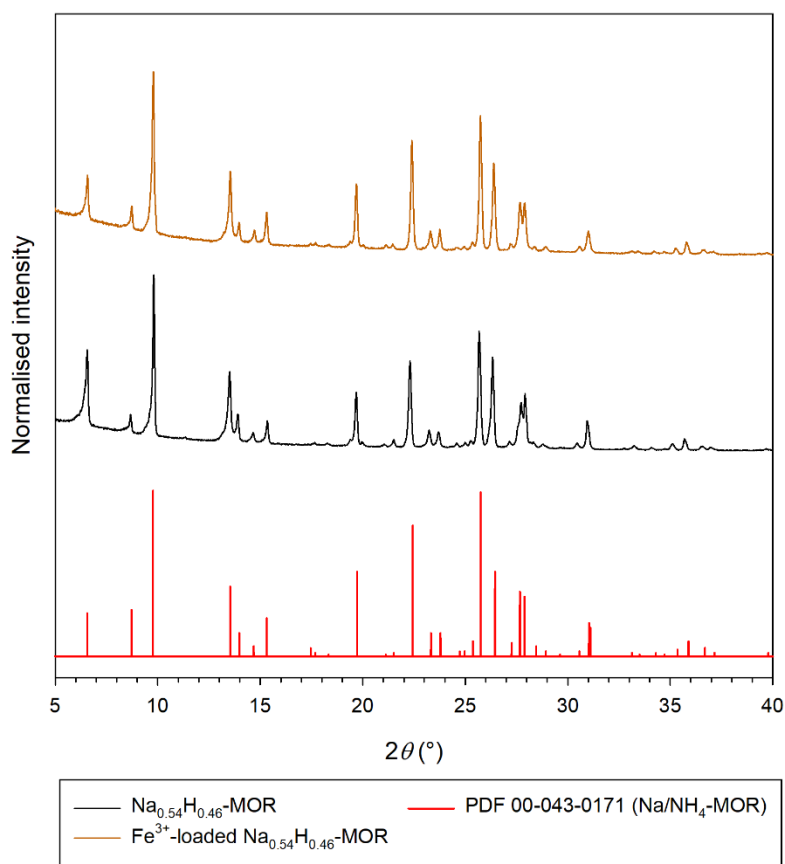


Figure 6.11. PXRD patterns recorded for Na<sub>0.54</sub>H<sub>0.46</sub>-MOR and Fe<sup>3+</sup>-loaded Na<sub>0.54</sub>H<sub>0.46</sub>-MOR.

Table 6.5. Lattice constants for Na<sub>0.54</sub>H<sub>0.46</sub>-MOR and Fe<sup>3+</sup>-loaded Na<sub>0.54</sub>H<sub>0.46</sub>-MOR.

Zeolite	<i>a</i> (Å)	<i>b</i> (Å)	<i>c</i> (Å)	<i>V</i> (Å <sup>3</sup> )
Na <sub>0.54</sub> H <sub>0.46</sub> -MOR	18.08(1)	20.42(1)	7.500(3)	2770(5)
Fe <sup>3+</sup> -loaded Na <sub>0.54</sub> H <sub>0.46</sub> -MOR	18.10(1)	20.39(1)	7.481(8)	2761(9)

Equilibrium fluoride loadings have been measured for the iron-loaded calcined mordenite sample from 1:1 NaF:HNO<sub>3</sub> solutions at 25°C across the concentration range, 5 – 60 ppm F<sup>-</sup>. The equilibrium fluoride uptake data has been fitted to the linear Freundlich, Temkin, Langmuir and Dubinin-

Radushkevitch (DR) isotherms, with  $R^2$  values from linear regression analysis, as well as appropriate isotherm constants, presented in Table 6.6. While poor fits are observed to the Temkin and Langmuir isotherms (plots in Appendix 1), good fits to the Freundlich (Figure 6.12) and Dubinin-Radushkevitch isotherms (Figure 6.13) are observed, with  $R^2 > 0.99$ . The value of the exponent in the Freundlich plot indicates adsorption of fluoride is favourable; moreover, a similar value for  $n$  is observed for iron(III)-loaded GME. The characteristic adsorption energy ( $E_c$ ) calculated from the DR isotherm for iron(III)-loaded  $\text{Na}_{0.54}\text{H}_{0.46}\text{-MOR}$  ( $7.0 \text{ kJ mol}^{-1}$ ) is close to the threshold for chemisorption, the mode of action by which fluoride would be anticipated to interact with surface bound iron(III).<sup>59,108</sup> Furthermore, the characteristic adsorption energy is similar to the value observed for iron(III)-loaded GME ( $7.7 \text{ kJ mol}^{-1}$ ). Values below  $8 \text{ kJ mol}^{-1}$  may still be ascribed to chemisorption, with the reduced values reflecting lower favourability, in line with all fluoride loadings measured from 1:1  $\text{H}^+:\text{F}^-$  solutions.

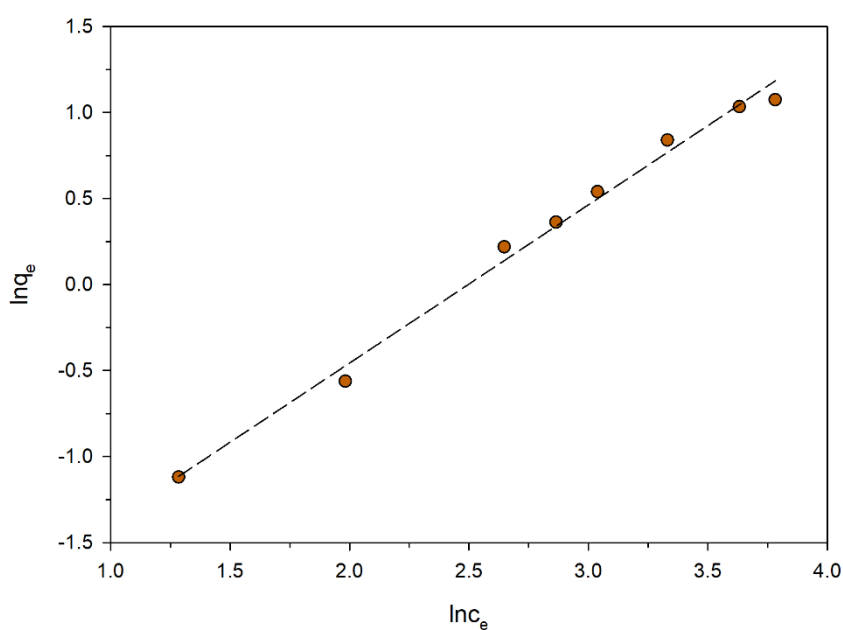


Figure 6.12. Freundlich plot for  $\text{Fe}^{3+}$ -loaded  $\text{Na}_{0.54}\text{H}_{0.46}\text{-MOR}$ .

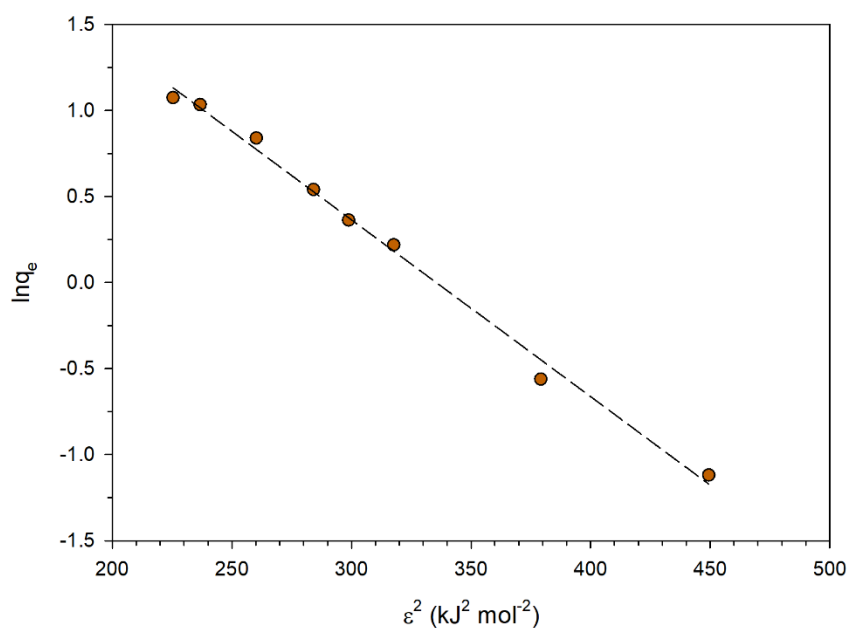


Figure 6.13. Dubinin-Radushkevitch plot for Fe<sup>3+</sup>-loaded Na<sub>0.54</sub>H<sub>0.46</sub>-MOR.

Table 6.6.  $R^2$  and isotherm parameters for fits to the listed isotherms for Fe<sup>3+</sup>-loaded Na<sub>0.54</sub>H<sub>0.46</sub>-MOR. (The units of  $K_F$  are ((mg g<sup>-1</sup>)/(mg L<sup>-1</sup>)<sup>n</sup>)).

Freundlich			Dubinin-Radushkevitch			Temkin	Langmuir
$R^2$	$K_F$	$n$	$R^2$	$E_C$ (kJ mol <sup>-1</sup> )	$K$ (x 10 <sup>-3</sup> mol <sup>2</sup> kJ <sup>-2</sup> )	$R^2$	$R^2$
0.992	0.10	0.92	0.994	7.0	10.3	0.934	0.659

While iron(III)-loaded Na<sub>0.54</sub>H<sub>0.46</sub>-MOR displays intermediate morphology (Si/Al = 8.6(3); Na/Al = 0.54(3)), iron loadings have also been demonstrated on calcined spherical (Si/Al = 8.2(2); Na/Al = 0.46(3)) and prismatic (Si/Al = 10.2(4), Na/Al = 0.95(3)) samples. Following an analogous treatment with 0.25 M iron(III) nitrate, the iron content on the treated spherical sample was 0.17(1) wt% Fe, equivalent to 0.24 wt% Fe<sub>2</sub>O<sub>3</sub> and Fe/Al = 0.02. A higher iron content, 0.29(2) wt% Fe, was measured in the prismatic sample, corresponding to 0.42(2) wt% Fe<sub>2</sub>O<sub>3</sub> and Fe/Al = 0.04.

### 6.3.2.2 Proton Ion Exchange and Iron(III) Modification

Attempts to dealuminate mordenite by reported methods have been unsuccessful in increasing the bulk Si/Al ratio of the product measured by XRF spectrometry. The high Si/Al ratio of mordenite samples necessitate driving conditions for dealumination to occur, such as heating concentrated mineral acid solutions containing the zeolite under reflux.<sup>142</sup> Refluxing mordenite with 6 M hydrochloric acid for 24 hours did not lead to a reduction in the Si/Al ratio of the calcined sample (Si/Al = 8.6(3)); however, some ion exchange between aqueous H<sup>+</sup> and intrapore Na<sup>+</sup> appears to have occurred as a reduction in the Na/Al ratio from 0.54(3) to 0.39(2) was measured. PXRD patterns recorded on the parent material, Na<sub>0.54</sub>H<sub>0.46</sub>-MOR, and the partially proton-exchanged mordenite, Na<sub>0.39</sub>H<sub>0.61</sub>-MOR, show some changes in relative peak intensities following ion exchange (Figure 6.14). Some changes to the *a* and *b* lengths are observed following proton ion exchange (Table 6.7); however, there is still overlap between the confidence intervals of each lattice constant for the parent material and proton exchanged product. Na<sub>0.39</sub>H<sub>0.61</sub>-MOR has been loaded with iron(III), giving rise to a relatively low iron content in the product, 0.04 wt% Fe, corresponding to 0.06 wt% Fe<sub>2</sub>O<sub>3</sub> and Fe/Al < 0.01. The PXRD pattern of Fe<sup>III</sup>-loaded Na<sub>0.39</sub>H<sub>0.61</sub>-MOR shows further changes in relative intensity (Fig. 6.14), the origin of which is unclear. No significant change in the lattice constants is observed following iron(III) loading.

Table 6.7. Lattice constants for Na<sub>0.54</sub>H<sub>0.46</sub>-MOR, Na<sub>0.39</sub>H<sub>0.61</sub>-MOR and Fe<sup>3+</sup>-loaded Na<sub>0.39</sub>H<sub>0.61</sub>-MOR.

Zeolite	<i>a</i> (Å)	<i>b</i> (Å)	<i>c</i> (Å)	<i>V</i> (Å <sup>3</sup> )
Na <sub>0.54</sub> H <sub>0.46</sub> -MOR	18.08(1)	20.42(1)	7.500(3)	2770(5)
Na <sub>0.39</sub> H <sub>0.61</sub> -MOR	18.17(2)	20.34(2)	7.481(5)	2766(9)
Fe <sup>3+</sup> -loaded Na <sub>0.39</sub> H <sub>0.61</sub> -MOR	18.18(2)	20.35(2)	7.486(5)	2769(9)

Fluoride loadings for Na<sub>0.39</sub>H<sub>0.61</sub>-MOR and iron(III)-loaded Na<sub>0.39</sub>H<sub>0.61</sub>-MOR following 1 hour and 24 hours of contact with a 20 ppm F<sup>-</sup> 1:1 NaF:HNO<sub>3</sub> solution have been measured. Following 1 hour of contact, fluoride loadings of 0.84 mg F<sup>-</sup> g<sup>-1</sup> and 0.88 mg F<sup>-</sup> g<sup>-1</sup>, equivalent to 23% and 25% fluoride

removal, are measured for  $\text{Na}_{0.39}\text{H}_{0.61}\text{-MOR}$  and iron(III)-loaded  $\text{Na}_{0.39}\text{H}_{0.61}\text{-MOR}$ , respectively. Following 24 hours of contact, fluoride loadings of  $2.17 \text{ mg F}^{-1} \text{ g}^{-1}$  and  $2.73 \text{ mg F}^{-1} \text{ g}^{-1}$ , equivalent to 61% and 72% fluoride removal, are measured for  $\text{Na}_{0.39}\text{H}_{0.61}\text{-MOR}$  and iron(III)-loaded  $\text{Na}_{0.39}\text{H}_{0.61}\text{-MOR}$ , respectively. Iron(III) modification increases the fluoride loadings attained by  $\text{Na}_{0.39}\text{H}_{0.61}\text{-MOR}$ , despite the relatively low iron content. The significantly improved fluoride loading achieved by  $\text{Na}_{0.39}\text{H}_{0.61}\text{-MOR}$ , compared with  $\text{Na}_{0.54}\text{H}_{0.46}\text{-MOR}$ , is likely due to the increased intrapore proton concentration in the former, providing a greater number of protons which may participate in fluorination reactions. The enhanced favourability of intrapore protons participating in the fluorination reaction compared with protons adsorbed from solution has been shown previously (Section 5.3.7). The increase in accessible surface area anticipated for  $\text{Na}_{0.39}\text{H}_{0.61}\text{-MOR}$ , compared with  $\text{Na}_{0.54}\text{H}_{0.46}\text{-MOR}$ , may also contribute to the increased fluoride loadings.

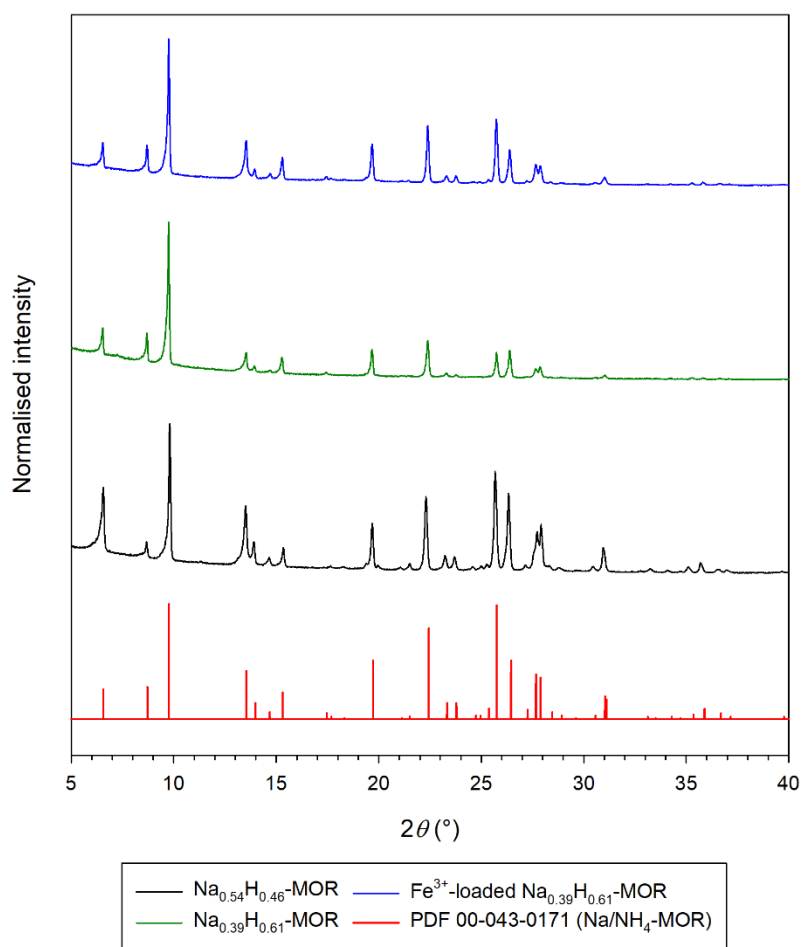


Figure 6.14. PXRD patterns for  $\text{Na}_{0.54}\text{H}_{0.46}\text{-MOR}$ ,  $\text{Na}_{0.39}\text{H}_{0.61}\text{-MOR}$  and  $\text{Fe}^{3+}\text{-loaded Na}_{0.39}\text{H}_{0.61}\text{-MOR}$ .

### 6.3.2.3 Divalent Metal Ion Exchange

Ion exchange between aqueous divalent cations ( $\text{Ca}^{2+}$ ,  $\text{Sr}^{2+}$ ,  $\text{Ba}^{2+}$  and  $\text{Cu}^{2+}$ ) and  $\text{Na}_{0.54}\text{H}_{0.46}\text{-MOR}$  has been achieved by batch ion exchange experiments at  $60^\circ\text{C}$  with 0.25 M solutions of the divalent cation. PXRD patterns recorded on the partially exchanged zeolites are presented in Figure 6.15; in Figure 6.15, intensities have been normalised relative to the 202 reflection at  $2\theta = 25.7^\circ$ , as while the relative intensities of some reflections change significantly upon ion exchange, the 202 reflection was similar in intensity in all patterns, permitting more convenient comparisons in relative intensity in the normalised patterns. Unit cell parameters for the exchanged products and parent material, presented in Table 6.8, show no significant variation following ion exchange. Upon exchange with each divalent metal ion, the relative intensities of the 110 and 200 reflections at  $2\theta = 6.6^\circ$  and  $2\theta = 9.8^\circ$ , respectively, decrease significantly compared to the relative intensities in the parent material.

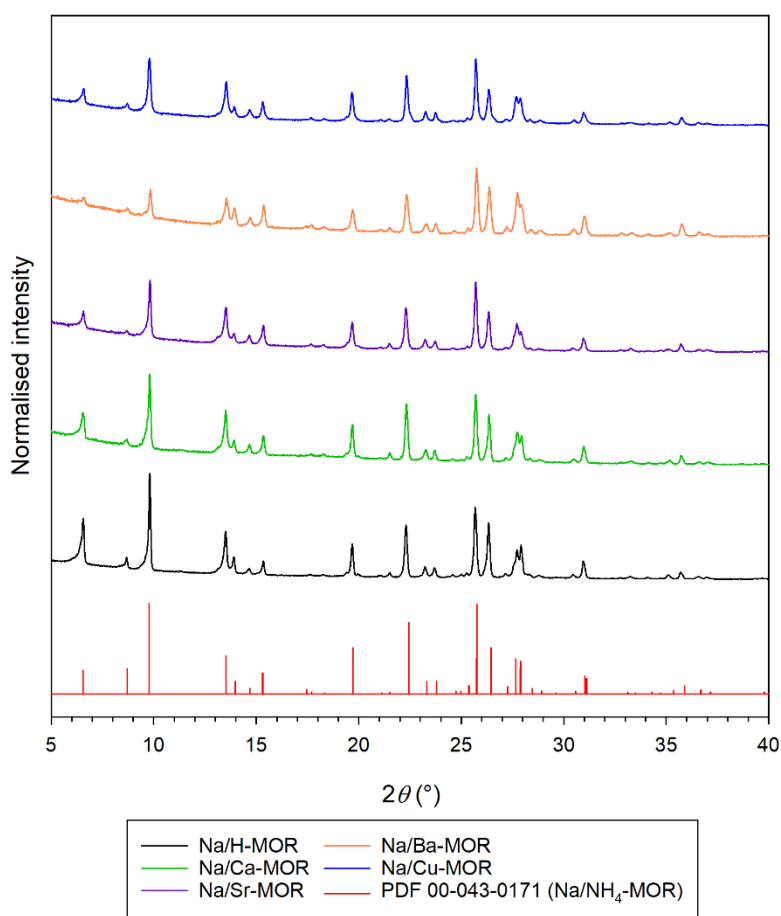


Figure 6.15. PXRD patterns recorded on  $\text{Na}_{0.54}\text{H}_{0.46}\text{-MOR}$  ( $\text{Na/H-MOR}$ ) and ion-exchanged products.

XRF spectrometry performed on the exchanged products attests ion exchange has occurred in each instance. Na/Al and M/Al ratios measured on the products are given in Table 6.8, where M is the appropriate divalent metal. The Na/Al ratio in the zeolite remains constant following ion exchange with calcium, strontium and barium, intimating the divalent metal ion only exchanges with protons in the zeolite. Ion exchange with copper(II) leads to a modest decrease in the Na/Al ratio, indicating some replacement of sodium with copper(II). The total cation contents ( $2(M/Al) + (Na/Al)$ ) inferred from XRF spectrometry (1.2 – 1.8) are significantly greater than the expected value (1.0); accordingly, there may be significant error in the measured M/Al ratios. Potential sources of error in the quantitative results determined by XRF spectrometry may include error inherent to the analysis of samples containing elements with disparate fluorescence yields,<sup>64</sup> in addition to the possible occurrence of “over exchange” phenomena and adsorption of divalent metal complexes on the zeolite surface,<sup>133,134</sup> as discussed previously in Section 5.4.2. While there is a relatively high error in the M/Al ratios determined by XRF spectrometry, critically the M/Al ratios demonstrate the divalent metals are present in the sample, and changes in the relative intensities in the PXRD patterns support that ion exchange has occurred.

Table 6.8. Unit cell parameters and volumes for ion-exchanged mordenites, as well as Na/Al and M/Al ratios measured by XRF spectrometry.

Zeolite	$a$ (Å)	$b$ (Å)	$c$ (Å)	$V$ (Å <sup>3</sup> )	Na/Al	M/Al
Na/H-MOR	18.08(1)	20.42(1)	7.500(3)	2770(5)	0.54(3)	-
Na/Ca-MOR	18.09(2)	20.42(1)	7.500(5)	2769(8)	0.55(3)	0.39(3)
Na/Sr-MOR	18.07(1)	20.43(1)	7.503(4)	2770(6)	0.53(3)	0.37(3)
Na/Ba-MOR	18.11(1)	20.38(1)	7.479(4)	2761(6)	0.56(3)	0.65(4)
Na/Cu-MOR	18.11(1)	20.38(1)	7.489(5)	2764(5)	0.42(3)	0.38(3)

Fluoride loadings, and the percentage of fluoride removed from solution, by MOR partially ion-exchanged with divalent cations, following both an hour and 24 hours of contact with a 20 ppm F<sup>-</sup> 1:1 NaF:HNO<sub>3</sub> solution, are presented in Table 6.9. The introduction of all divalent cations, except

barium, led to a modest increase in the fluoride loading following an hour of contact; however, loadings were still much lower than those observed for iron(III)-modified MOR and H<sup>+</sup>-exchanged MOR under the same conditions. In the highest instance, the fluoride loading achieved by MOR partially ion-exchanged with strontium is 0.13 mg F<sup>-</sup> g<sup>-1</sup>, equivalent to removal of just 4% of the fluoride in solution under these conditions. Partial ion exchange with the divalent cations also leads to a moderate enhancement in fluoride loadings following 24 hours of contact.

Table 6.9. Fluoride loadings attained following an hour ( $q(60 \text{ min})$ ) of contact and at equilibrium for Na<sub>0.54</sub>H<sub>0.46</sub>-MOR (Na/H-MOR) and ion-exchanged products.

	$q(60 \text{ min})$ (mg F <sup>-</sup> g <sup>-1</sup> )	Fluoride removed after 60 mins (%)	$q_e$ (mg F <sup>-</sup> g <sup>-1</sup> )	Fluoride removed after 24 hours (%)
Na/H-MOR	0.00	0	0.32	9
Na/Ca-MOR	0.07	2	0.44	12
Na/Sr-MOR	0.13	4	0.45	12
Na/Ba-MOR	0.00	0	0.62	14
Na/Cu-MOR	0.09	2	0.34	9

#### 6.3.2.4 Conclusions

Iron(III) loading and divalent metal ion exchange have been successfully applied to mordenite, with both leading to increased fluoride loadings. Modest increases in fluoride loadings are observed following ion exchange with divalent metal ions, with mordenite partially exchanged with strontium giving rise to the highest fluoride loading following an hour of contact. Iron(III) loading leads to greater fluoride loadings than divalent metal-ion exchange, despite the relatively low iron content in the iron(III)-loaded sample (< 0.2 wt% Fe). Attempts to dealuminate mordenite have been unsuccessful in increasing the sample Si/Al ratio; however, some ion exchange between intrapore sodium and aqueous protons was observed following refluxing with 6 M HCl. The partially proton-exchanged

zeolite, and iron(III) loaded product thereof, give rise to the highest fluoride loadings observed of any post-synthetic modifications attempted for mordenite.

### 6.3.3 Large Crystals of Zeolites A and X

#### 6.3.3.1 Iron(III) Treatments

Relatively dilute iron(III) solutions are sufficiently acidic to partially dissolve large zeolite A crystals, owing to the polarising nature of aqueous iron(III) ions and the low Si/Al ratio of the zeolite.<sup>138</sup> Scanning electron micrographs recorded on zeolite A treated with 0.01 M (pH = 2.39), 0.025 M (pH = 2.10) and 0.25 M (pH = 1.90) iron(III) nitrate solutions are presented in Figure 6.16. Zeolite A crystals treated with 0.01 M and 0.025 M iron(III) nitrate solutions comprise mostly fractured cubic crystals, and in some cases have smaller particulate material deposited on the crystal surfaces. PXRD patterns for the products of iron(III) treatments on zeolite A and X were recorded on a Bruker D2 diffractometer with a Co  $K_{\alpha}$  X-ray source ( $\lambda = 1.7902 \text{ \AA}$ ). The PXRD pattern recorded on zeolite A treated with 0.01 M iron(III) nitrate shows crystalline zeolite A is present in the sample (Figure 6.17). The relative intensity of the 100 reflection at  $2\theta = 8.3^{\circ}$ , however, is significantly reduced compared with patterns recorded on the parent material. The PXRD pattern of the product treated with 0.025 M iron(III) nitrate shows no detectable trace of crystalline zeolite A remains following the treatment (Figure 6.17). Upon increasing the concentration to 0.25 M, no trace of cubic crystals remain in micrographs of the product, rather the product only comprises smaller fragments. A PXRD pattern could not be recorded on zeolite A treated with 0.25 M iron(III) nitrate as an insufficient yield was recovered, owing to dissolution of the zeolite.

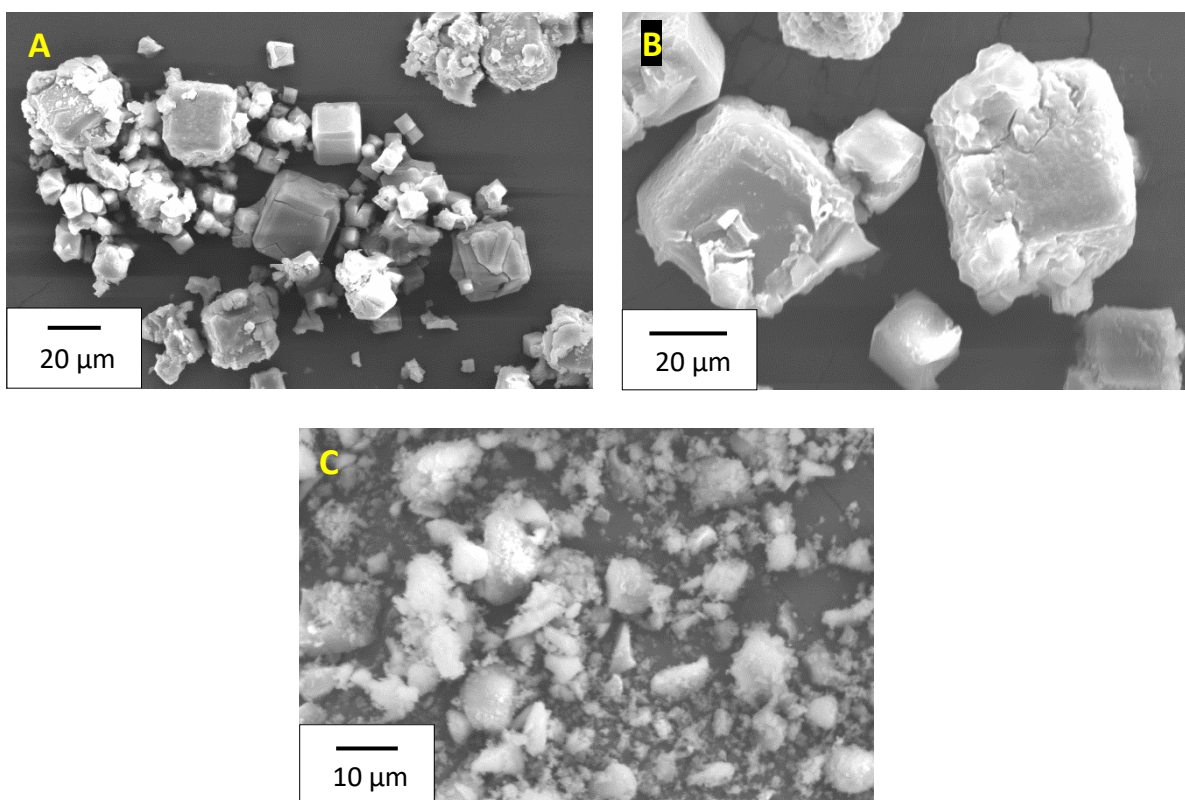


Figure 6.16. Scanning electron micrographs of products of treatments with (A) 0.01 M, (B) 0.025 M and (C) 0.25 M  $\text{Fe}(\text{NO}_3)_3$  on zeolite A crystals.

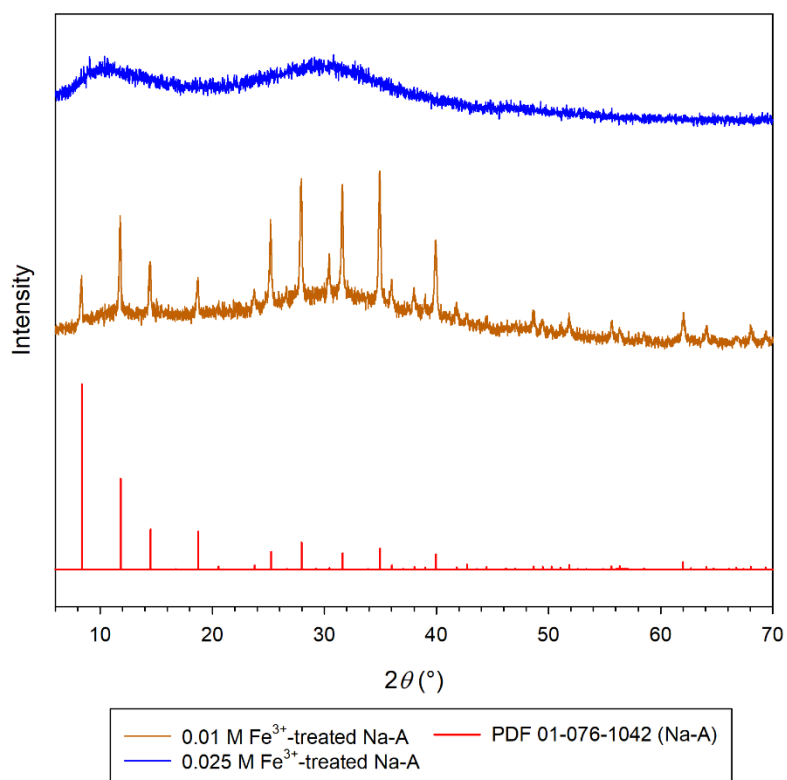


Figure 6.17. PXRD patterns of products of zeolite A crystals following treatment with 0.01 M and 0.025 M  $\text{Fe}(\text{NO}_3)_3$  solutions, recorded on a Bruker D2 diffractometer with a  $\text{Co } K_\alpha$  X-ray source ( $\lambda = 1.7902 \text{ \AA}$ ).

The issues arising from the acidity of iron(III) solutions cannot be ameliorated by buffering to a higher pH, at which the zeolite would be stable, as the addition of alkali to iron(III)-containing solutions leads to precipitation of an amorphous, red-brown, hydrous iron(III) oxide.<sup>143</sup> At pH > 2.5, the precipitation of the amorphous hydrous iron(III) oxide is possible, as condensation of the discrete iron(III) complexes and dimers which predominate at lower pH (< 2.5) may occur.<sup>138</sup> No hydrous iron(III) oxide is anticipated in iron(III)-loaded Na-GME, as the product is a yellow colour intimating the formation of surface bound iron(III) hydroxo-containing species. In contrast, the products of iron(III) treatment on zeolite A are brown in colour indicating the precipitation of an amorphous iron(III) species.<sup>138</sup> A significantly higher iron content is observed for zeolite A treated with 0.01 M iron(III) nitrate compared with the iron loadings achieved for GME and MOR following analogous treatments with more concentrated iron(III) solutions (Sections 6.3.1.3 and 6.3.2.1). The iron content of zeolite A treated with 0.01 M iron(III) nitrate is 8.2 wt% Fe, corresponding to 11.8 wt% Fe<sub>2</sub>O<sub>3</sub> and Fe/Al = 0.33(3). The significantly higher iron contents in the products, the presence of additional material in the micrographs and the brown colour of the products all support that the precipitation of an amorphous iron(III)-containing phase has occurred. The formation of the amorphous hydrous iron(III) oxide in the zeolite A system may be rationalised by the consumption of protons in the extrication of aluminium, and consequent dissolution of the framework, increasing the solution pH to conditions conducive with the precipitation of the amorphous hydrous iron(III) oxide. Conversion of the amorphous material to crystalline iron(III)-containing phases only occurs upon heating above 100°C.<sup>143</sup>

Analogously to zeolite A, scanning electron micrographs reveal octahedral zeolite X crystals treated with 0.01 M iron(III) nitrate are fractured and fragmented (Figure 6.18), owing to the high aluminium content of the zeolite and the acidity of the solution. PXRD demonstrates crystalline zeolite X is still present following treatment with 0.01 M iron(III) nitrate (Figure 6.19); however, the relative intensity of the 111 reflection at  $2\theta = 7.1^\circ$  is significantly reduced compared with other reflections in the pattern. Additional reflections are also present in the PXRD pattern, most notably at  $2\theta = 14.5^\circ$  and  $2\theta = 20.8^\circ$ , corresponding to zeolite P. The spherical particles observed in samples of zeolite X grown

for 4 weeks in Section 4.3.2 are, therefore, likely zeolite P particles. No discernible zeolite P reflections are observed in PXRD patterns of the parent zeolite X crystals, due to the quantity and high crystallinity of the zeolite X present; however, upon reducing the crystallinity of zeolite X following treatment with iron(III) solutions, the previously undiscernible peaks become apparent.

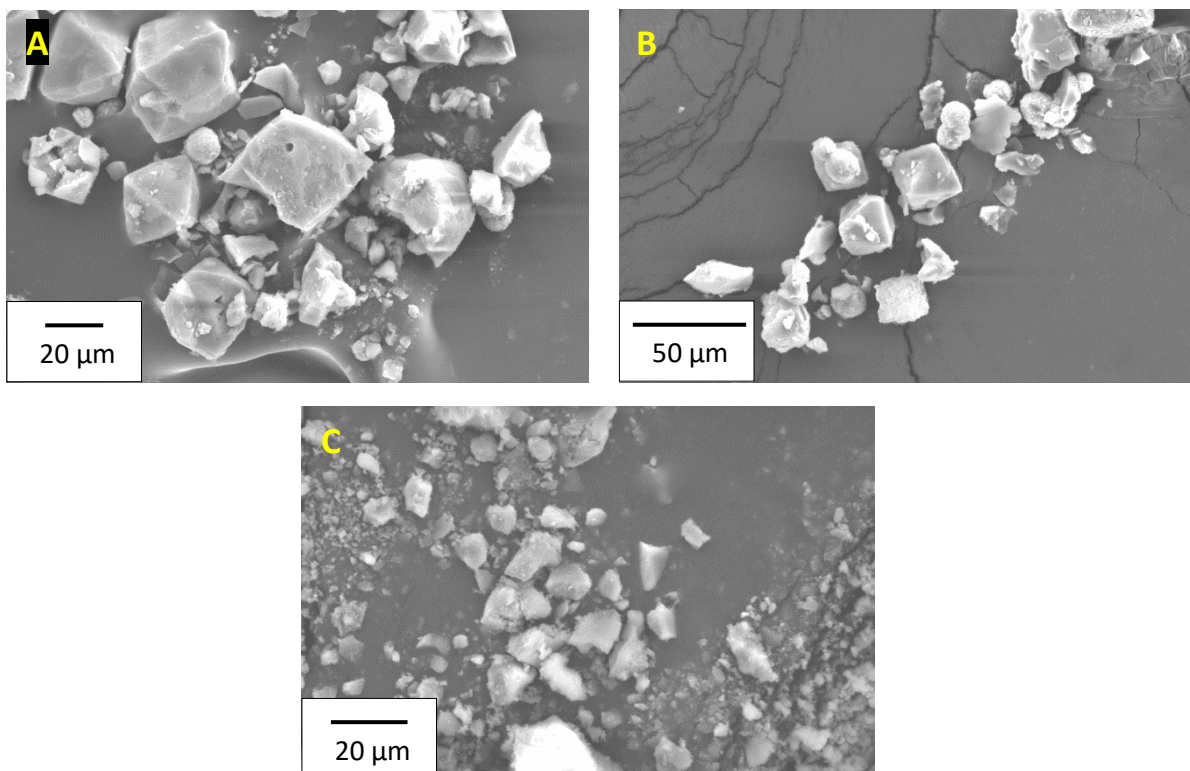


Figure 6.18. Scanning electron micrographs of products of treatments with (A) 0.01 M, (B) 0.025 M and (C) 0.25 M  $\text{Fe}(\text{NO}_3)_3$  on zeolite X crystals.

Treating zeolite X with 0.025 M iron(III) nitrate also leads to fractured and fragmented crystals; however, there are no reflections in the product PXRD pattern, indicating no detectable quantity of crystalline zeolite X remains in the sample. Upon further increasing the iron(III) nitrate concentration to 0.25 M, no octahedral crystals remain in the product. The treatment with 0.25 M iron(III) nitrate leads to extensive dissolution of the zeolite, such that the yield is insufficient for a PXRD pattern to be recorded on the recovered product. In agreement with observations in the zeolite A system, the

products of iron(III) treatment on zeolite X are brown in colour; moreover, following treatment with 0.01 M iron(III) nitrate, a high iron loading is observed in the product, 4.2 wt% Fe (equivalent to 6.0 wt% Fe<sub>2</sub>O<sub>3</sub> and a sample Fe/Al of 0.17(2)). The product colour, high iron contents and presence of additional material on some crystal surfaces all intimate the precipitation of an amorphous iron(III)-containing phase, for analogous reasons to those outlined for zeolite A.

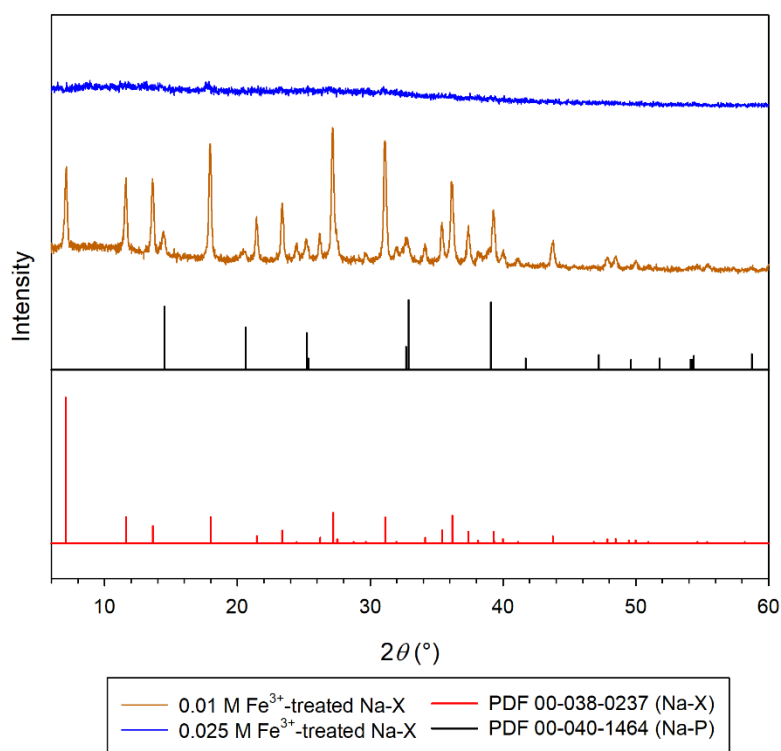


Figure 6.19. PXRD patterns of products following treatment of zeolite X crystals with 0.01 M and 0.025 M Fe(NO<sub>3</sub>)<sub>3</sub> solutions, recorded on a Bruker D2 diffractometer with a Co K<sub>α</sub> X-ray source ( $\lambda = 1.7902 \text{ \AA}$ ).

The immersion of large zeolite A and X crystals in relatively dilute iron(III) nitrate solutions leads to a reduction in the crystallinity of the sample and compromises the structural integrity of the crystals, even in the most dilute solutions tested (0.01 M). Increasing the concentration leads to dissolution of the zeolite and destruction of the crystals, caused by the acidity of the iron(III) nitrate solutions and the low framework Si/Al ratios inherent to the zeolites. It is well established that under sufficiently acidic conditions, protons extricate aluminium from zeolite frameworks, and in the case of low Si/Al

zeolites, such as zeolite A and X, breakdown of the framework ensues.<sup>137</sup> While more dilute solutions (0.01 M and 0.025 M) do not lead to the complete dissolution of the crystals, the consumption of protons, and influence on solution pH, gives rise to the precipitation of an amorphous iron(III) phase engendering the brown colour of the products. Ultimately, the surface modification of zeolites A and X with iron(III) from aqueous solutions is not possible without compromising the structural integrity of the crystals; therefore, it is unsuitable for modifying zeolite A and X crystals to enhance fluoride loadings.

#### 6.3.3.2 EDTA Treatments

Dealumination of zeolites A and X to any appreciable extent is not possible, as the selective removal of aluminium from zeolite frameworks with Si/Al  $\approx$  1 cannot be achieved without the destruction of the framework. The effects of H<sub>4</sub>EDTA treatments on the morphology and crystallinity of large zeolite A crystals have been studied by adding a fixed amount of the zeolite to slurries with different EDTA contents. Products are labelled E1 – 4 according to the ratio of the mass of H<sub>4</sub>EDTA to zeolite in the slurry (i.e. mass(H<sub>4</sub>EDTA)/mass(zeolite)), for E1 the ratio is 0.41, and for E2, E3 and E4, the ratios are 0.54, 0.68 and 0.82, respectively. Scanning electron micrographs of the products are presented in Figure 6.20, a PXRD pattern recorded on the product E1 is presented in Figure 6.21 and PXRD patterns recorded on products E2 – 4 are presented in Figure 6.22. For (E1)-Na-A, there is little change in the PXRD pattern recorded following treatment with H<sub>4</sub>EDTA, but some cracks and cavities produced by the action of H<sub>4</sub>EDTA are apparent on the large zeolite A crystals. The localised dissolution of the framework leading to the formation of cavities may be rationalised by the insolubility of H<sub>4</sub>EDTA, giving rise to lower mobility than would be expected for dissolved species, resulting in the H<sub>4</sub>EDTA molecules acting on the framework in localised areas.

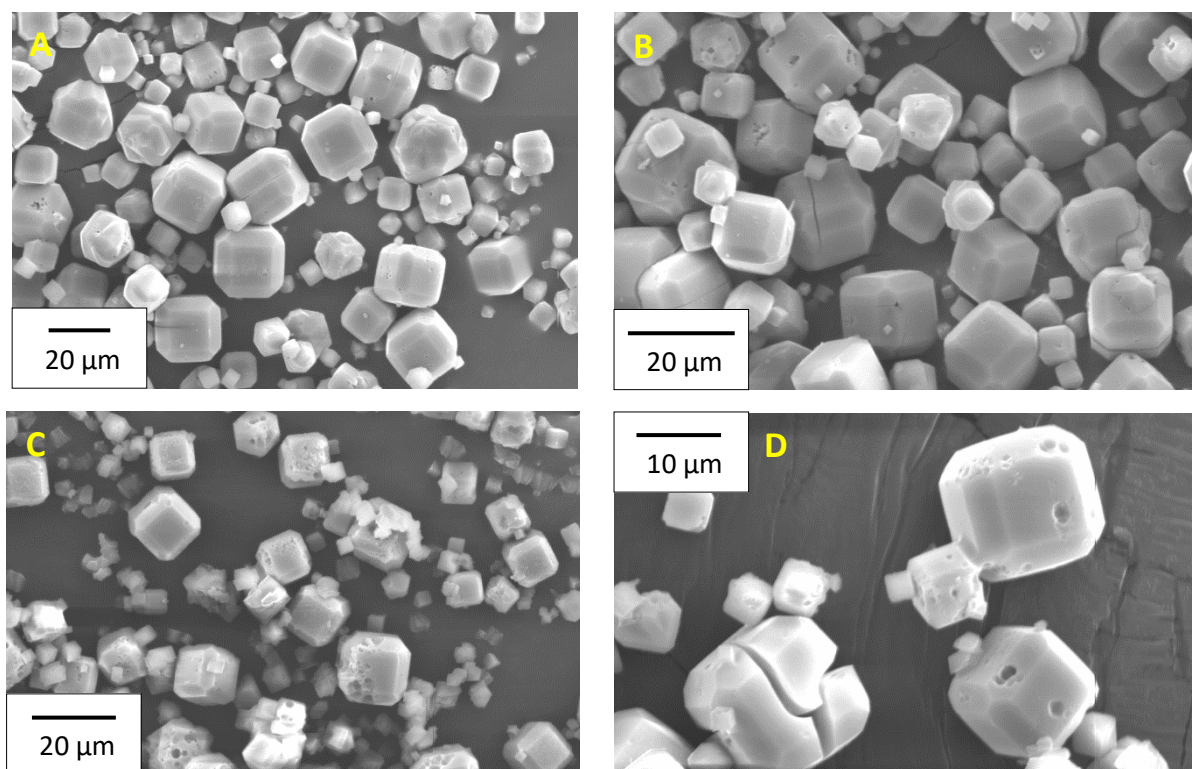


Figure 6.20. Scanning electron micrographs of zeolite A crystals treated with EDTA: (A) (E1)-Na-A, (B) (E2)-Na-A, (C) (E3)-Na-A and (D) (E4)-Na-A.

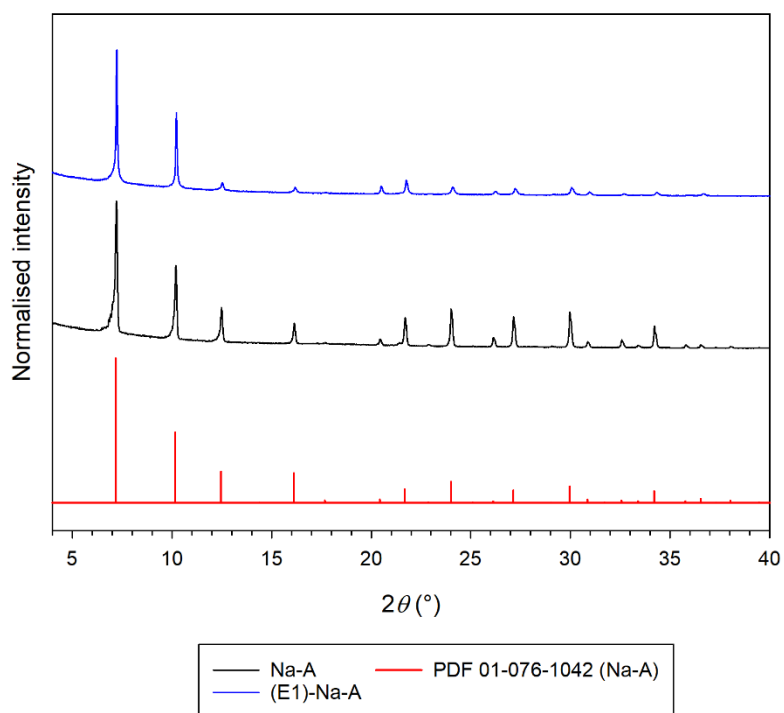


Figure 6.21. PXRD patterns for zeolite Na-A and (E1)-Na-A.

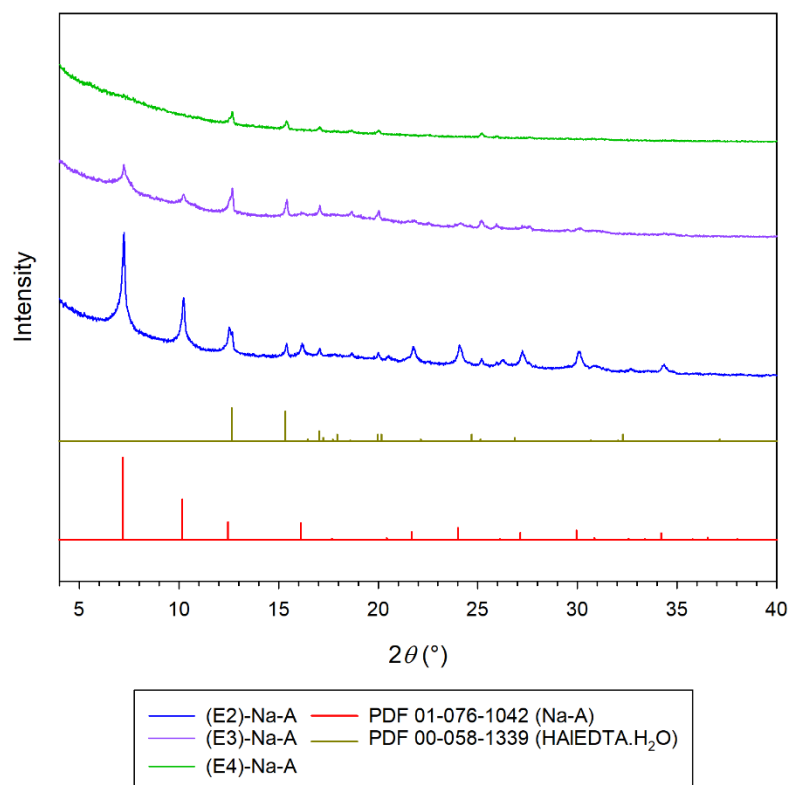


Figure 6.22. PXRD patterns for (E2)-Na-A, (E3)-Na-A and (E4)-Na-A.

Increasing the EDTA content of the slurry leads to a reduction in the relative intensities of Na-A reflections in the PXRD pattern recorded on (E2)-Na-A, as well as the appearance of additional reflections at  $2\theta = 12.7^\circ$  and  $2\theta = 15.4^\circ$ , corresponding to the 021 and 100 reflections, respectively, of HAI[EDTA].H<sub>2</sub>O (*P*2<sub>1</sub>*C*,  $a = 5.7 \text{ \AA}$ ,  $b = 14.9 \text{ \AA}$ ,  $c = 19.1 \text{ \AA}$  and  $\beta = 90.7^\circ$ ).<sup>144</sup> The precipitation of HAI[EDTA].H<sub>2</sub>O is noteworthy, as EDTA typically extricates aluminium from frameworks as soluble NaAl[EDTA].H<sub>2</sub>O complexes, leaving silanol nests in the framework as illustrated in Section 5.5.1.<sup>132</sup> The formation of HAI[EDTA].H<sub>2</sub>O could arise from incomplete dissociation of some H<sub>4</sub>EDTA molecules upon complexing aluminium(III) ions. As the EDTA content in the slurry increases, the product yields decrease (detailed in Section 6.2.3.3), further attesting dissolution of the framework.

Cracks and cavities in zeolite A crystals are also present in (E2)-Na-A. The frequency with which cracks and cavities are observed in large zeolite A crystals increases with the amount of EDTA in the slurry, as observed in scanning electron micrographs of (E3)-Na-A and (E4)-Na-A. As the EDTA content in the

slurry increases, the relative intensities of Na-A reflections decrease in the product PXRD pattern, with no discernible zeolite A reflections present in the PXRD pattern of (E4)-Na-A. The Si/Al ratio measured for (E4)-Na-A is 0.85(2), decreasing from the parent due to framework dissolution and the precipitation of the aluminium-containing phase,  $\text{HAl[EDTA]}\cdot\text{H}_2\text{O}$ .

In line with observations in the zeolite A system, EDTA treatments on zeolite X render the octahedral crystals fractured and fragmented (Figure 6.23). There is little difference between the PXRD patterns recorded on zeolite (E1)-Na-X and the parent material (Figure 6.24). Increasing the EDTA content in the slurry, however, leads to a significant reduction in the relative intensities of Na-X reflections in the PXRD pattern (Figure 6.25), as observed for zeolite A. The precipitation of  $\text{HAl[EDTA]}\cdot\text{H}_2\text{O}$  is also observed in the products of treatments with higher EDTA contents, (E2)-Na-X, (E3)-Na-X and (E4)-Na-X.

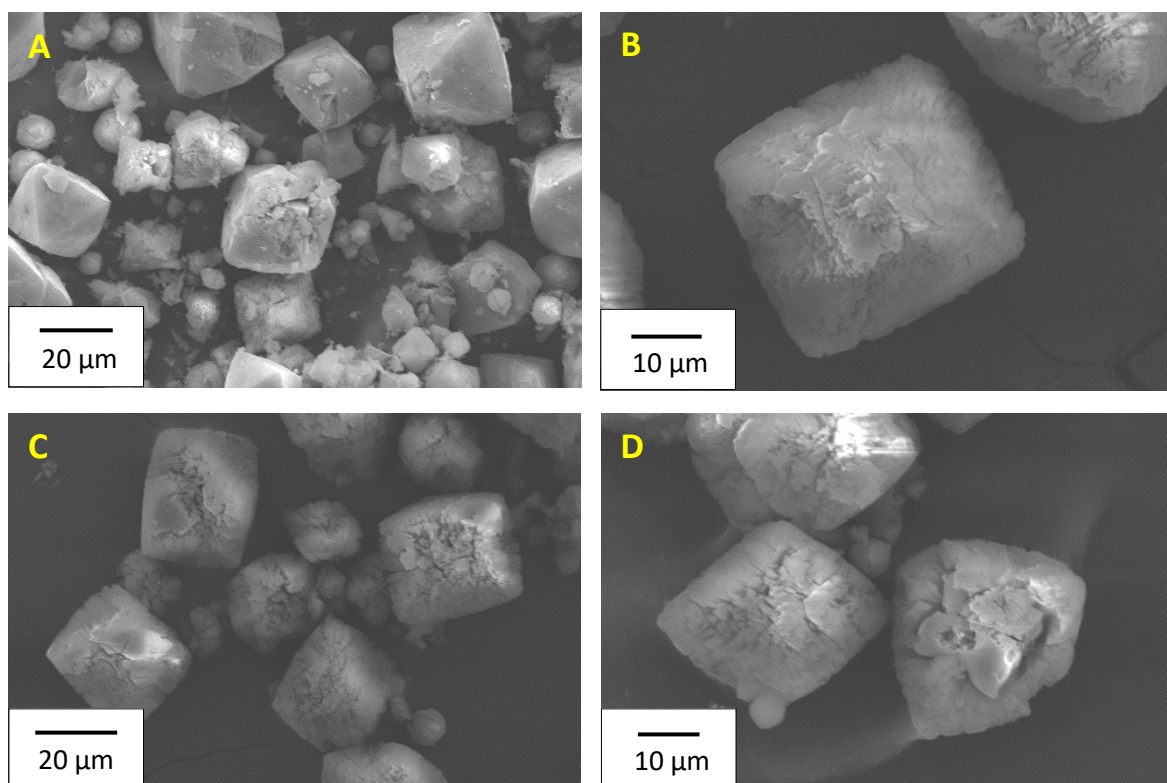


Figure 6.23. Scanning electron micrographs on zeolite A crystals treated with EDTA: (A) (E1)-Na-X, (B) (E2)-Na-X, (C) (E3)-Na-X and (D) (E4)-Na-X.

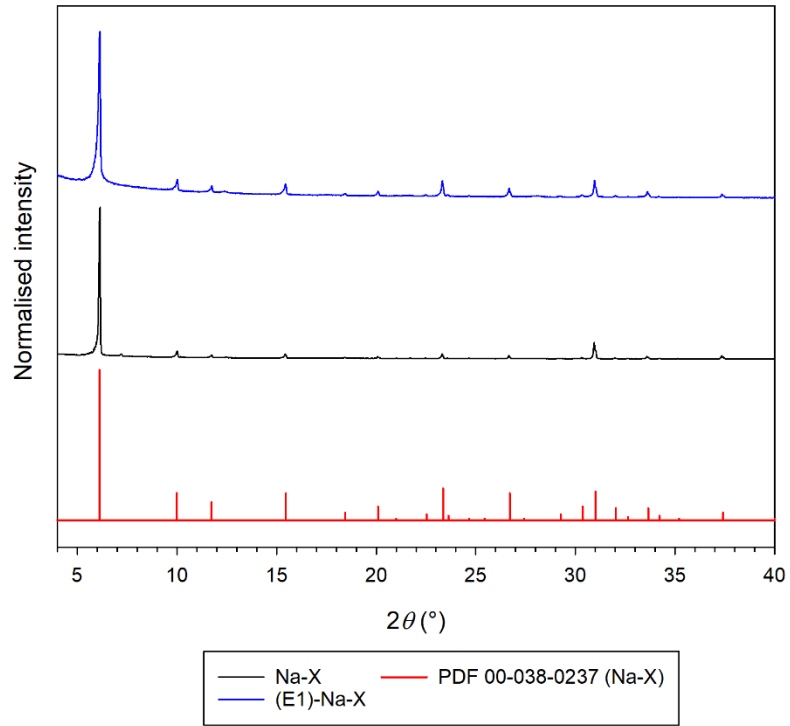


Figure 6.24. PXRD patterns of Na-X and (E1)-Na-X.

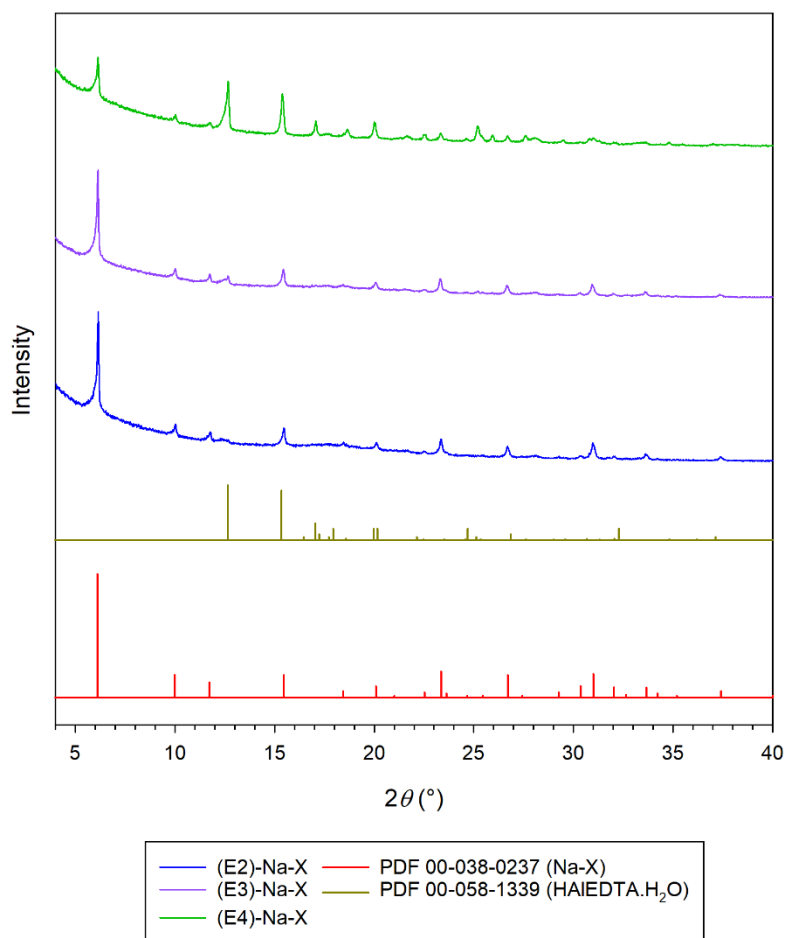


Figure 6.25. PXRD patterns recorded for (E2)-Na-X, (E3)-Na-X and (E4)-Na-X.

### 6.3.3.3 Divalent Metal Ion Exchange

Ion exchange between aqueous divalent cations ( $\text{Ca}^{2+}$ ,  $\text{Sr}^{2+}$ ,  $\text{Ba}^{2+}$  and  $\text{Cu}^{2+}$ ) and zeolites Na-A and Na-X have been achieved by batch ion exchange experiments at 60°C. In the case of calcium, strontium and barium ion exchange, 0.25 M solutions of the appropriate metal nitrate were used; however, for copper(II) ion exchange, 0.01 M and 0.025 M copper(II) nitrate solutions were employed for zeolites A and X, respectively. Lower concentration copper(II) nitrate solutions were used as attempts to exchange with 0.25 M solutions led to co-precipitation of  $\text{Cu}_2(\text{OH})_3(\text{NO}_3)$ , (monoclinic,  $P2_1$ ,  $a = 5.6 \text{ \AA}$ ,  $b = 6.1 \text{ \AA}$ ,  $c = 6.9 \text{ \AA}$ ,  $\beta = 94.7^\circ$ ), in the case of zeolite X. In the case of zeolite A, only  $\text{Cu}_2(\text{OH})_3(\text{NO}_3)$  is present in the PXRD pattern of the material recovered following treatment with 0.25 M copper(II) nitrate. The PXRD patterns of the products of both zeolite A and X following treatments with 0.25 M

copper(II) nitrate are presented in Appendix 4. The precipitation of  $\text{Cu}_2(\text{OH})_3(\text{NO}_3)$  along with the dissolution of the zeolites is caused by the acidity of the 0.25 M copper(II) nitrate solution ( $\text{pH} = 3.41$ ). In contrast, lower concentration solutions were less acidic, ( $\text{pH} = 4.24$  and  $\text{pH} = 4.10$  for 0.01 M and 0.025 M copper(II) nitrate, respectively), enabling ion-exchange to occur with preservation of the crystal structure.

XRF spectrometry performed on the exchanged products attest ion exchange has occurred in each instance. Si/Al, Na/Al and M/Al ratios measured on the products are given in Table 6.10, where M is the appropriate divalent metal. In all samples of zeolite A, the measured Si/Al ratio is within error of the anticipated value (Si/Al = 1.0). In contrast, the Na/Al ratio for large zeolite A crystals is significantly greater than the anticipated value (1.0), as such the error in the value must be greater than the calculated error, therefore no associated errors are reported in Table 6.10. The origin of the greater Na/Al ratio is not clear. Ion exchange with calcium, strontium and barium leads to a significant reduction in the Na/Al ratio; however, the total cation contents ( $2(\text{M}/\text{Al}) + \text{Na}/\text{Al}$ ) are greater than the theoretical value (1.0), but agree reasonably well with the measured Na/Al ratio for the product. The replacement of sodium with copper(II) is lower than for the other exchanged zeolites, owing to the lower concentration of the supernatant solution during ion exchange. As outlined in Section 5.4.2, several possible explanations may be proposed for the origin of inflated M/Al ratios, including errors inherent to measuring elements with disparate fluorescence yields,<sup>64</sup> deposition of divalent metal ion complexes on the zeolite surface, or the occurrence of “over exchange” phenomena.<sup>133,134</sup>

PXRD patterns recorded on partially exchanged zeolite A samples are presented in Figure 6.26, where the intensities have been normalised relative to the 410 reflection at  $2\theta \approx 30.0^\circ$ , as while the relative intensities of some reflections change significantly upon ion exchange, the 410 reflection was similar in intensity in all patterns, permitting more convenient comparisons in relative intensity in the normalised patterns. A significant reduction in the relative intensity of the 100 and 110 reflections at  $2\theta \approx 7.2^\circ$  and  $2\theta \approx 10.2^\circ$ , respectively, is observed following exchange with both strontium and barium;

moreover, the 111 reflection at  $2\theta \approx 12.5^\circ$  is not present following barium exchange and significantly reduced in intensity after strontium exchange. In contrast, the intensity of the 100 reflection, relative to the 410 reflection, increases following ion exchange with calcium and copper(II). In PXRD patterns recorded on calcium and strontium exchanged zeolite A, an additional peak is present at  $2\theta \approx 14.4^\circ$  corresponding to the 200 reflection, which is typically very weak in PXRD patterns of Na-A. The lattice constants for zeolite A following ion exchange show a contraction of the unit cell in each instance (Table 6.10); however, the confidence interval of all lattice constants, except for Ba-exchanged A, overlaps with that of the parent material.

Table 6.10. Unit cell parameters and volumes, along with Na/Al, M/Al and Si/Al measured for both Na-A and Na-X and their ion-exchanged products.

	$a$ (Å)	$V$ (Å <sup>3</sup> )	Na/Al	M/Al	Si/Al
Na-A	24.56(1)	14,814(18)	1.23	-	0.96(3)
Ca-A	24.48(1)	14,670(18)	0.09	0.66	0.98(3)
Sr-A	24.538(1)	14,775(4)	0.08	0.50	1.06(3)
Ba-A	24.400(1)	14,527(4)	0.16	0.62	0.97(3)
Cu-A	24.46(1)	14,634(18)	0.75	0.22	0.97(3)
Na-X	25.01(1)	15638(19)	1.20	-	1.10(3)
Ca-X	24.92(1)	15475(19)	0.09	0.53	1.10(3)
Sr-X	25.125(7)	15861(13)	0.03	0.56	1.10(3)
Ba-X	25.00(3)	15658(22)	0.12	0.67	1.06(3)
Cu-X	24.93(1)	15488(19)	0.00	0.69	1.12(4)

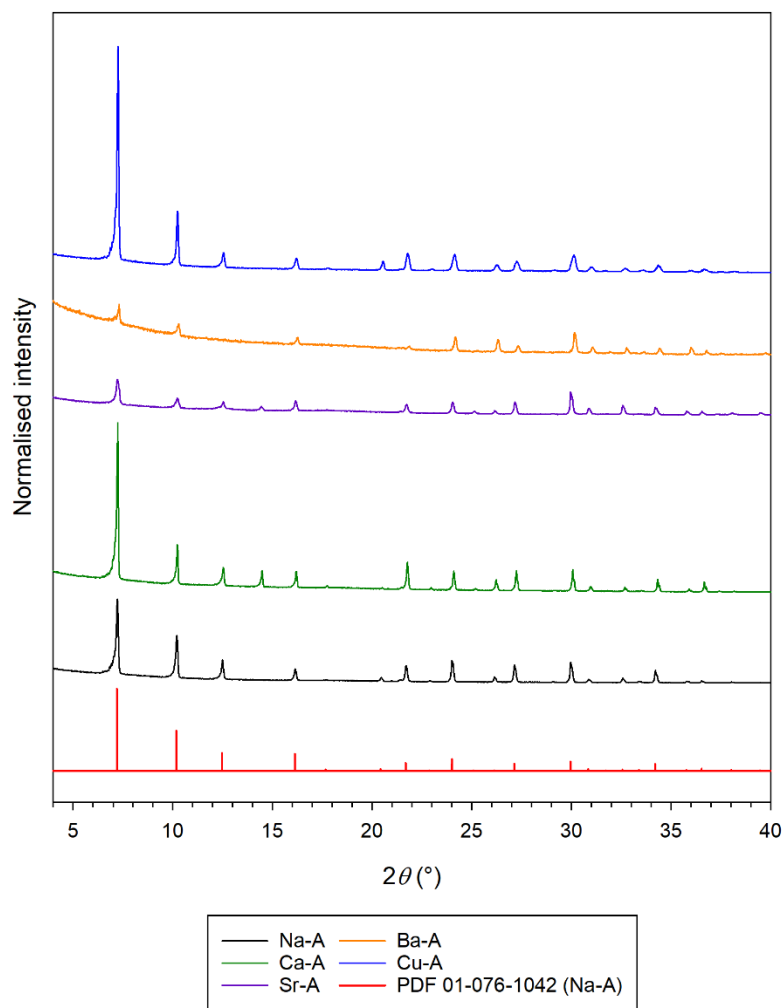


Figure 6.26. PXRD patterns recorded on Na-A and ion-exchanged products.

XRF spectrometry attests significant ion exchange has occurred in zeolite X samples. As in the case of zeolite A, a higher than expected Na/Al ratio is observed as well as inflated M/Al ratios. Possible causes of inflated M/Al ratios in quantitative analysis by XRF spectrometry have been outlined previously in Section 5.4.2 and include: error inherent to samples containing elements with disparate fluorescence yields,<sup>64</sup> and the possible occurrence of “over exchange” phenomena and surface adsorption.<sup>133,134</sup> The co-presence of zeolite A and P impurities in the samples introduces a further source of error, as it is unclear to what extent each phase contributes to the overall compositional ratios.

PXRD patterns recorded on partially exchanged zeolite X samples are presented in Figure 6.27. PXRD patterns in Figure 6.27, excluding the Na-X pattern, are normalised to the 533 reflection at  $2\theta \approx 23.3^\circ$ .

The relative intensities of the 111 reflections at  $2\theta \approx 6.1^\circ$ , compared with the 533 reflections, are much greater in the calcium and copper(II)-exchanged zeolite X samples than in patterns of the strontium and barium-exchanged samples. Additional reflections, that are allowed but not typically observed for Na-zeolite X, are present in the PXRD patterns of each exchanged zeolite, most notably at  $2\theta \approx 12.2^\circ$ , corresponding to the 222 reflection, in the strontium, barium and copper(II)-exchanged samples. A contraction of the unit cell is observed upon exchange with calcium and copper(II) (Table 6.10), in contrast strontium exchange leads to an increase in the unit cell. The barium-exchanged unit cell appears similar to the parent material in size but with higher associated errors in each lattice constant, caused by uncertainty in the peak positions engendered by the low relative intensities.

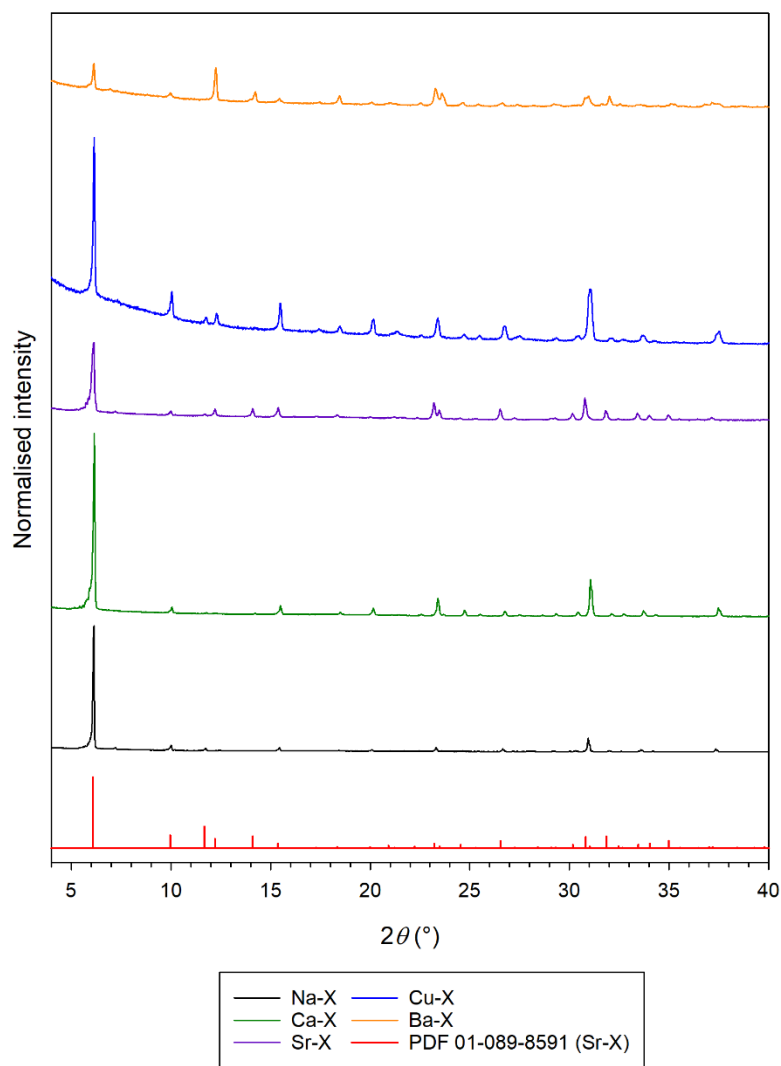


Figure 6.27. PXRD patterns recorded on Na-X and ion-exchanged products.

Fluoride loadings from 20 ppm  $F^-$  1:1 NaF:HNO<sub>3</sub> solutions for Na-A, Na-X and the divalent metal-exchanged derivatives of each zeolite are presented in Table 6.11, along with the percentage of fluoride removed from solution in each instance. The introduction of all divalent metal ions, except copper(II), into zeolite A leads to an increase in fluoride loadings attained following both an hour and 24 hours of contact. Compared with the other ion-exchanged zeolite A species, a lower fluoride loading is measured for Cu<sup>2+</sup>-exchanged zeolite A, which may be attributed to the lower copper content in the zeolite compared with the metal loadings in the other exchanged zeolites. The highest fluoride loading following both 1 and 24 hours of contact is observed for Ca-exchanged zeolite A. Similarly, ion exchange with the divalent metal ions in zeolite X leads to an increase in fluoride loadings

following an hour and 24 hours, in each instance. Ca-exchanged zeolite X achieved the highest fluoride loading following both an hour and 24 hours of contact.

Table 6.11. Fluoride loadings attained following an hour ( $q(60 \text{ min})$ ) of contact and at equilibrium ( $q_e$ ) for both zeolites Na-A and Na-X and their ion-exchanged products.

	$q(60 \text{ min})$ ( $\text{mg F}^- \text{ g}^{-1}$ )	Fluoride removed after 60 mins (%)	$q_e$ ( $\text{mg F}^- \text{ g}^{-1}$ )	Fluoride removed after 24 hours (%)
Na-A	0.21	6	0.26	7
Ca-A	0.75	20	0.83	22
Sr-A	0.65	17	0.68	17
Ba-A	0.67	17	0.69	18
Cu-A	0.21	6	0.39	9
Na-X	0.15	4	0.21	6
Ca-X	1.08	27	2.05	51
Sr-X	0.74	19	0.99	26
Ba-X	0.84	23	1.62	43
Cu-X	0.51	12	1.46	36

Adsorption data measured from 1:1 NaF:HNO<sub>3</sub> solutions at 25°C, over the range 5 – 60 ppm F<sup>-</sup>, by zeolites Ca-A and Ca-X has been fitted to the Freundlich, Temkin, Langmuir and Dubinin-Radushkevitch isotherms;  $R^2$  and appropriate isotherm parameters are presented in Table 6.12. Fluoride loadings measured over the concentration range for both zeolites are plotted in Figure 6.28. For both zeolites, poor fits are observed to the Langmuir model (plots in Appendix 1). For Ca-A, a poor fit to the Temkin isotherm is observed (Figure 6.29), but good agreement is observed to both the Freundlich and Dubinin-Radushkevitch isotherms (Figures 6.30 and 6.31, respectively). In contrast for Ca-X, lower  $R^2$  values are observed for the Freundlich and DR isotherms. Acceptable fits are observed for Ca-X to the Temkin, Freundlich and DR isotherms (Figures 6.29, 6.30 and 6.31, respectively); however, none of the plots contain a linear distribution of data points over the entire concentration range examined. Nevertheless, the acceptable fits permit valid interpretations of the isotherm

parameters. The characteristic sorption energy ( $E_C$ ) in both cases is below the value expected given the acid-mediated fluorination mechanism by which fluoride loading is anticipated to proceed by. The lower values are consistent with those observed for both calcium-exchanged and sodium-bearing zeolites in acidic media. The magnitude of the Freundlich isotherm parameters,  $K_F$  and  $n$ , also indicate fluorination under these conditions is an unfavourable process; however, a greater  $E_C$  and less unfavourable values for  $K_F$  and  $n$  are observed for Ca-X, compared with Ca-A, indicating that fluorination is more favourable for Ca-X than Ca-A.

Table 6.12.  $R^2$  and isotherm parameters for fits to the listed isotherms for zeolites Ca-A and Ca-X. (The units for  $K$  are  $\times 10^{-3} \text{ mol}^2 \text{ kJ}^{-2}$  and for  $K_F$  are  $(\text{mg g}^{-1})/(\text{mg L}^{-1})^n$ )

Zeolite	Freundlich			Dubinin-Radushkevitch			Temkin	Langmuir
	$R^2$	$K_F$	$n$	$R^2$	$E_C$ ( $\text{kJ mol}^{-1}$ )	$K$	$R^2$	$R^2$
Ca-A	0.984	0.005	1.70	0.990	5.1	1.95	0.872	0.568
Ca-X	0.953	0.03	1.62	0.968	5.3	1.80	0.975	0.446

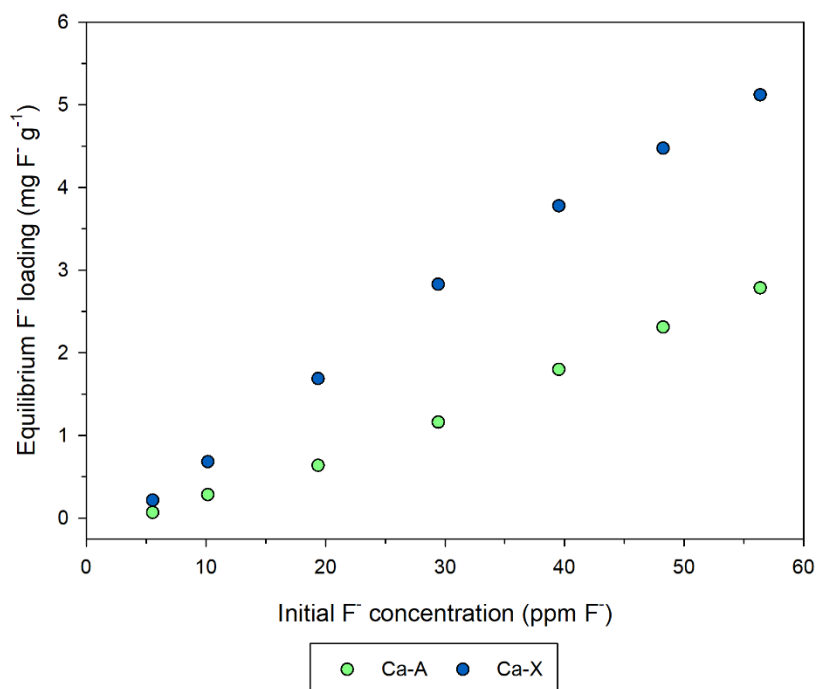


Figure 6.28. Equilibrium fluoride loadings as a function of initial fluoride concentration for Ca-A and Ca-X.

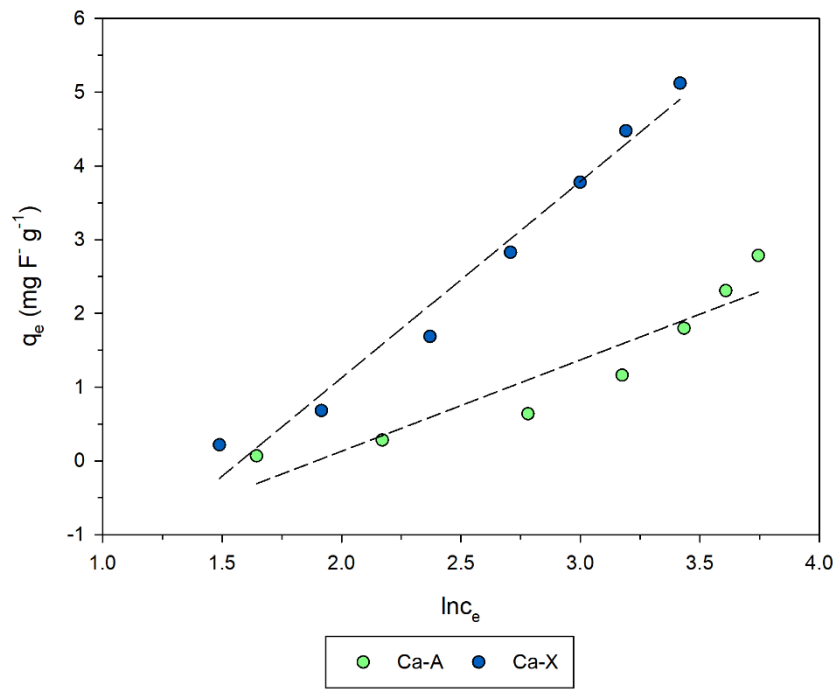


Figure 6.29. Temkin plots for Ca-A and Ca-X.

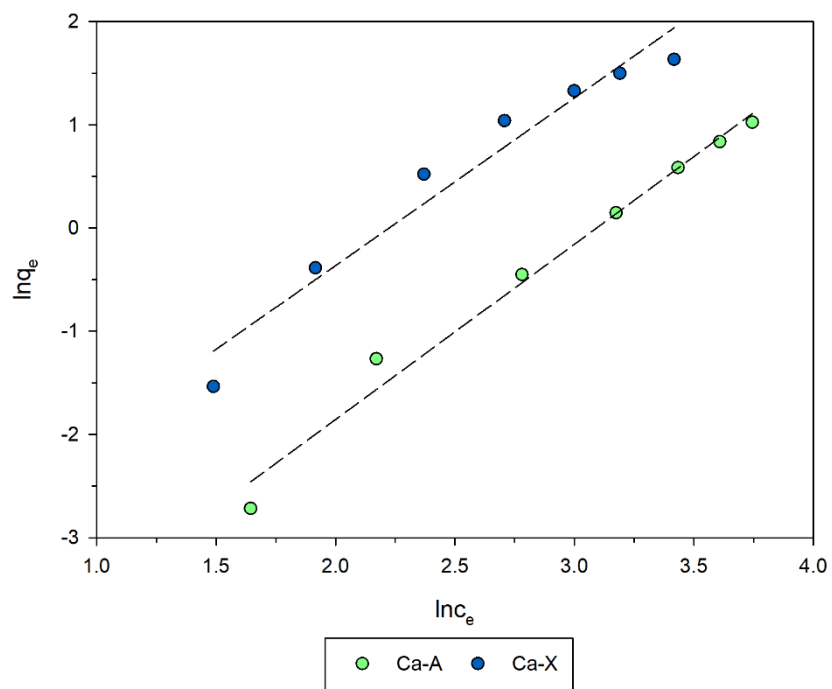


Figure 6.30. Freundlich plots for Ca-A and Ca-X.

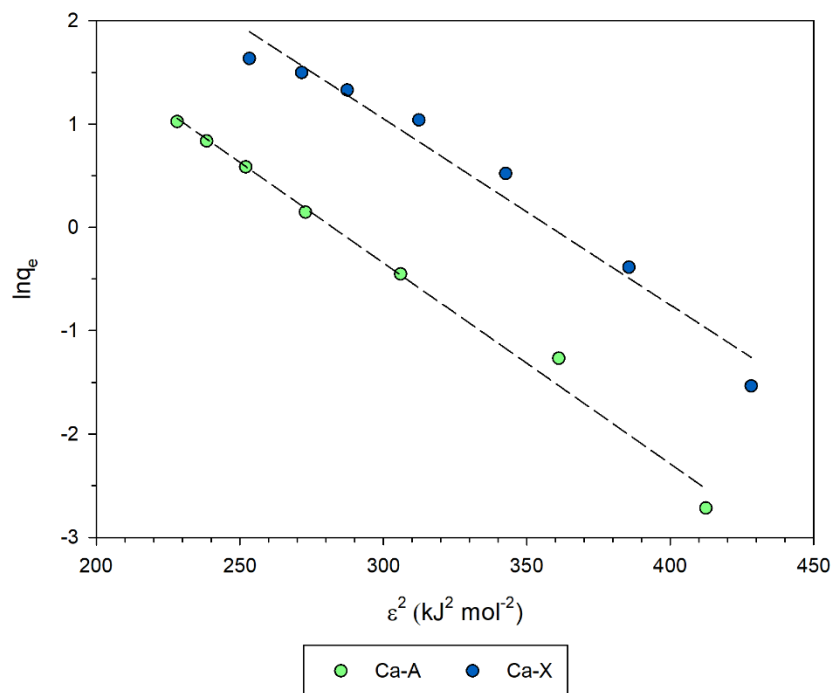


Figure 6.31. Dubinin-Radushkevitch plots for Ca-A and Ca-X.

#### 6.3.3.4 Conclusions

Aqueous iron(III) treatments are incompatible with zeolites A and X, as the acidity of even relatively dilute solutions leads to the destruction of the zeolite framework, compromising the mechanical integrity of the crystals, as well as leading to the precipitation of an amorphous iron(III)-containing phase. Dealumination can also not be applied to zeolites A and X, owing to the low Si/Al ratios inherent to the zeolites. The effect of EDTA treatments on the crystallinity and particle morphology of large zeolite A and X crystals have been examined. Ion exchange with divalent metal cations is effective in enhancing fluoride loadings in both zeolite A and X crystals; for both zeolites, the highest loadings are attained following calcium ion exchange. Adsorption isotherms have been applied to fluoride uptake by Ca-A and Ca-X, indicating low favourability, despite the appreciable loadings, in common with observations for fluoride uptake in acidic media by all sodium or divalent metal-containing zeolites examined.

#### 6.4 Overall conclusions

Post-synthetic modifications, *viz.* dealumination, iron(III) surface sorption and ion exchange with divalent cations, enhance fluoride loadings from acidic solutions for each zeolite where the modifications can be successfully applied. Ion exchange with divalent cations ( $\text{Ca}^{2+}$ ,  $\text{Sr}^{2+}$ ,  $\text{Ba}^{2+}$  and  $\text{Cu}^{2+}$ ) to some extent can be achieved universally for zeolites A, X, GME and MOR. In general, the presence of divalent cations in the zeolite enhances fluoride loadings attained following an hour of contact, and at equilibrium, compared with the parent material. For all the zeolites examined, except for mordenite, the Ca-exchanged form achieves the highest loadings following both an hour and 24 hours of contact with acidic fluoride solutions.

GME may be dealuminated by facile treatment with  $\text{H}_4\text{EDTA}$ , reducing the Si/Al ratio from 2.2(1) to 4.0(2). The dealuminated zeolite achieves exceptional fluoride loadings from acidic solutions over the range probed and isotherm parameters attest the highly favourable nature of the reaction. The dealumination treatment compromises the structural integrity of the microspheres, however, rendering the particles unsuitable for application as PEPT tracers. In zeolites A and X, owing to the inherently low framework Si/Al ratios, dealumination is not possible and treatment with  $\text{H}_4\text{EDTA}$  slurries leads to fracturing of the zeolite crystals, a reduction in crystallinity and, ultimately, dissolution of the zeolites. In contrast, the high Si/Al ratio of mordenite necessitates driving conditions to extricate aluminium from the framework. Attempts to dealuminate mordenite by reflux with concentrated hydrochloric acid solutions showed no reduction in bulk Si/Al ratio following the treatment; however, some appreciable degree of ion exchange between intrapore sodium ions and aqueous protons was observed.

Surface modification with iron(III) ions may be achieved for both mordenite and GME. Despite relatively low iron loadings (< 0.5 wt% Fe), fluoride uptakes by the iron(III)-loaded zeolites are significantly improved compared with the parent zeolites. Higher fluoride loadings are achieved by both iron(III)-loaded MOR and GME, than the respective  $\text{Ca}^{2+}$ -exchanged zeolites, rendering iron(III)-surface sorption a more efficacious method for enhancing fluoride loadings in the zeolites. Fluoride

loadings attained by iron(III)-loaded GME are lower than for dealuminated GME, but critically the spherical morphology and mechanical integrity are preserved in GME following loading with iron(III), making iron(III)-loaded GME more suitable than dealuminated GME for application as positron imaging tracers. The polarising nature of aqueous iron(III) ions gives rise to solutions sufficiently acidic to dissolve, or at least partially dissolve, crystals of zeolites A and X. The consumption of protons in this process in turn increases the solution pH to a range conducive with precipitation of amorphous brown iron(III)-containing phases that are not observed in the other systems. Ultimately, iron(III)-surface modification from aqueous solutions is not possible for zeolites A and X.

## CHAPTER 7: MOVING FORWARD, THE FUTURE OF PEPT TRACERS

At present PEPT labelling is a rudimentary but effective process, in which the desired tracer particle is selected under an optical microscope then transferred to a suitable vessel using an object, such as a micropipette tip, adhering the particle by suction or static attraction. After an aliquot of water (0.5 – 2 ml) containing fluorine-18 is added to the vessel containing the tracer, the vessel is then agitated under both a heat lamp and a flow of nitrogen gas, until the solution has evaporated, taking approximately an hour. The radioactive particle is then recovered from the vessel in the same manner as it was placed there and transferred to the system under study.

The present method is effective for manipulating the larger tracers that are labelled in fluorine-18 containing solutions ( $d \approx 200 - 1000 \mu\text{m}$ ); however, as tracer particle sizes become smaller, the manual manipulation of the particles becomes more challenging. The large zeolites particles ( $d \approx 10 - 50 \mu\text{m}$ ) produced in chapters 3 and 4 are much smaller than particles routinely employed as PEPT tracers, in line with the aim of this research project: the development of smaller PEPT tracers with controlled dispersity and particle morphology to expand the possible applications of PEPT, as well as potentially improving the accuracy of results. While adhering large zeolite particles to a fine pointed object, such as a sewing needle, by static attraction is facile, issues arise as many particles in the sample often adhere. It is therefore difficult to determine how many particles adhere to the object; moreover, it is even more difficult to selectively manipulate a single particle. In turn, this makes placing a known number of particles in solution for labelling difficult, and recovering a single particle is virtually impossible.

As outlined in Chapter 1, PEPT imaging relies on incorporating a single labelled particle into the system under study, as such a method to isolate a single particle and manipulate it is essential to the labelling process. Accordingly, a different method for separation and manipulation is required for particles within the size range of interest for new smaller tracers,  $d \approx 5 - 50 \mu\text{m}$ . The effective separation of single biological cells, with comparable size, and manipulation thereof can be achieved by optical

micromanipulation, apparatus also termed “optical tweezers”, utilising laser beams to direct the cell in aqueous media.<sup>145</sup> Moreover, optical tweezers have been successfully integrated into microfluidic devices.<sup>146</sup> Briefly, microfluidics is the field concerning the development of devices with channel architectures on the order of microns, designed to accommodate and direct the flow of liquids and particles suspended in liquids.<sup>147</sup> Microfluidic devices have been developed for the synthesis of radiolabeled  $\beta^+$ -emitting molecules, containing  $^{18}\text{F}$ , applied as tracers in positron emission tomography.<sup>148,149</sup>

An integrated microfluidic system is envisaged for PEPT labelling, involving first the isolation of a single particle, using optical micromanipulation, followed by transfer of the single particle to a chamber with heating capacity. Labelling may then take place by loading an aliquot of fluorine-18 containing water into the chamber. After a suitable time period allowing labelling to occur, the particle may be retrieved from the solution and placed into the system under study. The device could be further functionalised by integrating a final coating step with a suitable material to render fluoride adsorption on the particle irreversible in solution. Ultimately, the development of the requisite microfluidic device is beyond the scope of this project; however, the utility of such a device is unquestionable and would greatly expand the sizes of possible tracers available for PEPT imaging, including, but not limited to, large zeolite particles.

Appendix 1: Supplementary Isotherms

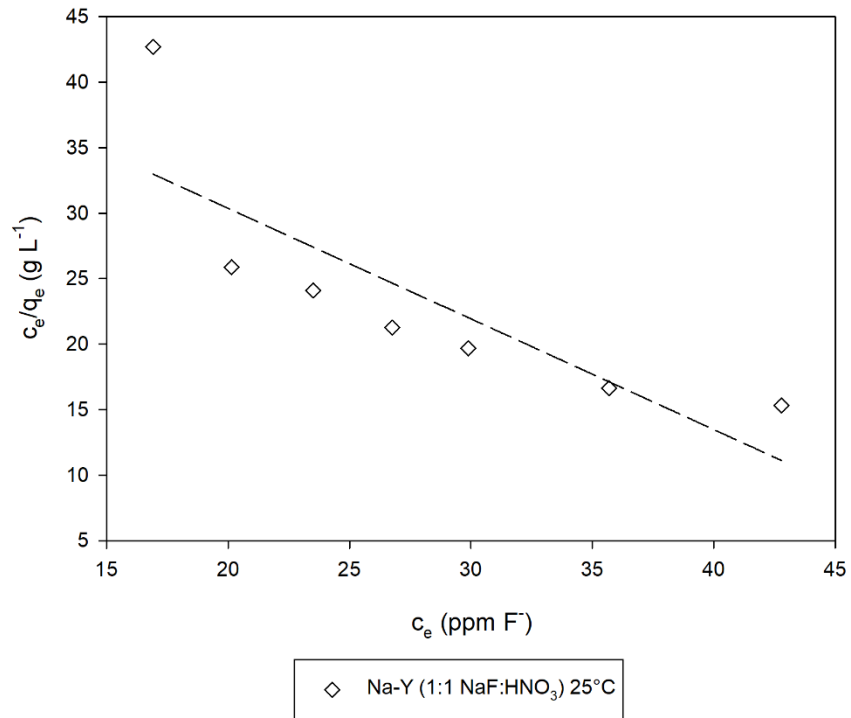


Figure 8.1. Langmuir plot for fluoride uptake by Na-Y in 1:1 NaF:HNO<sub>3</sub> solutions at 25°C.

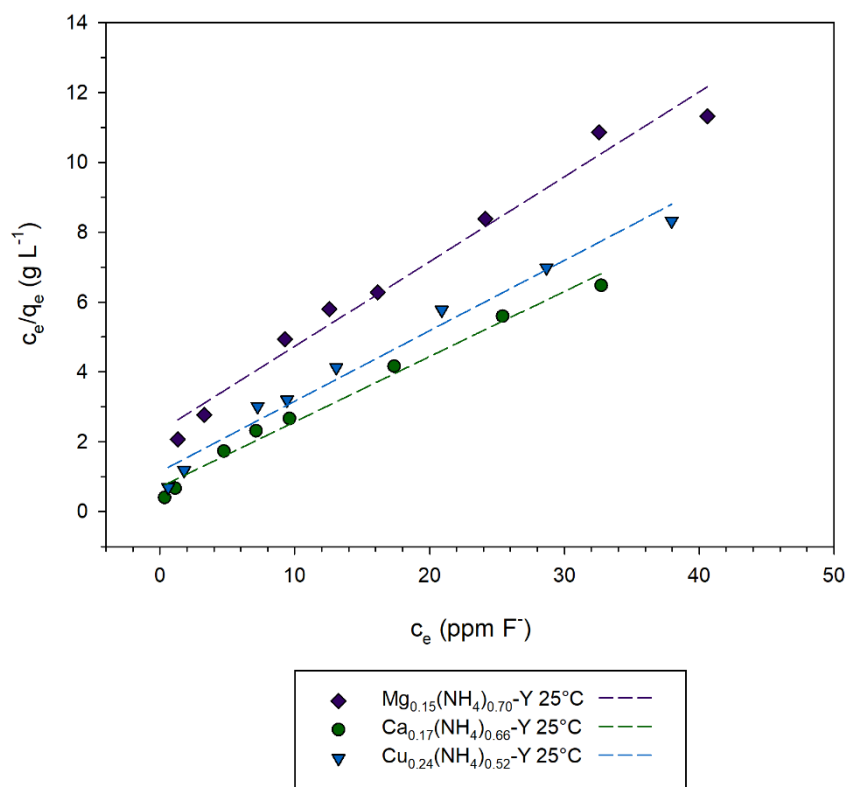


Figure 8.2. Langmuir plot for fluoride uptake by  $M_x(NH_4)_{1-2x}-Y$  species at 25°C, where M = Mg, Ca and Cu.

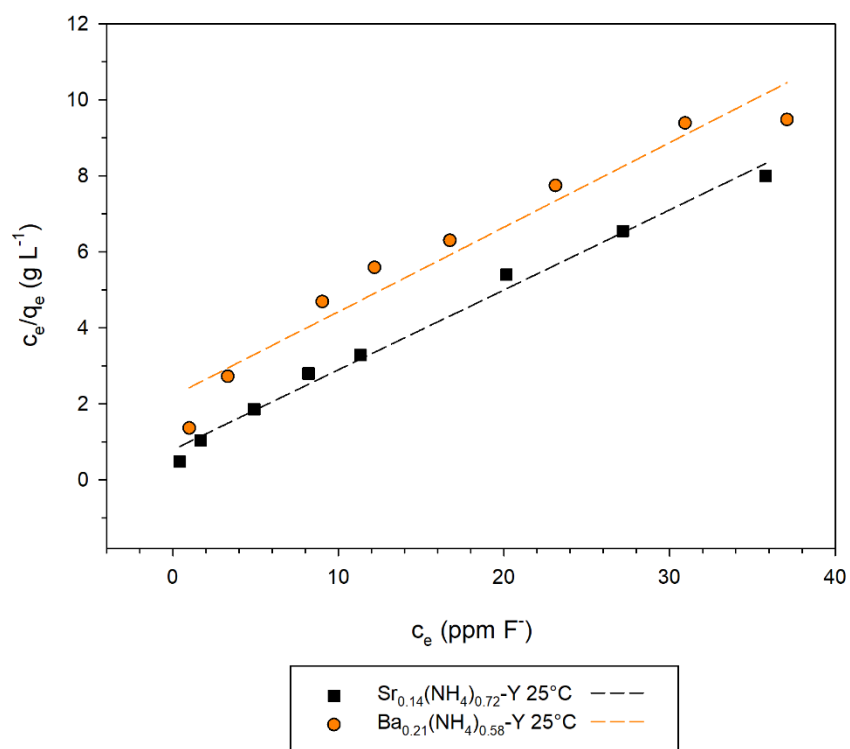


Figure 8.3. Langmuir plot for fluoride uptake by  $M_x(NH_4)_{1-2x}-Y$  species at 25°C, where M = Sr and Ba.

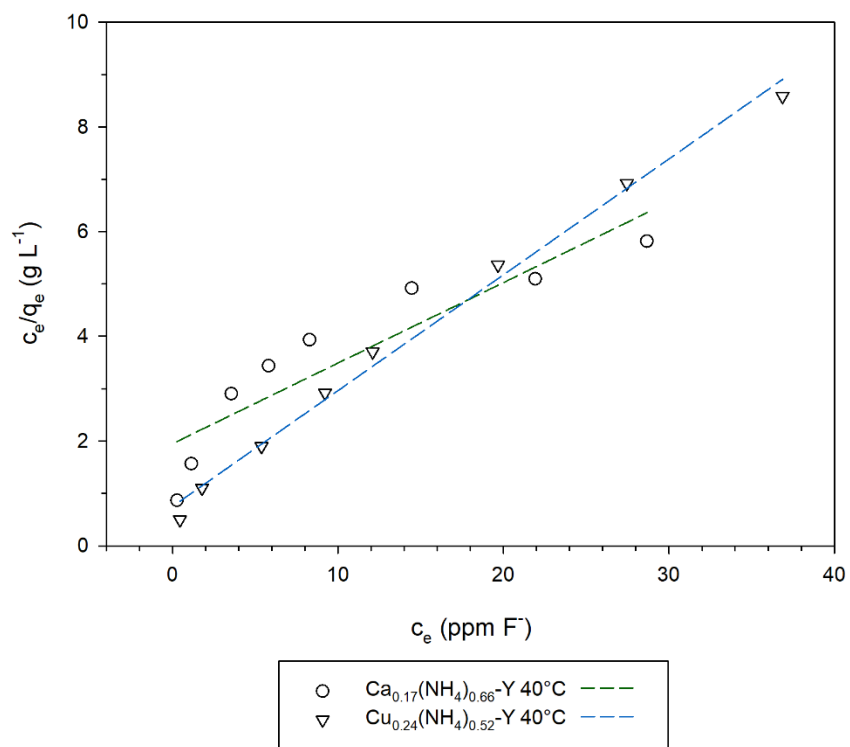


Figure 8.4. Langmuir plot for fluoride uptake by  $M_x(NH_4)_{1-2x}-Y$  species at  $40^\circ C$ , where  $M = Ca$  and  $Cu$ .

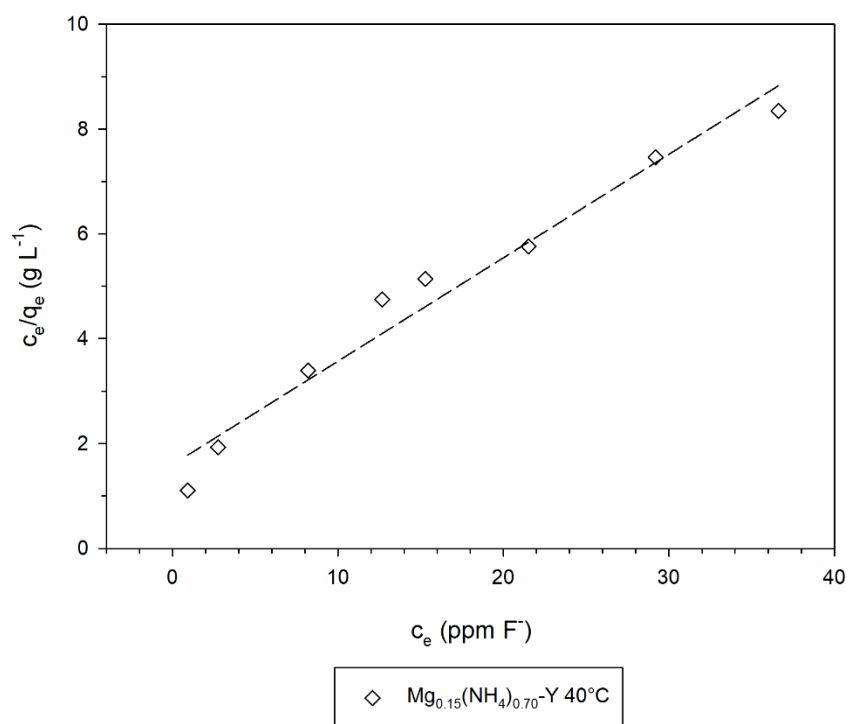


Figure 8.5. Langmuir plot for fluoride uptake by  $Mg_{0.15}(NH_4)_{0.70}-Y$  species at  $40^\circ C$ .

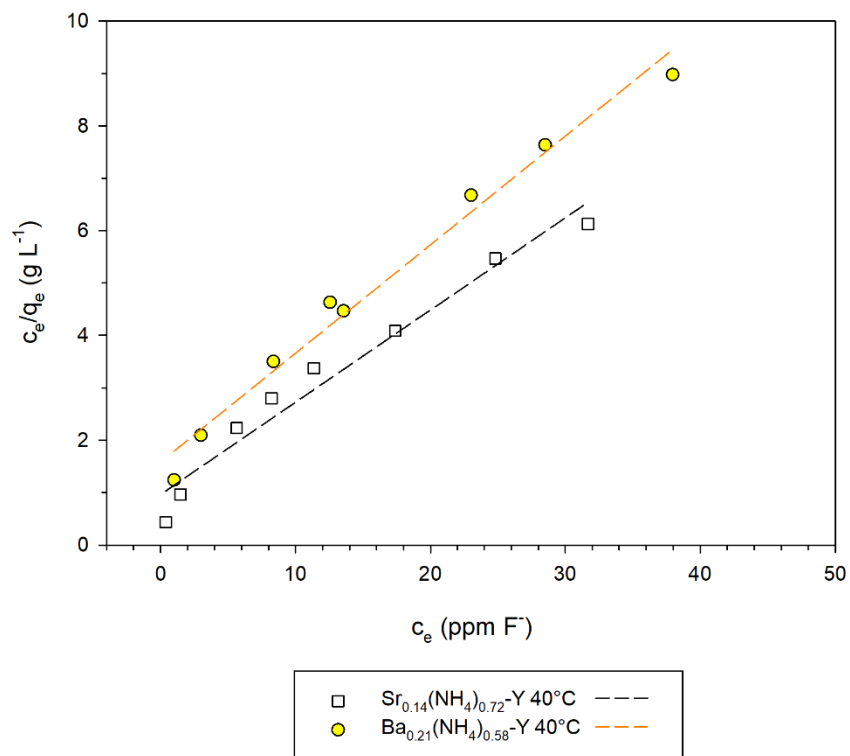


Figure 8.6. Langmuir plot for fluoride uptake by  $M_x(NH_4)_{1-2x}-Y$  species at  $40^\circ C$ , where  $M = Sr$  and  $Ba$ .

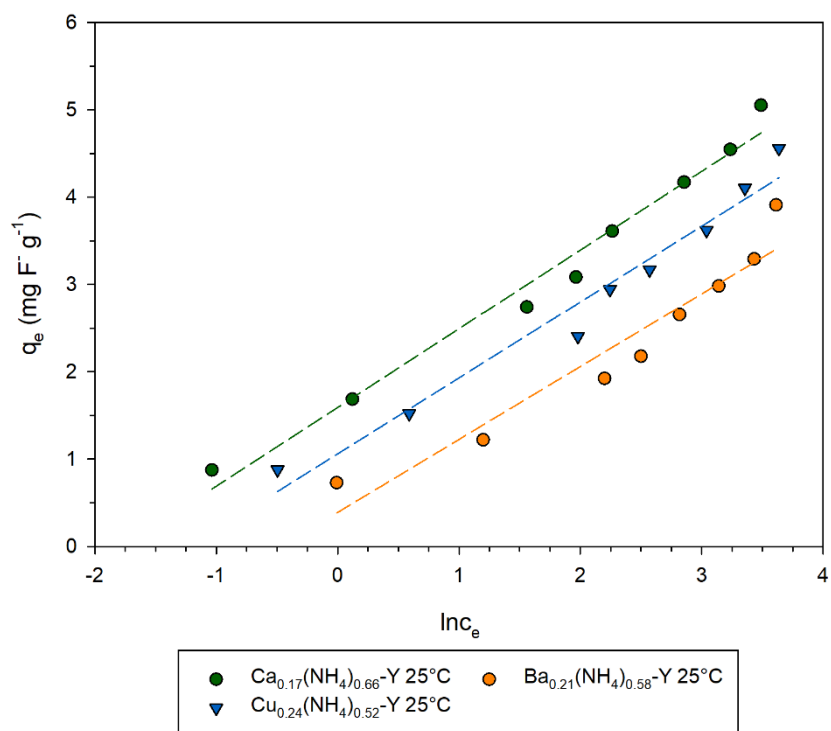


Figure 8.7. Temkin plot for fluoride uptake by  $M_x(NH_4)_{1-2x}-Y$  species at  $25^\circ C$ , where  $M = Ca, Cu$  and  $Ba$ .

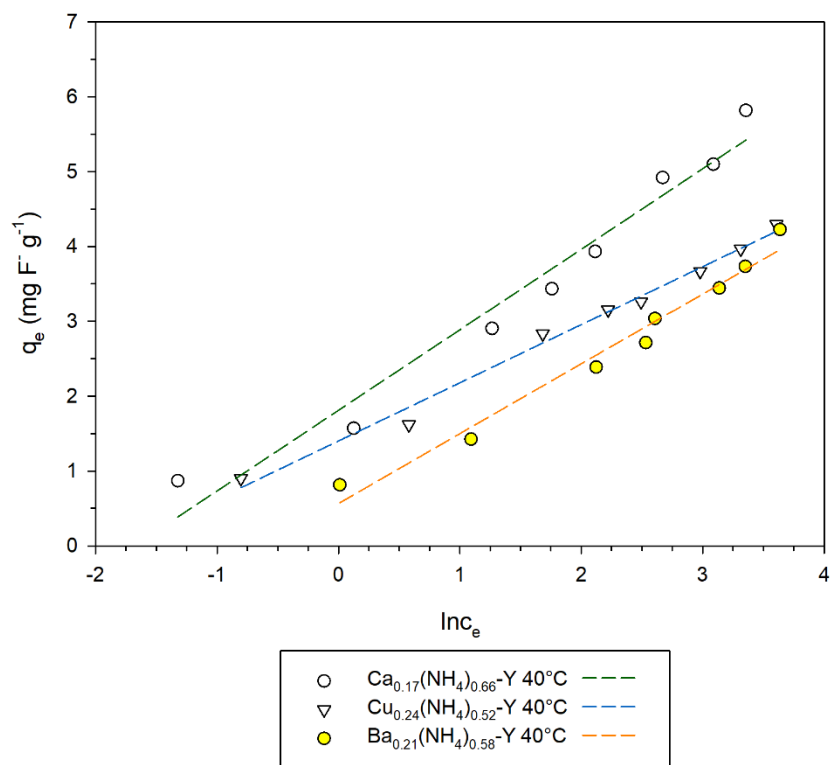


Figure 8.8. Temkin plot for fluoride uptake by  $M_x(NH_4)_{1-2x}Y$  species at 40°C, where M = Ca, Cu and Ba.

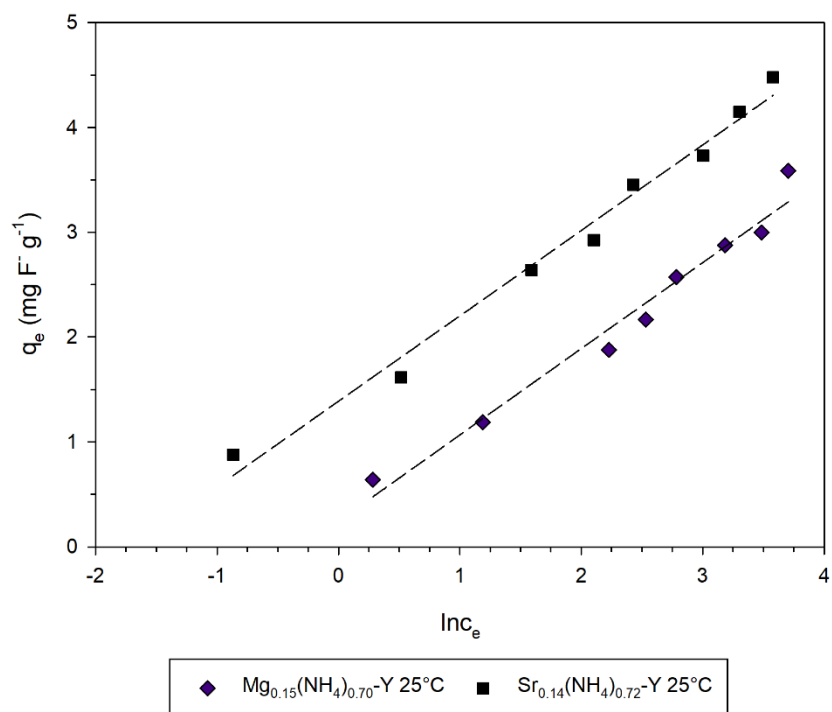


Figure 8.9. Temkin plot for fluoride uptake by  $M_x(NH_4)_{1-2x}Y$  species at 25°C, where M = Mg and Sr.

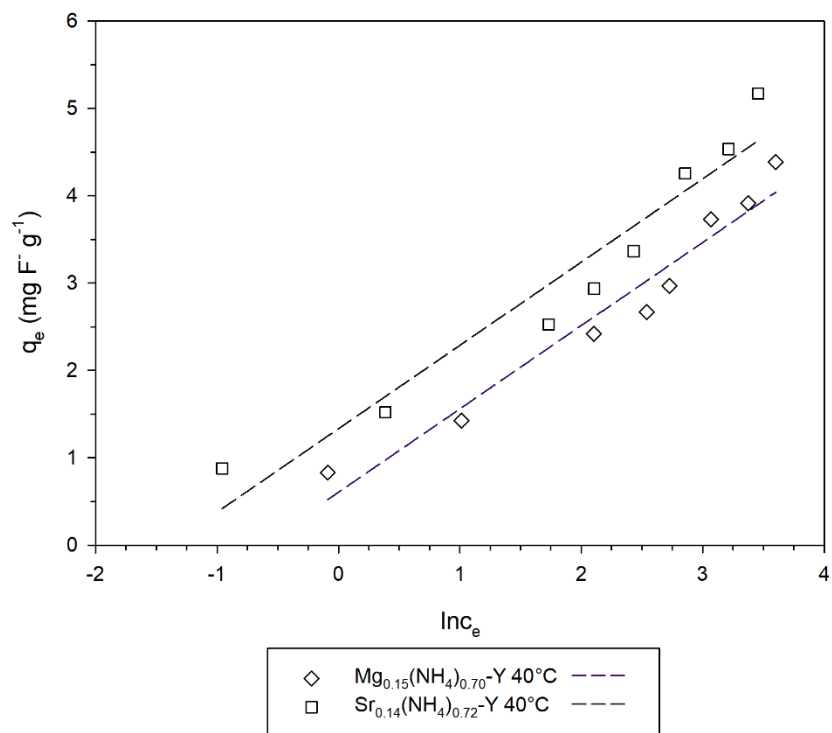


Figure 8.10. Temkin plot for fluoride uptake by  $M_x(NH_4)_{1-2x}Y$  species at 40°C, where M = Mg and Sr.

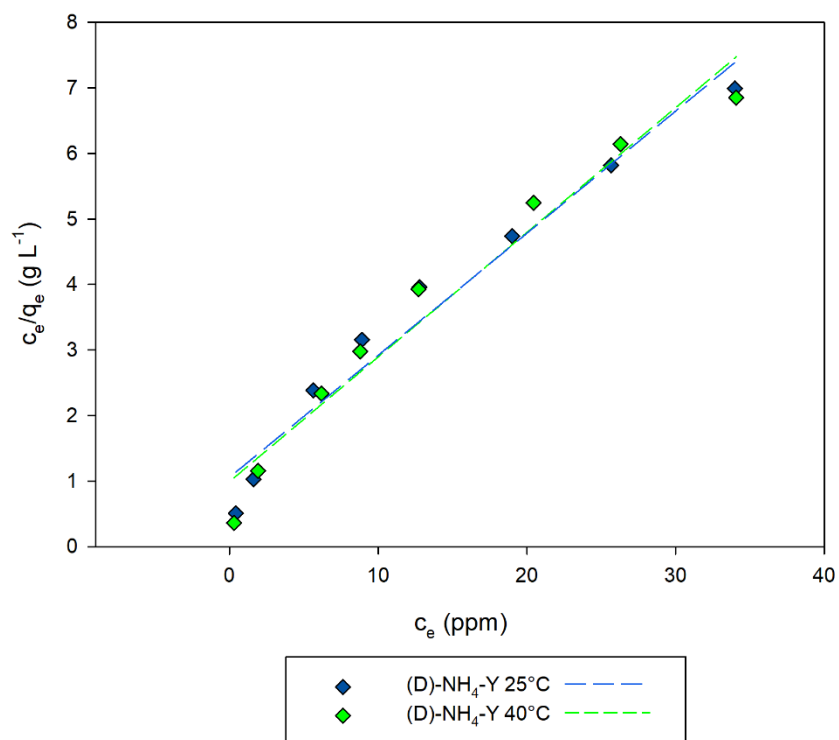


Figure 8.11. Langmuir plot for fluoride uptake by (D)-NH<sub>4</sub>-Y at both 25°C and 40°C.

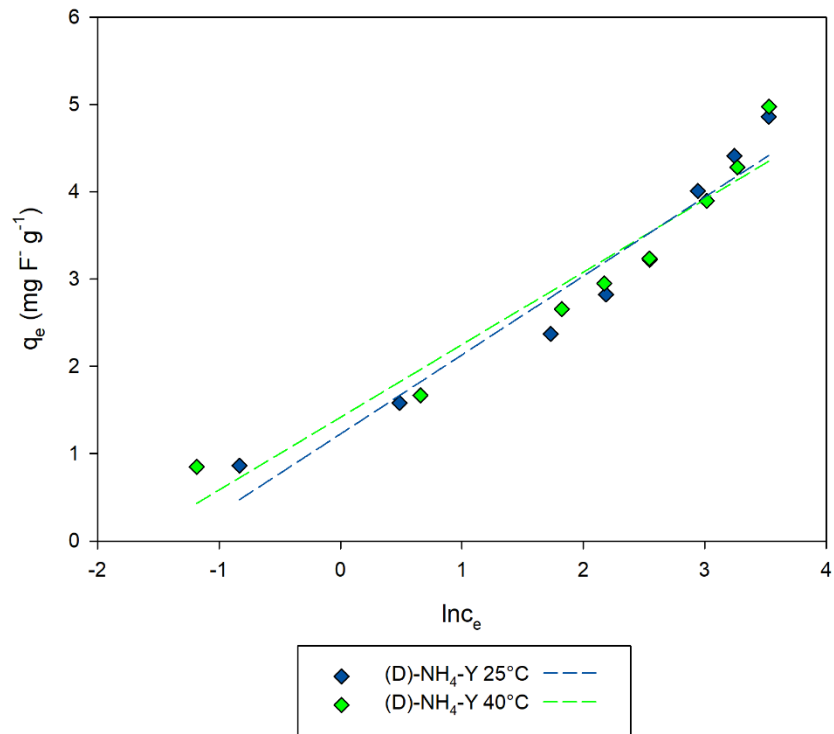


Figure 8.12. Temkin plot for fluoride uptake by (D)-NH<sub>4</sub>-Y at both 25°C and 40°C.

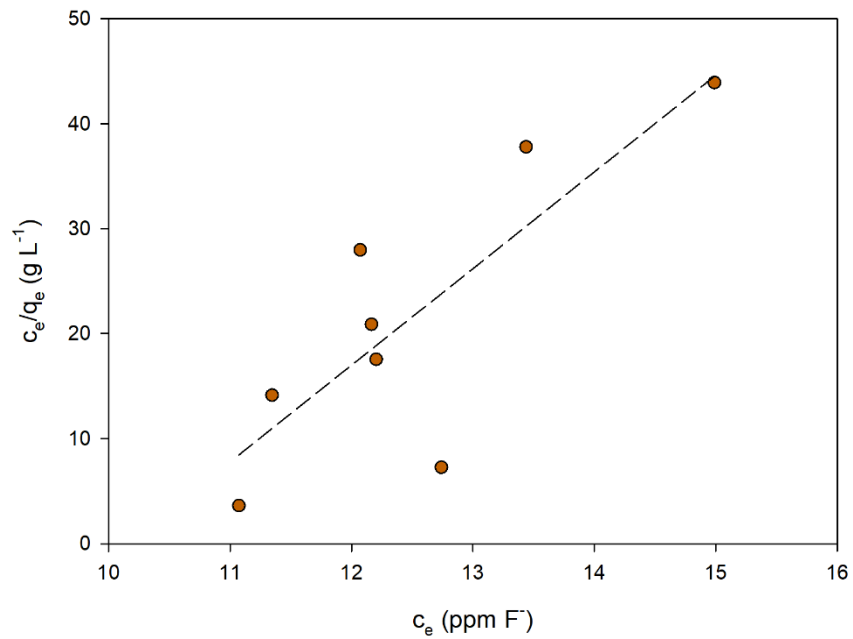


Figure 8.13. Langmuir plot for fluoride uptake by Fe<sup>3+</sup>-loaded MOR at 25°C.

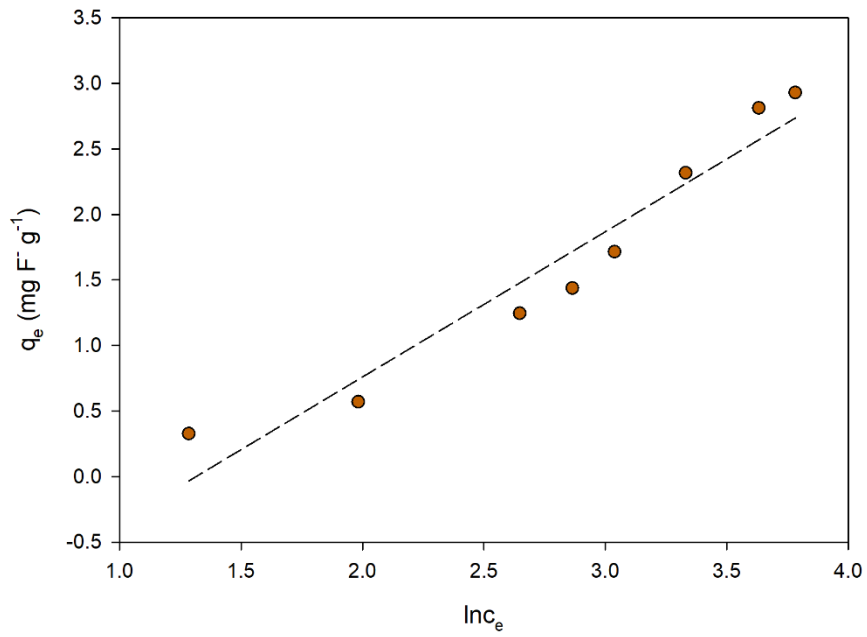


Figure 8.14. Temkin plot for fluoride uptake by Fe<sup>3+</sup>-loaded MOR at 25°C.

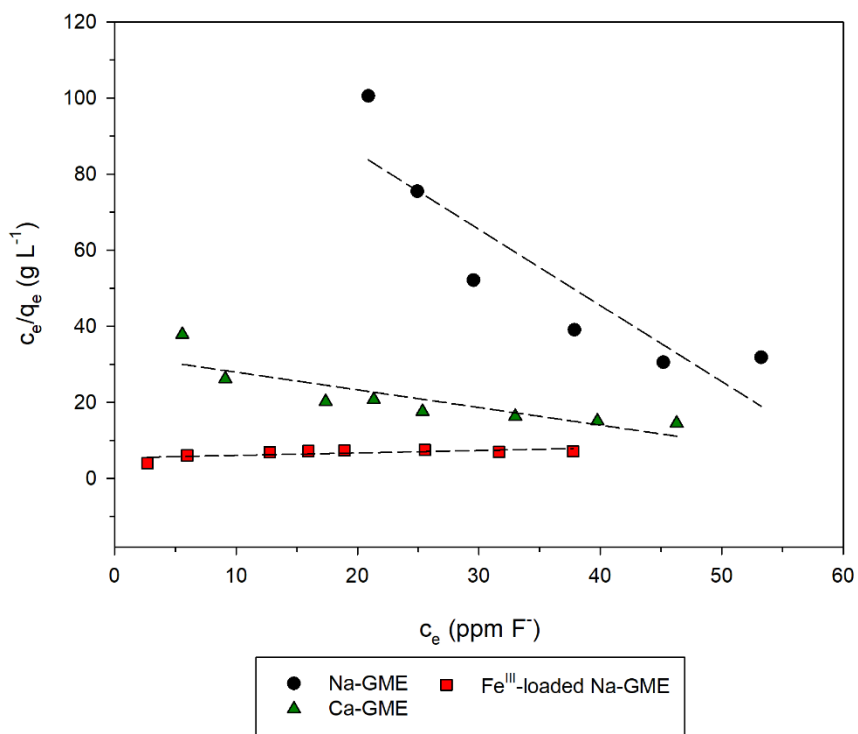


Figure 8.15. Langmuir plot for fluoride uptake by Na-GME, Ca-GME and Fe<sup>III</sup>-loaded Na-GME at 25°C.

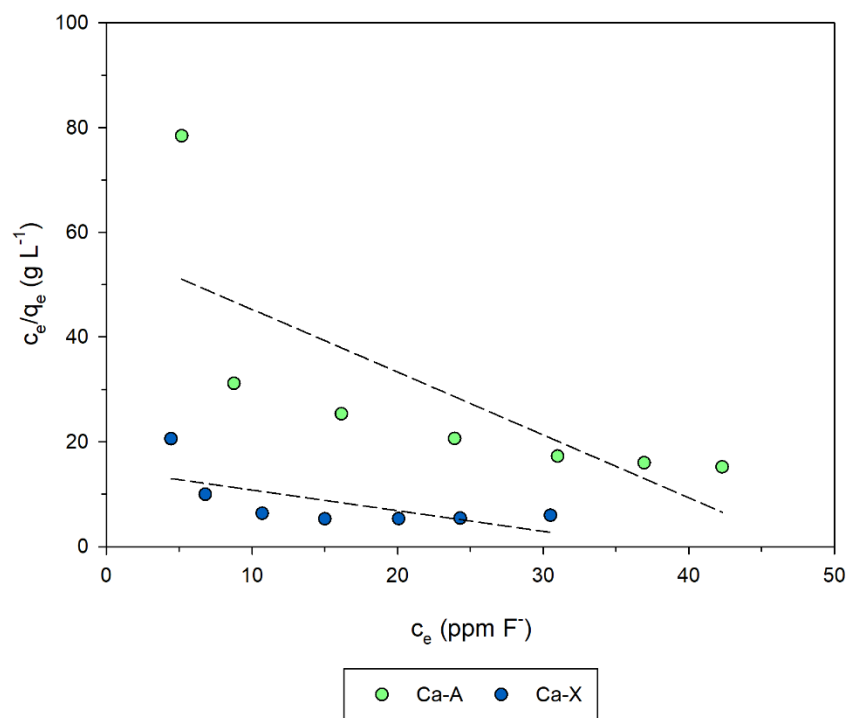


Figure 8.16. Langmuir plot for fluoride uptake by Ca-A and Ca-X at 25°C.

## Appendix 2: Supplementary NMR spectra

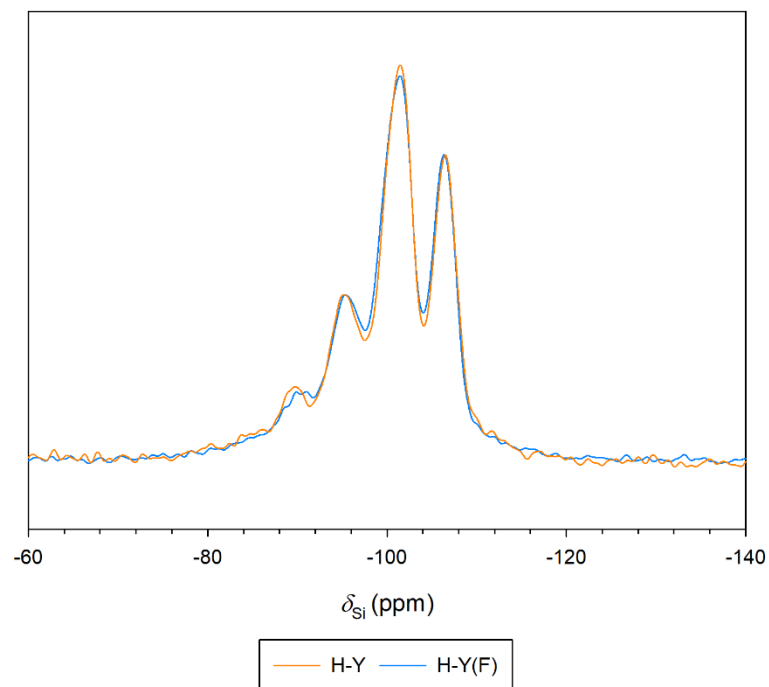


Figure 8.17.  $^{29}Si\{^1H\}$  CP MAS NMR spectra recorded on H-Y and fluorinated H-Y, H-Y(F).

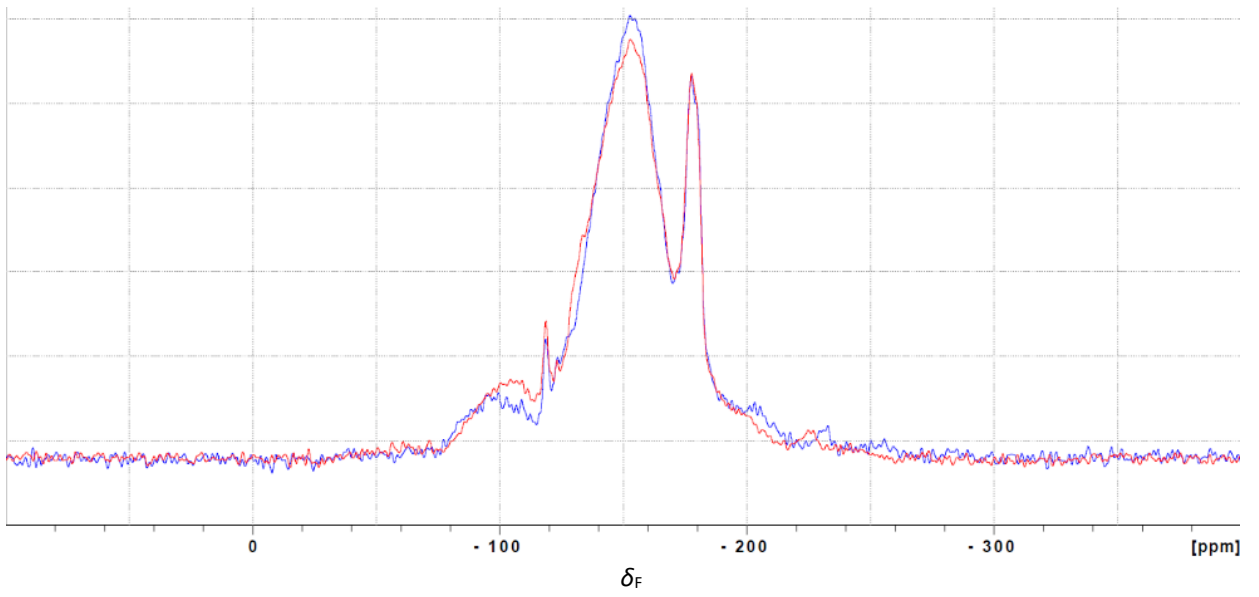


Figure 8.18.  $^{19}\text{F}$  MAS NMR spectra recorded on H-Y at a spin rate of 18 kHz (red) and 20 kHz (blue).

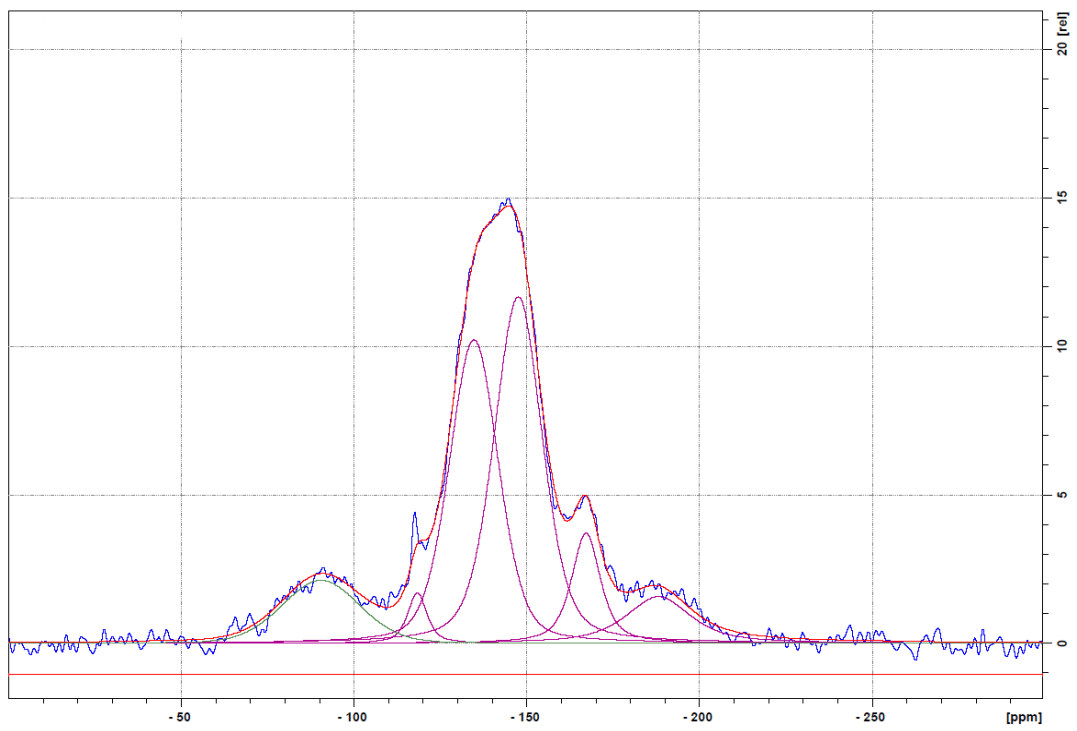


Figure 8.19. Peak fit of the  $^{19}\text{F}$  MAS NMR spectrum of H-Y(F).

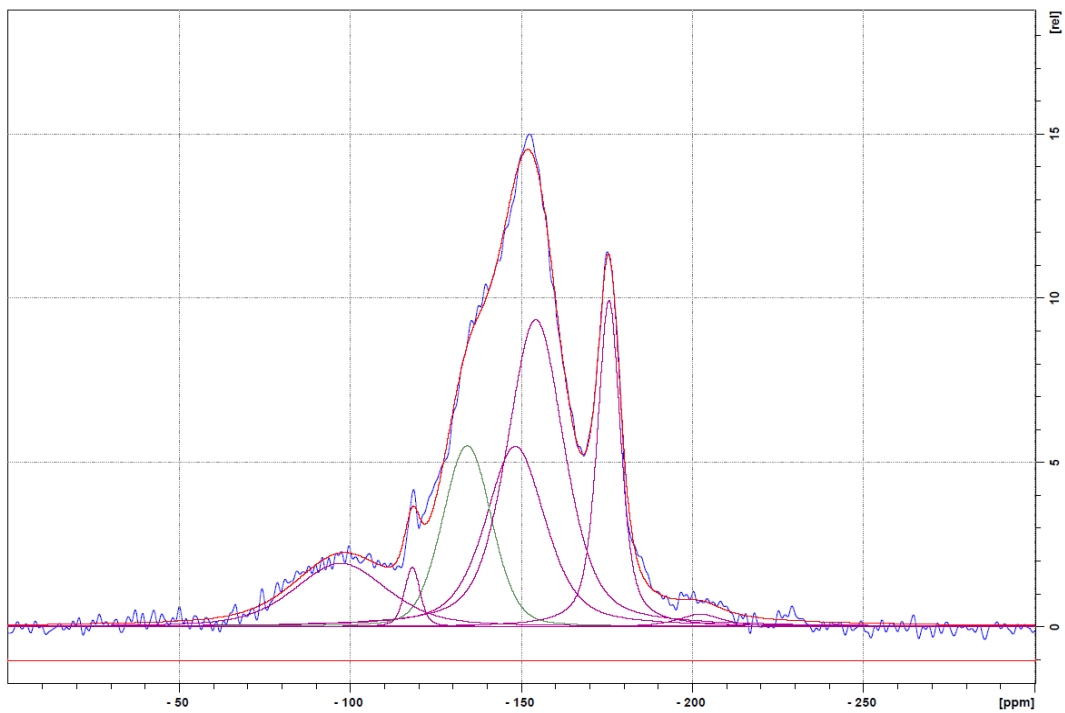


Figure 8.20. Peak fit of the  $^{19}\text{F}$  MAS NMR spectrum of  $\text{NH}_4\text{-Y}(\text{F})$ .

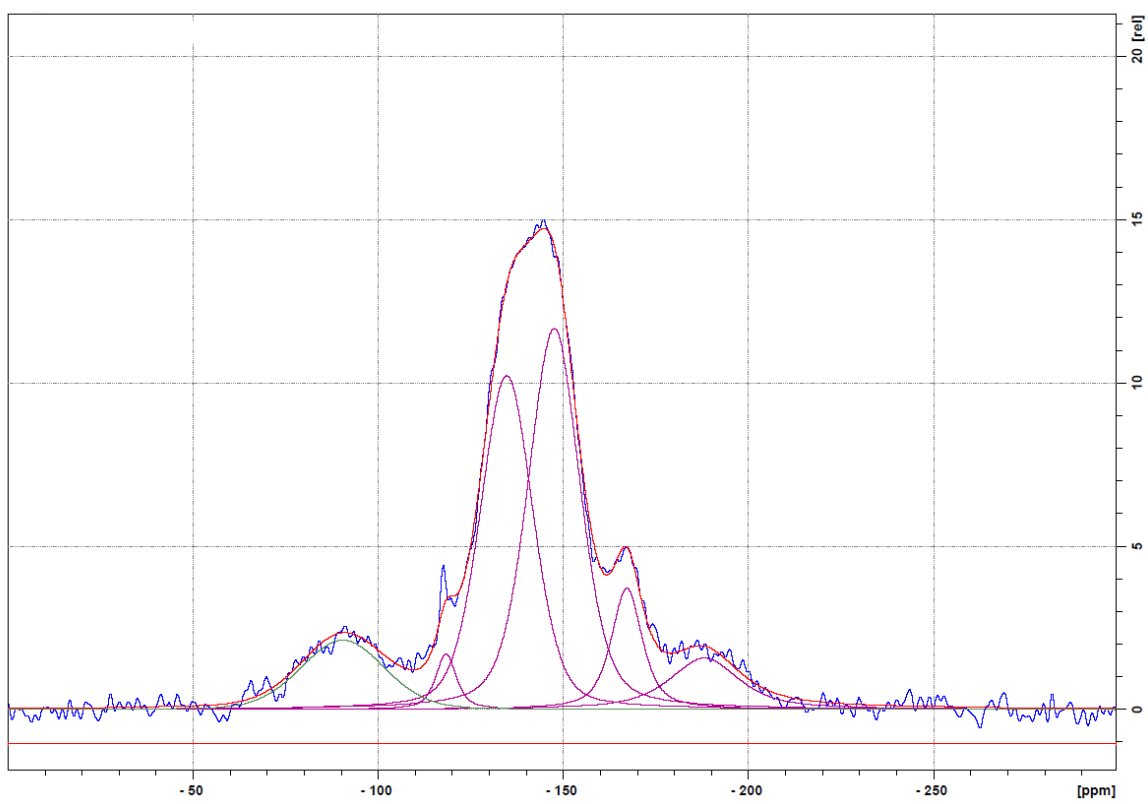


Figure 8.21. Peak fit of the  $^{19}\text{F}$  MAS NMR spectrum of fluorinated  $\text{Ca}_{0.17}(\text{NH}_4)_{0.66}\text{-Y}$ .

### Appendix 3: Scaled-up Zeolite Syntheses Characterisation Data

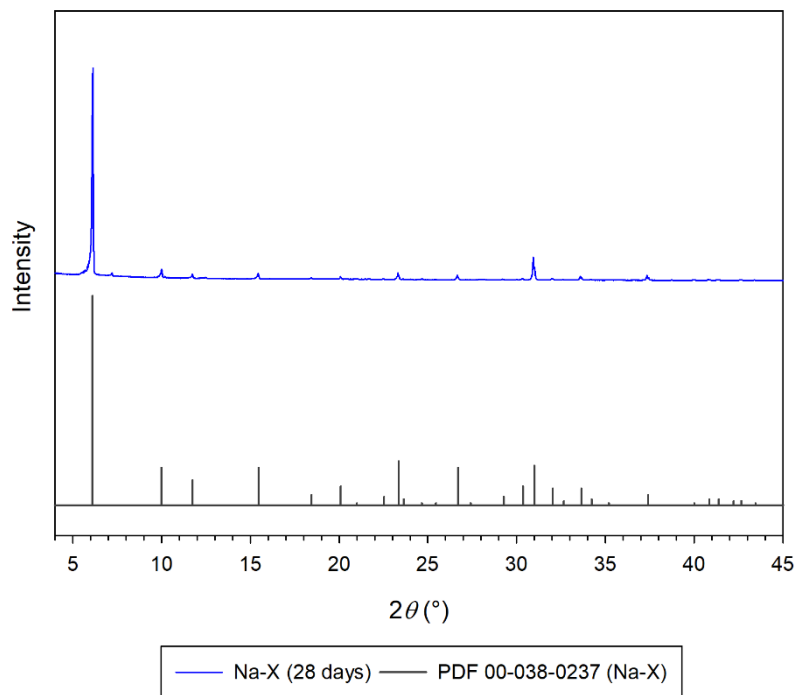


Figure 8.22. PXRD pattern recorded on Na-X grown for 28 days in a scaled-up synthesis.

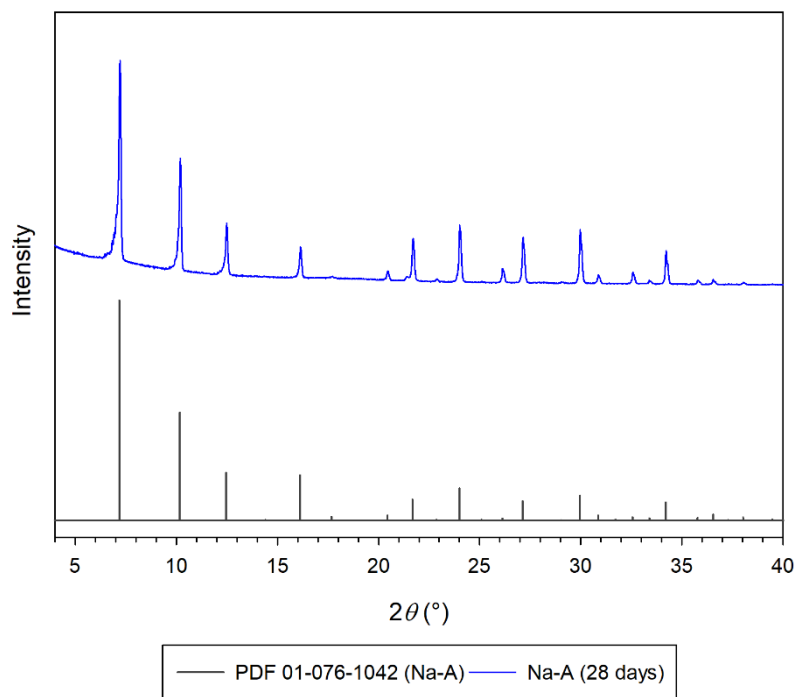


Figure 8.23. PXRD pattern recorded on Na-A grown for 28 days in a scaled-up synthesis.

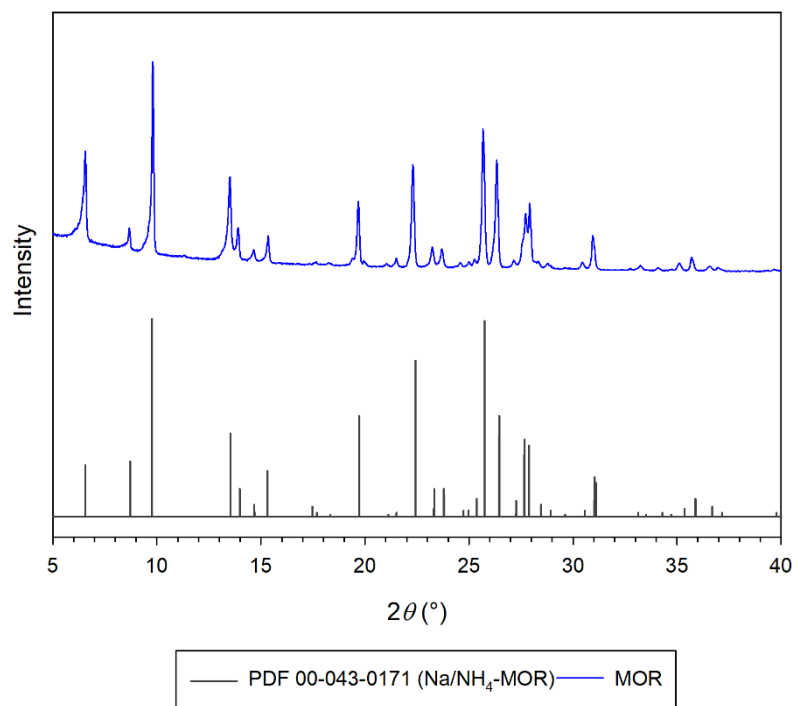


Figure 8.24. PXRD pattern recorded on MOR produced by a scaled-up synthesis.

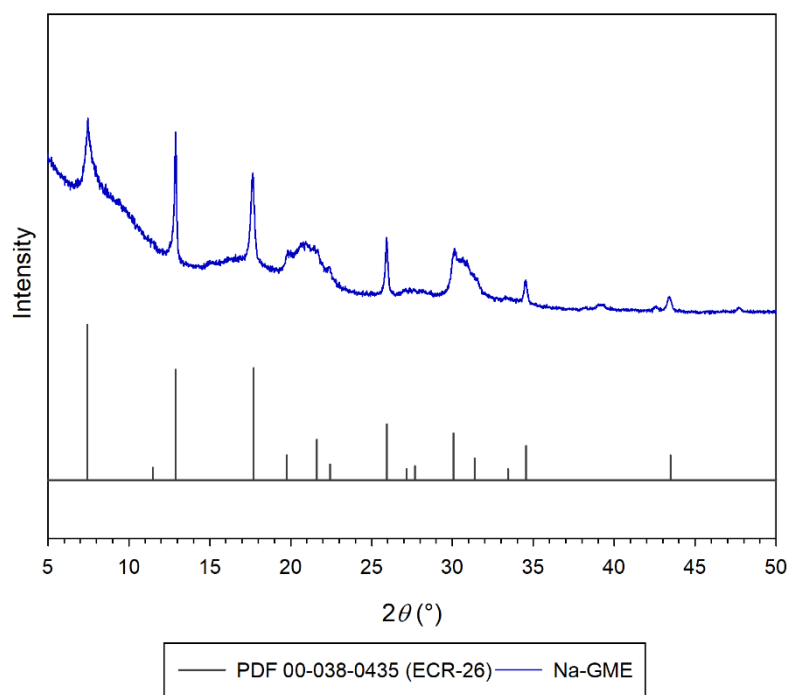


Figure 8.25. PXRD pattern recorded on Na-GME grown for 21 days in a scaled-up synthesis.

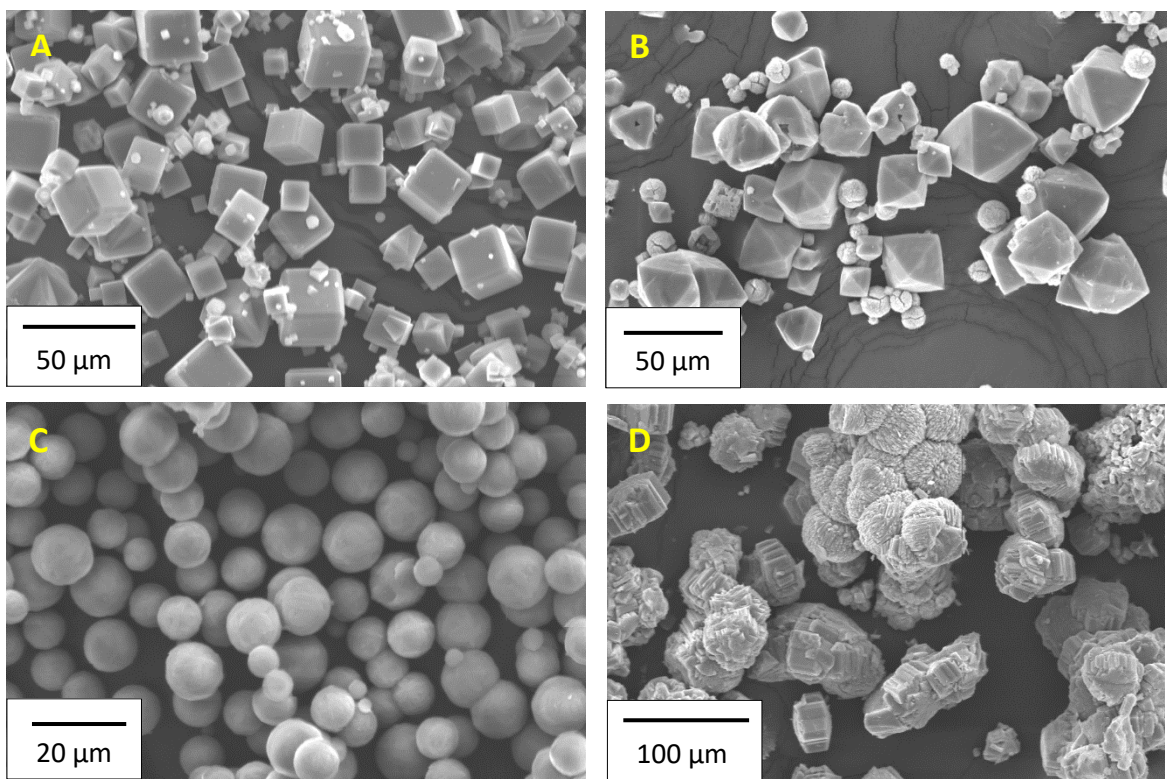


Figure 8.26. Scanning electron micrographs of (A) zeolite A, (B) zeolite X, (C) GME and (D) MOR produced from scaled up syntheses.

#### Appendix 4: Products of Zeolites A and X Treated with 0.25 M Copper(II) Nitrate

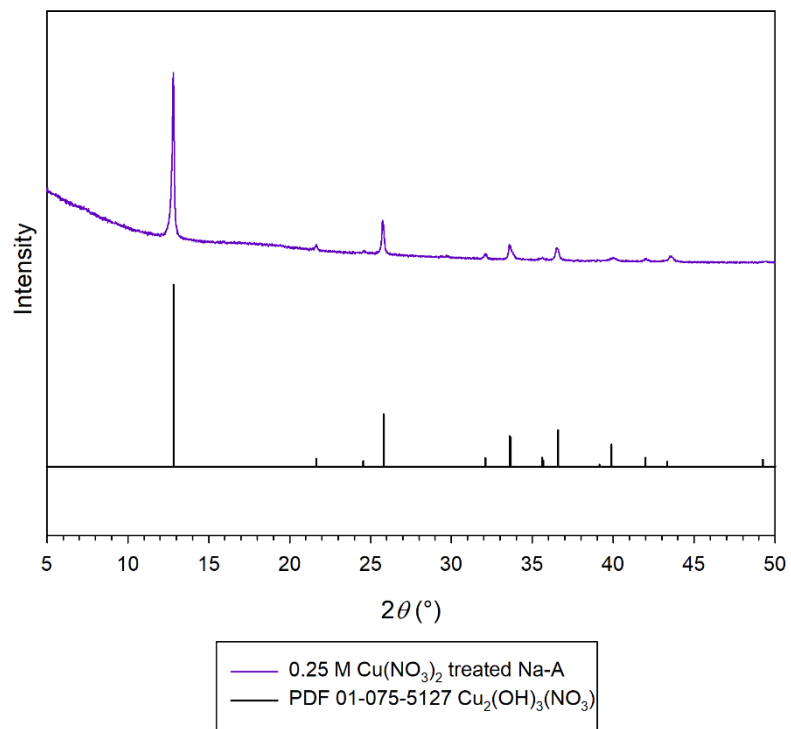


Figure 8.27. PXRD pattern recorded on the product of zeolite A treated with 0.25 M  $\text{Cu}(\text{NO}_3)_2$ .

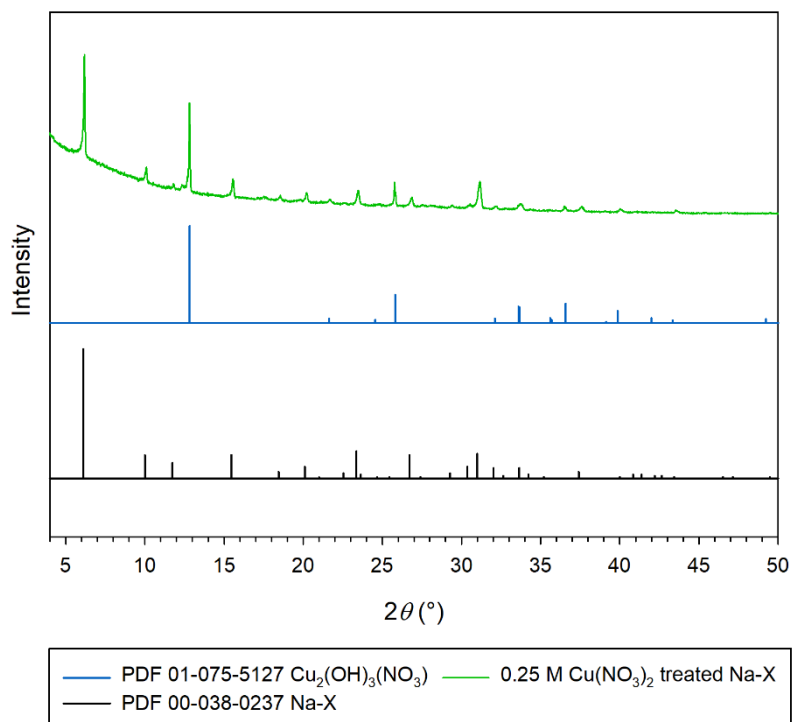


Figure 8.28. PXRD pattern recorded on the product of zeolite X treated with 0.25 M  $\text{Cu}(\text{NO}_3)_2$ .

## Appendix 5: X-ray Fluorescence Data

Table 8.1. Elemental weight fractions (wt%) of mordenite samples discussed in sections 3.3.1 – 3.3.5.

	Si (wt%)	Al (wt%)	Na (wt%)
Section 3.3.1			
TEOS system, gel Si/Al = 7.7	26.8	3.29	1.27
TEOS system, gel Si/Al = 8.3	27.7	3.27	1.29
TEOS system, gel Si/Al = 8.9	25.7	2.87	1.32
TEOS system, gel Si/Al = 9.5	27.5	2.80	2.19
Section 3.3.3			
Colloidal silica system, gel Si/Al = 7.5	27.0	3.36	1.26
Colloidal silica system, gel Si/Al = 8.8	32.9	3.45	1.28
Colloidal silica system, gel Si/Al = 10.0	28.4	2.84	1.51
Section 3.3.4			
Colloidal silica system, 5 ml ethanol added	27.6	3.58	1.54
Colloidal silica system, 10 ml ethanol added	26.2	3.10	1.87
Colloidal silica system, 15 ml ethanol added	23.0	2.40	1.62
Section 3.3.5			
TEOS system, 1 ml ethanol added	26.1	3.05	1.17
TEOS system, 2 ml ethanol added	22.7	2.22	1.29

Table 8.2. Elemental weight fractions (wt%) of mordenite samples discussed in sections 3.3.7.

	Si (wt%)	Al (wt%)	Na (wt%)	Ga (wt%)
Ga-loaded calcined MOR (pH = 2.95)	37.7	4.00	3.84	1.09
Ga-loaded calcined MOR (pH = 2.5), adjusted with HCl	35.8	3.73	3.63	0.60
Ga-loaded calcined MOR (pH = 2.5), adjusted with H <sub>2</sub> SO <sub>4</sub>	35.7	3.61	3.22	0.28
Ga-loaded uncalcined MOR (pH = 2.95)	29.3	4.39	3.56	0.81

Table 8.3. Elemental weight fractions (wt%) of zeolite Y samples employed in chapter 5, M refers to the divalent metal in materials with the general formulae:  $M_x(NH_4)_{1-2x}-Y$  or  $M_xNa_{1-2x}-Y$ .

Material	Si (wt%)	Al (wt%)	Na (wt%)	M (wt%)
H-Y	27.6	9.65	-	-
NH <sub>4</sub> -Y	26.2	8.90	-	-
Na-Y	24.1	8.64	8.10	-
Mg <sub>0.15</sub> (NH <sub>4</sub> ) <sub>0.70</sub> -Y	29.5	10.5	-	1.40
Ca <sub>0.17</sub> (NH <sub>4</sub> ) <sub>0.66</sub> -Y	29.4	10.2	-	2.68
Sr <sub>0.14</sub> (NH <sub>4</sub> ) <sub>0.72</sub> -Y	29.7	10.4	-	4.86
Ba <sub>0.21</sub> (NH <sub>4</sub> ) <sub>0.58</sub> -Y	24.7	8.96	-	9.72
Cu <sub>0.24</sub> (NH <sub>4</sub> ) <sub>0.52</sub> -Y	27.8	9.59	-	5.52
Mg <sub>0.37</sub> Na <sub>0.39</sub> -Y	24.3	8.64	2.90	2.89
Ca <sub>0.46</sub> Na <sub>0.14</sub> -Y	23.6	8.85	2.29	6.06
Sr <sub>0.45</sub> Na <sub>0.18</sub> -Y	21.9	7.34	1.10	10.6
Ba <sub>0.33</sub> Na <sub>0.44</sub> -Y	19.8	8.00	3.03	13.3
Cu <sub>0.41</sub> Na <sub>0.29</sub> -Y	24.3	9.17	2.24	8.80
(D)-NH <sub>4</sub> -Y	35.4	7.00	-	-

Table 8.4. Elemental weight fractions (wt%) of zeolite Y samples treated with 60 ppm F<sup>-</sup> NaF solutions at the specified temperature. M refers to the divalent metal in materials with the general formula:  $M_x(NH_4)_{1-2x}-Y$ .

Material	T (°)	Si (wt%)	Al (wt%)	Na (wt%)	M (wt%)
NH <sub>4</sub> -Y	25	25.0	8.75	1.02	-
Mg <sub>0.15</sub> (NH <sub>4</sub> ) <sub>0.70</sub> -Y	25	25.9	8.96	0.75	1.19
Ca <sub>0.17</sub> (NH <sub>4</sub> ) <sub>0.66</sub> -Y	25	25.2	9.01	0.59	2.36
Sr <sub>0.14</sub> (NH <sub>4</sub> ) <sub>0.72</sub> -Y	25	24.1	8.27	0.70	3.96
Ba <sub>0.21</sub> (NH <sub>4</sub> ) <sub>0.58</sub> -Y	25	26.4	9.33	1.10	8.72
Cu <sub>0.24</sub> (NH <sub>4</sub> ) <sub>0.52</sub> -Y	25	23.0	7.58	0.43	3.88
NH <sub>4</sub> -Y	40	25.8	9.22	1.04	-
Mg <sub>0.15</sub> (NH <sub>4</sub> ) <sub>0.70</sub> -Y	40	26.4	9.15	0.69	1.04
Ca <sub>0.17</sub> (NH <sub>4</sub> ) <sub>0.66</sub> -Y	40	22.8	8.27	0.43	2.44
Sr <sub>0.14</sub> (NH <sub>4</sub> ) <sub>0.72</sub> -Y	40	21.7	7.95	0.40	4.42
Ba <sub>0.21</sub> (NH <sub>4</sub> ) <sub>0.58</sub> -Y	40	23.0	8.76	0.52	9.49
Cu <sub>0.24</sub> (NH <sub>4</sub> ) <sub>0.52</sub> -Y	40	27.3	9.75	0.68	4.75

Table 8.5. Elemental weight fractions (wt%) for scaled-up zeolites employed in Chapter 6.

Material	Si (wt%)	Al (wt%)	Na (wt%)
Na-A	10.7	9.40	11.0
Na-X	12.9	9.92	11.4
Na-GME	19.0	7.95	8.51
Na <sub>0.54</sub> H <sub>0.46</sub> -MOR	22.6	2.51	1.16

Table 8.6. Elemental weight fractions (wt%) for products of dealumination treatments.

Material	Si (wt%)	Al (wt%)	Na (wt%)
(D)-GME	23.7	5.89	5.02
Na <sub>0.39</sub> H <sub>0.61</sub> -MOR	35.5	4.32	1.40
(E4)-Na-A	10.7	12.7	4.59

Table 8.7. Elemental weight fractions (wt%) for Fe<sup>3+</sup>-treated zeolite samples.

Material	Si (wt%)	Al (wt%)	Na (wt%)	Fe (wt%)
0.01 M Fe <sup>3+</sup> -treated GME	23.8	9.81	3.76	0.38
0.025 M Fe <sup>3+</sup> -treated GME	25.1	7.84	1.68	0.76
0.01 M Fe <sup>3+</sup> -treated A	11.8	12.1	3.40	8.26
0.01 M Fe <sup>3+</sup> -treated X	14.6	11.9	6.56	4.19
Fe <sup>3+</sup> -loaded Na <sub>0.54</sub> H <sub>0.46</sub> -MOR	35.4	4.30	1.32	0.12
Fe <sup>3+</sup> -loaded prismatic MOR	37.9	4.28	4.43	0.29
Fe <sup>3+</sup> -loaded spherical MOR	27.4	3.70	1.01	0.17
Fe <sup>3+</sup> -loaded Na <sub>0.39</sub> H <sub>0.61</sub> -MOR	33.7	4.08	1.36	0.06

Table 8.8. Elemental weight fractions (wt%) for zeolites A, X, GME and MOR samples following ion-exchange.

Material	Si (wt%)	Al (wt%)	Na (wt%)	M (wt%)
Ca-A	10.2	10.5	0.84	10.2
Ca-X	14.3	13.1	0.96	10.2
Ca-GME	20.9	9.38	0.18	7.00
Na/Ca-MOR	28.7	3.75	1.76	2.15
Sr-A	8.74	9.59	0.91	16.5
Sr-X	10.6	9.70	0.91	17.7
Sr-GME	17.4	7.63	0.48	11.4
Na/Sr-MOR	27.1	3.34	1.51	4.06
Ba-A	13.3	12.2	1.22	23.0
Ba-X	17.5	14.7	1.06	29.3
Ba-GME	14.9	6.73	-	21.8
Na/Ba-MOR	29.5	3.81	1.81	12.6
Cu-A	12.4	12.2	7.84	6.43
Cu-X	10.9	8.90	0.26	9.68
Cu-GME	17.6	7.78	0.25	8.96
Na/Cu-MOR	28.6	3.37	1.19	3.03

## REFERENCES

- <sup>1</sup> M. F. L'Annunziata, *Radioactivity: Introduction and History*, Elsevier, Oxford, 2007.
- <sup>2</sup> P. E. Valk, D. L. Bailey, D. W. Townsend and M. N. Maisey, *Positron Emission Tomography: Basic Science and Clinical Practice*, Springer-Verlag, London, 2003.
- <sup>3</sup> D. Parker in *Industrial Tomography*, M. Wang, Elsevier, Oxford, ch. 8, pp. 223 – 234.
- <sup>4</sup> X. Fan, D. J. Parker & M. D. Smith, *Nucl. Instrum. Methods Phys. Res., Sect. A*, 2006, **562**, 345.
- <sup>5</sup> C. Loch, B. Maziene and D. Comar, *J. Nucl. Med.*, 1980, **21**, 1971.
- <sup>6</sup> G. B. Saha, *Physics and Radiobiology of Nuclear Medicine*, Springer-Verlag, New York, 1993, p. 44.
- <sup>7</sup> R. T. M. de Rosales, C. Finucane, S. J. Mather and P. J. Blower, *Chem. Comm.*, 2011, 4847.
- <sup>8</sup> X. Fan, D. J. Parker & M. D. Smith, *Nucl. Instrum. Methods Phys. Res., Sect. A*, 2006, **558**, 542.
- <sup>9</sup> D. Kunii & O. Levenspiel, *Fluidization Engineering*, Butterworth-Heinemann, London, 1991, 2<sup>nd</sup> edn.
- <sup>10</sup> Y. Li, H. Fan and X. Fan, *Chem. Eng. Sci.*, 2014, **117**, 455.
- <sup>11</sup> P. Fede, O. Simonin and A. Ingram, *Chem. Eng. Sci.*, 2016, **142**, 215.
- <sup>12</sup> M. Van de Velden, J. Baeyens and K. Smolders, *Chem. Eng. Sci.*, 2007, **62**, 2139.
- <sup>13</sup> M. Pore, G. H. Ong, C. M. Boyce, M. Materazzi, J. Gargiuli, T. Leadbetter, A. J. Sederman, J. S. Dennis, D. J. Holland, A. Ingram, P. Lettieri and D. J. Parker, *Chem. Eng. Sci.*, 2015, **122**, 210.
- <sup>14</sup> M. Aghbashlo, R. Sotudeh-Gharebagh, R. Zarghami, A. S. Mojumdar and N. Moustoufi, *Drying Technol.*, 2015, **33**, 684.
- <sup>15</sup> K. E. Cole, A. Buffler, N. P. van der Meulen, J. J. Cilliers, J-P. Franzidis, I. Govender, C. Liu and M. R. van Heerden, *Chem. Eng. Sci.*, 2012, **75**, 235.
- <sup>16</sup> S. Tebianian, K. Dubrawski, N. Ellis, R. A. Cocco, R. Hays, S.B. Reddy Karri, T. W. Leadbeater, D. J. Parker, J. Chaouki, R. Jafari, P. Garcia-Trinanes, J. P.K. Seville and J. R. Grace, *Chem. Eng. Sci.*, 2015, **127**, 310.
- <sup>17</sup> M. Stein, Y. L. Ding and J. P. K. Seville, *Chem. Eng. Sci.*, 2002, **57**, 3649.
- <sup>18</sup> S. Tebianian, K. Dubrawski, N. Ellis, R. A. Cocco, R. Hays, S.B. Reddy Karri, T. W. Leadbeater, D. J. Parker, J. Chaouki, R. Jafari, P. Garcia-Trinanes, J. P.K. Seville and J. R. Grace, *Powder Technol.*, 2016, **296**, 45.
- <sup>19</sup> F. F. Snieders, A. C. Hoffmann, D. Cheesman, J. G. Yates, M. Stein and J. P. K. Seville, *Powder Technol.*, 1999, **101**, 229.
- <sup>20</sup> L. Atares, F. Depypere, J. G. Pieters and K. Dewettinick, *J. Food. Eng.*, 2012, **113**, 415.
- <sup>21</sup> J. M. Smith, *Chem. Eng. Res. Des.*, 1990, **68**, 3.
- <sup>22</sup> S. M. Kresta, R. Krebs and T. Martin, *Chem. Eng. Technol.*, 2004, **27**, 208.
- <sup>23</sup> Y. Saito, A. Ingram, X. Fan and J. P. K. Seville, *J. Visualization*, 2009, **12**, 291.
- <sup>24</sup> D. J. Parker and P. A. McNeil, *Meas. Sci. Technol.*, 1996, **7**, 287.

- <sup>25</sup> B. F. C. Laurent and P. W. Cleary, *Powder Technol.*, 2012, **228**, 71.
- <sup>26</sup> K. T. Lee, A. Ingram and N. A. Rowson, *Eur. J. Pharm. Biopharm.*, 2012, **81**, 666.
- <sup>27</sup> A. Guida, X. Fan, D. J. Parker, A. W. Nienow and M. Barigou, *Chem. Eng. Des. Res.*, 2009, **87**, 421.
- <sup>28</sup> B. F. C. Laurent, *Chem, Eng. Sci.*, 2005, **60**, 3805.
- <sup>29</sup> K. Cole, A. Buffler, J. J. Cilliers, I. Govender, J. Y. Y. Heng, C. Liu, D. J. Parker, U. V. Shah, M. van Heerden and X. Fan, *Powder Technol.*, 2014, **263**, 26.
- <sup>30</sup> J. C. Clark and D. J. Silvester, *Int. J. Appl. Radiat. Isot.*, 1966, **17**, 151.
- <sup>31</sup> P. Benezeth, I. I. Diakonov, G. S. Pokrovski, J. L. Dandurand, J. Schott and I. L. Khodakovskiy, *Geochim. Cosmochim. Acta.*, 1997, **61**, 1345.
- <sup>32</sup> P. Sipos, T. Megyes and O. Berkesi, *J. Solution Chem.*, 2008, **37**, 1411.
- <sup>33</sup> W. W. Rudolph and C. C. Pye, *PCCP Phys. Chem. Chem. Phys.*, 2002, **4**, 4319.
- <sup>34</sup> H. Kanno and J. Hirashi, *Phys. Chem. Lett.*, 1979, **68**, 46.
- <sup>35</sup> J. M. Newsam, *Science*, 1986, **231**, 1093.
- <sup>36</sup> L. Smart & E. Moore, *Solid State Chemistry: an introduction*, Chapman & Hall, London, 1992, ch. 5.
- <sup>37</sup> R. M. Barrer, *Zeolites and Clay Minerals as Sorbents and Molecular Sieves*, Academic Press, London, 1978.
- <sup>38</sup> S. Allen, S. Carr, A. Chapple, A. Dyer and B. Heywood, *Phys. Chem. Chem. Phys.*, 2002, **4**, 2409.
- <sup>39</sup> A. Dyer, J. A. Hriljac, N. Evans, I. Stokes, P. Rand, S. Kellet, R. Harjula, T. Moller, Z. Maher, R. Heatlie-Branson, J. Austin, S. Williamson-Owens, M. Higgins-Bos, K. Smith, L. O'Brien, N. Smith and N. Bryan, *J. Radioanal. Nucl. Chem.*, 2018, **318**, 2473.
- <sup>40</sup> K. Momma and F. Izumi, *J. Appl. Crystallogr.*, 2011, **44**, 1272.
- <sup>41</sup> S. Wang and Y. Peng, *Chem. Eng. J.*, 2010, **156**, 11.
- <sup>42</sup> J. F. Charnell, *J. Cryst. Growth*, 1971, **8**, 291.
- <sup>43</sup> Y. Mao, Y. Zhou, H. Men, J. Xie, W. Zhang and J. Wang, *New J. Chem.*, 2014, **38**, 3295.
- <sup>44</sup> *Atlas of Zeolite Framework Types*, ed. Ch. Baerlocher, L. B. McCusker and D. H. Olson, Elsevier, Amsterdam, 6<sup>th</sup> edn., 2007.
- <sup>45</sup> A. K. Cheetham, C. A. Fyfe, J. V. Smith and J. M. Thomas, *J. Chem. Soc., Chem. Commun.*, 1982, 823.
- <sup>46</sup> L. B. McCusker in *Introduction to Zeolite Molecular Sieves*, eds. J. Cejka, H. van Bekkum, A. Corma and F. Schueth, Elsevier, Amsterdam, 3<sup>rd</sup> edn., 2007.
- <sup>47</sup> R. H. Daniels, G. T. Kerr and L. D. Rollman, *J. Am. Chem. Soc.*, 1978, **100**, 3097.
- <sup>48</sup> M. Sacerdoti, E. Passaglia and R. Carnevali, *Zeolites*, 1995, **15**, 276.
- <sup>49</sup> B. R. Albert, A. K. Cheetham, J. A. Stuart and C. J. Adams, *Microporous Mesoporous Mater.*, 1998, **21**, 133.

- <sup>50</sup> U. Hakansson, L. Farth and S. Hansen, *Acta Cryst.*, 1990, **C46**, 1363.
- <sup>51</sup> C. S. Cundy and P. A. Cox, *Microporous Mesoporous Mater.*, 2005, **82**, 1.
- <sup>52</sup> *Verified Syntheses of Zeolitic Materials*, ed. H. Robson, Elsevier, Amsterdam, 2<sup>nd</sup> rev. edn., 2001.
- <sup>53</sup> A. Dyer in *Introduction to Zeolite Science and Practice*, eds. J. Cejka, H. van Bekkum, A. Corma and F. Schuth, Elsevier, Amsterdam, 3<sup>rd</sup> rev. edn., 2007, ch. 17.
- <sup>54</sup> R. P. Townsend and E. N. Coker in *Introduction to Zeolite Science and Practice*, eds. H. van Bekkum, E. M. Flanigen, P. A. Jacobs, and J. C. Jansen, Elsevier, Amsterdam, 2<sup>nd</sup> rev. edn., 2001, ch. 11.
- <sup>55</sup> P. Atkins and J. de Paula, *Atkins' Physical Chemistry*, Oxford University Press, Oxford, 9<sup>th</sup> edn., 2010.
- <sup>56</sup> E. Worch, *Adsorption technology in water treatment: fundamentals, processes and modelling*, De Gruyter, Boston, 2012, ch. 3.
- <sup>57</sup> K. Y. Foo and B. H. Hameed, *Chem. Eng. J.*, 2010, **156**, 2.
- <sup>58</sup> Q. Hu and Z. Zhang, *J. Mol. Liq.*, 2019, **277**, 646.
- <sup>59</sup> M. S. Onyango, Y. Kojima, O. Aoyi, E. C. Bernardo and H. Matsuda, *J. Colloid Interface Sci.*, 2004, **279**, 341.
- <sup>60</sup> A. R. West, *Basic Solid State Chemistry*, Wiley, Chichester, 1988, ch. 3.
- <sup>61</sup> U. Mueller, *Inorganic Structural Chemistry*, Wiley, Chichester, 1993.
- <sup>62</sup> *International Tables for Crystallography, Volume A: Space-Group Symmetry*, ed. Th. Hahn, 5<sup>th</sup> edn., 2002.
- <sup>63</sup> J. K. Cockcroft and A. N. Fitch in *Powder Diffraction: Theory and Practice*, eds. R. Dinnebier and S. Billinge, RSC Publishing, Cambridge, 2008, ch. 2.
- <sup>64</sup> E. Margui and R. van Grieken, *X-ray fluorescence spectrometry and related techniques: an introduction*, Momentum Press, New York, 2013, ch. 1.
- <sup>65</sup> Y. Leng, *Materials Characterization*, Wiley, New York, 2013, 2<sup>nd</sup> edn.
- <sup>66</sup> H. Guenther, *NMR Spectroscopy: Basic principles, concepts and applications in chemistry*, Wiley-VCH, Weinheim an der Bergstrasse, 2013, 3<sup>rd</sup> edn., ch. 2.
- <sup>67</sup> D. C. Apperley, R. K. Harris and P. Hodgkinson, *Solid-state NMR: Basic principles and practice*, Momentum Press, New York, 2012.
- <sup>68</sup> E. Lippmaa, M. Magi, A. Samoson, G. Engelhardt and A. R. Grimmer, *J. Am. Chem. Soc.*, 1980, **102**, 4889.
- <sup>69</sup> E. Lippmaa, M. Magi, A. Samoson, M. Tarmak and G. Engelhardt, *J. Am. Chem. Soc.*, 1981, **103**, 4992.
- <sup>70</sup> G. Engelhardt, U. Lohse, A. Samoson, M. Magi, M. Tarmak and E. Lippmaa, *Zeolites*, 1982, **2**, 59.
- <sup>71</sup> Y. Tanizawa, H. Tsuchikanem, K. Samawura and T. Suzuki, *J. Chem. Soc. Faraday Trans.*, 1991, **87**, 2235.

- <sup>72</sup> D. C. Harris, *Quantitative Chemical Analysis*, 2012, W. H. Freeman and Company, New York, 2010, 8<sup>th</sup> edn., p. 325.
- <sup>73</sup> M. S. Frant and J. W. Ross, *Science*, 1966, **154**, 1553.
- <sup>74</sup> F. J. Holler and S. R. Crouch, *Skoog and West's Fundamentals of Analytical Chemistry*, Cengage Learning, 2014, 9<sup>th</sup> edn., ch. 28.
- <sup>75</sup> P. Simonic and T. Armbruster, *Am. Mineral.*, 2004, **89**, 421.
- <sup>76</sup> T. Selvam, G. T. P. Mabande, W. Schwieger, Y. Sugi, I. Toyama, Y. Kubota, H. S. Lee and J. H. Kim, *Catal. Lett.*, 2004, **94**, 17.
- <sup>77</sup> L. Li, Q. Wang, H. Liu, T. Sun, D. Fan, M. Yang, P. Tian and Z. Liu, *ACS Appl. Mater. Interfaces*, 2018, **10**, 32239.
- <sup>78</sup> G. J. Kim and W. S. Ahn, *Zeolites*, 1991, **11**, 745.
- <sup>79</sup> T. Sano, S. Wakabagashi, Y. Oumi and T. Uozimi, *Microporous Mesoporous Mater.*, 2001, **46**, 67.
- <sup>80</sup> Y. Yuan, L. Wang, H. Liu, P. Tian, M. Yang, S. Xu and Z. Liu, *Chin. J. Catal.*, 2015, **36**, 1910.
- <sup>81</sup> M. A. Cambor, A. Mifsud and J. Perezpariente, *Zeolites*, 1991, **11**, 792.
- <sup>82</sup> U. Khalil and O. Murata, *Microporous Mesoporous Mater.*, 2010, **132**, 211.
- <sup>83</sup> ICDD (2019). PDF-4+ 2019. International Centre for Diffraction Data, Newtown Square, PA, USA.
- <sup>84</sup> J. Laugier and B. Bochu, *LMGP Suite of Programs*, Laboratoire des Matériaux et du Génie Physique, France, 2002.
- <sup>85</sup> SigmaPlot Version 14.0.
- <sup>86</sup> C. A. Schneider, W. S. Rasband and K. W. Eliceiri, *Nat. Methods*, 2012, **9**, 671.
- <sup>87</sup> M. Rosenblatt, *Ann. Math. Stat.*, 1956, **27**, 832.
- <sup>88</sup> E. Parzen, *Ann. Math. Stat.*, 1962, **33**, 1065.
- <sup>89</sup> *US Pat.*, US5336824A, 1994.
- <sup>90</sup> R. Fricke, H. Kosslick, G. Lischke and M. Richter, *Chem. Rev.*, 2000, **100**, 2303.
- <sup>91</sup> G. T. Kerr, *Zeolites*, 1983, **3**, 295.
- <sup>92</sup> M. Kragovic, A. Dakovic, M. Markovic, J. Krstic, G. D. Gatta and N. Rotiroti, *Appl. Surf. Sci.*, 2013, **283**, 764.
- <sup>93</sup> C. S. Jeon, K. Baek, J. K. Park, Y. K. Oh and S. D. Lee, *J. Hazard Mater.*, 2009, **163**, 804.
- <sup>94</sup> O. A. Annunziata and L. B. Pierella, *Catal. Lett.*, 1993, **19**, 143.
- <sup>95</sup> S. Ferchiche, J. Warzywoda and A. Sacco, *Int. J. Inorg. Mater.*, 2001, **3**, 773.
- <sup>96</sup> B. W. Garney, *Fusion Technol.*, 1992, **21**, 604.
- <sup>97</sup> G. Scott, R. W. Thompson, A. G. Dixon and A. Sacco, *Zeolites*, 1990, **10**, 44.
- <sup>98</sup> A. Yu. Efimov, V. P. Petranovsky, M. A. Fedotov, M. K. Khripun and L. A. Myund, *Zh. Strukt. Khim.*, 1993, **34**, 63.

- <sup>99</sup> Z. A. D. Lethbridge, J. J. Williams, R. I. Walton, K. E. Evans and C. W. Smith, *Microporous Mesoporous Mater.*, 2005, **79**, 339.
- <sup>100</sup> *US Pat.*, US5283047A, 1994.
- <sup>101</sup> D. P. Serrano and R. van Grieken, *J. Mater. Chem.*, 2001, **11**, 2391.
- <sup>102</sup> E. Garcia-Romero and M. Suarez, *Mineral. Mag.*, 2018, **82**, 171.
- <sup>103</sup> J. A. Mandarino and V. Anderson, *Monteregion Treasures: The minerals of Mont-Saint Hilaire, Quebec*, Cambridge University Press, Cambridge, 1989, p. 96.
- <sup>104</sup> G. T. Kokotailo and S. L. Lawton, *Nature*, 1964, **203**, 621.
- <sup>105</sup> M. Adem, T. Sani, Y. Chebude, G. Fetter, P. Bosch and I. Diaz, *Bull. Chem. Soc. Ethiop.*, 2015, **29**, 53.
- <sup>106</sup> M. Maruthamuthu and A. Sivasamy, *Fluoride*, 1994, **27**, 81.
- <sup>107</sup> L. G. Hortiguela, A. B. Pinar, J. P. Pariente, T. Sani, Y. Chebude and I. Diaz, *Microporous Mesoporous Mater.*, 2014, **193**, 93.
- <sup>108</sup> Y. Sun, Q. Fang, J. Dong, X. Cheng and J. Xu., *Desalination*, 2011, **277**, 121.
- <sup>109</sup> M. S. Onyango, Y. Kojima, A. Kumar, D. Kuchar, M. Kubota and H. Matsuda, *Sep. Sci. Technol.*, 2006, **41**, 683.
- <sup>110</sup> S. Samatya, U. Yuksel, M. Yuksel and N. Kabay, *Sep. Sci. Technol.*, 2007, **42**, 2033.
- <sup>111</sup> X. Fang, Q. Wang, A. Zheng, Y. Liu, L. Lin, H. Wu, F. Deng, M. He and P. Wu, *Phys. Chem. Chem. Phys.*, 2013, **15**, 4930.
- <sup>112</sup> Y. Yang, J. Ding, B. Wang, J. Wu, C. Zhao, G. Gao and P. Wu, *J. Catal.*, 2014, **320**, 160.
- <sup>113</sup> X. Fang, Q. Wang, A. Zheng, Y. Liu, Y. Wang, X. Deng, H. Wu, F. Deng, M. He and P. Wu, *Catal. Sci. Technol.*, 2012, **2**, 2433.
- <sup>114</sup> X. Lu, W. Zhou, Y. Guan, A. Liebens and P. Wu, *Catal. Sci. Technol.*, 2017, **7**, 2624.
- <sup>115</sup> R. Le Van Mao, T.S. Le, M. Fairbairn, A. Muntasar, S. Xiao and G. Denes, *Appl. Catal. A*, 1999, **185**, 41.
- <sup>116</sup> S. Kowalak, E. Szymkowiak and M. Laniecki, *J. Fluorine Chem.*, 1999, **93**, 175.
- <sup>117</sup> I. Ogino, M. Nigra, S. Hwang, J. Ha, T. Rea, S. I. Zones and A. Katz, *J. Am. Chem. Soc.*, 2011, **133**, 3288.
- <sup>118</sup> H. M. Kao and Y. Liao, *J. Phys. Chem. C*, 2007, **111**, 4495.
- <sup>119</sup> A. Bolshakov, N. Kosinov, D. E. Romero Hidalgo, B. Mezari, A. J. F. van Hoof and E. J. M. Hensen, *Catal. Sci. Technol.*, 2019, **9**, 4239.
- <sup>120</sup> J. Prech, K. N. Bozhilov, J. El Fallah, N. Barrier and V. Valtchev, *Microporous Mesoporous Mater.*, 2019, **280**, 297.
- <sup>121</sup> G. T. Kerr, *J. Phys. Chem.*, 1968, **72**, 2594.

- <sup>122</sup> A. S. Cattaneo, R. P. Lima, C. E. Tambelli, C. J. Magon, V. R. Mastelaro, A. Garcia, J. E. de Souza, A. S. S. de Camargo, C. C. de Araujo, J. F. Schneider, J. P. Donoso and H. Eckert, *J. Phys. Chem. C*, 2008, **112**, 10462.
- <sup>123</sup> J. G. Reynolds and J. D. Belsher, *J. Chem. Eng. Data*, 2017, **62**, 1743.
- <sup>124</sup> Y. Hong and J. J. Fripiat, *Microporous Mater.*, 1995, **4**, 323.
- <sup>125</sup> C. E. Housecroft and A. G. Sharpe, *Inorganic Chemistry*, Pearson Education Limited, Harlow, 2001.
- <sup>126</sup> R. E. Youngman and S. Sen, *J. Non-Cryst. Solids*, 2004, **349**, 10.
- <sup>127</sup> H. Koller, A. Wölker, H. Eckert, C. Panz and P. Behrens, *Angew. Chem. Intl. Ed.*, 1997, **36**, 2823.
- <sup>128</sup> L. Delmotte, M. Soulard, F. Guth, A. Seive, A. Lopez and T. L. Guth, *Zeolites*, 1990, **10**, 778.
- <sup>129</sup> G. Zhang, B. Wang, W. Zhang, M. Li and Z. Tian, *Dalton Trans.*, 2016, **45**, 6634.
- <sup>130</sup> E. Y. Chekmenev, S. K. Chow, D. Tofan, D. P. Weitekamp, B. D. Ross and P. Bhattacharya, *J. Phys. Chem. B*, 2008, **112**, 6285.
- <sup>131</sup> T. R. Krawietz, P. Lin, K. E. Lotterhos, P. D. Torres, D. H. Barich, A. Clearfield and J. F. Haw, *J. Am. Chem. Soc.*, 1998, **120**, 8502.
- <sup>132</sup> Ed. D. R. Lide, *CRC Handbook of Chemistry and Physics*, CRC Press, Boca Raton, FL, 73<sup>rd</sup> ed., 1973.
- <sup>133</sup> M. Boveri, C. Marquez-Alvarez, M. A. Laborde and E. Sastre, *Catal. Today*, 2006, **114**, 217.
- <sup>134</sup> M. J. Kim, M. S. Jeong, Y. Kim and K. Seff, *Microporous Mesoporous Mater.*, 1999, **30**, 233.
- <sup>135</sup> A. Zheng, S. Liu and F. Deng, *J. Phys. Chem. C*, 2009, **113**, 15018.
- <sup>136</sup> H. P. Ebrahimi and M. Tofazzoli, *Concepts Magn. Reson., Part A*, 2012, **40**, 192.
- <sup>137</sup> R. Szostak in *Introduction to Zeolite Science and Practice*, ed. H. van Bekkum, E. M. Flanigen, P. A. Jacobs and J. C. Jansen, Elsevier, Amsterdam, 2<sup>nd</sup> edn, 2001, ch. 6.
- <sup>138</sup> F. A. Cotton and G. Wilkinson, *Advanced Inorganic Chemistry*, John Wiley & Sons, New York, 5<sup>th</sup> edn., 1988, p. 717.
- <sup>139</sup> N. G. Chernorukov, Yu. N. Mikhailov, A. V. Knyazev, A. S. Kanishcheva and E. N. Bulanov, *Russ. J. Inorg. Chem.*, 2005, **50**, 775.
- <sup>140</sup> G. Sethia, R. S. Somani and H. C. Bajaj, *RSC Adv.*, 2015, **5**, 12773.
- <sup>141</sup> D. W. Breck, W. G. Eversole, R. M. Milton, T. B. Reed and T. L. Thomas, *J. Am. Chem. Soc.*, 1956, **78**, 5963.
- <sup>142</sup> J. Sarkany, J. L. d'Itri and W. H. M. Sachtler, *Catal. Lett.*, 1992, **16**, 241.
- <sup>143</sup> C. M. Flynn, *Chem. Rev.*, 1984, **84**, 31.
- <sup>144</sup> A. B. Ilyukhin and S. P. Petrosyants, *Crystallogr. Rep.*, 2001, **46**, 845.
- <sup>145</sup> S. Ishii, K. Tago and K. Senoo, *Appl. Microbiol. Biotechnol.*, 2010, **86**, 1281.
- <sup>146</sup> T. Fang, W. Shang, C. Liu, J. Xu, D. Zhao, Y. Liu and A. Ye, *Anal. Chem.*, 2019, **91**, 9932.
- <sup>147</sup> S. Colin, *Microfluidics*, ISTE, London, 2010.
- <sup>148</sup> J. Wang, P. H. Chao and R. M. van Dam, *Lab Chip*, 2019, **19**, 2415.